An Investigation of Gauze Supported Platinum Alumina and Cobalt Supported Oxide Oxidation Catalysts

By

Michael James Ronane, B.Sc. (Hons.)

A Thesis presented to Dublin City University for the degree of Master of Science

This work was carried out under the supervision of Dr. Michael Tiernan and Dr. Odilla Finlayson, School of Chemical Sciences, at Dublin City University.

September 2005.

I hereby certify that this material, which I now submit for assessment on the programme of study leading to the award of M.Sc. is entirely my own work and has not been taken from the work of others save and to the extent that such work has been cited and acknowledged within the text of my work.

Signed: Michael Ronane ID: 99144948

Michael Ronane

Date: 19/09/05

Table of Contents

Abstract

The aim of this research involved preparation and optimisation of Pt/Al_2O_3 gauze supported catalysts with high thermal stability and surface area with a well-dispersed layer of Pt. Preparation involved nucleation/whiskering of an FeAl metallic alloy substrate forming hair like crystal of Al_2O_3, followed by application of alumina washcoat support onto the crystals. The washcoated substrate support was then impregnated with an active phase material (i.e. Pt metal). Evaluation and characterisation of the metallic substrate support (i.e. gauze material) onto which the alumina support and Pt were impregnated were investigated with a view to developing, optimizing and scale up of the process to pilot plant for commercial scale. Catalysts characterisation was carried out using AAS, BET surface area (N_2 physisorption) to determine metal loadings and surface area of the substrate and alumina washcoat supports. Metal surface area, Pt dispersion and metal particle size together with activity of the Pt supported catalysts were measured using Pulse chemisorption and combustion activity techniques. In addition particle size measurement of alumina (i.e. Puralox powders) employed in the washcoat support were investigated using Malvern Mastersize Analyser, in a view to discover if a correlation between surface area and thermal stability of the washcoat support existed. It was found a smaller particle size washcoat solution produce a more thermally stable support material. Finally the use of Scanning electron microscopy (SEM) and Energy dispersive X-ray analysis (EDX) was used in the surface and subsurface characterisation of both the whiskered gauze (including whiskering under different atmospheres and conditions) and final Pt/Al_2O_3 prepared catalysts.

The second area of research involved preparation and characterisation of various supported and unsupported single metal oxide combustion catalysts as alternatives to the more expensive noble metal catalysts. The investigation reports on the potential use of supported and unsupported cobalt oxides for the combustion of methane. Particular emphasis is placed on the role played by various thermal analysis techniques in the elucidation of factors which affect catalyst performance.

Two combined thermal analysis-mass spectroscopy techniques have been used to ascertain the effects of various support materials on the preparation and subsequent

combustion activity of supported cobalt oxide catalysts. Both techniques used involved small sample masses in order to minimise temperature and pressure gradient throughout the sample during reaction as the sample temperature was increased at a linear heating rate. Temperature programmed reduction (TPR) techniques employed not only reveal reduction, but also distinguish it from the adsorption (or evolution) of the H_2 and the loss of adsorbed water. The thermal induced decomposition of supported and unsupported cobalt nitrate hexahydrate was studied using solid insertion probe mass spectrometer (SIP-MS) system operating under high vacuum. The support material was found to affect the decomposition process significantly. In particular, the decomposition of cobalt nitrate dispersed on γ–Al_2O_3 occurred via a markedly altered process in comparison with the unsupported nitrate. The ZrO_2 and CeO_2 supports both exhibited a less pronounced effects on the decomposition process. After calcinations of the dispersed cobalt nitrate species, methane combustion activity was found to be much lower for the alumina-supported samples relative to the other supports used. A combined temperature-programmed reduction-mass spectrometry (TPR-MS) technique was used to elucidate a correlation between the catalysts activity and reducibility. Constant thermal rate analysis (CRTA) was also used to investigate the reduction of Co_3O_4/CeO_2.

The main conclusion from the research found the use of cobalt as a viable alternative to, noble metal combustion catalysts. Deactivation problems due to sintering of the active Co_3O_4 phase and reaction with the alumina support forming inactive mixed oxides (i.e. $CoAl_2O_4$ spinel) were also establish. Cobalt oxide supported on ceria or zirconia as well as cerium support were shown to be a highly active catalyst for the combustion of CH_4. However, in both cases deactivation was observed upon exposure to the reaction mixture which maybe associated with sintering or the conversion of Co_3O_4 to a less active CoO phase. However, despite such problems with the existing formulation, research into the use of Co_3O_4 may provide a greater understanding of the origins to low-temperature combustion activity and design of new automotive exhaust applications in the drive to develop new catalytic technologies.

Acknowledgements

I wish to thank my supervisors, Dr. Odilla Finlayson and Dr. Michael Tiernan, for they support and guidance. I would also like to thank my industrial sponsors Catalytic Industries for the funding throughout my studies. May I also express my gratitude to my fellow postgraduate and the academic and technical staff in the School of Chemical Science

I would like to thank in particular Mairead Feeley, Wasim Bashirs, and Orla Kelly for they help and support through my years in Dublin City University.

May I also pay a heartfelt word of gratitude to my family and friends, especially my parents for they encouragement, drive and help. Thank you.

Chapter 1

Catalytic Oxidation of Hydrocarbons and Thermally Stable Support Materials.

General Introduction

Catalysts are now an essential component of the chemical industry as without them many reactions would proceed more slowly, or less efficiently. Catalysts are widely used in reactions involving total and partial oxidation and can be classified as either heterogeneous catalysts, homogeneous catalysts or biological catalysts.

Industrial oxidation processes over heterogeneous catalysts include the production of raw materials, destruction of industrial waste, treatment of automotive exhaust gases, production of fuels that power our engines and removal of environmental pollutants. The use of heterogeneous catalysts provides many advantages over the use of alternative processes (e.g. flame combustion) [1]:

- Reactions can be initiated at lower temperatures.
- The product and catalysts can be easily separated.
- It allows for better control of oxidation over a wider range of fuel – air ratios.
- Produces less emissions of hazardous material compared with flame combustion.
- In some cases, catalytic process can provide improved fuel efficiency.

The main disadvantages encountered with the use of these catalysts are (a) that the main catalyst constituents (the noble metals Pt, Pd and Rh) are rare and expensive (b) the high operating temperatures employed in the process can lead to poisoning and sintering of the active phase. This can result in deactivation and reduced selectivity. (c) In the case of supported catalysts, thermal degradation of the support material can produce a gradual decline in performance (i.e. deactivation) [1, 14-15].

The main criteria required when producing an efficient combustion catalyst for any process include high catalytic activity, high thermal stability and good resistance to poisons. The latter criteria is of little importance when dealing with applications involving high operating temperatures of 1100-1400^{o}C, as at these temperatures common poisons, such as sulphur and lead compounds, show little tendency to form stable compounds with the catalysts surface due to their high volatility [14]. In addition, when operating at such high temperatures, differences in specific activity of different materials

is negligible, thus high activity may not play a major factor in the selection of catalysts [14]. This thesis is focused on the catalytic total oxidation of iso-butane and propane, using alternative catalysts. The main part of the work involved investigation, preparation and optimisation of a noble metal catalyst supported on metal gauze material. The second part of the work involved the investigation of single metal oxide catalyst, namely cobalt, as oxidation catalysts as an alternative to the noble metal catalysts.

The thesis consists of four chapters. Chapter one is a literature review on catalytic combustion, concentrating on the total oxidation of alkanes over noble metals, perovskites and single metal oxides. Metallic supports are reviewed including whiskering and washcoating. Chapter two details the analytical and characterisation techniques employed in analysis of the Pt/Al_2O_3 catalysts used in this study.

Chapter three comprises the bulk of the work carried out in this research project. It details the preparation variables and characterisation results for the catalysts. The use of metallic gauze as a support was investigated and its pre-treatment was optimised. An alumina washcoat was added to the metal gauze and the preparation of this material was examined in detail. The physical properties of the alumina materials (i.e. puralox powders SCFa-250 and SCFa-140) using XRD is examined. Total metal content, surface properties and propane combustion activity of both fresh and aged Pt/Al_2O_3 catalysts supported on FeAl alloy gauze were investigated. Scanning electron microscopy with EDX-ray analysis was used to analyse the morphology and nature of the substrate support. The activities of Pt catalysts supported on Al_2O_3 and on metallic gauze were compared.

The final chapter describes the preparation, characterisation and activity of Co/Al_2O_3, Co/ZrO_2 and Co/CeO_2 catalysts involving BET surface area, surface analysis, thermal analysis and propane activity measurements.

1.0 Introduction

Catalytic combustion has received considerable attention during the last decade as an attractive alternative to conventional flame combustion for producing thermal energy [1]. It allows efficient and complete combustion of fuels at temperatures lower than that achieved through conventional thermal combustion and without yielding undesired by-products in the process, such as unburned hydrocarbons, carbon monoxide, nitrous oxides and particulates [2, 3]. One of the most interesting and potential applications of catalytic combustion is in the natural gas fuelled burners for gas turbine power generation [4]. Application of catalytic combustion in stationary and mobile systems has also shown significant advantages in controlling pollutant emissions and provides a more efficient use of energy sources. The lower operating temperatures in catalytic combustion preclude the formation of toxic compounds such as nitrous oxides from nitrogen and oxygen. As a result, this technology has been utilised in incinerators as catalytic combustion typically operates at temperatures below 400^0C. The main advantages offered by catalytic combustion over thermal combustion are:

- Catalytic combustion can be carried out over a wide range of fuel to air ratio at low temperatures;
- The use of low temperature results in significantly lower NO_x emission levels than would be achievable with conventional flame combustors.

The catalysts used for combustion are mainly noble metals (i.e. Pt, Pd and Rh or combinations) supported on materials such as pellets, honeycomb ceramic monoliths, parallel plates, filter pads and expanded metal gauzes or sintered metals. A particular advantage of using precious metal catalysts in supported form is that the support disperses the metal over a greater surface area allowing optimisation of the metal sites. However, supported noble metal and simple metal oxide catalysts, are not resistant to the high temperatures thus limiting their usage in high temperature applications [1, 14]. As a result, the development of new materials as supports to withstand these high temperatures in a stream of gases is needed.

It has been found that structured catalytic materials, for example made from woven fibres, or expanded metal such as gauze materials; present an innovative alternative in the designing of catalyst supports for combustion reactors [6-10]. These materials are used because they combine mechanical elasticity and resistance to thermal stress under the harsh operating conditions.

In the next section, the mechanisms involved in the catalytic combustion process will be discussed with reference to kinetics of the gas phase reaction.

1.1 Principles of catalytic combustion

The aim of introducing a catalyst into the combustor is to carry out heterogeneous oxidation on the surface of the catalyst. By suitable choice of a catalyst, one can ensure that the activation energy for the heterogeneous reaction is much lower than that for the purely homogeneous reaction. As a result, heterogeneous oxidation rates can be obtained with fuel concentration and temperatures much lower than those needed for the homogeneous reaction to occur.

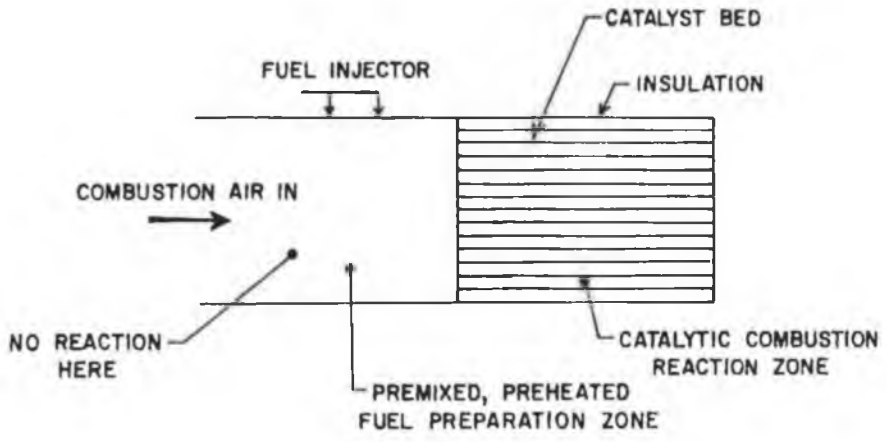

Fig.1.1: a schematic diagram of the catalytic combustor [1]

Fig. 1.1 shows a schematic diagram of a combustion catalyst system. The chemical kinetics of importance in catalytic combustors involves both heterogeneous as well as homogeneous reactions.

Fig. 1.2 below illustrates an observed rate for a heterogeneous catalytic oxidation reaction as a function of temperature. At low temperature, the reactions are dominant on the catalyst surface. Although the overall reaction can be controlled by the surface kinetics or mass transfer, the reaction still occurs on the catalyst surface and is said to be surface kinetically controlled (see region A, in Fig 1.2). As the temperature is raised, the bulk gas temperature is high enough that the homogenous gas phase reaction and catalytic reaction occur simultaneously. At this point the reaction is said to be heat and mass transfer

controlled (see region B, in Fig 1.2). In this region (B), the reaction rate increases exponentially with temperature. Under these conditions any specific activity of a solid catalyst becomes of secondary importance. At this point it was noted that reaction rate was insensitive to temperature change. As the exothermic surface reaction proceeds, the temperature increases to a point, where the bulk gas temperature reaches a maximum that the gas phase reaction occurs simultaneously with the catalytic reaction and complete combustion occurs (see region C, in Fig 1.2).

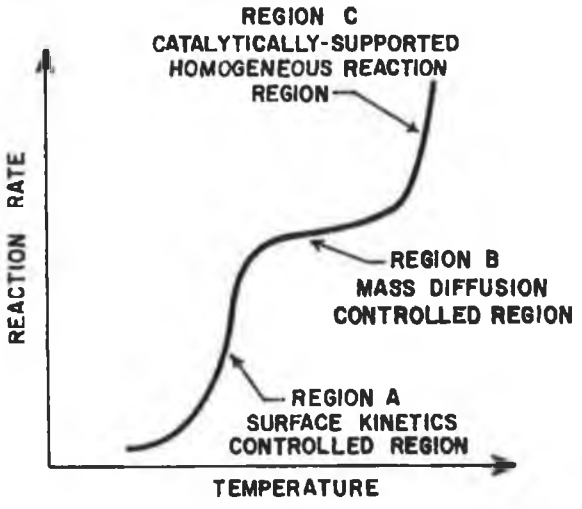

Fig.1.2: Overall reaction rate vs. temperature for a typical reactor used in catalytic combustion. Regions A, B, and C denote regimes of heterogeneous kinetic control, mass transfer control and homogenous kinetic control respectively or alternatively A: ignition; light-off; B: mass transfer limitation; C: homogenous reaction. [1].

The substrate in the catalytic combustors has been found to initiate and stabilise the combustion process. The surface reactions, coupled with the large thermal inactivity of the bed, enable the catalytic combustor to have stable, high combustion rates over a range of stoichiometric ratios. The low temperatures employed in the operations of catalytic combustors to carry out combustion at low fuel concentration diminish the emissions of toxic NO_x. In reducing the combustion temperature, the emission of CO and hydrocarbons generally increased. Several authors found that the rate of major reactions responsible for the oxidation of $CO \rightarrow CO_2$ decreased as the temperature decreased [11].

In conclusion, it can be stated that at low temperatures the importance of the catalytic component is a major factor, whereas the support determines the high temperature behaviour.

In the next section, oxidation catalysts and a survey on the different metal groups (i.e. noble metals and transition metal oxides) will be discussed briefly.

1.2 Introduction to Oxidation Catalysis

Catalytic oxidation, both partial and complete, is an important process for such reactions as the partial oxidation of ethene and propene, ammoxidation of propene to acrylonitrile, maleic anhydride production, production of sulphuric acid, and the oxidation of hydrocarbons in automotive exhaust systems.

Industrial catalytic oxidation reactions are carried out at high reactant concentration over a variety of supported metal catalysts. Some typical industrial catalytic oxidation reactions are represented below.

$2NH_3 + 5/2O_2 \longrightarrow 2NO + 3H_2O$ Pt - Rh wire gauze 810 - 850^{0}C

Hydrocarbon + $O_2 \longrightarrow CO_2 + H_2O$ (Automotive exhaust) Pt-Pd-Rh on cordierite or mullite 400-600^{0}C

For total oxidation a highly active, non-selective catalyst is required [15]. Basically two types of conventional catalyst are used for oxidation reactions, namely noble metals and metal oxides (supported and unsupported). Oxidation reactions have always been carried out over either noble metals or transition metal oxides. Zwinkels and Järas however, reported that noble metals have been applied almost exclusively to complete catalytic oxidation of hydrocarbons, whereas different transition metals have found application in both selective (e.g. V_2O_5) and complete oxidation (e.g. Co_3O_4) [1]. The mechanism of oxidation differs over noble metals and metal oxide catalysts. Also, different metal oxide species may undergo an alternative oxidation reaction path to that of the parent oxide.

Metal oxide catalysts are defined as oxides of metals in groups III-B through II-B of the periodic table. These oxides are characterised by high electron mobility and positive oxidation states. These catalysts are generally less active than the supported noble metals, but are somewhat more resistant to poisons. This poison resistance may be due to the high active surface of the metal oxides compared to the noble metal catalyst [13]. The high surface areas of supported oxides play a primary role in the high oxidation activities. Golodets divided the metal oxides by their stability [13]. Those forming the most stable oxides (ΔH^0_{298} > 65 Kcal/g-mole 0) are the alkali and alkaline earth metals, such as Sc,

Ti, Cr, Mn, the rare earth metals and the actinides, Ge, In, Sn, Zn, and Al. Those oxides with intermediate stability (ΔH^0_{298} = 40-65 Kcal/g-atom 0) include Fe, Co, Ni, Cd, Sb, and Pb. Oxides that are unstable (ΔH^0_{298} < 40 Kcal/g-atom 0) are the noble metals Ru, Rh, Pd, Pt, Ir, Au, and Ag.

The classification of oxide catalysts by oxide stability suggests there is some optimum level of metal oxygen interaction in oxide catalysts. This is because the catalytic activity of a metal oxide catalyst is inversely related to the strength of chemisorption, provided the adsorption is sufficiently strong for high surface coverage [14]. This suggests a relationship exists between adsorption strength and catalytic activity.

Trimm and several authors, [12, 16-24] reported such a correlation between the rate of hydrocarbon oxidation and adsorption strength. This correlation is represented in Fig 1.3 as a so-called volcano plot. This is due to the fact that catalytic activity of a catalyst is inversely proportional to the strength of the chemisorption of the reactants on the surface provided that the adsorption is sufficiently strong for the reactants to achieve high surface coverage [14].

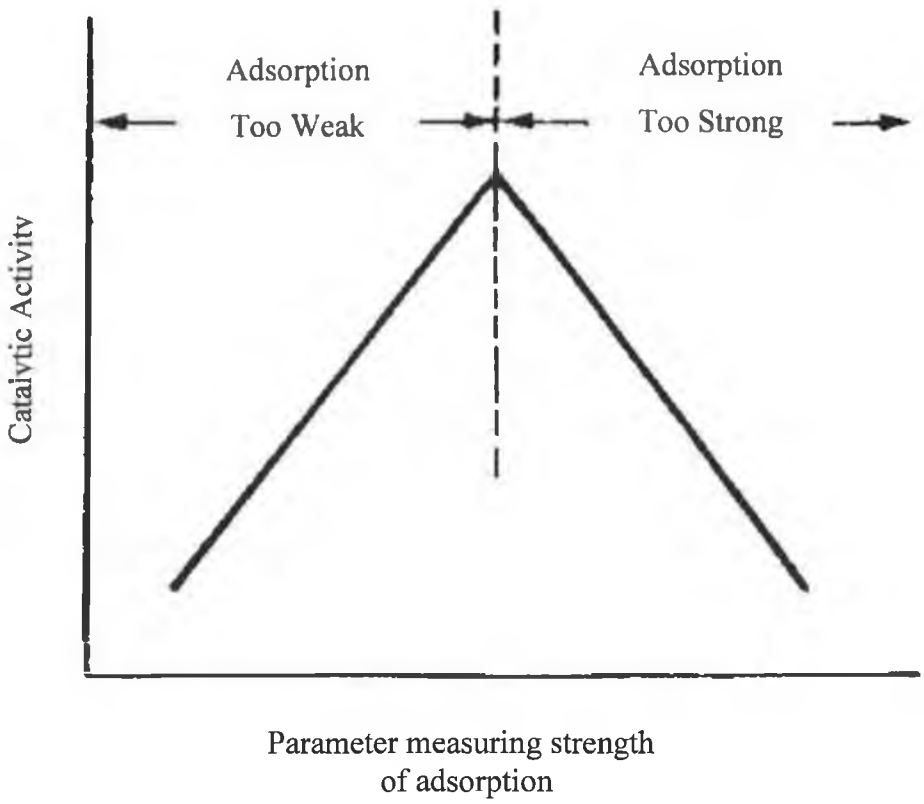

Fig.1.3: illustrates the volcano plot of adsorption of reactants versus catalytic activity [14].

The volcano plot diagram can be explained as follows: if the reactants are weakly adsorbed, then only a small portion of the surface is covered and few intermediates can be formed, resulting in low activity. However, if the reactants are strongly chemisorbed, then the adsorbed species remain on the surface, resulting in deactivation of the catalyst as the active sites are irreversibly covered (this is one definition of poisoning) [14].

Metal oxides catalysts can generally be divided into 3 groups in so far as catalytic reactions are concerned [15]. These are n-type semiconductors, p-type semiconductors and insulators. The basis for this classification was electrical conductivity, which is related to their catalytic activity.

In n-type metal oxides, electrical conductivity arises by means of quasi-free electrons that exist because of an excess of electrons present in the lattice. However, in general, n-type metal oxides are not active towards oxidation. Spivey reported a notable exception in vanadium pentoxide (V_2O_5) [15]. The p-type oxides are active oxidation catalysts with

electron deficient lattices and conduct electrons by means of positive holes. Insulators have very low electrical conductivity due to the stoichiometric metal oxygen ratio in the lattice and very low mobility of electron or positive holes mobility and are generally not active, but have been used as catalyst supports [15].

The electrical and chemical properties of n-type and p-type conductors differ on heating in air, the n-type loses oxygen and the p-type gains oxygen. Fierro and de la Banda discuss quantitatively the behaviour of oxygen desorption on various metal oxides and found that oxygen adsorption sites were more easily reduced on the surface of less stable metal oxides [65]. Oxygen adsorption occurs more rapidly on p-type oxides, because electrons are easily removed from the metal cation forming active species such as O^-; on n-type oxides, oxygen adsorption occurs on pre-reduced surface only, forming lattice oxide ions O^{2-}. This difference leads to a profound difference in oxidation reactions. Because adsorbed oxygen species are more reactive than lattice oxide ions, p-type oxides are generally more active, especially for deep oxidation reactions. Bond demonstrated the differences between these oxides catalyst, using the mechanism for CO oxidation [14], as shown below (a) and (b).

On p-type oxides such as NiO, adsorbed O^- formed upon oxygen adsorption, reacts with CO via:

(a) $O_2 + 4Ni^{2+} \rightarrow 4Ni^{3+} + 2O^{2-}$

$CO_{(g)} \rightarrow CO_{(ads)}$

$[O^- \text{---- } Ni^{3+}] + CO_{(ads)} \rightarrow CO_{2\,(ads)} + Ni^{2-}$

$CO_{2\,(ads)} \rightarrow CO_{2\,(g)}$

The mechanism of CO oxidation occurs via lattice O^{2-}, on n-type oxides such as ZnO:

(b) $CO + 2O^{2-} \rightarrow CO_3^{2-} + 2e^-$

$CO_3^{2-} \rightarrow CO_2 + O^{2-}$

Followed by oxide regeneration:

$2e^- + Zn^{2+} \rightarrow Zn$

$Zn + O_2 \rightarrow 2Zn^{2+} + O^{2-}$

The mechanism of reaction of base metals for oxidation of CO and hydrocarbons requires the metal ions to assume more than one valence state and to participate in the reduction-oxidation reaction. Sokolovskii stated two requirements regarding oxidation reactions on solid oxide catalysts [26].

(a) For efficient oxidation the catalyst had to provide a high primary rate of oxygen activation. Therefore, the catalyst had to be able to donate or accept electrons and have a large number of active sites to coordinate molecular oxygen. He stated that metal oxides with unfilled 3d configurations exhibited these properties.
(b) The catalyst must provide a slow transformation of active oxygen to lattice oxygen. For this situation to occur the reactant composition and reaction temperature had to provide a sufficiently low concentration of oxygen vacancies in the oxide in order to decrease the rate of the active to lattice oxygen transition.

The oxides of transition metals have been found to be the most active of the simple oxides for oxidation activity [27]. The activity of these metal oxide catalysts were determined by the d-shell electron configuration [28]. Metal oxides with 3, 6 and 8 d-electrons showed maximum activity, while minimum activity is seen for zero, 5 and 10 d-electrons. The transition metal oxides of Cr_2O_3 and Co_3O_4 show peaks of activity [29]. Mixtures of oxides have been reported to exhibit greater stability and activity compared to single oxides [30, 31, 32]. For example, Cr_2O_3-Co_3O_4 was found to suppress the

formation of nitrogen oxides from fuel-bound nitrogen. This is of importance in catalytic combustion applications as the low specific activity and higher ignition temperature of the metal oxides are a disadvantage. Among the oxides, only those that are refractory and can maintain activity at high temperatures have potential applications as combustion catalysts. Co_3O_4 has been the most active catalyst for the oxidation of CO and hydrocarbons with NiO, Cr_2O_3 and CuO as promising alternative catalysts [1, 30, 33]. The binary transition metal catalyst of Cr_2O_3-Co_3O_4 supported on an alumina washcoated ceramic support is active for the combustion of propane-air stoichiometric mix [30, 33]. This catalyst under 400hrs operation at temperatures of up to 1100^0C showed significant resistance to deactivation [30, 33]. Recently, considerable attention has been focused on the use of perovskites as catalysts for high temperature applications due to their high activity and considerable thermal stability and poison resistance [40-46]. The use of monolithic perovskites [47, 48], have also received attention in low-pressure drop systems such as automobile exhaust systems. For example, catalysts comprising of La_2O_3-Cr_2O_3 perovskite structure and NiO appear to be promising even at high temperatures [34]. These perovskite-based catalysts will be discussed in more detail in section 1.3.2. The use of Pt-Pd based systems as oxidation catalysts is already well developed. However, the use of noble metal based perovskite catalysts may offer an economical alternative, which preserves the resources of the expensive noble metals. For example, the noble metal catalysts are susceptible to poisoning in exhaust streams. However, small amounts of Pt incorporated into perovskites can drastically improve their poison resistance [49, 50]. Metal oxides catalysts typically have lower catalytic activity and higher light off temperatures than noble metal catalysts. The use of traces of noble metals has been reported to enhance the performance of base metal oxide catalysts [15].

Catalytic combustion over noble metal catalysts has been the subject of extensive study for several decades [1]. Compared to base metal oxides, their application as oxidation catalysts has been favoured, because of their higher specific activity. However, practical limitations such as cost, limited supply, ease of oxidation and high volatility have restricted their use. High temperature catalysts for hydrocarbon and CO oxidation are generally made up with noble metals or base metal oxides. A general sequence of the activity of noble metals for oxidation of hydrocarbons was reported as Ru, Rh, Pd, Os, Ir, and Pt [15]. The noble metals mainly used for oxidation are defined herein as Pt, Pd, Ag,

and Au. These noble metals are often alloyed with the closely related metals Ru, Rh, Ir, and Os, and they are usually supported on oxide supports, such as γ-alumina or SiO_2 [1, 11, 15, 35-37].

These metals can also be supported on metal gauze substrates coated with a high surface area porous material, such as alumina washcoat. In most practical systems only Pt and Pd and a few alloys are used because the temperatures employed in most oxidation catalytic applications (e.g., catalytic incineration, automotive systems) can cause sintering, volatility loss, and irreversible oxidation of the other metals. However, limited supply and the resulting high cost of these metals minimises their use [38]. Infact Zwinkels et al. [1] have reported the use of Pt and Pd as complete oxidation catalyst has always been favoured. Theses metal catalysts have been reported as the most active towards oxidation of a range of hydrocarbons [1, 23, 39, 51].

The high activity associated with these metals has been linked to their ability to activate H_2, O_2, C-H, and O-H bonds. The Pd catalyst for oxidation of CO, olefins and methane has been found to be more active than the Pt catalyst, while studies have shown similar activity for aromatic compounds [38]. For the oxidation of higher hydrocarbons with C_3 and greater, Pt catalysts are more active [38]. Oxidation over noble metals is generally recognised to be structure sensitive process [16, 17, 20, 21, 34, 52-55]. Several papers have reported combustion of light alkanes and aromatics, such as methane [55, 56], propane [57], butane [58], heptane [59], and benzene [60] showing increased oxidation turnover rates with increasing platinum particle size and greater ease of oxidation with increasing carbon chain length. Methane has been found to be the most difficult hydrocarbon to activate, while ethane, propane and butane are of intermediate difficulty and the ease of oxidation increases for higher hydrocarbons. This has been reported to be due to the ease of adsorption of the different hydrocarbons on the oxides and oxidised metal surface [61]. Burch, Crittle and Hayes reported the strength of adsorption of the saturated hydrocarbon was an indicator of the rate of combustion [62]. The strength of the C-H bond is not the only factor which influences the combustion process. An additional factor is the "stickiness" of the molecule to the oxidised surface. Burch et al. reported the adsorption of large molecules in a pre-dissociated form to be much more effectively than for small molecules [61].

In general the higher molecular weight hydrocarbons were more easily oxidised than the lower molecular hydrocarbons. Hydrocarbons of a given carbon number increased in reactivity according to a series [63]: Aromatic < branched chains, alicyclic < normal paraffin < olefinic < acetylenic.

Dywer stated a set of guidelines for the ease of oxidation of hydrocarbons, in order of ease of oxidation [63].

- Aliphatic > Alicyclic > Aromatic.
- $C_n > C_4 > C_3 > C_2 >$ Methane.
- Ethynes > Olefins > Saturated.
- Branched chains > Straight chains.

Typical catalysts for high conversion of particular hydrocarbons are shown in Table 1.1 [63].

Table 1.1: Characteristic catalysts for high conversion of hydrocarbons [63]

Catalyst	Hydrocarbon
Platinum, Palladium	Methane, pentane, isooctane, ethylene, propene, acetylene, benzene, cyclohexane
Copper oxide	Methane
Spinels (Co, Mn.)	Ethylene, propene, isooctane, benzene, cyclohexane,

In a review of catalytic oxidation on noble metals, Spivey [39] proposed that the oxidation of hydrocarbons over noble metals followed either a Langmuir-Hinshelwood type mechanism or an Eley-Rideal type mechanism. The Langmuir-Hinshelwood mechanism involved reaction between the adsorbed reactant and adsorbed oxygen molecules forming a new product. This mechanism was mostly found in oxidation reactions with mixtures of different compounds and where competitive adsorption occurred. For example, nucleophilic reactants such as olefins are strongly adsorbed on metal surfaces [24]. Otto [55] stated that reactions governed by the Langmuir-

Hinshelwood mechanism could not take place on isolated sites and required a minimum site ensemble, which may include sites on the support material. For example, the hydrogen spillover reactions are predominantly consistence with Langmuir-Hinshelwood mechanism. The Eley-Rideal mechanism was found in reactions involving olefin compounds; the mechanism involved a reaction of the adsorbed oxygen with gas phase reactant forming a new product. Equations 1 and 2 illustrate the Langmuir-Hinshelwood and Eley-Rideal mechanism respectively.

1. $A_{ads} + B_{ads} \rightarrow AB_{ads}$
2. $A_{ads} + B_{g} \rightarrow AB_{ads}$

In the next segment of this chapter, the literature on the oxidation of methane and higher alkanes over noble metals and metal oxides catalysts will be discussed. This discussion will be divided up into two sections. The first section 1.3 deals with total oxidation over noble metals, metal oxide and perovskite catalysts. Section 1.4 examines the total oxidation of hydrocarbons, mainly focusing on the oxidation of propane over Pt catalysts discussing the effect of various supports, metal loadings, surface area effects and particle size.

1.3 Total Oxidation of methane

The concentration of methane in the atmosphere is continuously increasing [102]. Since methane has a much larger green house effect than carbon dioxide, the elimination of methane emissions from natural gas engines and power plants as well as petroleum and petrochemical industries by complete combustion to carbon dioxide is an environmental necessity. The large reserves of methane in the form of natural gas has also been utilised as an energy source because CH_4 has the highest ratio of hydrogen to carbon and natural gas has low levels of sulphur and nitrogen impurities. The production of energy by the combustion of natural gas (CH_4) is well established; see equation.

$$CH_4 + 2O_2 \rightarrow CO_2 + 2H_2O \quad \Delta H_{298} = -191.8 \text{ Kcal/mol}$$

Methane is the most inert and difficult hydrocarbon to activate, hence its oxidative destruction by complete combustion at low temperatures is rather difficult and as such requires the most active catalyst. The oxidation of methane over a series of noble metal supported catalysts has been extensively investigated as a route to solving this problem. The noble metal catalysts showed higher activity in the combustion of lighter hydrocarbons [2-4] and methane [5-10] at low temperature compared with metal oxides and perovskite catalysts [103].

1.3.1 Methane Oxidation on Noble metals

Anderson et al. tested the effectiveness of catalytic oxidation of methane over a series of supported catalysts in a microcatalytic reactor [18, 66]. This device allowed screening of the catalysts and provided information on the kinetics of oxidation. The catalysts were prepared by impregnation of support materials with the aqueous solution of the metal nitrate salt or chloride salts followed by drying and calcining at 250^{O}C in air. They reported that the activity of the metals or metal oxides per gram of active metal decreased in the following sequence: Pt > Pd > Cr > Mn > Cu > Ce > Co > Fe > Ni > Ag. Palladium and platinum supported on alumina were shown to be more active than the metal oxides and silver. Coln and Haley [68] investigated the activity of noble metals supported on

alumina towards methane oxidation and found the activity to decrease in the following order: Rh > Pd > Id > Ru > Pt. Anderson et al [66] also compared catalytic activity of palladium and platinum catalysts supported on alumina and found palladium to be more active for the oxidation of methane.

Firth and Holland [69] investigated the kinetics of the catalytic oxidation of methane on Pd, Pt, Rh and Ir supported on alumina. The IR study was an attempt to gain information of the effect of the electronic structure of the catalyst on the reaction. The catalysts studied were prepared by depositing an active metal onto alumina by thermal decomposition at 900°C of an aqueous solution of the metal salt. Before use, all the catalysts were treated in a 12% methane-air mixture at 900°C to reduce any oxide to the metal. The reactions on the alumina-supported metals were studied using a microcalorimetric method. The activation energies for Pt, Rh and Ir at a CH_4 partial pressure of 0.02atm and oxygen partial pressure of 0.215atm were calculated to be 48, 27 and 17Kcal mol^{-1} respectively. The Pd activation energy was determined to be 12Kcal mol^{-1} below 290°C, while above 290°C the activation energy increased to 33Kcal mol^{-1}. The observed increase in activation energy was recorded as being close to the heat of formation of PdO at 20Kcal mol^{-1} [24]. Cullis and Willatt suggested that the oxygen in PdO was similar to the oxygen adsorbed at higher temperatures [71].

The kinetics studies suggested that the rate of methane oxidation was proportional to the methane concentration (i.e. first order) but independent of oxygen concentration (i.e. zero order) [71]. Firth and Holland [69], Mezaki and Watson [72] and Cullis et al. [73] proposed a mechanism, in which the rate determining step in the reaction over the metals was the interaction of CH_4 with the chemisorbed oxygen. Based on this, Cullis and Willatt [71] proposed a similar mechanism involving the reaction of methane with strongly adsorbed oxygen. However, at lower temperature and partial pressure of oxygen, some oxygen adsorption sites were vacant and thus competitive adsorption of methane and oxygen became significant. Cullis and Willatts results indicated that methane might be adsorbed on two types of reaction sites, one that adsorbs oxygen and one that cannot adsorb oxygen. The measured activation energies were found to be proportional to the Pauling bond energies of the oxygen metal-bond in the region where the oxygen order is low. Therefore, it was assumed that with increasing bond energy values for surface

oxygen, one would expect decreasing catalytic activities. Firth and Holland [69] stated that with increasing metal-oxygen bond energies, the activation energies decreased. This conclusion was stated unlikely due to inaccuracies in the bond energy calculation; besides, the high activation energies of the metals suggested a reaction mixture composition that would cause oxygen retardation. Hence a direct correlation was found to exist between bond energy of the metal-oxygen and the apparent activation energies for the different metals (below 290°C) Fig 1.4, [69]. Therefore, as the single metal-oxygen bond increased the apparent activation energy decreased, implying metal-oxygen bond formation in the reaction sequence.

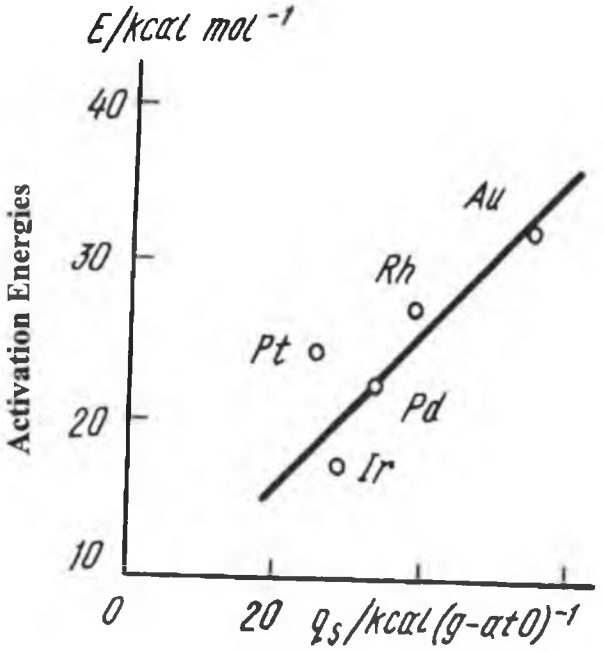

Fig.1.4: Correlation between the activation energies for CH_4 oxidation over different metals below 290°C and the metal-oxygen bond strength [69].

Cullis and Willatt [71] examined the kinetics of methane oxidation using a pulse flow microreactor technique on palladium and platinum catalysts supported on a number of metal oxide materials in order to determine the mechanism of reaction and elucidate the role played by the support materials in the oxidation. In particular, they examined the role of oxygen adsorption. The effect of the particle size of the precious metal and relationship between the metal and the support materials were also evaluated. The reaction was studied in the temperature range 500 – 873K using a 10% v/v methane-oxygen reactant mixture with CH_4: O_2 ratios varying from 1/10 to 10/1. Cullis and Willatt [71] suggested that under the conditions studied that homogeneous oxidation and interparticle diffusion appeared absent and that the reaction rate was thought to depend only on catalyst surface reaction. The precious metal catalysts studied were prepared by adding aqueous solution of the required metal salt onto the powdered metal oxide, followed by refluxing to remove water. The precious metal loading was varied between 1 to 40 wt%. The following supports were investigated γ–Al_2O_3, SnO_2, SiO_2, ThO_2 and TiO_2. The catalysts were characterised by N_2 physisorption, H_2 chemisorption, transmission electron microscopy (TEM), X-Ray Photoelectron Spectroscopy (XPS) and scanning electron microscopy (SEM).

The activity of the support alone for the methane oxidation was assessed by exposing them to the reaction mixture of CH_4/O_2 or pure methane alone. They found that in the temperature range studied that the SnO_2 showed considerable activity, whereas the other supports showed little activity. In the case of SnO_2, at 873K, 25% conversion in pure methane stream (2.8×10^{-7} mol) was achieved and in a CH_4/O_2 atmosphere at the same temperature 100% conversion was obtained. The activity of the metal supported catalysts for CH_4 oxidation is shown in Table 1.2.

Table 1.2:

Activity of metal supported catalysts for CH_4 oxidation [71].

Supported catalysts	Reaction rate (10^{-2} mol.s^{-1}.g^{-1} of precious metal (10^{-2} mol.s^{-1}.m^{-2} precious metal)			
	623K	683K	623K	683K
2.7 wt% Pd/TiO_2	7.53 (1.65)	16.57 (3.64)	0.89 (0.20)	2.57 (0.57)
20 wt% Pd/TiO_2	2.24 (0.77)	3.05 (1.05)	0.45 (0.15)	0.99 (0.45)
40 wt% Pd/TiO_2	1.63 (-----)		0.34 (-----)	
2.7 wt% $Pd/\gamma-Al_2O_3$	13.72 (3.57)	21.56 (5.60)	2.17 (0.56)	3.50 (0.91)
11 wt% $Pd/\gamma-Al_2O_3$		6.42 (3.34)	0.64 (0.34)	1.33 (0.69)
3.0 wt% Pd/ThO_2	2.21 (0.48)	4.99 (1.08)		
2.7 wt% Pt/TiO_2	3.77 (0.34)	13.60 (1.36)		
2.7 wt% $Pt/\gamma-Al_2O_3$	11.11 (1.11)	18.29 (1.84)		
10 wt% $Pt/\gamma-Al_2O_3$	5.46 (-----)	7.93 (-----)		
3.0 wt% Pt/ThO_2	1.36 (-----)	4.24 (-----)		

Both the Pd and Pt metals in methane rich and oxygen rich atmosphere appeared to exhibit increased activity when supported on oxide materials with large surface area, such as $\gamma-Al_2O_3$ An increase in metal loading on certain supports was also found to decrease activity for the overall rate of methane oxidation in both reducing and oxidising atmospheres. However, in the case of Pd metal the activity per unit mass and per unit area decreased with increased loading. Similar results in methane rich atmosphere were obtained for Pt. From Table 1.2, it can be seen in general, slightly lower rates of methane oxidation were obtained with platinum than with palladium catalysts. In conclusion, Cullis and Willatt stated that both the support and metal play a significant role in determining catalytic activity.

The influence of precious metal particle size on a number of supported catalysts were also examined [71]. The metal particle sizes determined from TEM for given supports were found to increase with metal loading, although the method of preparation was also found to adversely affect particle size as well as the pretreatment temperature. Similar particle size resulted in similar activity; for example a 2.7-wt% Pd/γ-Al_2O_3 and Pd/TiO_2 showed similar particle sizes and overall rate of methane oxidation. Similar results were found for Pt. However, on pretreatment of the 2.7 wt% Pd/γ-Al_2O_3 in flowing air at 823K for 40 days, the average diameter of the metal particle size increased from 14nm to 80nm with no apparent increase in catalytic activity towards methane oxidation under CH_4 rich conditions. Therefore, Cullis and Willatt concluded that the rate of methane oxidation was independent of particle size under methane rich conditions [71].

Cullis and Willatt [71] also studied the rate of methane oxidation as a function of temperature (Fig. 1.5) for a number of Pd supported catalysts. They measured the rates of methane oxidation in terms of production of oxides of carbon. From the $\log_{10}$ plots a sudden change in slope (i.e. transition temperature) was observed, which was found to vary depending on the metal catalyst, support and the composition of the methane-oxygen mixture. Platinum catalysts showed a sudden increase in activity at the transition temperature. For example, on a 3.0 wt% Pt/ThO_2 catalyst, the methane oxidation rate doubled between 642K and 647K; above this temperature all oxygen was reportedly consumed. Over a 2.7 wt% Pt/γ-Al_2O_3 catalyst the reaction rate increased by a factor of eight between 610K and 673K. However, a more gradual transition occurred with palladium catalysts and all the oxygen was reportedly consumed below the transition temperature [71]. Cullis and Willatt proposed that a relationship between the apparent activation energy and oxidation of methane in the presence and absence of oxygen existed. Activation energies for a number of Pt and Pd catalysts were calculated. The activation energies for Pt catalysts were higher than those for the Pd catalysts below the transition temperature while the reverse was found to be the case above the transition temperature. The activation energies over Pd catalysts in the low and high temperature regions were 83 ± 5 to 95 ± 6 kJ/mol and 23 ± 3 to 45 ± 2 kJ/mol respectively whereas for the corresponding Pt catalysts, values in the low and high temperature regions were 116 ± 4 to 108 ± 3 kJ/mol and 24 ± 2 to 19 ± 2 kJ/mol respectively. In general, an increase in metal loading was found to have little effect on the activation energies.

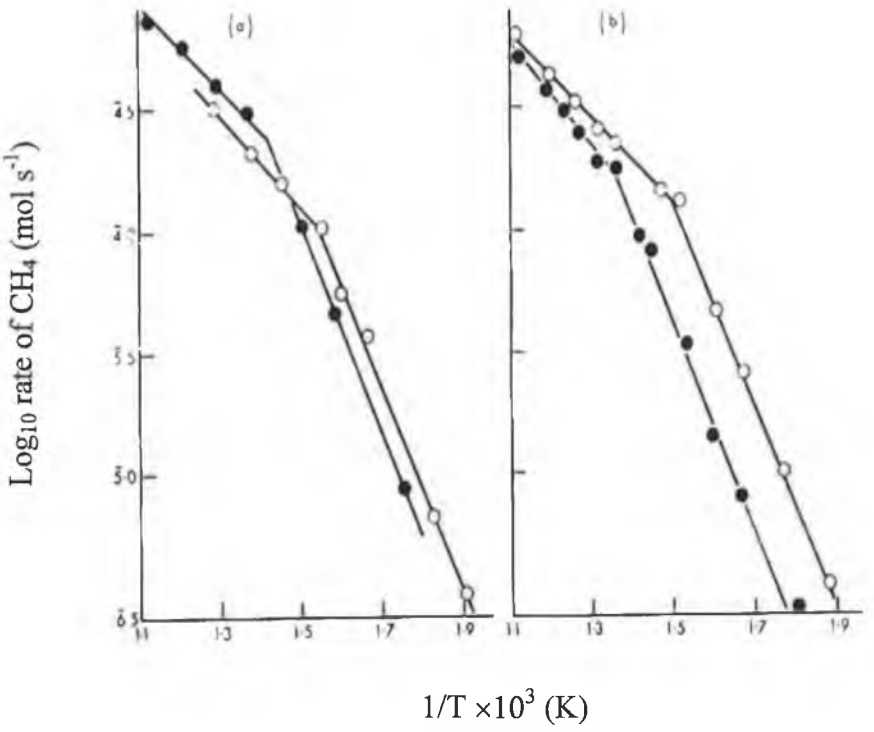

Fig 1.5: Variation of rate of methane oxidation on Pd supported catalysts with temperature. (a) (○) 2.7 wt% Pd/TiO_2; (●) 2.7 wt% Pd/γ-Al_2O_3; (b) (○) 20 wt% Pd/ThO_2; (●) 2.7 wt% Pd/α-Al_2O_3 [71].

Cullis and Willatt [71] also examined the adsorption of oxygen by the precious metal supported catalysts. As previously discussed, the adsorption of oxygen was found to vary depending on: a) the % loading of the metals, b) nature of the support and c) temperature. Fig 1.6 illustrates the effect of temperature on Pd supported surface. For example, Pd on γ–Al_2O_3 adsorbed roughly 100 times more oxygen than a corresponding platinum catalyst, despite the fact that γ–Al_2O_3 was found not to adsorb oxygen itself. The amount of adsorption of oxygen by Pd supported on ThO_2 and TiO_2 was significantly less, however, the oxides once formed appeared to be more stable. Therefore, oxygen adsorption onto the catalyst surface was deemed an essential step in the methane oxidation reaction. From this Cullis and Willatt [71] illustrated a direct correlation between the oxygen adsorption by Pd supported catalysts and rate of methane oxidation (see Fig 1.7) [71].

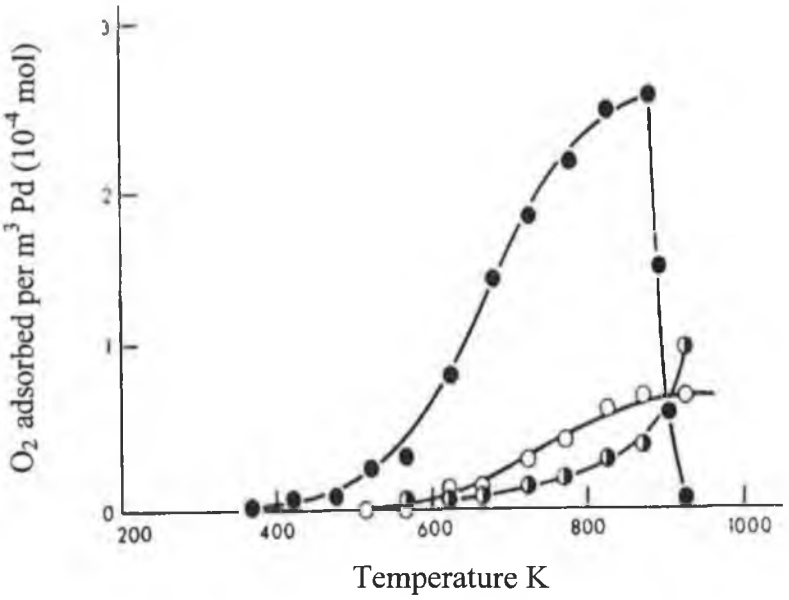

Fig 1.6: Variation of amount of adsorbed O_2 with temperature over supported palladium catalysts. (O) 8.7 wt% Pd/TiO_2 (●) 11wt% $Pd/\gamma-Al_2O_3$ (◑) 5wt% Pd/ThO_2 [71].

From Fig 1.6 the optimum temperature for adsorption of oxygen onto the $Pd/\gamma-Al_2O_3$ catalyst was 873K, but with increasing temperature the level of oxygen uptake dropped dramatically. This in turn was found to have a detrimental effect on the methane oxidation activity as it resulted in tightly bound oxygen, similar to that of PdO, which was less reactive. The methane conversion (Fig 1.7) also showed an optimum activity at 775K suggesting some form of competition for oxygen between Pd to form the oxide and CH_4 to undergo oxidation. Therefore, Cullis and Willatt [71] concluded that optimum activity for methane oxidation was only achieved when sufficient oxygen was adsorbed from the gaseous reactant mixture onto a previously reduced surface. Cullis and Willatt [71] suggested that Pd could adsorb oxygen into its bulk, thus providing an oxygen reservoir, which could prevent the decomposition of the methane on the surface. Anderson et al [74], Lee and Trimm [75] stated at low temperatures (800K), Pd exhibited high activity towards the oxidation of methane. However, at temperatures between 800 and 1000K this activity was found to drop dramatically in low oxygen concentration. McCarty [76] attributed this to the dissociation of highly active palladium oxide to the

metallic form (i.e. palladium). Farrauto et al. proposed that this may be attributed to a decrease in adsorption of oxygen by Pd above the transition temperature and thus inhibited methane oxidation [32].

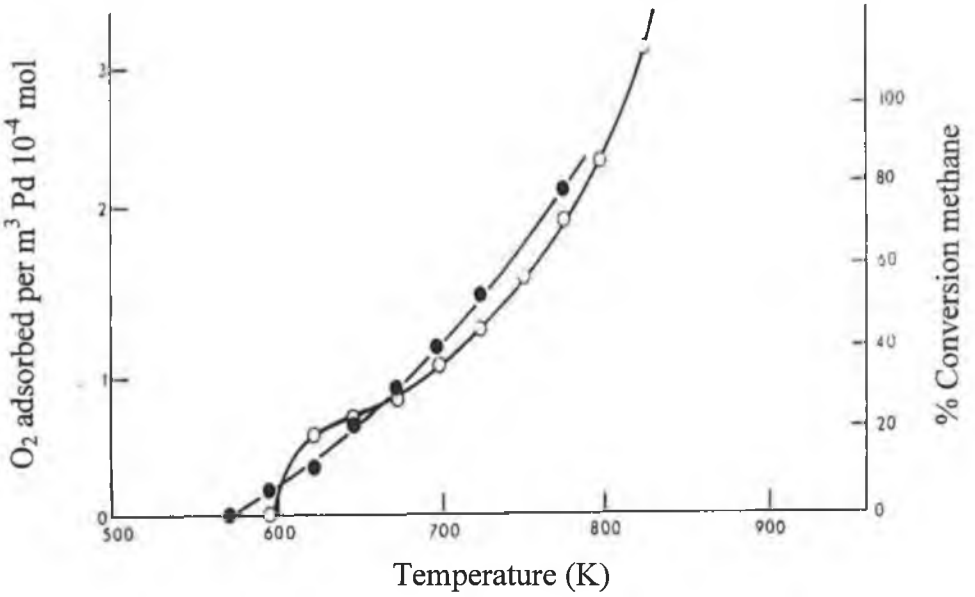

Fig 1.7: Variation of O_2 adsorption and methane conversion with temperature over a 2.7-wt% Pd/TiO_2 catalysts with variation in temperature and oxygen adsorption, (○) Oxygen adsorption (●) Methane conversion [71].

Cullis and Willatt [71] compared the rate of methane oxidation over platinum and palladium and found that palladium was more active. This was attributed to the different abilities of the Pd and Pt metals to adsorb oxygen [71]. As discussed above, palladium, unlike platinum, can adsorb oxygen into the bulk structure, which provides a reservoir of oxygen, thus preventing methane pyrolysis. In addition, platinum had a greater surface area available for adsorption and subsequent pyrolysis of methane. A similar conclusion by Schwartz and Wise stated catalytic properties of the metals varied with the degree of oxygen coverage exhibited by the metals [77]. For Pd, sorption data [78] and thermodynamic studies [79] indicated the existence of both a strongly bound oxygen adsorbate with high surface coverage and a metal oxide compound.

Hicks et al [20] tested a series of supported Pt and Pd catalysts for the oxidation of methane, to determine the effect of catalyst structure on the intrinsic activity of Pt and Pd. They compared turnover frequencies for Pt and Pd supported on γ–Al_2O_3, α–AlOOH, ZrO_2 and 12-wt% Y_2O_3/ZrO_2. The catalysts tested were prepared by ion exchange or by incipient wetness impregnation on supports with the aqueous solution of the metal chloride salt. The catalysts were then dried at 150^{O}C overnight, followed by calcining in air at either 500 or 700^{O}C for 2hrs. The metal loading varied from 0.50 wt% to 2.3 wt%.

The reaction was studied in a fixed bed microreactor at 260-370^{O}C in an oxygen rich atmosphere [20]. A catalyst sample of between 0.05 and 0.2g was loaded into the fixed bed reactor. On line gas chromatography equipped with Carbosphere packed column and TCD was used to analyse the reaction products. Conversions were kept below 2% and carbon dioxide was the only reaction product observed. The catalytic rate of the samples were measured by heating in 50cm^3/min helium at 300^{O}C, followed by reducing in 50cm^3/min flow of hydrogen for 1hr at 300^{O}C The reaction was found to be structure sensitive over the supported Pt and Pd catalysts indicated by the intrinsic rates, which varied by more than 5000 from the least active to the most active catalysts. The structure sensitivity of the methane oxidation reaction was though to be related to the differences in the reactivity of the adsorbed oxygen on the metal surface.

A strong correlation between the turnover frequencies and infrared spectrum for CO adsorption was found. Two distinct phases of Pt were identified from the infrared spectrum. These were dispersed Pt with a low turnover frequency at 2068cm^{-1} and a crystalline phase with a high turnover at 2080cm^{-1}. The activity of the dispersed Pt was found to be 10-100 times lower than that of the platinum crystallites. This was attributed to the dispersed phase being converted to PtO_2, while the crystallite phase was covered with more reactive adsorbed oxygen. The latter was found to decrease in concentration relative to the PtO_2 as the Pt dispersion increased. The phases formed depended on the support material and method of preparation, rather than the degree of Pt dispersion. The two phases were found to coexist on the γ–Al_2O_3 supports, the highly dispersed phase was stabilised by alumina and the crystalline phase interacted weakly with the support. The zirconia support and low surface area inert alumina support did not stabilise the Pt dispersed phase and Pt crystalline phases were formed.

The turnover frequency for the methane oxidation over palladium was found to depend on particle size and maybe site distribution on the metal surface [20]. Under the reaction conditions studied, small crystallites supported on alumina were converted into dispersed PdO, while large crystallites were converted into smaller crystallites with a chemisorbed layer of oxygen. The methane oxidation activity of the dispersed PdO was 10 to 100 times lower than that of the small palladium crystallites. Hicks et al proposed that the dispersed PdO on alumina was much less active than the chemisorbed oxide layer on Pd and that oxidation breaks apart the palladium crystals exposing the oxide [20]. They also found that the rate of oxidation increases with decreasing particle size and increasing number of crystal imperfections.

Otto [55] measured the rates of methane oxidation over platinum catalysts. The reaction was studied in a recirculation batch reactor and mass spectrometer with a reactant mixture of 10 torr CH_4, 60 torr O_2 and 600 torr Ar. The oxygen pressure used in the CH_4 oxidation was 3 times the required pressure. Platinum supported on γ-alumina with loadings from 0.03 to 30 % wt and Pt black samples were examined. Over Pt the oxidation of methane was reported as first order with respect to CH_4 and zero order with respect to oxygen pressure in the range explored ($2.5 < O_2/CH_4 < 60$). Platinum supported on alumina was found to be structure sensitive for the oxidation of methane. The turnover frequency was found to increase with Pt loadings reaching a maximum at 5wt% (i.e. TOF 5.3×10^{-3} s^{-1}) where particulate Pt particles were found. At higher concentration between 10-100wt% (Pt black) loading a steep decline in reaction rates were observed by Otto [55]. They attributed this decline to a substantial decrease in the fraction of active Pt surface atoms with increasing particle size. From the TOF values particulate Pt particles were shown to be 4 times more active than dispersed particles. The structure sensitivity also reflected a change in the apparent activation energies. For lower Pt concentration in which essentially all the Pt atoms were surface atoms, activation energies of 35.2 ± 1.6 Kcal/mol were obtained. At higher concentration the activation energies were found to decrease due to the presence of larger Pt atoms, these larger particles were found to be more active due to the formation of subsurface atoms. The activation energies for Pt black (unsupported Pt) were found to be similar to that of the supported Pt at higher loadings (i.e. 30-100wt %). Therefore, Otto proposed that

sintering of the platinum at these high concentrations may be responsible for the decrease in the methane oxidation rates.

The effects of sample pre-treatment on the rate of methane oxidation over Pt/γ-Al_2O_3 were also investigated by Otto [55]. The rate of oxidation was found to increase with hydrogen pre-treatment and decrease with oxygen pretreatment. According to Yao et al. [80] sintering of the Pt particles occurred in hydrogen atmosphere at temperatures between 450-550^{O}C, while oxygen treatment resulted in Pt redispersion. Fig 1.8 shows the activity of a 0.4% Pt sample after different pretreatment conditions.

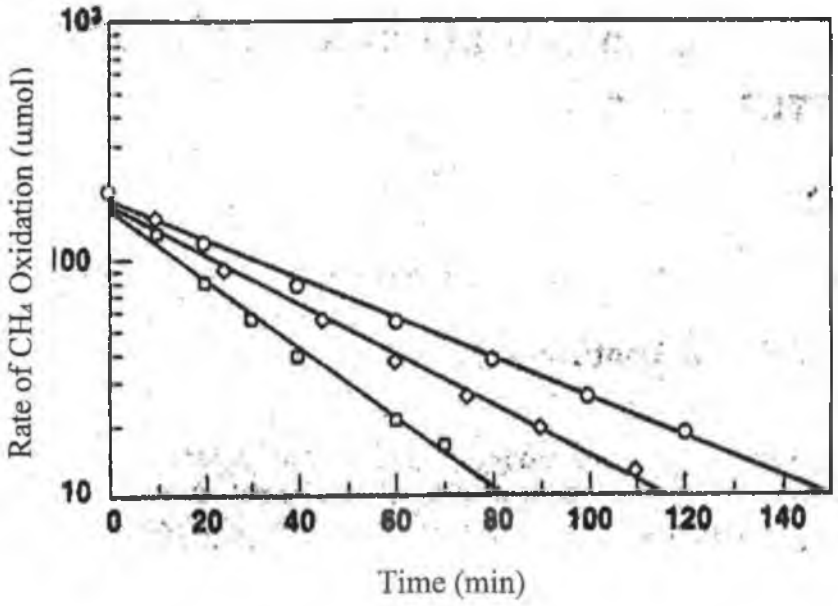

Figure 1.8: Changes in rate of CH_4 oxidation on 0.4 wt. % Pt/γ–Al_2O_3 caused by different pretreatments. Pretreatment: (O) heated in oxygen at 500^{O}C for over 20 h; (□) heated in hydrogen at 500^{O}C for 20 h; (◇) heated in oxygen at 500^{O}C for 20 h [55].

On exposure to hydrogen at elevated temperatures over prolonged time periods, an increase in rate constant resulted, while exposure to oxygen under similar conditions reduced the rate constant. Further exposure to hydrogen again caused an increase in catalytic activity by a magnitude of 1 compared with initial runs. However, further exposure failed to increase the rate constant values further.

Otto noted that Pt sintering and redispersion was very slow and barely noticeable at 450^{O}C and only became apparent at 500^{O}C [55]. The total activity of the Pt particles was found to increase with sintering in spite of the reduced Pt surface area, whereas redispersion in oxygen, which increased Pt surface area, lowered the total activity. Thus, Otto proposed that the total activity Pt was associated with the particle size and that the reaction was structure sensitive.

In conclusion, the oxidation of CH_4 over Pt/γ-Al_2O_3 was found to be structure sensitive. At least two different Pt entities with different oxidation states and particle size, termed dispersed and particulate platinum oxide, were characterised from methane oxidation kinetics. Otto also found that at higher Pt concentration the larger particles exhibited similar kinetic characteristics as unsupported Pt black [55]. Reaction kinetics of the oxidation of methane depended strongly on sample pre-treatment of the platinum since oxidation tends to disperse Pt, while reduction caused sintering. The oxidation reaction based on site density calculation and theoretical and empirical kinetics were found to be inconsistence with an Eley-Rideal type mechanism.

Briot et al. [16] studied the impact of particle size on the oxidation of methane over 1.95wt% Pt/Al_2O_3 catalysts. Artificial ageing of the catalyst was achieved in a CH_4:O_2:N_2 mixture at 600^{O}C for 14hrs and this pretreatment resulted in an increase in platinum mean particle size. The catalysts were prepared by a wet incipient impregnation method of the support materials (i.e. $\delta-$ Al_2O_3 and $\gamma-$ Al_2O_3 mixture) with an aqueous solution of H_2PtCl_6 acid. The catalysts were then subsequently dried at 100^{O}C, followed by calcining in N_2 at 500^{O}C and reducing in H_2 at 500^{O}C overnight. Activity measurements were carried out in a continuous flow reactor with a 1:4:95 vol/vol/vol methane/oxygen/nitrogen ratio mixtures at a flow rate of 6.3 dm^3h^{-1}. The byproducts of the oxidation reaction were analysed by gas chromatography. The catalysts samples exposed to the reactant mixture at 600^{O}C for 14hrs, followed by purging in N_2 under similar temperatures and finally cooled to room temperature were more active at temperatures 300-450 than catalysts not subjected to this pretreatment. A comparison of combustion activities for freshly reduced and aged samples versus temperature is illustrated in Fig 1.9.

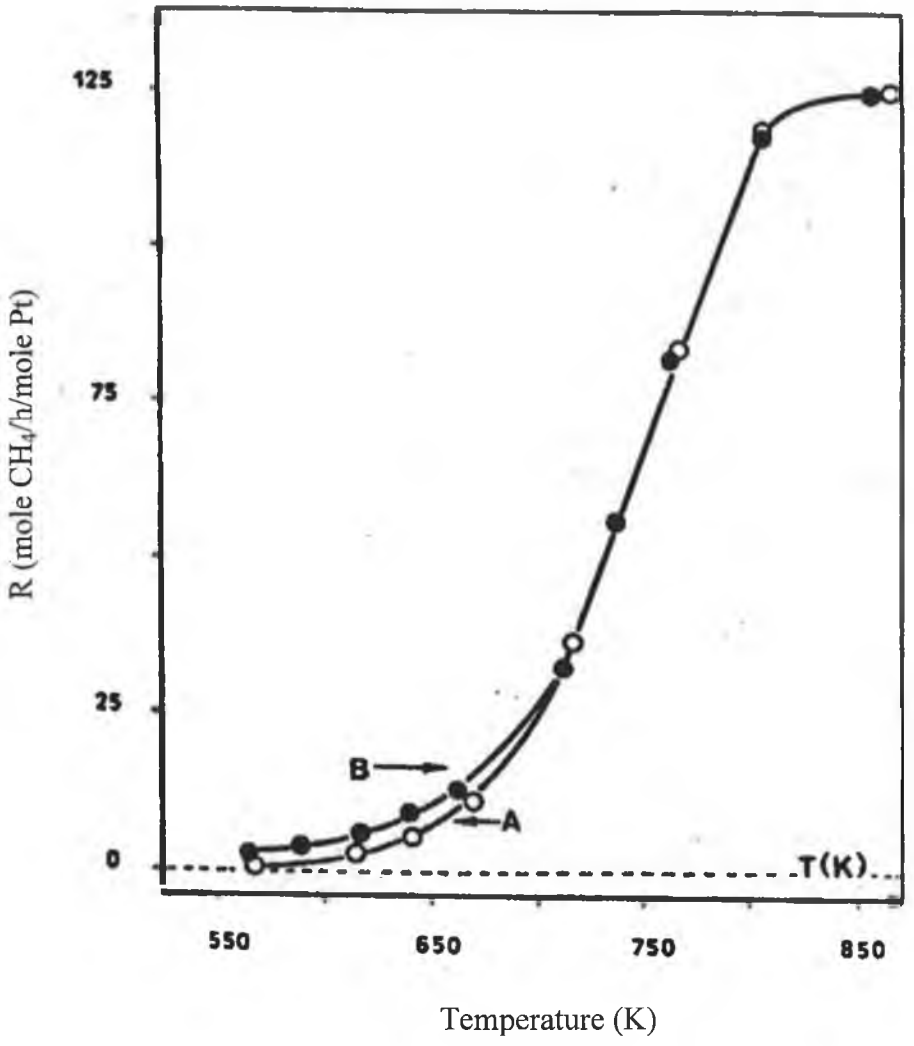

Figure 1.9: CH_4 oxidation rate versus temperature for fresh (A) and aged (B) Pt/Al_2O_3 samples. Oxidation rate is expressed as moles CH_4 converted /h/mole of introduced metal [16].

The apparent activation energy for the CH_4 oxidation in the above temperature range over the untreated catalysts (i.e. freshly reduced) was ~100kJ/mol compared with 71kJ/mol over the treated catalysts (i.e. aged sample). Briot et al. [16] found that an increase in mean particle size of the Pt from 2 to 12nm occurred for samples that underwent this ageing pretreatment. Thus, it was concluded that the larger Pt particles were more active than smaller ones toward CH_4 oxidation. Microcalorimetric measurements of the heat of oxygen chemisorption, Q_{ads}, showed a small decrease in Q_{ads} as the platinum particle

size increased. The larger Pt particles were also found to adsorb less oxygen. Briot et al. proposed that the larger platinum particles were more active because the strength of the Pt-O bonds was lower on these particles, whereas a higher Pt-O bond strength was observed for smaller particles [16]. The authors also suggested that the increase in activity on the large Pt particles were due to the present of facet and not spherical crystallites as shown by TEM analysis. In conclusion, Briot et al. stated the reaction was structure sensitive.

Briot and Primet [17] found in a subsequent investigation that a 1.95% Pd/Al_2O_3 catalyst exhibited similar behaviour for methane oxidation. The reaction again was found to be structure sensitive and the aged catalyst was more active than the fresh one, especially at low temperature (i.e. <400^{O}C). Ageing of the catalysts in the reaction mixture at 600^{O}C led to a decrease in metal dispersion, which resulted in an increase in activity compared with the freshly reduced sample. The mean particle size of the Pd as measured using transmission electron microscopy (TEM) was found to increase from 7nm to 16nm and the turnover numbers increased by a factor of 20 on the larger Pd particles at 400^{O}C. The larger Pd particles were shown to be more active in adsorption of oxygen, which paralleled the increase in rate of CH_4 oxidation with particle size. A comparison of combustion activities for freshly reduced and aged samples versus temperature is shown for the Pd/Al_2O_3 catalysts in Fig 1.10.

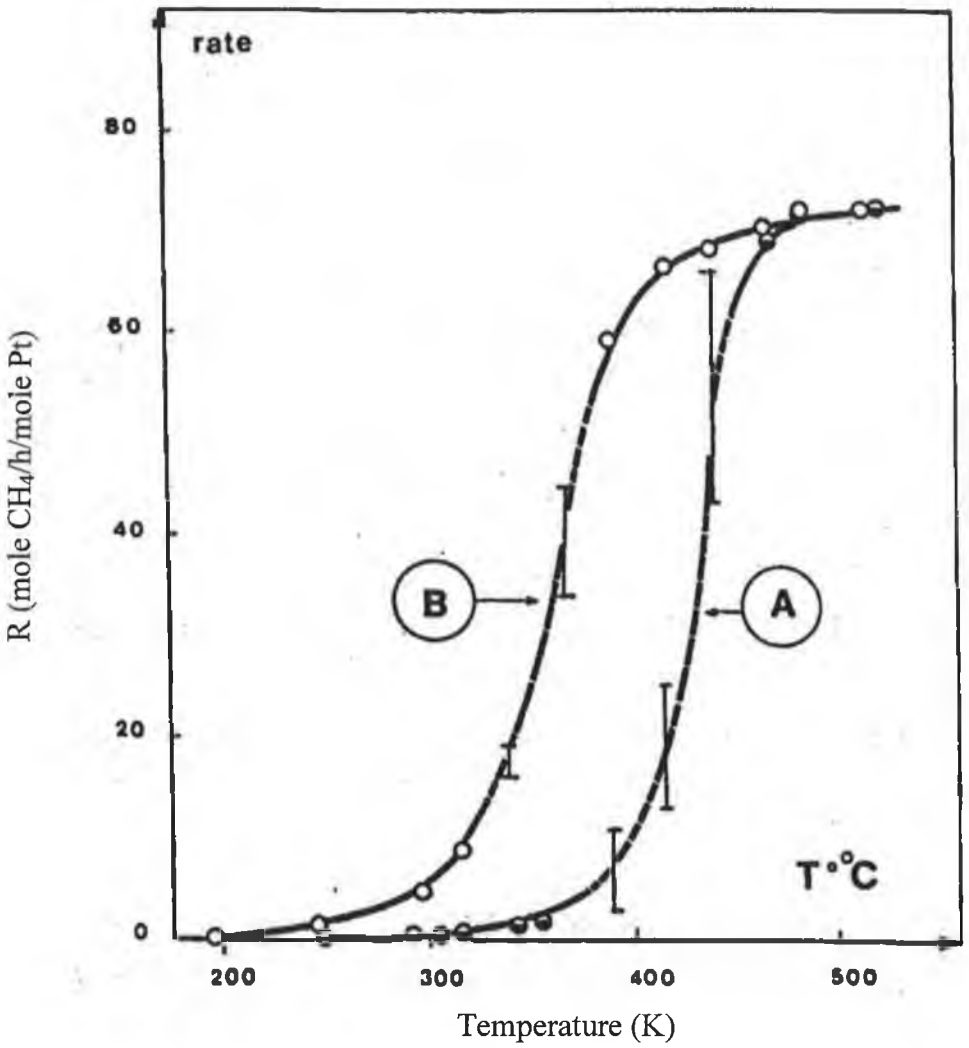

Figure 1.10: CH_4 oxidation rate versus temperature for fresh (A) and aged (B) Pd/Al_2O_3 samples. Oxidation rate is expressed as moles CH_4 converted /h/mole of introduced metal [17].

The apparent activation energy for CH_4 oxidation in the above temperature range over the untreated catalysts (i.e. freshly reduced) was ~104kJ/mol compared with 74kJ/mol over the treated catalysts (i.e. aged sample). Again it was observed as in the previous study on Pt systems that the aged samples with larger particles were more active than the freshly reduced samples. Briot et al proposed the increase in metal particle size is not solely responsible for the changes in catalytic activity of the Pd catalysts [17]. Hicks and co-workers [20] found that an increase in Pd particle size was accompanied with decrease in turnover numbers for CH_4 oxidation. Thus, it was concluded that other factors may be

accountable for some of the activity, such as deposition of carbon causing active site modification and restructuring of the surface under the reactant conditions employed. Temperature programme oxidation investigations showed that palladium was in the bulk PdO state for reaction temperatures of >400^{O}C. The PdO was found to form predominately on the larger Pd particles (16nm) compared with the smaller particles. In summary, the presence of both methane and oxygen were required for the enhancement of activity. Both studies concluded that catalytic oxidation of methane occurred over the PdO phase formed during oxidation in an oxidising atmosphere (i.e. oxygen-rich mixture); even if the catalysts were present in an initially reduced form.

Farrauto et al. investigated the high temperature oxidation of methane over Pd supported on alumina using thermogravimetric analysis [32]. They found that Pd/γ-Al_2O_3 decomposed in two distinct steps in air at one atmosphere depending on temperature, agreeing with earlier work by Lieske and Volter [81]. At temperatures between 750^{O}C and 800^{O}C the first step is believed to be the decomposition of palladium oxygen species dispersed on bulk palladium metal designated (PdO_x/Pd). The second decomposition occurred in the temperature range 800^{O}C and 850^{O}C and behaved like crystalline palladium oxide designated (PdO). Lowering the temperature below 650^{O}C reformed the PdO species. The reformed PdO species was found to be readily active towards methane combustion at temperatures above 550^{O}C. Farrauto et al. [32] attributed this to the ability of the palladium oxide to adsorb oxygen, whereas above this temperature oxygen adsorption was inhibited. This was found to be due to the reduction of the PdO species to metallic metal.

A fresh 4%PdO/Al_2O_3 catalyst was heated in air at 20^{O}C/min to give a thermogravimetric profile of the sample. From the PdO profile a gradual weight increase was shown, followed by an increase in oxygen adsorption between 570 and 600^{O}C and continuing to 750^{O}C similar to that reported on Pd metal [82]. This resemblance suggested that at low temperatures the Pd metal chemisorbs oxygen and forms a PdO species, which at increased temperature promoted oxygen chemisorption forming a (PdO_x/Pd) species. Farrauto et al. [32] suggested that once a skin forms, subsequent oxygen adsorption above 570^{O}C occurred forming a reservoir of oxygen in the bulk layer of Pd metal. Cullis and Willatt [71], Turner and Maple [83] reported similar conclusions, suggesting two

distinct types of oxygen residing on the surface, chemisorbed oxygen and a more strongly bound oxide species. Baldwin and Burch [54] and Briot and Primet [17] proposed that aged catalysts were more active at low temperatures for methane oxidation than fresh samples. They proposed that this increased activity was due to the restructuring of the PdO crystallites. Ruckenstein and Chen [86] proposed this restructuring of the PdO crystallites, may be due to formation of pits and cavities by oxidation of the underlying Pd metal exposed by migration of the PdO on to alumina.

Farrauto et al. [32] determined methane oxidation activity of PdO/Al_2O_3 catalyst as a function of temperature. A fresh Pd/Al_2O_3 catalyst was prepared by impregnation (i.e. incipient wetness method) of γ-alumina support calcined at 950^{O}C for 2hrs with a Pd nitrate salt, followed by reduction with aqueous hydrazine, drying overnight at 120^{O}C and calcining at 500^{O}C for 2hrs. The reaction was investigated in the temperature range 340 to 1000^{O}C with a 1% v/v methane / air mix. Fig 1.11 shows a plot of methane oxidation versus temperature.

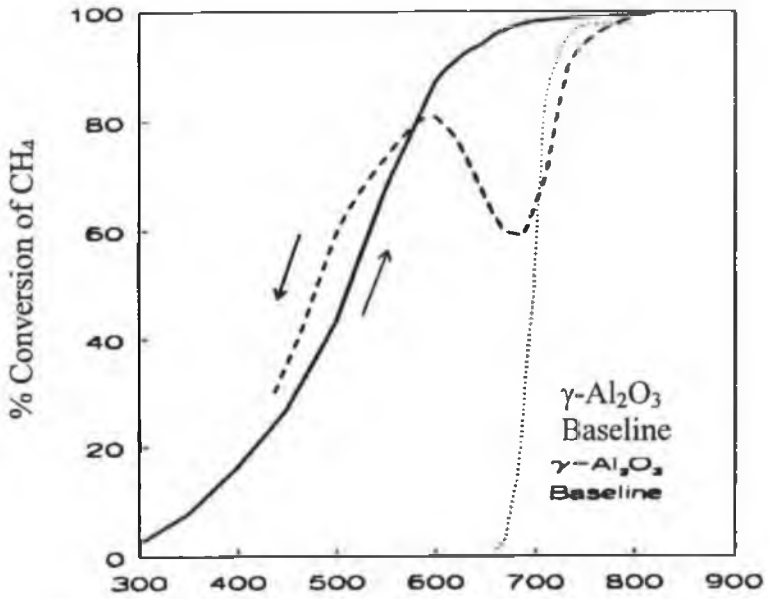

Fig 1.11: Methane conversion versus temperature over a 4% PdO/Al_2O_3; (——) heating, (-----) cooling, (· · · ·) baseline [32].

Initial methane conversion during heat up is observed by the solid line at 340^{O}C and at 430^{O}C had risen by 30%, approaching complete conversion at 650^{0}C due to PdO species. At 700^{O}C, the dotted line indicates a small but significant catalytic activity by alumina for methane oxidation with no contribution from the palladium. They proposed this trend in activity was due to the PdO being reduced to metallic Pd at this temperature. A sudden restoration of activity was observed on cooling below 680^{O}C with nearly 80% conversion near 600^{O}C. They attributed this to the reoxidation of metallic Pd to PdO species. In conclusion, they determined the PdO species was an essential requirement for methane combustion when the catalysts were held at temperatures below 680^{0}C.

Ribeiro et al. [87] investigated the complete oxidation of methane over Pd/ZrO_2 and $PdSiO_2$-Al_2O_3 in a fixed bed reactor under steady state conditions. The catalyst examined were prepared by impregnation (i.e. incipient wetness method) the support materials with an aqueous solution of the ammine nitrate and chloride salts, followed by calcining in air at temperatures between 500 to 850^{O}C. Under the conditions studied, turnover frequencies for the methane oxidation varied from 2×10^{-2} to 8×10^{-2} s^{-1}. In conclusion Ribeiro et al. found that oxidation over palladium was structure insensitive under steady state conditions [87]. The large variation in TOFs' reported were attributed to the use of partial activated samples. The product gases (i.e. CO_2 and H_2O) were found to inhibit the oxidation reaction over the PdO species. This inhibition ability of H_2O was thought to be due to competitive adsorption between the CH_4 and H_2O for surface sites. They proposed that the active PdO site may react at the surface to form $Pd(OH)_2$, blocking CH_4 adsorption onto the PdO phase. The inhibition affect of the CO_2 was more difficult and hence a true explanation was unclear. Treatment of the catalyst samples in air at temperatures below 827^{O}C and at atmospheric pressure resulted in the formation of a stable PdO active phase that formed a monolayer on the support material and exhibited low activity.

Anderson and Tsai [88] using a flow microreactor system at a total partial pressure of 1 atmosphere investigated the oxidation of methane over a number of catalysts. A series of eight different catalyst samples were studied, supported Cr_2O_3 on pummice, as well as unsupported MgO, MgO/BaO, acidified ferric sulphate, H-ZSM5 and Pd supported on γ-Al_2O_3 and SiO_2 with or without charcoal. The reaction was investigated in the

temperature range 495K to 791K with varying CH_4/O_2 molar ratios from 99 to 0.28. The $\%CH_4$ conversion varied from 19.1%, at a molar ratio of 1.68 CH_4/O_2 over Pd/charcoal, to 1.2% over H-ZSM5 at a CH_4/O_2 molar ratio of 8.35. The active phase surface area of the catalysts and reaction conditions employed were not taken into account. Thus, no comparison of catalytic activity for the reaction could be made. Anderson and Tsai made no attempt to study the kinetics of the CH_4 oxidation reaction over the catalyst samples.

Seimanides and Stoukides [89] investigated the oxidation kinetics of CH_4 on porous polycrystalline palladium supported on yttria-stabilised zirconia. The Pd supported on yttria-stabilised zirconia was prepared by depositing a few drops of Pd resinate solution onto the support material, followed by drying at 100^OC for 4hrs, calcining at 550^OC for 6hrs and further heating to 650^OC for 4hrs. The oxidation kinetics were studied in the temperature range 450 to 600^OC, at partial pressures between 1.23×10^{-2} and 7.85×10^{-2} bar for CH_4 and oxygen partial pressure between 0.24×10^{-2} and 6.83×10^{-2} bar. Under the reaction conditions studied, homogeneous gas phase oxidation was absent. The rate of the reaction at high O_2 partial pressure was found to be independent of O_2 partial pressure, but at low oxygen pressure in the range 550-600^OC the rate was found to be proportional to O_2 pressure. Under all the reaction conditions investigated, the rate was first order with respect to CH_4. Seimanides and Stoukides proposed that gaseous methane reacted with chemisorbed atomic oxygen via an Eley-Rideal type mechanism.

At low temperatures Fujimoto et al. [90] examined the structure and reactivity of PdO_x/ZrO_2 catalysts for the CH_4 oxidation and compared it to PdO_x/Al_2O_3. The catalysts were prepared by incipient wetness impregnation of the support with an aqueous solution of $Pd(NH_3)_2(NO_2)_2/HNO_3$, followed by drying in air at 373K for 24hrs. Pretreatment in stagnant air at 773K for 24hrs was carried out on some samples. Other samples were treated in 200-500cm^3 min^{-1} flowing dry air at 773K for 24hrs. These two drying procedures produced different initial methane reaction rates, but were found not to influence steady-state turnover rates. Reaction and turnover rates were measured at 5% methane conversion on all catalysts to ensure similar product concentration and inhibition effects.

The methane oxidation turnover rates of PdO_x under steady state conditions were found to increase with increasing crystallite size on the ZrO_2 and Al_2O_3, without significant change in activation energies. At 553K CH_4 oxidation turnover rates were observed to increase from 0.030 to 0.179 s^{-1} with decreasing dispersion of the metal from 0.381 to 0.120. Ribeiro et al. [87] reported similar turnover rates under similar reaction conditions. The variation in the turnover rates may be attributed to inaccuracies in the dispersion values of the surface area PdO crystallites calculated from chemisorptive titration on the catalysts reduced at low temperatures. Differences in turnover rates have also been attributed to PdO_x clusters with surface structures that vary with the identity of the support and PdO_x cluster sizes [20-21, 87]. Several other authors have reported conflicting results. For example, Baldwin and Burch [53] found rates over Pd/Al_2O_3 varied by a factor of 100 with no direct correlation with PdO_x crystallite size. Cullis and Willatt [71] reported turnover rates were unaffected by crystallite size. However, Briot and Primet [17] and Hicks et al. [20, 21] supported Fujimoto et al. [90] conclusion. However, the reactivity observed on the alumina system was consistent with Fujimoto results on the PdO/ZrO_2 and PdO/Al_2O_3 catalysts. Thus, it was found that the precursors used in preparation of the PdO/ZrO2 catalyst were also found to affect structural changes of the PdO_x crystallites and CH_4 oxidation rates.

In conclusion, methane oxidation turnover rates appear to be related to changes in the density and stability of oxygen vacancies on the PdO_x crystallite surface, as a result of the observed crystallite size, temperature effects and decomposition of PdO to Pd metal.

Marti et al. [91] investigated the catalytic oxidation of methane under both reducing and oxidising atmosphere over Pd supported on zirconia by oxidation of amorphous Pd_1Zr_3 metal alloy under different conditions. The catalyst samples were prepared from both crystalline and amorphous alloys. A 5% Pd/ZrO_2 samples was prepared by impregnation (i.e. incipient wetness method) of the zirconia with an aqueous solution of $PdCl_4(NH_4)$, followed by calcining in air at 773K for 2hrs and reduced in hydrogen at 573K for 2hrs. A second Pd/ZrO_2 catalyst containing 25.6% loading was prepared with a molar ratio 1:3 of Pd/Zr by calcinations of a water-soluble hydroxide, preceded by reduction. The catalyst was then prepared by a co-precipitation method, followed by calcining and reduction in hydrogen as above. Both catalyst samples were crushed and sieved down to 150-500μm for catalytic testing. Under oxygen rich condition, the freshly reduced 5%

Pd/ZrO_2 treated in the gas mixture at 723K for 2hrs, showed significant activity. This activity was attributed to the dispersion of Pd. Marti et al [48] proposed the increase in activity may be due to restructuring of the Pd oxide particles. The overall activities of the catalysts prepared from Pd_1Zr_3 were dependent on the activation conditions. The catalysts prepared from Pd_1Zr_3 exhibited turnover frequencies twice as high as the corresponding Pd/ZrO_2 prepared by conventional methods. For example, a turnover frequency of 3.3×10^{-3} s^{-1} and a reaction rate of 1.41 kg h^{-1}/mol for a catalyst prepared from Pd_1Zr_3 amorphous alloy precursor in situ activation at 698K compared with values of 0.8×10^{-3} s^{-1} and 0.17 kg h^{-1}/mol for a 5 wt% Pd/ZrO_2 were obtained. Activation energies for the catalysts prepared from Pd_1Zr_3 varied between 87-97kJ/mol while 93kJ/mol was recorded for 5-wt% Pd/ZrO_2. The catalytic test without activation pre-treatment of the amorphous or crystalline Pd_1Zr_3 precursor showed almost zero activity for methane oxidation. This was attributed to an intrinsically low surface area of the amorphous alloy precursor. Activating pre-treatment in an oxygen-containing atmosphere at temperature above 570K transformed the precursor into an active catalyst. Marti et al. proposed that structural changes in the surface occurred forming an extremely large interfacial area between the Pd and PdO phases and ZrO_2 [91]. Several authors draw similar conclusions in previous studies [92, 93].

Catalytic activity under CH_4 rich conditions was examined focussing on reaction products. 3 catalyst samples were examined under reducing condition (Table 1.3); 5 wt% Pd/ZrO_2, 25.6 wt% Pd/ZrO_2 and the catalyst prepared from the Pd_1Zr_3 alloy.

Table 1.3: Detail of catalytic activity of three catalysts under CH_4 rich condition [91].

Catalysts	Total CH_4 conversion (%)	Yield of CO (%)	Yield of H_2 (%)
Pd_1Zr_3	23.8	23.2	23.6
25.6% Pd/ZrO_2	24.7	24.2	24.5
5% Pd/ZrO_2	24.3	24.0	24.2

Reaction conditions: 16.64% CH_4, 2.08% O_2 and balance helium with the alloy sample activated in situ at 623K.

The major products of the reaction were found to be CO, H_2, CO_2, and H_2O. The catalysts derived from the Pd_1Zr_3 alloy showed a high selectivity towards CO_2 compared to the references catalysts. However, under reducing conditions at high temperatures 870K, the catalyst showed selectivity for CO and H_2 gases. This was attributed to the formation of carbonaceous deposits at on the catalysts surface.

To date a detailed mechanism of the oxidation of methane on noble metals is not yet well understood. Oh et al. [94] proposed a mechanism (Fig 1.12) based on methane chemisorption and methane-deuterium exchange experiments investigated by other authors [95, 96]. They illustrated the dissociation of adsorbed methyl or methylene radicals, as a result of abstraction of a hydrogen atom from chemisorption of methane on the noble metals [95, 96]. The adsorbed methane (i.e. methyl or methylene radicals) subsequently interacts with the adsorbed oxygen. This was proposed to lead to direct oxidation of the methane to CO_2 and H_2O as the main products or to formation of side products, such as formaldehyde, methyl peroxide or methylene oxide intermediates. The proposed mechanism for methane oxidation is given in Fig. 1.12.

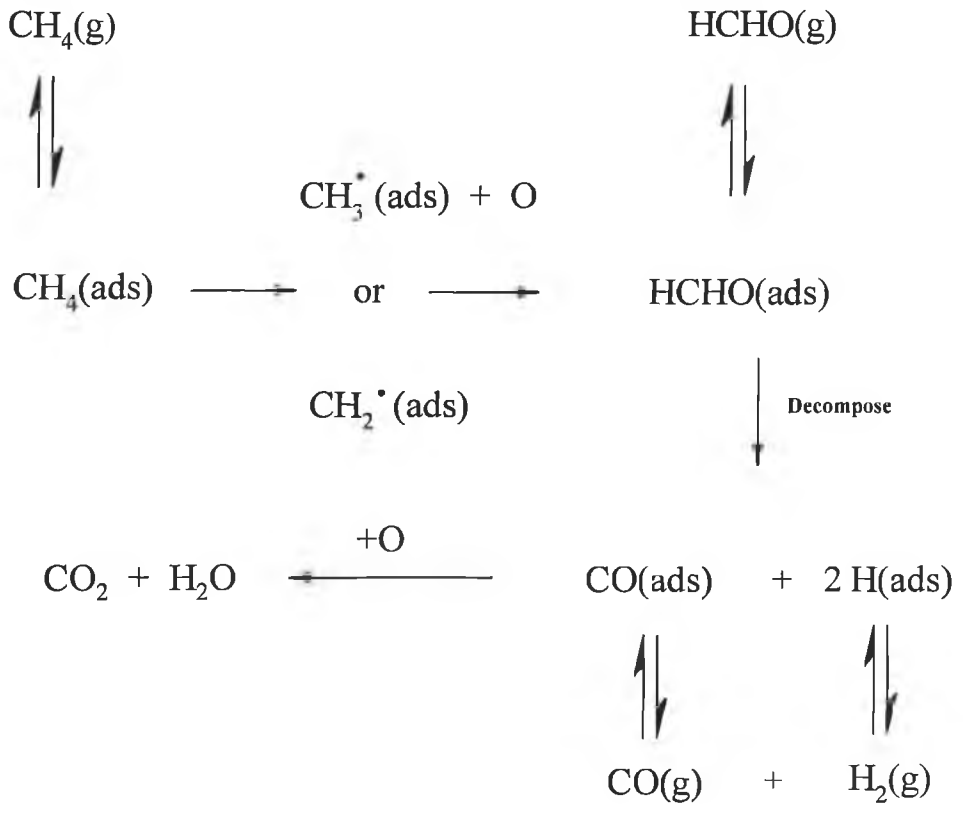

Fig 1.12: Oh et al. proposed mechanism for CH_4 oxidation on noble metals [94].

Under oxygen rich conditions (i.e. oxidising) the metal was fully covered with O_2 because of competitive adsorption of oxygen, while under fuel-rich conditions (i.e. reducing), the metal surface was fully reduced and was likely to be covered with carbonaceous species, or in the case of partially reduced surface, the surface could be covered with both carbonaceous and oxygen species. The above mechanism was consistent with the results for methane combustion under fuel-rich conditions. This suggested that under the reaction conditions examined an adsorbed formaldehyde intermediate would rapidly decompose to CO and H, once formed, rather than desorb into the gas phase as formaldehyde molecules. Based upon their reaction conditions, it was thought the water gas shift equilibrium reaction may alter the product selective for the methane oxidation over the noble metals.

1.3.2 Methane Oxidation on Perovskites

The general formula of perovskite structures are A'A''B'B''O_3, where A' and A'' are lanthanides (such as La, Ce, Pr and Nd) and alkaline earth metals (Ba, Sr and Ca). The transition metals (i.e. Co, Fe, Mn, Cr, Cu and V) and noble metals (Pt, Pd and Rh) are usually incorporated in the B position [1, 97]. Perovskite based catalysts with noble metals incorporated are quite active and have found application in low temperature devices. Perovskites without noble metals in the structure have found applications in exhaust gas clean up [101]. The catalytic activity of the perovskite systems have been attributed to the B-site cation, whereas the thermal stability of the catalyst is due to the lanthanide ions in the A-site position. $LaCoO_3$ structures have been reported to exhibited comparable activity to Pt/Al_2O_3 catalysts at conversion up to T_{50} [44]. $LaCoO_3$ and $LaFeO_3$ were found to be most active for methane oxidation at 530-630^{O}C, followed by $LaMnO_3$, whereas $LaNiO_3$ and $LaRuO_3$ systems exhibited lower activity [22, 100]. Zwinkels et al. [1] proposed that varying the B ion in the ABO_3 is much more effective in optimising the catalytic activity than incorporating different lanthanide metals in the perovskite structure. The $La_{1-x}Sr_xMnO_3$ (where X = 0.2 or 0.4) was very active for methane combustion. Several authors found $La_{1-x}Sr_xMnO_3$ supported on lanthanum aluminate was more active in methane oxidation than a Pt/Al_2O_3 when both were calcined over 600^{O}C [127]. It was also found that the Pt catalyst achieved 100% conversion at approximately 100^{O}C lower than perovskite. Zwinkels et al. [1] proposed that the active species in the oxidation over Pt was dissociated adsorbed oxygen, while in the perovskite the weakly adsorbed oxygen species reacts at lower temperature. At high temperatures the weakly bound oxygen to the oxide surface desorbs more easily than the oxygen adsorbed on Pt. Consequently, lower surface coverage found on perovskite based system suppresses the activity with temperature.

Ferri and Forni [98] investigated the oxidation of methane on perovskite based mixed oxides. The perovskite catalysts, of general formula $La_{1-x}A'_xBO_3$ were prepared via the amorphous citrate method by adding an aqueous solution of starting nitrates to an aqueous solution of citric acid in a molar ratio of 1:1. The resulting solution was evaporated at 70^{O}C, followed by drying in a vacuum at 70^{O}C overnight. The catalyst was then crushed and calcined in flowing air for 2hr at a temperature determined from TGA

analysis. The perovskites examined in this study were $La_{1-x}Sr_xCoO_3$, where x = 0, 0.2 and 0.4, $La_{0.8}Sr_{0.2}BO_3$ (B = Fe or Ni) and $La_{0.9}Sr_{0.1}A'CoO_3$ (A' = Eu or Ce).

Activity measurements were preformed using a $40cm^3$/min gas flow of CH_4 (i.e. 0.5 v/v. % methane) in a nitrogen : air gas mixture. The effluent gases were analysed by gas chromatography. It was found that for the $La_{1-x}Sr_xCoO_3$ (where x = 0, 0.2 and 0.4) catalysts, the maximum activity was attributed to the x = 0.2 system. For example, the $La_{0.8}Sr_{0.2}NiO_3$ was more active than the $La_{0.8}Sr_{0.2}FeO_3$ and $La_{0.9}Ce_{0.1}CoO_3$ was more active than the $La_{0.9}Eu_{0.1}CoO_3$. CO was never detected as a reaction product and methane combustion occurred between 300 to 600^{O}C. Temperature Programmed Desorption analysis (TPD) showed that oxygen activation was possible at approximately 200^{O}C, while activation of the hydrocarbon bond (C-H) was only possible above 300^{O}C. The lower temperature peak has been attributed to suprafacial adsorbed oxygen, while the oxygen released around 500^{0}C may be considered as coming from the bulk of the solid. This occurred at ~500^{O}C with suprafacial adsorbed oxygen being released at ~200^{O}C. This oxygen species occupies the inner vacancies created by substitution of the Sr for La or by segregation of the La-containing phase as present in Co samples. At almost the same temperature Ce_{01}-Co released a larger amount of oxygen with respect to $Eu_{0.1}$-Co, resulting in large amounts of oxygen being available for methane oxidation, as indicated by TPD. In fact it has been shown that methane oxidation rate depends on CH_4 partial pressures only at lower temperatures, whereas at higher temperatures CH_4 reacts with oxygen supplied by the catalysts and coming from the bulk [70]. Hence, the rate of methane oxidation was found to increase with increasing bulk oxygen supply.

In conclusion, Ferri and Forni found the most active catalysts to be that of $La_{0.9}Ce_{0.1}CoO_3$ showing complete methane conversion at 500^{0}C.

Marchetti and Forni [99] also investigated the catalytic oxidation of methane over La based catalysts of general formula $La_{1-x}A_xMnO_3$ (A = Sr, Eu, and Ce), prepared using the amorphous citrate technique by adding an aqueous solution of citric acid and the metal nitrates in equal molar ratio. The catalysts were characterized by BET surface area (Carlo Erba Sorptomatic 1800), X-ray diffraction (XRD) and X-ray photoelectron Spectroscopy (XPS) methods. XRD analysis showed diffraction patterns with well ordered crystalline perovskite structures for all of the catalysts studied.

Activity measurements were carried out with 5% v/v CH_4/Air gas mixture feed and the balance nitrogen at a 40cm^3min^{-1} total flow rate. The by-products and reactant gases were analysed by an on line gas chromatography with flame ionisation detector (FID). Catalytic activity tests showed $La_{0.9}Eu_{0.1}MnO_3$ was the most active catalyst for the oxidation of CH_4. Catalytic tests on stream over 100 hr duration showed no variation in catalytic performance, therefore it was concluded the perovskite exhibited good thermal stability.

Temperature programmed Reduction – Mass spectroscopy (TPR-MS) was carried out on $La_{1-x}A_xMnO_3$ catalysts and results showed activity in the temperature range 400^OC to 500^0C and total conversion was achieved within 500-600^OC range. Two trends were observed for the effect of Sr substitution. At high temperatures, the activity varied in the order $LaMnO_3 > La_{0.8}Sr_{0.2}MnO_3 > La_{0.6}Sr_{0.4}MnO_3$, while the reverse was true at lower temperatures. $La_{0.6}Sr_{0.4}MnO_3$ was the most active catalyst at low temperature; Marchetti and Forni attributed this to the adsorbed oxygen on the surface [99]. At high temperature, the $LaMnO_3$ catalyst was more active due to the excess oxygen present in the structure; they attributed this to the availability of lattice oxygen at these temperatures. TPR-MS analysis also confirmed the presence of two active oxygen species, (a) surface adsorbed oxygen, which is active at low temperatures and (b) lattice oxygen, which is active at high temperatures. The oxidation reaction examined here involved CH_4 and surface oxygen on the catalysts. As a result, TDS-MS analysis was preformed with all the catalysts by monitoring the reaction products obtained by reacting CH_4 and $^{18}O_2$ (reaction conditions 1mbar CH_4:O_2 with the temperature raised from 50-550^0C at 5^0C min^{-1}. The catalyst was first pretreated to remove moisture and impurities in a vacuo (<10^{-6} mbar) at 500^0C. The sample was then activated with 1 mbar of $^{16}O_2$. The TDS-MS experiments showed a peak m/z = 44 for CO_2 ($C^{16}O_2$), indicating no direct reaction between gas phase $^{18}O_2$ and CH_4. However, the m/z = 36 ($^{18}O_2$) and m/z = 32 ($^{16}O_2$) peaks suggest $^{18}O_2$ replace oxygen on the catalysts surface ($^{16}O_s$). This implies that an oxygen exchange reaction occurs before the increase in catalytic activity. This can clearly be observed when increasing the value of x in the series of $La_{1-x}Sr_xMnO_3$. By doing this it was found an anionic vacancy was created and as a result the oxygen exchange reaction occurred more readily [99]. Thus, explaining the high activity of this catalyst towards methane oxidation.

1.3.3 Methane Oxidation on Metal oxides

Low temperature methane oxidation over a series of transition metal stabilized ZrO_2, pure ZrO_2 and Mn-impregnated catalysts were examined by Choudhary et al. [102]. A series of Cr, Mn, Fe, Co, Ni and Cu-stabilised ZrO_2 catalysts with a molar ratio of 0.25 Zr-metal were prepared using co-precipitation method by mixing the metal nitrate with aqueous solutions of zirconyl nitrate. The metal hydroxide was then co-precipitated out of solution at pH 8 with a 25% aqueous tetramethylammonium hydroxide with vigorous stirring at $30^{O}C$, followed by washing with deionised water and drying at $110^{O}C$ for 2h, with subsequent calcining in air at $500^{O}C$ for 8h and then $600^{O}C$ for 1h. A pure ZrO_2 catalyst was also prepared for comparison work using the above procedure. A Mn-impregnated ZrO_2 catalyst was also prepared for study by incipient wetness method with aqueous nitrate salt of Mn. The catalyst was dried and calcined as above. XRD analysis showed a cubic structure for Mn, Co and Fe doped ZrO_2 catalyst and a monoclinic structure for Mn-impregnated ZrO_2.

Activity measurements of all catalysts were measured with a 1% mol CH_4/air mixture between 300-$600^{O}C$ with in-line gas chromatograph for gas analysis. The Mn-stabilised ZrO_2 catalysts show the highest measured surface area and activity of all the samples (see Table 1.4). From activity measurements, the stabilised cubic ZrO_2 catalysts of Co, Mn and Fe exhibit greater activity in comparison with Ni-, Cu-, Cr-stabilised samples towards methane combustion with complete conversion within the temperature range studied. The Mn-impregnated sample did not reach complete conversion but in comparison with the pure ZrO_2 sample was quite active. The Mn-stabilised ZrO_2 showed the highest activity of all stabilised samples and is much larger than the Mn-impregnated sample. Choudhary et al. [102] proposed the high activity was attributed to the transition metal doping, which stabilised the ZrO_2 and thus drastically increased the lattice oxygen atoms and the high oxygen mobility in the stabilised ZrO_2.

Table 1.4: Methane activity and surface area measurements for a series of metal oxides [102].

Catalysts	S_A m^2g^{-1}	T_{50} (^OC)	T_{90} (^OC)
Fe-stabilised ZrO_2	102	503	557
Co-stabilised ZrO_2	98	464	550
Mn-stabilised ZrO_2	105	450	545
Ni-stabilised ZrO_2	-	~545	-
Cu-stabilised ZrO_2	-	~530	-
Cr-stabilised ZrO_2	-	~490	-
Mn-impregnated ZrO_2	-	~560	-
Pure ZrO_2	-	-	-

S_A = Surface Area, T_{50} = Temperature for 50% Activity.

In summary, Choudhary et al. [102] found the enhancement of the lattice oxygen reactivity resulted from transition metal doping of ZrO_2, which in turn created crystal defects stabilizing the ZrO_2. This resulted in the formation of low coordinated lattice oxygens and transition metal sites on the surface and both surface and bulk oxygen mobility in the catalyst was increased.

Arnone et al. [103] investigated the potential use of simple and mixed transition metal oxides containing Co, Mn, Cr and Fe as methane combustion catalysts. They also tested the use of Zn and Mg ferrite along with Co_3O_4 and γ–Fe_2O_3 catalysts. The oxide catalysts studied are listed below (Table 1.5). The catalysts were prepared by precipitation, while the catalysts containing Zn and Mg ferrites were prepared as aerogels and Co_3O_4 and γ–Fe_2O_3 were commercially provided materials. All catalysts were reduced in flowing air at 600^{O}C with a 2 wt. % H_2/Ar mixture at heating rate of 10^{O}C min^{-1} up to 600^{O}C.

Table 1.5: XRD crystalline phases, specific surface areas and thermal properties of the catalyst [103].

Catalysts	XRD phase	S_A m^2g^{-1}	T_{onset} (^{O}C)	T_{max} (^{O}C)	Ea (KJ/mol)
Co_3O_4	Normal Spinel	15	264	382, 470	83.6
Mn_3O_4	Random Spinel	24	187	385, 520	83.6
Cr_2O_3	Corundum	18	182	295, 470	83.6
γ–Fe_2O_3	Non-stoichiometric Spinel	22	373	448, 535	83.6
α–Fe_2O_3	Corundum	102	336	460, 520	83.6
$CoCr_2O_4$	^Normal Spinel	110	185	225	83.6
$ZnFe_2O_4$	^Normal Spinel	27	284	-	125.4
$Mg_{0.5}Zn_{0.5}Fe_2O_4$	Random Spinel	37	236	-	125.4
$MgFe_2O_4$	^Inverted Spinel	56	248	-	125.4

* Ea – Activation energy

*S_A – Specific surface area

^ Normal spinel are spinel structures in which identical cations occupy the octahedral sites, whereas inverted spinel have two cations sharing the octahedral sites.

From XRD results all samples exhibit a spinel structure except Cr_2O_3 and one of the ferric oxides, which crystallize in the corundum structure. BET surface area analysis reveals low surface area for the simple oxides of about $20m^2g^{-1}$ except α–Fe_2O_3, while mixed oxides exhibited higher surface areas. TG/DTA analysis on all samples except Co_3O_4, Mn_3O_4 and γ–Fe_2O_3 showed structural stability up to 1000^{O}C. The reducibility of the oxide samples was examined using TPR. The reductions for all oxides occurs in 2 or more steps starting at quite low temperatures and complete reduction below 600^{O}C for the simple oxides of Co_3O_4, Mn_3O_4 and Cr_2O_3. Arnone et al. [103] reported that all reduction-oxidation reactions were reversible with the exception of the Fe based system.

The oxidation reaction was studied in a fixed bed quartz micro-reactor with a feed composition of 0.4% CH_4 and 10% O_2 in a balance of N_2. Complete conversion of methane was achieved below 600^{O}C with total selectivity towards CO_2 for all catalysts

except γ–Fe_2O_3. The catalyst samples were allowed to cool down to room temperature and retested. The results for the second cycle exhibited similar activity to the first cycle apart from the Fe based samples, which gave rise to some loss in activity suggesting these oxides undergo a deactivation under the reaction conditions. The $CoCr_2O_4$ catalysts exhibited the highest activity of all the oxides. Arnone et al. [103] proposed that this was due to the larger surface area compared with the other oxides of Co, Mn, and Cr.

The kinetics of the oxidation reaction was studied assuming the methane oxidation followed a first order rate equation. Conversion rates of CH_4 ranging from 10 to 90% were used to evaluate activation energies of the catalysts. The authors observed activation energies of approximately 84KJ/mol for all single oxides containing Co, Mn, Cr and Fe and for $CoCr_2O_4$. The mixed Fe oxides were also evaluated and higher activation energy of 125KJ/mol was recorded. This was attributed to the dilution of the Fe^{3+} with the bivalent cation, which modified the methane oxidation mechanism.

In conclusion, all catalysts (i.e. simple and mixed oxides) were activated at a lower temperature than the perovskite oxides [104] and the activity of the Cr_2O_3, Co_3O_4 and Mn_3O_4 were comparable to the noble metals [105] with 100% selectivity towards CO_2. The reaction mechanism for the oxidation of methane of the simple oxides also follows a similar path regardless of the transition metal.

Green et al. [106] examined a series of cobalt based supported catalysts for their effectiveness as methane combustion catalysis. The catalysts were prepared by incipient wetness of the support material with an aqueous cobalt nitrate salt, followed by drying at $100^{O}C$ overnight and calcining in air at $600^{O}C$ for 4hrs. The supports examined were ZrO_2 (S_A $51m^2g^{-1}$), Al_2O_3 (S_A $149m^2g^{-1}$), TiO_2 (S_A $150m^2g^{-1}$) and MgO (S_A $22.4m^2g^{-1}$). Metal loadings varied from 1-15 wt. % for the zirconium support oxide.

The influence of calcination temperature and its ability to resist sintering at high temperatures were examined for Co/ZrO_2. In this investigation, a 10% CoO_x/ZrO_2 was calcined at $1000^{O}C$ for 4hrs and its activity tested for methane combustion at low temperatures. The CH_4 oxidation reaction started at $550^{O}C$ and complete conversion to CO_2 was reached at $750^{O}C$. The activity of a 10% Co/ZrO_2 catalyst calcined at lower

temperatures and ZrO_2 support under the same conditions were also determined and showed higher activity than the Co/ZrO_2 catalysts calcined at 1000^0C. Green et al. [106] concluded the zirconia supported cobalt catalysts were very active and stable when calcination and reaction temperatures were no more than 900^0C. Calcining the catalysts above this temperature for more than 1h was found to decrease the catalytic activity. XRD pattern of the ZrO_2 exhibited sharp and some split peaks, which were due to large particles of ZrO_2 being formed at the high temperatures and sintering of the ZrO_2 support, or formation of new ZrO_2 phase. BET analysis revealed a decrease in surface area from $51.5m^2g^{-1}$to $1.5m^2g^{-1}$ due to the sintering of ZrO_2 support. Raman spectra also revealed no structure (surface state) difference between the ZrO_2 before and after calcination. Therefore, Green et al. concluded the activity decrease was due to loss in surface area [106].

The activity of the support materials for methane oxidation is shown in Fig. 1.13. The ZrO_2 and Al_2O_3 exhibit the highest activity with complete conversion to CO_2 within a temperature range of 600-650^OC with Al_2O_3 exhibiting greater activity. The TiO_2 and MgO supports were active above 600^OC and complete conversion of methane occurred over 700^OC. Yang et al. proposed that the activity trend of the supports was due to the oxygen mobility, acidity and thermal conductivity of the catalyst [107]. Hence among the supports TiO_2 and MgO exhibited high oxygen mobility and conductivity but lower acidity than the ZrO_2 and Al_2O_3. Activity measurements were also determined over Co supported catalysts with metal loadings of 10 wt. % (Fig. 1.14). The Co/ZrO_2 catalyst showed the highest activity with complete combustion to CO_2 at 520^OC. The Co/MgO had lower activity but was more active than TiO_2 towards methane oxidation. However, among all the Co supported catalysts tested, the Co/Al_2O_3 exhibited the lowest activity. From previous studies [108] the low activity of the Co/Al_2O_3 system was attributed to metal support interaction forming an inactive catalytic species (i.e. $CoAl_2O_4$).

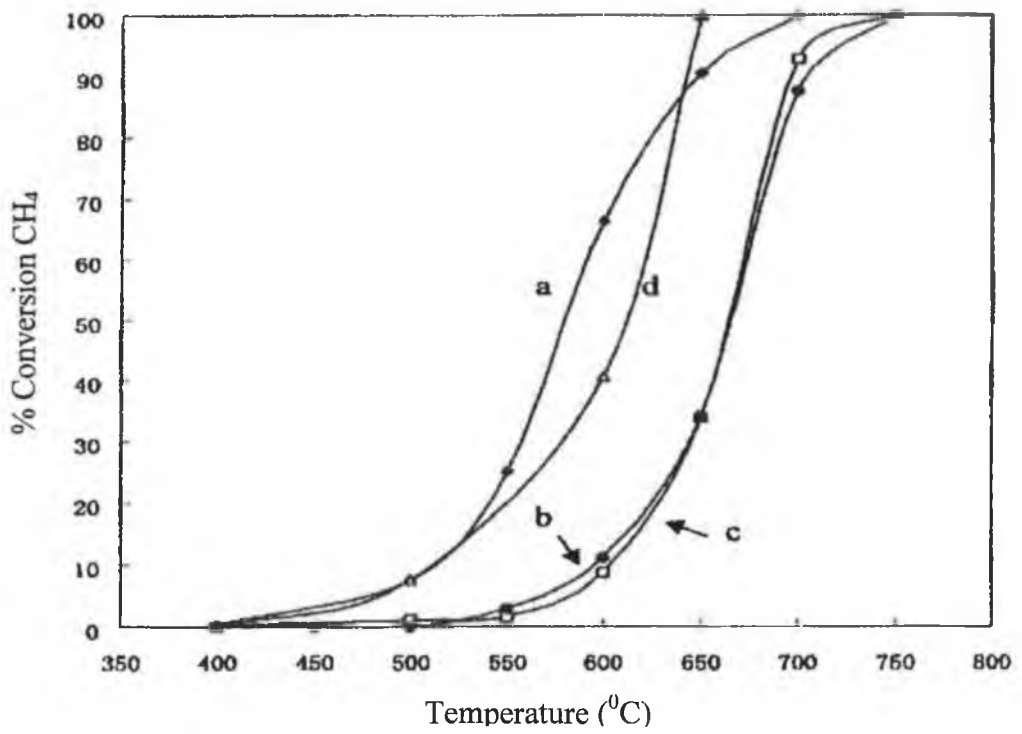

Figure 1.13: Catalytic activity of different supports for CH_4 combustion: (a) ZrO_2 (b) MgO (c) TiO_2 (d) Al_2O_3 [106].

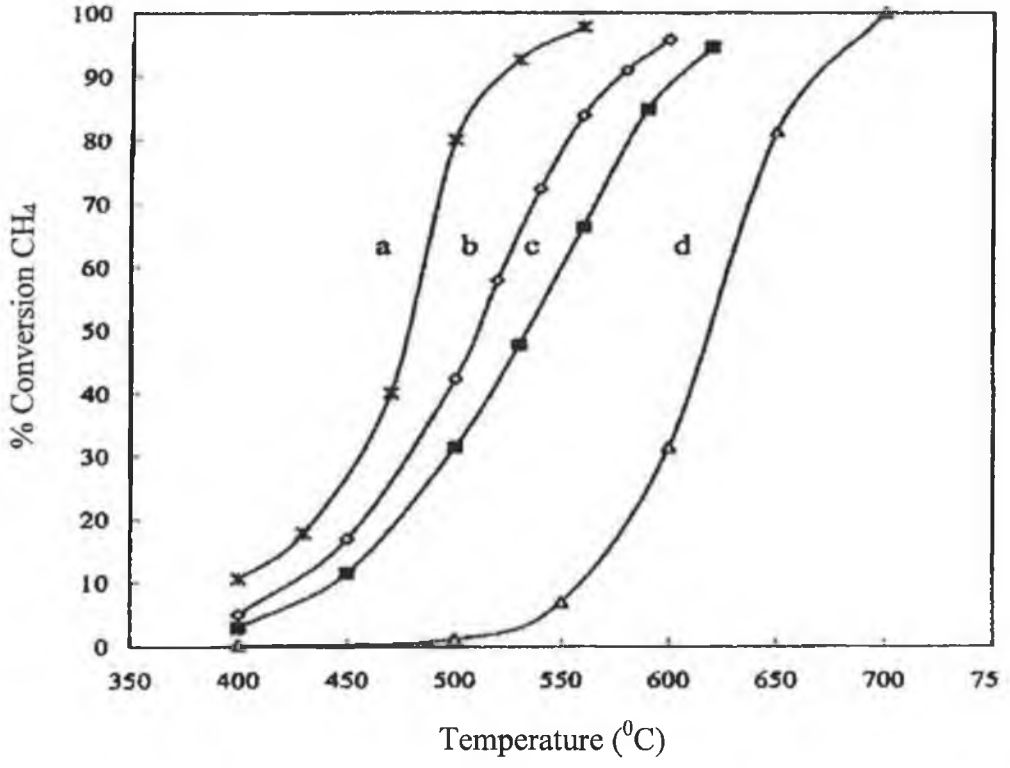

Figure 1.14: Catalytic activity of different supports for CH_4 combustion: (a) 10% Co/ZrO_2 (b) 10% Co/MgO (c) 10% Co/TiO_2 (d) 10% Co/Al_2O_3 [106].

A range Co/ZrO_2 catalysts with metal loadings in the 1-15 wt. % range were tested. The surface area determinations showed a decreasing surface area with increasing Co content. The 1.0% Co catalyst exhibited the highest activity for CH_4 oxidation indicating that although Co_3O_4 was the most active component for the oxidation, high metal loading can be detrimental to the combustion of methane. Therefore, Green et al. proposed that a synergism between the Co_3O_4 and ZrO_2 might play an important role in the methane oxidation process. XRD, LR (Laser Raman), IR results and activity tests suggest that the active site for the low content Co catalyst is the highly dispersed Co_3O_4 promoted by ZrO_2 and the active site for the high-content Co are the bulk Co_3O_4 particles. This highly dispersed Co_3O_4 phase accounts for the increased activity for the 1% Co/ZrO_2.

In summary, Green et al. [106] found the low loading Co/ZrO_2 the most effective catalyst for the combustion of methane. However, the catalytic activity decreases dramatically on exposure to high temperature ($1000^{O}C$) due to loss in surface area and forming of less active bulk Co_3O_4. The Co/TiO_2 was found to be less active due to the present of bulk Co_3O_4 oxide. The Co/Al_2O_3 was found to be the least active containing poorly dispersed Co_3O_4.

1.4 Total Oxidation of higher Hydrocarbons

The total oxidation of hydrocarbon follows the generalized reaction:

$$C_n H_{2n+2} + (3n + 1)/2 \quad O_2 \rightarrow nCO_2 + (n+1) H_2O$$

Several authors have reported the noble metals of Pt and Pd to exhibit higher catalytic activity than the metal oxides for the deep oxidation of hydrocarbons (C_2 to C_8) [1, 109-113].

Morooka et al. [24] evaluated a series of metal and metal oxides catalysts for the oxidation of propane in a flow system micro-reactor at atmospheric pressure with a feed composition of 2-vol% hydrocarbon and 50-vol% O_2 in a balance of N_2. Values for both activation energies and reaction orders along with reaction temperatures were given (Table 1.6). Regardless of the catalyst employed selective conversion was achieved in the oxidation reaction with CO_2 being the only product formed. The activity trend showing the order of decreasing catalytic activity as follows:

$$Pt > Co_3O_4 > Cr_2O_3 > Pd, MnO_2 > CuO > NiO > Fe_2O_3 > CeO_2 > ThO_2$$

Pt was nearly two orders of magnitude more active than Co_3O_4. However, it should be noted the above data is only qualitative since differences in the surface area of the samples were not taken into consideration.

The kinetics of the propane oxidation reaction was also study and described by a power rate law:

$$r = k P_{C_3H_8}^{m} P_{O_2}^{n} = k P_{C_3H_8}^{1}$$

The reaction was found to be first order with respects to propane and independent of the oxygen concentration.

Table 1.6: The kinetic characterisation for the deep oxidation of propane over metal and metal oxide catalysts [24]

Catalysts	Temperature (^{O}C)	Log r*	Ea kcal/mol	Reaction orders C_3H_8, m	O_2, n	Overall order M + n
Pt	220-260	-5.09	17.0	0.83	-0.09	0.74
Pd	337-368	-6.99	36.3	1.30	-1.60	-0.30
Co_3O_4	275-341	-6.76	24.5	0.94	0.30	1.24
Cr_2O_3	283-341	-6.88	21.9	0.78	0.17	0.95
MnO_2	294-358	-7.01	28.3	1.01	0.00	1.01
CuO	309-363	-7.13	28.7	0.54	0.16	0.70
NiO	350-416	-8.33	26.2	0.89	0.40	1.29
Fe_2O_3	395-425	-8.83	35.9	0.68	0.22	0.90
CeO_2	383-450	-9.21	27.8	0.67	0.25	0.92
ThO_2	373-418	-9.26	368	-	-	-

r* is the reaction rate ($molm^{-2}s^{-1}$) at $300^{O}C$ with 2/50-vol% C_3H_8/O_2 mixture in balance N_2 calculated from the apparent activation energies.

Morooka et al. [24] examined the relationship between catalytic combustion activity and heats of formation (ΔH_0) of the metal oxides per unit oxygen atom (i.e. ΔH_0 represents the heats of formation of the oxides or the number of O_2 atoms present in the oxide molecule) further. Figure 1.15 illustrates a correlation for propane oxidation in which high values of ΔH_0 signified low combustion activity. Therefore the activity trend observed above was in agreement with the correlation. Morooka et al. also hypothesized that the oxidation reaction mechanism over the noble metals differed from that on the metal oxides and the slow step depended upon the heats of formation [24]. In conclusion, Morooka et al. proposed the slow step in the reaction mechanism for propane oxidation was the adsorption of oxygen on the Pt and Pd metals and surface reaction between the adsorbed hydrocarbons and adsorbed oxygen on metal oxides [24].

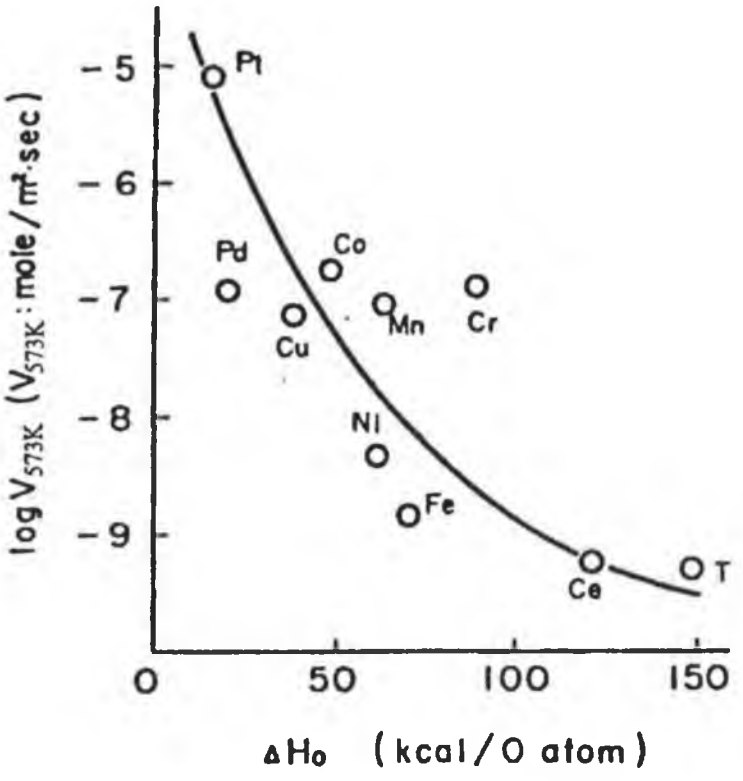

Figure 1.15: Relationship between the catalytic activity and ΔH_0 in the propane oxidation reaction [24].

The kinetics of propane oxidation over $Pt/\gamma-Al_2O_3$ and the influence of metal concentration and particle size were investigated [112]. Catalysts were prepared using the incipient wetness method by multiple impregnations with H_2PtCl_6 of the alumina support. The metal loading ranged from 0.03 to 30 wt. %. The catalysts were calcined at 600^{O}C, followed by reduction at 400^{O}C for 2h and subsequent heating in O_2 at 500^{O}C for 20hrs for sample pretreatment. The reaction kinetics were studied under oxygen rich conditions in a recirculation batch reactor with 1.5 mol% C_3H_8 and 15 mol% O_2 initial mixtures in Ar carrier gas. Under the conditions studied, the reaction was first order with respect to propane and zero order with respects to oxygen. Therefore they expressed the rate of C_3H_8 oxidation by the product of propane concentration Cp and the rate constant k.

$$\frac{d_{Cp}}{dt} = -K_{Cp}.$$

As the Pt loading was increased, larger particles sizes were formed with large amounts of subsurface Pt atoms. The rate constant k^1 for the C_3H_8 oxidation increased from 1.25×10^{-3} min^{-1} at a loading of 0.03% to 8.04×10^{-3} min^{-1} for a 30 wt% Pt catalyst suggesting that propane oxidation was sensitive to particle size with increasing Pt concentration, dispersion decreased and particle size increased [112]. The turnover frequencies per Pt surface atom was determined from the chemisorption data and an increase in activity yielding a k^1 value of 1.15×10^{-3} min^{-1} for the highly dispersed Pt at 0.03 wt% was observed, which increased by a factor of 80 for the 30 wt% Pt to 9.20×10^{-2} min^{-1}. The apparent activation energy for the reaction remained constant at 22.1 ± 3.4 kcal/mol over the particle size range studied. This indicated that the change in rate-determining step was not associated with the change in C_3H_8 oxidation rate with particle size. Therefore oxidation on the larger particles was thought to be coupled with a change in reaction site density.

Several authors [80, 114] have reported increasing Pt particle size due to sintering in hydrogen above $500^{O}C$ from previous TEM studies. The sintering was found to increase the propane oxidation rate [112]. Redispersion of the sintered particles was also found by treating the Pt sample under oxygen at $500^{O}C$ [55, 80, 114-118]. Sintering experiments were carried out with highly dispersed Pt samples (i.e. 0.12 wt %). The sample was pretreated in hydrogen at $500^{O}C$ for 63hrs, this resulted in an increase in the rate constant from 1.5×10^{-3} min^{-1} to 4.6×10^{-3} min^{-1} [112]. As predicted, the rate changed on sintering, which in turn varied with temperature and time exposure. The maximum rate constant of 10.3×10^{-3} min^{-1} was determined following sintering at $800^{O}C$. Further sintering at temperatures of $900^{0}C$ was found to result in diminished activity due to a fraction of the surface atoms being lost to the bulk.

In conclusion, the oxidation of propane over Pt/γ–alumina was a structure sensitive reaction apparent by a rate increase with particle size and followed a Langmuir-Hinshelwood mechanism. Sintering and redispersion occurred with thermal treatment under different gaseous atmosphere. The variation in particle size depended on Pt loading and thermal pretreatment under a hydrogen atmosphere and in turn the propane oxidation rate was limited by very large Pt particles indicated by the loss in surface atoms to the bulk.

Renken et al. [119] investigated the oxidation of propane over a series of Pd and Pt catalysts supported on glass fiber, The glass fiber support (GF) used was prepared from woven aluminoborosilicate followed by pretreatment in aqueous HCl solution at $90^{O}C$, this pretreatment resulted in an increased surface area of the support material from 2 to $275m^2g^{-1}$. The second support (SGF) used was a commercial woven form of chemical composition of 97% SiO_2 used without sample pretreatment. Modification of the GF and SGF supports by titania (TGF), zirconia (ZGF) and alumina (AGF) was made by wet impregnation with an aqueous solution of the salts, followed by calcining in air. The Pd/Pt catalysts with loadings in the range of 0.1-0.3 wt.% were subsequently prepared by ion exchange or impregnation of the support materials in aqueous ammonia solution (pH10) of the Pt and Pd salts (i.e. H_2PtCl_6 and $PdCl_2$), followed by drying and calcining in air at $450^{O}C$ for 1h. Catalytic activities were measured on a 0.4g mass sample with a varying fed concentration between 0.1-2.5 vol. % C_3H_8 and 1-30 vol. % O_2.

Propane oxidation over all the Pt supported catalysts tested exhibited higher activity than the Pd samples even at metal loadings as low as of 0.05 wt. % with CO_2 and H_2O being the only reaction products formed. Kinetics of the Pt/Pd propane oxidation was examined in both oxidizing and reducing conditions. The reaction orders with respect to C_3H_8 over Pd was $0.5 \leq n \leq 0.6$ and positive with respect to O_2, while over Pt the reaction orders were n=1, n= - 0.5 with respect to C_3H_8 and O_2. The negative order with respect to oxygen on Pt was attributed to adsorption competition between the C_3H_8 and O_2. Therefore, under oxygen rich conditions propane oxidation rate over Pt decreased due to inhibition by oxygen.

The morphology of fiber surface and the effect of modification by the oxides of Al_2O_3, TiO_2 and ZrO_2 on the metal dispersion were examined using TEM and HREM. Surface modifications by the oxides were found to affect surface area and in turn influence catalytic activity of the samples [119]. The BET surface area values measured for the titania and zirconia modified supports gave the largest value for surface areas. Modification of the support with titania (TGF) and zirconia (ZGF) increased catalytic activity towards propane oxidation on both Pt and Pd catalysts, whereas support modification with the alumina oxides showed no such effect on catalytic activity. The increase in catalytic activity of TGF was thought to be due to small disordered crystallite

phase of the TiO_2 exposing a larger surface, thus allowing, a highly dispersed Pd/Pt metal. Increasing palladium loadings from 0.1 to 0.3 wt. % lead to a proportional increase in activity, thus indicating a constant Pd dispersion within this concentration range.

In conclusion, high specific surface area Pt/Pd supported on glass fibers were effective combustion catalysts. Modification with titania and zirconia of the Pt/Pd support catalyst was found to achieve propane conversion close to 100% at short residences times, the Pt being more active than the Pd in total propane oxidation, showing ignition temperatures of 200-220^{O}C. TEM and HREM studies showed higher dispersion of Pt and Pd on glass fiber surfaces.

Otto et al. [112] already evaluated the effect of Pt concentration and particle size on the oxidation of propane over Pt/γ–Al_2O_3. Hubbard et al. [120] in a subsequent study investigated propane oxidation activity as a function of Pt loading, metal surface area, and temperature over Pt/ZrO_2 catalysts. The oxidation reaction was found to be dependent not only on particle size but also support material. Catalysts with metal loadings ranging from 0.02 to 1.5 wt.% Pt were prepared by multiple impregnation of the support material with chloroplatinic acid followed by drying twice in air at 120^{O}C for 2hrs in between impregnation step. The catalyst samples were then calcined at 600^{O}C for 20hrs. Sample pretreatment carried out was kept constant with reduction in hydrogen at 400^{O}C for 2hrs, followed by heating in oxygen at 500^{O}C for 20hrs. In the study, a highly crystalline monoclinic ZrO_2 support with surface area ($5.5m^2g^{-1}$) was used and compared with γ–Al_2O_3 with a poor crystalline high surface area ($85m^2g^{-1}$) support.

Sample pretreatment as already demonstrated by Otto et al. [112] influenced catalytic activity. Hubbard et al. found at pretreatment in H_2 at 500^{0}C increased the propane oxidation rate over the Pt/ZrO_2 [120]. However, exposure of 0.10 wt. % Pt/ZrO_2 sample to oxygen up to 600^{O}C had no impact on the propane oxidation rate, whereas over the Pt/γ–Al_2O_3 the oxidation rate was found to decrease due to redispersion [112]. Redispersion under oxidising conditions at 500^{0}C after 12hrs for Pt/Al_2O_3 was shown to occur readily provided chloride was present, whereas pretreatment up to 96hrs at 500^{0}C for Pt/ZrO_2 showed very little improvement in redispersion. They attributed this to lack of metal support interaction on the Pt/ZrO_2, which prevented redispersion of the Pt [120],

whereas redispersion for the Pt/Al_2O_3 occurred readily under oxidising conditions at 500^0C provided chlorine was present as a result of metal interaction with the alumina [55, 114-118].

The complete combustion of propane to CO_2 requires only a 4 vol. % C_3H_8, air mixture. Under the excess oxygen conditions used [120], the propane oxidation rate was described by first order kinetics with respect to C_3H_8 and independent of O_2 concentration. The Pt/ZrO_2 catalysts exhibited a constant value for the apparent activation energy of 17.8 ±3.5 kcal/mol over the entire concentration range studied. This value agreed with previously reported activation energies of 17-22 kcal/mol over Pt for oxidation of C_3H_8 [121, 122]. Therefore, changes in propane oxidation rate were attributed to changes in the density of the active sites on the ZrO_2. The average activation energy obtained on $Pt/\gamma-Al_2O_3$ was 22.1±3.4 kcal/mol [112]. Hence, the differences in activation energies were within experimental error. The impact of Pt loadings on the propane oxidation rates was evaluated in terms of rate constant, k. The value of k for the Pt/ZrO_2 was found to decrease over the Pt concentration range studied by a factor of 20, from 152×10^{-3} to 6.55×10^{-3}. Therefore the rate constant was found to decrease with increasing Pt concentration on the ZrO_2 support. The fastest rate occurred over lower metal loading Pt/ZrO_2 samples with high dispersion and small particles [120]. This increase in activity was associated with surface roughness of the ZrO_2 support and the presences of step and kink sites, since these sites favour catalysis to a greater degree than planar or terrace sites on larger particles. A comparison of the specific rate constants as a function of metal loading between the Pt/ZrO_2 and $Pt/\gamma-Al_2O_3$ was made, (see Fig. 1.16) [120].

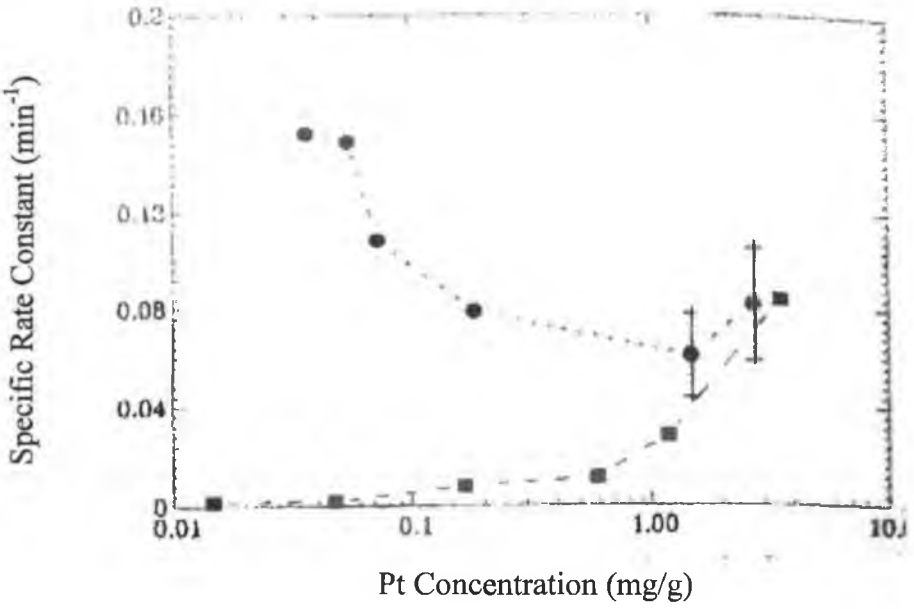

Figure 1.16: Specific rate constant for C_3H_8 oxidation at 275^{O}C per Pt surface atom versus Pt concentration [120]. (●) Pt/ZrO_2 (■) $Pt/\gamma-Al_2O_3$

This figure describes turnover rate per Pt surface atom by dividing the dispersion into rate constant. The maximum specific activity for the C_3H_8 oxidation of the Pt/ZrO_2 was found at the lower concentrations, while at the same concentration the $\gamma-Al_2O_3$ was found to be at its lowest activity, two orders of magnitude less than the Pt/ZrO_2 [120]. The difference in activity was attributed to the metal-support interactions on the $Pt/\gamma-Al_2O_3$ resulting in deactivation of the small Pt particles [112], whereas the activity of the Pt/ZrO_2 was not affected by metal support interactions. This was attributed to the extremely inert nature of the zirconia support. Based on previous studies [112] the impact of metal-support interactions on the alumina was confirmed, in which it was found that at high temperature, the small Pt particles supported on γ–alumina were reduced compared to the larger particles, which were observed to behave like bulk Pt [80, 112]. This interaction was not observed on the Pt/ZrO_2 sample due to the less reactive nature of the zirconia. The reactive nature of the supports was confirmed from infrared data showing a CO adsorption peaks for Pt on γ–alumina [20, 120]. Infrared data showed two CO adsorption bands at 2068cm^{-1} for the dispersed Pt on γ-alumina and at 2080cm^{-1} for crystalline Pt, whereas only one adsorption band at 2080cm^{-1} was observed over the entire concentration range on Pt/ZrO_2.

1.5 Thermally Stable Supports Materials.

In this section thermally stable supports required in todays demanding field of catalytic combustion, will be discussed, in relation to preparation and use as support materials.

Combustion catalysts have found application in automobile exhaust catalysts systems, and gas turbines, with much higher operating temperature than in conventional catalytic reactors. Therefore, the development of new types of catalyst supports with thermo-chemical stability in atmospheres, containing oxygen and steam up to 1200-1300^{0}C are required for the chemical industry [1]. Therefore, in this section whiskering of expanded metal based supports and how they provide the necessary mechanical strength will be discussed. The application and development of a sufficiently large and stable surface area support will also be discussed.

1.5.1 Whiskered Substrate Support

Whiskers are metallic or non-metallic filamentary small very thin single crystals with an extremely large length to diameter ratio and are grouped into three different groups: 1) wires, 2) fibers and 3) whiskers [136]. As a result, of their minute size, they possess a high degree of crystalline perfection both internal and external and are virtually flawless and the small dimension minimises the occurrence of defects that are responsible for the low strength of materials in bulk form. These properties are attributed to their extraordinarily high tensile strength; they are also known to be the strongest materials around today for use as catalytic support substrates. Whisker materials are composed of graphite, silicon carbide and aluminium oxide. The mechanical characteristics of some of these materials are listed in Table 1.7.

Table 1.7: Characteristics of some whiskered reinforced materials. [136]

Material	Specific Gravity	Tensile Strength psi × 10^6 (MPa × 10^3)	Specific Strength (psi × 10^6)	Modulus Of Elasticity psi × 10^6 (MPa × 10^3)	Specific Modulus (psi × 10^6)
Graphite	2.2	3 *(20)	1.36	100 *(690)	45.5
Silicon Carbide	3.2	3 *(20)	0.94	70 *(480)	22
Silicon Nitride	3.2	2 *(14)	0.63	55 *(380)	17.2
Aluminum oxide	3.9	2 – 4 *(14 – 28)	0.5 – 1.0	60 – 80 *(415 – 550)	15.4 - 20.5

*1 psi = 1.507436×10^5

Whiskers are well known to form on low melting point metals, such as Sn [137-145], In [146], Cd [146-148], Pb [143], and Zn [147, 148] and their alloys. Whiskers of single crystals are also grown on iron aluminium alloy metals with almost no defects. These aluminium oxide whiskers can grow to a length of 0.5 inches, and have a tensile strength of 960×10^{03} psi above 1371^0C.

The iron-aluminium alloys have received significant research over the last two decades due to their excellent thermal stability at high temperatures coupled with their unique properties such as low density, good room temperature and high-temperature tensile strengths [149-154]. Their excellent oxidation, corrosion and sulfidation resistance at high temperatures have also been reported and their reasonable strengths at high temperatures for use as structural materials [155-157]. From literature studies it is clear that whiskers are many times stronger than their bulk counterparts and α–Al_2O_3 whiskers are reportedly to process a strength of over 700 × 10^3 psi at temperatures as high as 1560^OC. This makes their application in automobile catalyst for emission control ideal, since temperatures don't exceed 1000^OC.

There are several methods by which whiskers can be grown including (a) stress-induced, growth by evaporation – condensation, (b) chemical reduction, (c) vapour-liquid-solid mechanism (VLS).

(a) Evaporation – Condensation method

Sublimation or evaporation of a source material, mass transport through the vapour phase and condensation at the growth site causes whisker growth under low super saturation. The high melting points and low vapour pressures used in this method have limited its application to the growth of oxide whiskers. Webb et al. established a high temperature induction furnace (Fig. 1.18) for growing aluminium oxide crystals as outlined [159].

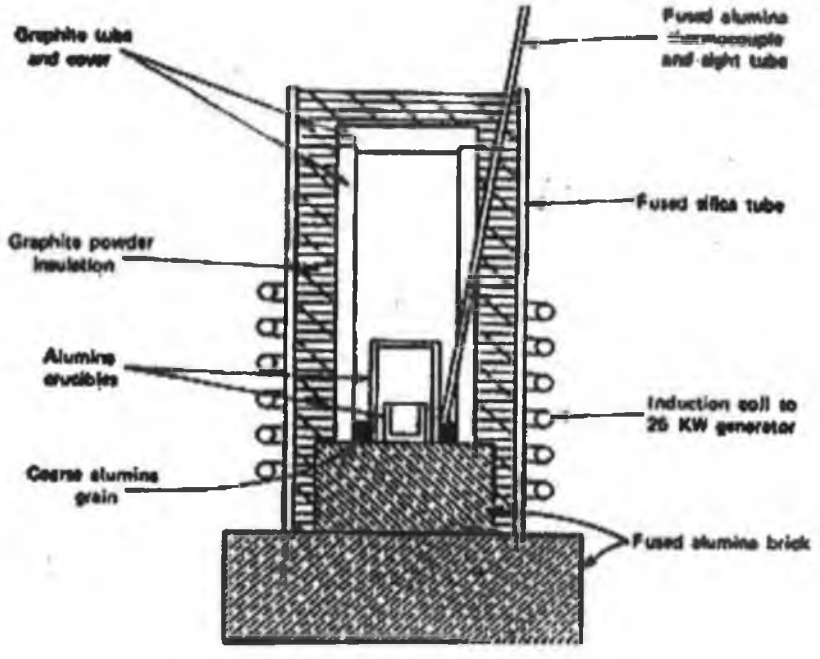

Figure 1.18: High temperature induction furnace [159].

Aluminium oxide whiskers formed in the cooler portion of the growth chamber when the source material was heated to 1960^{O}C. This has not been successful for many materials because of the small whisker size, low population, extended growth times and experimental difficulties encountered at the high temperatures employed in the technique.

(b) Chemical reduction method

Chemical reduction involved a reaction between a source material and an ambient gas phase to produce a volatile species, vapour transport to the growth site and condensation results in whisker growth under low supersaturation.

The apparatus consist of a tube furnace containing mullite, alumina or quartz tube, a ceramic boat filled with the source material, for example, aluminium and a controlled gas-flow system. In this system, the whiskers grow on the sides and top of the boat in relatively large, furry deposits. Growth times vary from 0.5 to 20 hours depending on the condition of the material. Whisker diameters range from submicron to 1um and lengths up to 10cm have been observed [160].

Webb and Forgeng [159] reported aluminium oxide whisker growth by passing wet hydrogen over a boat filled with molten aluminium. The temperature range used was between 1300 to 1450^{O}C with operating times of 2 to 20 hours. These conditions resulted in relatively large whisker deposits surrounding the boat with whisker lengths ranging from 1 to 30mm and hexagonal diameters of 3 – 50um were obtained.

Brenner [160] preformed similar experiments by heating a porcelain boat filled with aluminium to temperatures of 1250^{O}C in a flowing stream of hydrogen and some of the metal was oxidised to form a 'insulate' of whiskers over the top of the boat. According to Brenner whiskers grew abundantly at these temperatures only in porcelain boats. The diameters of the whiskers were reportedly in the range of a few microns up to 100um and grew up to 1.5cm in length.

(c) VLS crystal growth

Several authors [161] investigated crystal growth in the form of whiskers by the vapour-liquid-solid mechanism. Such whiskers or filamentary crystals of a unique form have been found to result from the anisotropic growth from the vapour. These crystals have a lengthwise dimension that is orders of magnitude larger than that of the cross section. For most filamentary crystals both the fast growth directional and directions of slow lateral growth have small miller indices. The special growth form for a whisker crystal implies that the tip surface of the crystal must be the preferred growth site.

Sears [162] suggested that whiskers contain a screw dislocation emergent at the growing tip. Such an axial dislocation provides a preferred growth site and accounts for the unidirectional growth. Price et al. [161] postulated that impurities arriving at the fast growing tip face become buried while those arriving on the surface of the slow growing lateral faces accumulate and thereby result in high aspect ratio whisker growth.

Frank's [143] studies suggested that whiskers generally grow from vapour or metallic deposits of gases or liquids on an aluminum film surface during heat treatments. Blech et al. [163] suggested that whisker formation was due to thermal stress caused by the difference in the thermal expansion coefficient between of the aluminium film and the substrate. Several studies [164, 165] suggested that a fabricated aluminium metal suffers mechanical stress and electromigration stress, resulting in hillocks (i.e. nodules) and whisker formation on the film surface. Several authors [150-153] have investigated whisker growth process on the metallic materials under various experimental conditions (i.e. temperature, time and gaseous atmospheres) and they proposed that whisker formation was due to the oxidation of the aluminium layer deposited on the metallic material. Vaneman [152] found that although whiskers may be grown on an iron-aluminium alloy without a low oxygen pretreatment, such a pretreatment was nonetheless preferred, to ensure consistent oxide growth over the entire surface. Oxidation at a temperature between about 870°C to 930°C for 8hours or longer was found to substantially cover the foil surface with a protective layer made up of high aspect oxide whiskers. Higher temperatures were reported to inhibit whisker growth probably due to the formation of non-whisker α-Al_2O_3 [153]. However, Vaneman [153] also reported the

growth of whiskers to be improved by heating the gauze in air within the typical temperature range (900-950^{0}C) for a relatively short period of time (< 2 hours) to initiate nucleation or growth of whiskers, and thereafter within a higher temperature range (above 950°C) to continue the growth of the whiskers at an accelerated rate, thereby reducing the processing time and expense involved in growing mature high aspect ratio whiskers [153]. He also noted that simply heating above 950°C without the initial heating step at the lower temperature resulted in the formation of non-whiskered Al_2O_3. Vaneman [152] reported that the particular uppermost whiskering growth temperature was sensitive to alloy composition.

Vaneman et al. [153] subsequently reported an accelerated method for growing oxide whiskers on aluminium containing stainless steel foil. They found the foil surface could be substantially covered with oxide whiskers on heating in air at initial temperatures of 900^{O}C and then increasing the temperature to >900^{O}C [153]. They proposed that the whiskers grown under these conditions were formed due to thermal and mechanical stress caused by the high temperature employed in the whiskering process. This study also revealed the presence of lumps of low aspect whisker (i.e. nodules) in some of the samples whiskered under different conditions. Cadien and Losee [166] reported that nodules seem to form frequently on aluminium films, and whiskers seem to form only in certain specific samples or under specific treatments. Succo et al. [168] reported whisker formation during aluminium alloy film deposition. The influence of environmental factors has also been reported to affect whisker growth [145-147]. Hazama et al. suggested whisker growth at an accelerated rate occurred at elevated temperatures in a vacuum environment [167]. The reverse observations were found using an oxidising atmosphere (i.e. with oxygen), during heat treatments that the nucleation and growth of whiskers was suppressed [164]. This indicates that the breaking of the aluminium surface oxide and/or rearrangement through surface diffusion has a critical role to play in the growth process of Al_2O_3 whiskers [164]. Vaneman et al [153] as previously stated in an early study found that when the foil was pretreated in a low oxygen atmosphere at temperatures between 875^{O}C and 925 ^{O}C improved whisker growth resulted. However, he found that with initial heating at lower temperatures, whisker growth was initiated and further temperature increases to temperatures in the range $\geq$ 900 ^{O}C accelerated the growth process.

1.5.2 Washcoat Supports

A washcoat is a thin layer of porous and refractory material used to increase the surface area of a low surface area support usually metallic alloy material. They usually consist of high surface area ($50 - 250 m^2 g^{-1}$) oxides. For example, Al_2O_3, SiO_2, TiO_2 and ZrO_2 are but a few together with bonding agents such as hydrous alumina, silica. It is important that the hydrous oxide forms strong bonds between the washcoat components [169]. The monolith substrate porosity and physical and chemical nature of the substrate surface play a large part in ensuring washcoat adherence.

In preparation of washcoat support materials, properties such as hardness, particle size, porosity, thermal expansion, are important in ensuring a high surface area support is formed. The thermal stability is also important as the surface area is subjected to ageing as operating temperature may exceed $1000^{O}C$. As a result, washcoats supports have been produced incorporating elements such as alkali metal oxides, alkaline earth metal oxides or rare earth oxides into the slurry mix, which act as surface area stabilisers. The introduction of such elements in alumina washcoat supports have been shown to retard the transition from the high surface area γ–Al_2O_3 phase to the dense lower surface area α– Al_2O_3 phase up to temperatures above $1100^{O}C$ [170].

The effect of particle size distribution of the starting powder and adhesion of γ-Al_2O_3 washcoats onto support substrates and the condition that can ensure integrity and endurance of the washcoat-substrate system under the severe operating conditions encountered in catalytic systems was investigated [158]. Adhesion of the washcoat on the support takes place by both mechanical mechanisms, such as anchoring and interlocking of the washcoat particles as well as with the surface irregularities of the support and via strong interfacial forces among the powder particles. Both of these mechanisms are influenced by particle size of the deposited material. As a result, they found that a certain threshold value around 5μm existed, below which the powder particle size has to be reduced, for achievement of satisfactory washcoat adhesion with support substrate.

Agrafiotis and Tseteskou subsequently investigated the adhesion of alumina washcoats with the aim of correlating the adhesion ability to the characteristics of the deposited powders. They showed that adhesion was principally dependent on the particle size of the deposited powders. Therefore, depending on the production method of the powders, some powders had large agglomerates and hence showed poor adhesion characteristics. They concluded in the study that particle size down to the order of 2-5 microns was necessary in order to ensure adhesion comparable to that of commercial catalysts [176].

Dispersal alumina is an active agent used to achieve improved adhesion of the washcoat and high dispersion of the active metal no matter what the concentration. Otterstedt et al. [173] reported good dispersion between 88-91% with 0.61 wt. % Pt loading from chemisorption over an alumina washcoat. The catalyst must also be able to withstand erosion and abrasion under the severe operating conditions encountered in a catalytic system. Therefore, it is essential that the support material processes a high thermal shock resistance. Thus, the hardness of the support material must be controlled. A method for producing a thermal shock resistant washcoated substrate involves introducing a buffering solution to control the pH at a certain value resulting in the formation of a gel within the washcoat mix. Formation of the gel prevents the washcoat from entering microcracks in the substrate support.

Physical characteristics such as crystalline phase, surface area and porosity are of great importance for the catalysts industry where a consistency and an unobtrusive nature of the washcoat support is highly desired. These characteristic are of great importance for a fluid and slurry bed reactions. Therefore porous alumina materials are used in the washcoat support in order to overcome the increase in diffusion resistances of the catalyst to the gas molecules during the catalytic process. These resistances are caused by impurities in the fuel sticking to the edge of the particle pores making gas flow into the catalyst somewhat difficult. The alumina processes a high degree of porosity, which allows for an increased surface area for impregnation of active metal. The amount of porosity is controlled by the technique of fabrication, starting material and the calcination time and temperature. In order to get a very porous final product, a material that will burn out during sintering is added during batch formulation [14, 169, 170, 174].

The thermal expansion coefficient of the washcoat and support must be similar in order to avoid washcoat-support separation. It must also maintain its surface area under the desired reaction conditions and lifetime of the catalysts. Loss of activity may occur as a result of loss of surface area caused by sintering (fusing together of atoms). This phenomenon is also crucial in the washcoat whereby loss of efficiency of the catalyst occurs due to active metal sintering [171]. Therefore alumina washcoat supports used for such processes use an element providing high-temperature stability. This property is important for the lifetime of the catalyst.

A problem associated with the high surface area alumina is its thermal stability as already mentioned. The presence of lanthanum (La) improves the thermal stability of the alumina washcoat support. This increase in stability can be related to the formation of lanthanum aluminate ($LaAl_2O_3$) with γ–Al_2O_3 through interfacial interaction [177, 178]. The addition of lanthanum also promotes better dispersion of the active metal and improved its resistance to sintering [178]. Honiche [177] investigated the addition of lanthanum to the alumina washcoat support as thermal stabiliser. Two different complex oxides with aluminium, i.e. lanthanum aluminate ($LaAlO_3$) and lanthanum hexa-aluminate (La-B-Al_2O_3), were examined and reported to bring about thermal stability.

Several patents have been lodged for producing thermally shock resistant washcoated substrates. Beauseigneur et al. [179] patent relates to a method for improving the thermal shock resistance of the washcoated substrate. They patented the addition of a buffer solution into the microcracks and the micropores of a porous sintered body; the pH of the buffer was selected so to result in gel formation on contact with the washcoat slurry. Formation of the gel prevented the high surface area oxide (i.e. alumina) washcoat slurry from entering the microcracks present on the metallic substrate. They found it was essential to block the microcracks during washcoating in order to preserve a high degree of thermal shock resistance. The washcoated slurry mix was then calcined at a temperature and time sufficient to form the washcoated substrate.

Shelef et al. [171] patented a series of washcoat solutions both with and without lanthana for an automotive catalyst system. The patent examined an γ–Al_2O_3 washcoat incorporating lanthanum oxide in the method to form a barrier between the OSC

components (i.e. ceria and praseodymia), which improved the preservation of both the OSC and dispersion of the active phase. A series of γ–Al_2O_3 washcoat and lanthana modified alumina washcoat solutions containing mixed phases of praseodymia and ceria were prepared as follows. Solutions of the mixed phases were prepared by adding the nitrate salts to dilute nitric acid (i.e. 25g to 500ml acid). The washcoat solution was subsequently prepared by mixing a ratio of alumina and lanthana-modified alumina with the mixed praseodymia and ceria phases, followed by calcining and ageing at temperature ranging from 500-800^{O}C over varying time frames.

The lanthana washcoat solutions were aged in a muffle furnace over 12hr periods at 800^{O}C and 900^{O}C to test for reducibility/stability. The washcoat solutions were examined by temperature-programmed reduction (TPR) to determine reducibility of the alumina washcoats (i.e. reducibility can be related to thermal stability). Shelef et al. reported that from these results, addition of lanthana had little effect of reducibility of the alumina washcoat at temperatures below 600^{O}C. However, on ageing at 800 and 900^{O}C, the lanthana samples showed much greater reducibility below 600^{O}C than alumina washcoats. In conclusion, addition of lanthanum oxide preserves OSC in a more reducible state.

Addiego et al. [181] investigated a method for producing a washcoated substrate for automobile catalysts. The washcoats are made fundamentally of AO-Al_2O_3 structure containing an ionisable compound of A, where A is Ba and/or Sr. The slurry washcoat solutions were prepared by contacting the elements of A in ionic form with aluminum oxide, followed by firing forming a homogeneously washcoat slurry with element A distributed throughout the alumina. The substrate was subsequently washcoated with the prepared BaO-Al_2O_3 washcoat slurry by contact with the substrate (metal) to form a green coating, which was subsequently heat treated to form the washcoat substrate. The washcoated system was then impregnated with an active metal followed by calcining forming a highly dispersed catalyst. The high surface area washcoat allowed active sites, especially metal to be preserved, thus increasing the catalysts lifetime. The washcoated catalysts exhibited a high surface area ($50m^2g^{-1}$), which was resistant to sintering on repeated exposures to temperatures over 500^{O}C. However, under catalytic reaction at temperatures above 600^{O}C, the surface area of γ-Al_2O_3 decrease significantly. Therefore

washcoat sintering had occurred resulting in loss of alumina surface area and adsorption sites for the metal catalysts. This impacted on metal dispersion causing a decrease in catalytic activity.

Addiego et al. also examined the impact of BaO %wt content in alumina washcoat and calcinations temperature on surface area (Fig. 1.20).

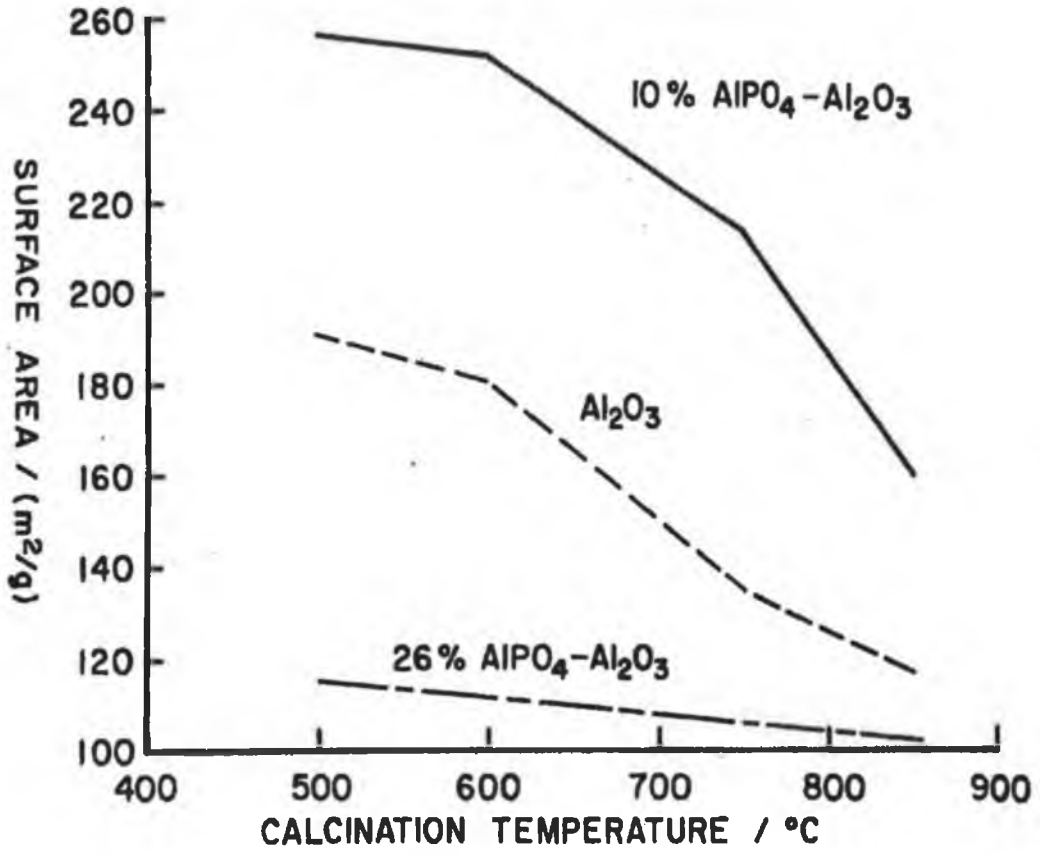

Figure 1.20: Plot of surface area versus BaO content %wt in the BaO-Al_2O_3 washcoat after calcining for 6 hrs at temperatures of 600^0C-1000^0C.

From the plot they found a decrease in surface area with increasing calcination temperature and %wt. BaO content. In conclusion, temperatures above 800^OC resulted in loss in surface area of the washcoat solution.

References

[1] M. F. M. Zwinkels, S. G. Järas, P. G. Menon, Catal. Rev. Sci. Eng., **35**(3), 319-358 (1993).

[2] M.F.M. Zwinkels, S. G. Järas, P.G. Menon, in: A. Cybulski, J. Moulijn (Eds.), Structured Catalysis and Reactors, Marcel Dekker, New York, pg. 149 (1998).

[3] Z.R. Ismagilov, M.A. Kerhentsev, Catal. Rev. Sci. Eng. **32**, 51 (1990).

[4] R. Dalla Betta, Catal. Today **35**, 129 (1997).

[5] Yuranov, L. Kiwi-Minsker, V. Barelko, A. Renken, in: G.F. Froment, K.C. Waugh (Eds.), Reaction Kinetics and the Development of Catalytic Processes, Elsevier Amsterdam, 191-198 (1999).

[6] L. Kiwi-Minsker, I. Yuranov, B. Siebenhaar, A. Renken, Catal. Today, Submitted for publication.

[7] D.M. Nicholas, Y.T. Shah, I.A. Zlochower, Ind. Chem. Prod. Res. Dev. **15**(1), 29-35, 35-41 (1976).

[8] A. Kalantar Neyestanaki, L.-E. Lindfors, Combust. Science Technol. **97**, 121-136 (1994).

[9] A. Kalantar Neyestanaki, L.-E. Lindfors, Combust. Science Technol. 110-111 303-320 (1997).

[10] D.L. Trimm, C.W. Lam, Chem. Eng. Sci., **35**, 1405-1413, 1731-1739 (1980).

[11] B.A. Tichenor and M.A. Palazzolo, 'Destruction of Volatile Organic Compounds Via Catalytic Incineration', presented at ACIHE Annual Meeting, Chicago, IL, (1985).

[12] D.L. Trimn, Appl; Catal., **7** 249-282 (1983).

[13] G.I. Golodets, 'Heterogeneous Catalytic Reactions Involving Molecular Oxygen', Elsevier, New York, (1983).

[14] G.C. Bond, Heterogeneous Catalysis: 'Principles and Applications', Clarendon Press, Oxford, UK, (1974).

[15] J. J. Spivey, Catalysis, **8**, 158 (1989).

[16] P. Briot, A. Auroux, D. Jones and M. Primet, Appl. Catal., **59**, 141-152 (1990).

[17] P. Briot and M. Primet, Appl. Catal., **68**, 301-314 (1991).

[18] K. C. Stein , J. J. Freeman, G. P. Thompson, J. F. Shultz, L. J. E. Hofer and R. B. Anderson, Ind., Eng. Chem., **52**, 671 (1960).

[19] O. V. Hrylov, Catalysis by Nonmetals, Academic Press, New York, (1970).

[20] R. F. Hicks, Haihua Qi, M. L. Young and R. G. Lee, J. Catal., **122**, 280-294 (1990).

[21] R. F. Hicks, Haihua Qi, M. L. Young and R. G. Lee, J. Catal., **122**, 295-306 (1990).

[22] J. G. McCarty and H. Wise, Catal. Today, **8**, 231-248 (1990).

[23] Y. Morooka and A. Ozaki, J. Catal., **5**, 116-124 (1966).

[24] Y. Morooka, Y. Morikawa, and A. Ozaki, J. Catal., **7**, 23-32 (1967).

[25] WWW.Cartoday.com/news 22 February 2001.

[26] V. D. Sokolovskii, Catal. Rev. Sci. Eng., **32**, 1 (1990).

[27] J. O. Petunci and E. A. Lombardo, Catal. Today, **8**, 201-219 (1990).

[28] P. D. L. Mercera et al., Appl. Catal., **71**, 363-391 (1991).

[29] M. Ledoux et al., J. Catal., **114**, 176-185 (1988)

[30] M. Funabiki and T. Yamada, SAE Technical Paper 881684 (1998).

[31] F. Oudet, P. Courtine, and A. Vejux, J. Catal., **114**, 112-120 (1988)

[32] R. J. Farrauto, M. C. Hobsob, T. Kennelly and E. M. Waterman, Appl. Catal. A: General, **81**, 227-237 (1992).

[33] S. Jaenicke and G. K. Chuah, Ber. Bunsenges. Phys. Chem., **96**(1), 1-9 (1992).

[34] R. F. Hicks, Synthesis and Properties of a novel catalyst for combustion of Methane, UCLA, GRI-89/0209 (1989).

[35] L. D. Pfefferle and W. C. Pfefferle, Catal. Rev. Sci. Eng., **29**, 219 (1987).

[36] F. Dywer, Catal. Rev. Sci. Eng., **6**, 261, (1972).

[37] G.I. Golodets, 'Heterogeneous Catalytic Reactions Involving Molecular Oxygen', Studies in Surface Sci., Catalytic, **15**, (1983).

[38] R. Prasad, L. A. Kennedy and E. Ruckenstein, Catal. Rev. Sci. Eng., **26**(1), 1-58 (1984).

[39] J. J. Spivey, in catalysis (Bond, G. C. and Webb, G., Edition) The Royal Society of Chemistry, Cambridge, UK, (1989).

[40] N. Yamazoe and J. Teraoka, Catal. Today, **8**, 175 (1990)

[41] O. Podyacheva, A. Ketov, Z.R. Ismagilov, V. Ushakov, A. Bos, H. Veringa, In: G. Centi, C. Cristiani, P. Forzatti, S. Perathoner (Eds.), Environmental Catalysis, Proc. 1st World Congress Environmental Catalysis – Pisa, Italy, 599 (1995).

[42] P. Ciambelli, V. Palma, S. F. Tikhov, V.A. Sadykov, L.A. Isupova, L. Lisi, In: Catalytic Combustion, Book Of abstracts 3rd Int. Workshop, Amsterdam, Netherlands, 23-25, p. 2.1, Sept' 1996.

[43] J. G. McCarty and H. Wise, Catal. Today, **8**, 231 (1990).

[44] H. Arai, T. Yamada, K. Eguchi, T. Seiyama, Appl. Catal., **26**, 265 (1986).

[45] J. Kirchnerova, D. Klvana, J. Vaillancourt, J. Chaouiki, Catal. Lett., **21,** 77 (1993).

[46] D. Klvana, J. Vaillancourt, J. Kirchnerova, J. Chaouiki, Appl. Catal. A: General, **109**, 181 (1994).

[47] L. A. Isupova, V. A. Sadykov, S. F. Tikhov, O. N. Kimikhai, O. N. Kovalenko, G. N. Kustova, I. A. Ovsyannikova, Z. A. Dovbii, G. N. Kryukova, A. V. F. and V. V. Lunin, A. Ya. Rozovskii, Catal. Today, **27**, 249 (1996).

[48] L. A. Isupova, V. A. Sadykov, S. F. Tikhov, T. V. Telyatnikova, E. A. Brushtein, G. I. Storozhenko, N. V. Kosova, E. G. Avvakumov, A. Ya. Rozovskii, V. V. Lunin, A. Andreev, L. Petrov, Ch. Bonev, G. Kadinov, I. Mitov (Eds.), In Heterogeneous Catalysis, Proc. 8th Int. Symp. Heterogeneous Catal., Varna, Bulgaria, Institute of Catalysis, **1**, Bulgarian Academy of Sciences, Sofia, p. 479 (1996).

[49] S. Katz, J. J. Croat, J. V. Laukonis, Ind. Eng. Chem. Prod. Re4s. Dev. **14**, 274 (1975); D. W. Johnson, Jr., P. K. Gallagher, E. M. Vogel, F. Schrey, in Thermal Analysis, I. Buzar, Ed. (Heyden, London, 1975), p. 181; P. K. Gallagher, D. W. Johnson, Jr., E. M. Vogel, F. Schrey, Mater. Res. Bull., **10**, 623 (1975).

[50] Y.-F. Y. Yao, J. Catal., **36**, 266 (1975).

[51] J. T. Kummer, Prog. Energy Combust. Sci., **6**, 177 (1980).

[52] R. F. Hicks et al., Chem. Eng. Sci., **45**(8), 2647-2651 (1990).

[53] T. R. Baldwin and R. Burch, Appl. Catal., **66**, 337-358 (1990).

[54] T. R. Baldwin and R. Burch, Appl. Catal., **66**, 359-381 (1990).

[55] K. Otto, Langmuir **5**, 1364-1369 (1989).

[56] M. Kobayashi, T. Kanno, A, konishi, H. Takeda, React. Kinet. Catal. Lett., **37**, 89 (1988).

[57] P. Marécot, A. Fakche, B. kellali, G. Mabilon, M. Prigent, J. Barbier, Appl. Catal., B: Environmental, **3**, 283 (1994).

[58] V. Labalme, E. Garbowsky, N. Ghilhaume, M. Primet, Appl. Catal., A: **138**, 93 (1996).

[59] R.F. Hicks, R.G. Lee, W.J. Han, A.B. Kooh, in: R.K. Graselli, W. Sleight (Eds.), Structure-activity and Selectivity Relationship in Heterogeneous Catalysis, Elsevier, Amsterdam, p. 127 (1991).

[60] T.F. Garetto, C.R. Apesteguia, Appl. Catal., **B**, submitted for publication.

[61] R. Burch and M. J. Hayes, J. Mol. Catal., **100**, 13 (1995).

[62] R. Burch, D. J. Crittle and M. J. Hayes, Catal. Today, **47**, 229-234 (1999).

[63] F. G. Dwyer, Catal. Rev., **6**, 261 (1972).

[64] R. E. Dickinson, R. J. Cicerone, Nature, **319**, 109-115 (1986).

[65] J. L. G. Fierro and J. F. G. de la Banda, Catal. Rev., **28**(2-3) 301-304 (1986).

[66] R. B. Anderson, K. C. Stein, J. J. Feenan and L. J. E. Hofer, U.S. Bureau of Mines, Pittsburgh Coal Research Center, Pittsburgh, Pa., Ind., Eng., Chem., **53**, 809 (1961).

[67] R. J. Kokes, H. Jr., Tobin, P. H. Emmett, J. Am. Chem. Soc., **77**, 5860 (1955).

[68] J. G. E. Cohn and A. Haley, J., Can. Patent, **597, 459** (may 3rd, 1960).

[69] J. G. Firth and H. B. Holland, J. Chem. Soc. Faraday Trans., **65**, 1121 (1969).

[70] J. l. G. Fierro, Catal. Today **8**, 153, (1990).

[71] C. F. Cullis and B. M. Willatt, J. Catal., **83**, 267-285 (1983).

[72] R. Mazaki and C. C. Watson, Ind. Eng. Chem. Process Des. Dev., **5**, 62 (1966).

[73] C. F. Cullis, T. G. Nevell and D. L. Trimm, J. Chem. Soc. Faraday Trans., **68**, 1406 (1972).

[74] R. B. Anderson, K. C. Stein, J. J. Feenan and L. J. E. Hofer, "Catalytic Oxidation of Methane", Ind. Eng. Chem., **53**(10), 809 (1961).

[75] J. Lee and D. L. Trimm, "Catalytic Combustion of Methane", Fuel Process Technol., **42**(2&3), 339, (1995).

[76] J. G. McCarty, "Kinetics of PdO Combustion Catalysis" Catalytic Today, **26**(3-4), 283 (1995).

[77] A. Schwartz, L. L. Holbrook and H. Wise, J. Catal., **21**, 199-207 (1971).

[78] D. Brennan, D. O. Hayward and B. M. W. Trapnell, Proc. Roy. Soc. Ser., A **256**, 81 (1960).

[79] W. E. Bell, R. E. Inyard and M. Tagami, J. Phys. Chem., **70**, 3735 (1966).

[80] H. C. Yao, M. Sieg, H. K., Jr., Plummer, J. Catal., **59**, 365 (1979).

[81] H. Lieske and J. Volter, J. Phys. Chem., **89**, 1841 (1985).

[82] G. Bayer and H. G. Wiedemann, Thermochim. Acta., **11**, 79 (1975).

[83] J. E. Turner and M. B. Maple, Surf. Sci., **147**, 647 (1984).

[84] C. T. Campbell, D. C. Foyt and J. M. White, J. Phys. Chem., **81**, 491 (1975).

[85] J. M. Guiot, J. Appl. Phys., **39**, 3509 (1968).

[86] E. Ruckenstein and J. J. Chen, J. Coll. Inter. Sci., **86**, 1 (1982).

[87] F. H. Ribeiro, M. Chow and R. A. Dalla Betta, J. Catal., **146**, 537-544 (1994).

[88] J. R. Anderson and P. Tsai, Appl. Catal., **19**, 141 (1985).

[89] S. Seimanides and M. Stoukides, J. Catal., **98**, 540 (1986).

[90] Ken-Ichiro Fujimoto, F. H. Ribeiro, M. Avalos-Borja and E. Iglesia, J. Catal., **179**, 431-442, (1998).

[91] P. E. Marti, M. Maciejewski and A. Baiker, J. Catal., **139**, 494-509 (1993).

[92] A. Baiker, D. Gasser, J. Lenzner and R. Schlőgl, J. Catal., **126**, 555 (1990).

[93] R. Schlőgl, G. Loose, M. Wesemann and A. Baiker, J. Catal., **137**, 139 (1992).

[94] S. H. Oh, P. J. Mitchell and R. M. Siewert, J. Catal., **132**, 287-301 (1991).

[95] A. Frennet, Catal. Rev. Sci. Eng., **10**, 37 (1974).

[96] C. Kemball, In "Advances in Catalysis" (D. D. Eley, P. W. Selwood and P. B. Weisz, Eds.), Vol. 11. p. 223, Academic Press, New York, (1959).

[97] S. Cimino, L. Lisi, R. Pirone, G. Russo and M. Turco, Catal. Today, **59**, 19-31 (2000).

[98] D. Ferri and L. Forni, Appl. Catal., B: Environmental, **16**, 119-126 (1998).

[99] L. Marchetti and L. Forni, Appl. Catal., B: Environmental, **15**, 179-187 (1998).

[100] M. A. Quinlan, H. Wise and J. G. McCarty, Basic Research on Natural Gas Combustion Phenomena – catalytic combustion, SRI International, Menlo Park, CA, GRI-89/0141 (1989).

[101] S. Stegenga, N. Dekker, J. Bijsterbosch, F. Kapteijn, J. moulijn, G. Belot and R. Roche, Catalysis and Automotive Pollution Control II, Elsevier Sci. Publisher B. V., Amsterdam (1991).

[102] V. R. Choudhary, B. S. Uphade, S. G. Pataskar and A. Keshavaraja, Angem. Chem. Int. Ed. Engt. **35**, No. 20, 2393 (1996).

[103] S. Arnone, G. Bagnasco, G. Busca, L. Lisi, G. Russo and M. Turco, Natural Gas Conversion, Journal of Surface Science and Catalysis, **119**, 65-70 (1998).

[104] L. G. Tejuca, J. L. G. Fierro and J. M. D. tascon, Adv. Catal., **36**, 37 (1989).

[105] R. Burch and P. K. Loader, Appl. Catal. B: Environ., **5**, 149 (1994).

[106] M. L. H. Green, S. Fu. Ji, Hai-tao Wang, K. S. Coleman and Tian-cun Xiao, J. of Molecular Catalysis A: Chemical **175**, 111-123 (2001).

[107] S. Yang A. Maroto-Naliente, M. Benito-Gonzalez, L. Rodriguez and A. Guerrero-Ruiz, Appl. Catal. B: Environ., J. Catal., **28**, 223 (2000).

[108] Yung-Fang Yu Yao, J. Catal. **33**, 108-122 (1974).

[109] L. Hiam, H. Wise and S. Chaikin, J. Catal., **10**, 272 (1968).

[110] A. Schwartz, L. Holbrook and H. Wise, J. Catal., **21**, 199 (1971).

[111] J. A. Barnard and D. S. Mitchell, J. Catal., **12**, 386 (1968).

[112] K. Otto, J. M. Andino and C. L. Parks, J. Catal., **131**, 243-251 (1991).

[113] J. Volter, G. Lietz, H. Spindler and H. Lieske, J. Catal., **104**, 375 (1968).

[114] H. K. Plummer, Jr. and K. Otto, in "Proceedings, 47th Annual Meeting of the Electron Microscopy Society of America, San Francisco, CA, 1989."

[115] H. Lieske, G. Lietz, H. Spindler and J. Volter, J. Catal., **81**, 8 (1983).

[116] J. M. Richard, L. Genovese, A. Moata and S. Nitsche, J. Catal., **121**, 141 (1990).

[117] J. A. Anderson, M. G. V. Mordente and C. H. Rochester, J. Chem. Soc. Faraday Trans. 1 **85(9)**, 2983 (1989).

[118] M. G. V. Mordente and C. H. Rochester, J. Chem. Soc. Faraday Trans. 1 **85**(10), 3495 (1989).

[119] A. Renken, I. Yuranov, E. Slanvinskaia, V. Zaikovskii and L. Kiwi-Minsker, Catal. Today, **59**, 61-68 (2000).

[120] C. P. Hubbard, K. Otto, H. S. Gandhi and K. Y. S. Ng, J. Catal., **139**, 268-276 (1993).

[121] L. Hiam, H. Wise and S. Chaikin, J. Catal., **10**, 272 (1968).

[122] Y. F. Y. Yao, Ind. Eng. Chem. Prod. Res. Dev., **19**, 293 (1980).

[123] R. W. McCabe, C. wong and H. S. Woo, J. Catal., **114**, 354-367 (1988).

[124] T. Uchijima, J. M. Herrmann, Y. Inoue, R. L. Burwell, Jr., and J. B. Cohen, J. Catal., **50**, 464 (1977).

[125] C. Wong and R. W. McCabe, J. Catal., **107**, 53 (1987).

[126] R. J. Farrauto, and R. M. Heck, Catal. Today., **51**, 351-360 (1999).

[127] M. F. M. Zwinkels, O. Haussner, P. G. Menon and S. G. Järas, Catal. Today, **47**, 73-82, (1999).

[128] J. T. Kummer, J. Phys. Chem., **90**, 4747 (1986).

[129] S. Stegenga, N. Dekker, J. Bijsterbosch, F. Kapteijn, J. Moulijn, G. Belot and R. Roche, ' Catalysis and Autonotive Pollution Control II', Elsevier Science Publisher B. V., Amsterdam 1991.

[130] K. Taylor, Catal. Rev. **35**(4) 457 (1993).

[131] B. Harrison, A. Didwell and C. Hallet, Precious Metals Rev., **32**(2) 73 (1988).

[132] G. Fisher, J. Theis, M. Casarella and S. Mahan, SAE 931034, 1993.

[133] A. Didwell, R. Rajaram, H. Shaw and T. Truex, Stud. Surf. Sci. Catal., **71**, 139 (1991).

[134] L. Mussmann, D. Lindner, E. Lox, R. Van Yperen, T. Kreuzer, I. Mitsushima, S. Tangiguchi and G. Carr, SAE 970465, 1997.

[135] J. Cuit, G. Blanchard, O. Touret, M. Marczi and E. Quemere, SAE 961906, 1996.

[136] W. D. Callister, 1940-. - Materials science and engineering: an introduction/ William D. Callister. - 2nd ed. - New York: Wiley & Sons Inc., 1991.

[137] C. Herring and J. K. Galt, Phys. Rev., **85**, 1060 (1952).

[138] E. Koonce and S. M. Arnold, J. Appl. Phys., **24**, 365 (1953).

[139] J. D. Eshelby, Phys. Rev., **91**, 755 (1953).

[140] F. C. Frank, Philos. Mag., **44**, 854 (1953).

[141] R. M. Fisher, L. S. darken and K. G. Carroll, Acta Metall., **2**, 368 (1954).

[142] R. R. hashiguchi, Acta Metall., **3**, 200 (1955).

[143] J. Frank, Acta Metall., **6**, 103 (1958).

[144] V. K. Glazunova and K. M. Gorbunova, J. Cryst. Growth, **10**, 85 (1971).

[145] P. Chaudhari, J. appl. Phys., **45**, 4339 (1974).

[146] J. B. Newkirk, Metal Prog. **6**, 88 (1955).

[147] K. G. Compton, A. Mendizza and S. M. Arnold, Corrosion, **7**, 327 (1951).

[148] S. M. Arnold, Bell Lab. Rec., **32**, 417 (1954).

[149] J. Bassett, C. R. Denney, H. G. Jeffery and J. Mendham, "Vogel Qualitative Inorganic analysis" 4th Edition, New York, (1996).

[150] General Motors Corporation, Detroit, Mich., (Chapman et al.), US Patent, 4,331,631 May 25, 1982.

[151] General Motors Corporation, Detroit, Mich. (Chapman et al.), US Patent, 4,318,828 March 9, (1982).

[152] General Motors Corporation, Detroit, Mich. (G. L. Vaneman et al.), European Patent, 0,358,309 A1, June 29 (1989).

[153] General Motors Corporation, Detroit, Mich. (G. L. Vaneman et al.), US Patent, 4,915,751 April 10 (1990).

[154] J. M. F. Ferreira and H. M. M. Diz, J. of Hard materials, **3**, 17-27 (1992).

[155] S. Taruta, N. Takusagawa, K. Okada and N. Otsuka, J. Ceram. Soc. of Japan, **104** 47-50 (1996).

[156] G. Tarì, J. M. F. Ferreira, A. T. Fonseca and O. Lyckfeldt, J. Euro. Ceram. Soc. **18**, 249-253 (1998).

[157] C. Agrafiotis and A. Tsetsekou, J. Euro. Ceram. Soc. **20**, 815-824 (2000).

[158] D. Nandini and H. S. Maiti, J. European Ceramic Society, **19**, 341, (1999).

[159] W. W. Webb and W. B. Forgeng, J. Appl. Phys., **28**, 12 (1957).

[160] S. S. Brenner, Acta. Met., **4**, 62 (1956).

[161] P. B. Price, D. A. Vermilyea and M. B. Webb, Acta. Met., **6**, 524 (1958).

[162] G. W. Sears, Acta. Met., **1**, 457 (1953).

[163] J. A. Blech, P. M. Petroff, K. L. Tai and V. Kumar, J. Cryst. Growth, **32**, 161 (1975).

[164] K. Hinode, Y. Homma and Y. Sasaki, J. Vac. Sci. Technol. A: **14**(4), 2570, (1996).

[165] K. Ramkumar, S. K. Ghosh and A. N. Saxena, 'Handbook of Multilevel Metallisation for Integrated Circuits', Edited by S. R. Wilson, C. J. Tracy and J. L. Freeman, Jr. Sec. 3 (1993).

[166] K. C. Cadien and D. L. Losee, J. Vac. Sci. Technol. B: **2**, 82 (1984).

[167] K. Hazama, Y. Nakamura and O. Nittono, Jpn. J. Appl. Phys., **27**, 1142 (1988).

[168] L. Succo, J. Esposito, M. Cleeves, S. Whitney, R. E. Lionetti and C. E. Wickersham, Jr., J. Vac. Sci. Technol. A: **7**, 814 (1989).

[169] G. J. K. Acres, A. J. Bird, J. W. Jenkins and F. King, 'The Design and Preparation of Supported Catalysts', London Chem. Soc., Catalysis **4**, (1981).

[170] J. W. Hightower, 'Catalysis for Autobile Emission Control', in B. Deiman, P. A. Jacobs and G. Poncelet, (Eds.), Studies in Surface Science and Catalysis, Elsevier Amsterdam **1**, 615 (1976).

[171] Ford Motor Company, Dearborn, Mich., (Shelef et al.) US Patent, 5,556,825, Sept. 17, 1996.

[172] J. C. Summers and S. A. Auser, J. Catal. **52**, 445-452 (1987).

[173] J. E. Otterstedt, L. O. Lowendahl and L. B. Lansson, 'Catalysis and Automobile Pollution Control', in A Crucq and A. Frennet, (Eds.) Studies in Surface Science and Catalysis, Elsevier Amsterdam **30**, 333 (1987).

[174] K. C. Taylor, 'Automobile Catalytic Converters', in A Crucq and A. Frennet, (Eds.), Catalysis and Automobile Pollution Control', Studies in Surface Science and Catalysis, Elsevier Amsterdam **30**, 313 (1987).

[175] Astro Met Associates, Inc., Cincinnati, Ohio, (Kinney, Jr. et al.) US Patent, 4,760,038 Jul. 26, 1988.

[176] C. Agrafiotis and A. Tseteskou, Journal of the European Ceramic Society **20**, 815-824 (2000).

[177] D. Honiche, Appl. Catal., **5**, 179-178 (1983)

[178] H. Schaper, E. B. M. Doesburg and L. L. Van Reijen, Appl. Catal., **7**, 211-220 (1983).

[179] Corning Incorporated, Corning, N.Y. (P. A. Beauseigneur et al.) US Parent, 5,346,722 Sept. 13, 1994.

[180] W. R. Grace & Co.-Conn., New York, (C. J. Pereira et al.) US Parent, 4,859,433 Aug. 22, 1989.

[181] Corning Incorporated, Corning, N.Y. (W. P. Addiego et al.) US Patent, 5,212,130 May 18, 1993.

Chapter 2

Catalyst Preparation and Characterisation Techniques.

2.0 Introduction

In this chapter, the preparation of Pt catalysts supported on alumina using chloroplatinic acid (CPA) solution is detailed. The various surface and analytical techniques employed in the characterisation of Pt/Al_2O_3 catalysts is also discussed. The techniques used for characterisation were Scanning Electron Microscopy (SEM), Energy Dispersive X-Ray Fluorescence (EDX), Particle size analyser, X-ray Powder Diffraction (XRD), Atomic Absorption Spectroscopy (AAS), BET Surface Area and H_2 Chemisorption. The use of Scanning Electron Microscopy in the investigation of the morphology of the gauze is discussed in terms of theory of operation. Energy Dispersive X-ray analysis used in determination of elemental composition within the gauze material, together with the software and operational mechanism is also examined. An investigation into the operation of the particle size analyser used in the determination of particle size of alumina within the washcoat support material employed in the preparation of the Pt/Al_2O_3 gauze catalysts will be examined. In addition, the background theory on the use of XRD, in determination of transition phase present in the puralox powder used in the preparation of the alumina washcoat support is discussed.

Finally, the use of Atomic absorption Spectroscopy (AAS), BET surface area analysis and H_2 Chemisorption in characterisation of the final prepared Pt/Al_2O_3 catalysts will be discussed in depth.

2.1 Catalyst preparation

Platinum supported alumina catalysts are largely used in industrial processes, especially in the field of reforming and are most commonly prepared by incipient wetness impregnation technique of γ–Al_2O_3 support using an aqueous H_2PtCl_6 (CPA) precursor. However, to date a unified picture of the chemical phenomena occurring during their preparation has failed to emerge. The behaviour of chloroplatinic acid in solution has been extensively studied [7]. It has been found [7] that the solution is a strong acid and upon dissociation yields two protons per molecule according to equation 1.

$$H_2PtCl_6 \Leftrightarrow PtCl_6^{2-} + 2H^+ \qquad (1)$$

The remaining complex in aqueous solution undergoes ligand exchange with water molecules, equation 2.

$$PtCl_6^{2-} + H_20 \Leftrightarrow (PtCl_5H_2O)^- + Cl^- \qquad (2)$$

This mono-aquo-chloro-complex can undergo further hydrolysis forming a weak acid solution, equation 3.

$$(PtCl_5H_2O)^- \Leftrightarrow (PtCl_5OH)^{2-} + H^+ \qquad (3)$$

And it's assumed that the substantial part of the platinum salt is present in solution as $(PtCl_5OH)^{2-}$ [7].

On impregnation of an alumina support with CPA solution the alumina undergoes an acid attack from the protons of the choroplatinic solution. The sites created act as strong adsorption sites for the $(PtCl_5OH)^{2-}$. The mechanism by which the platinum precursor salt adsorbs onto the alumina support is shown Fig. 2.1 [8]. Following the impregnation, catalyst activation is achieved by calcination.

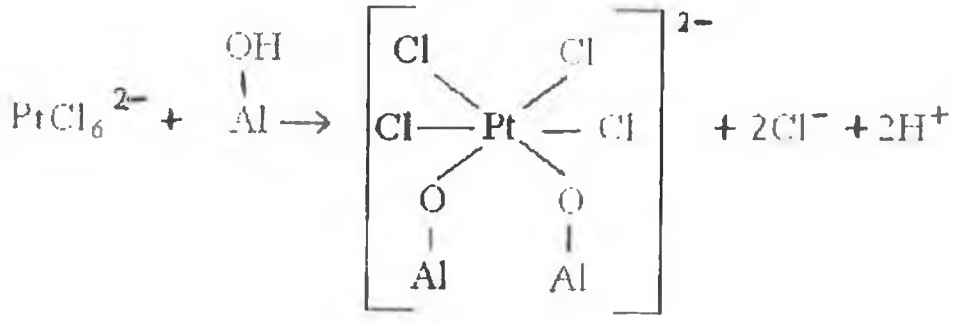

Fig 2.1: The mechanism of chlorine retention on a Pt-Al_2O_3 complex [8].

It is observed from the mechanism, that the adsorption of one molecule of CPA occupies four surface sites on the alumina in total (i.e. two by an oxyplatinum complex and two by the 2 released chloride ions. This allowed for increased distribution of the active metal component (i.e. Platinum) [8].

2.2 Scanning Electron Microscopy (SEM)

In the 20th Century, the development of the electron microscope has helped to facilitate the technique of micro – analysis, allowing a microscale view at the surfaces of solid objects.

A SEM operates by scanning a beam of focused electrons (incident beam) across the surface of the sample in a raster fashion. Interaction between the incident beam and the sample generates secondary signals, which can be detected by appropriate detectors to provide information about the sample. Using a detector designed to pick these secondary electrons, an image of the sample can be formed [9, 10]. A schematic diagram of an SEM chamber is given in Fig. 2.2 [11].

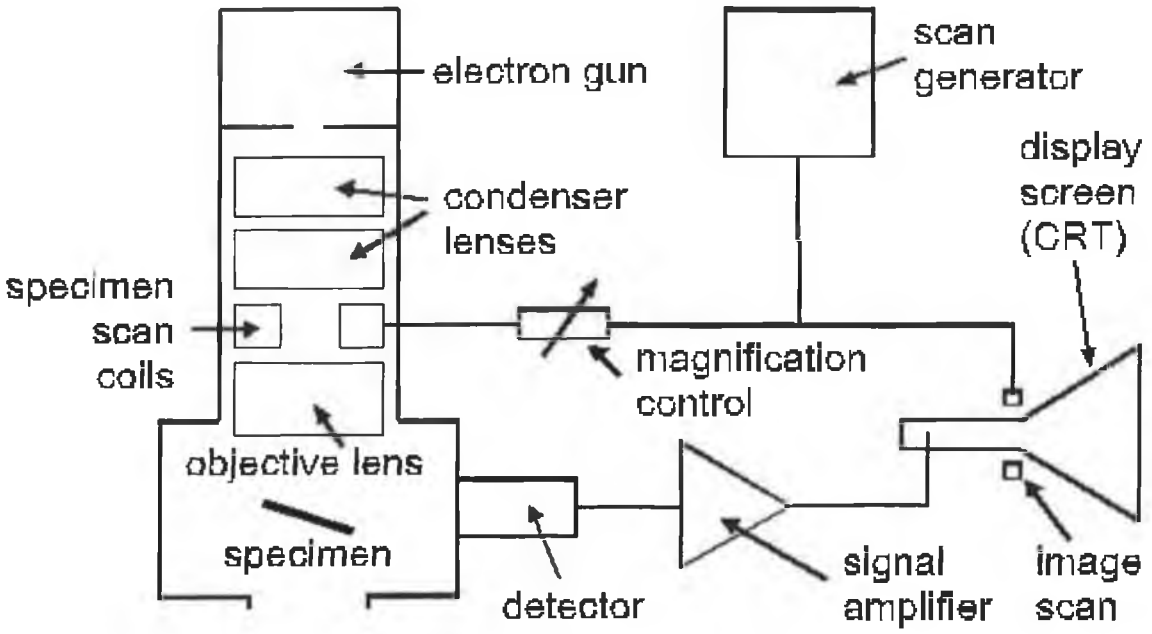

Fig. 2.2: Schematic diagram of SEM chamber [11]

The top of a SEM contains an electron gun with a filament, which is heated to approx. 2700K. Electrons are emitted from the filament and accelerated under a high voltage down the electron optic column. The column focuses the beam using electromagnetic lenses and forms a dimagnified image of the source, the filament. The beam passes between two scanning coils, which enable it to be rastered across a selected area on the surface of the sample.

Rastering can occur in various forms:

- A rectangular raster
- A single or repeated line scan
- Stationary spot

The electron beam interacts with the near surface of the sample to a depth of approx. a few microns, forming an interaction volume, from which signals are generated. A considerable number of incident electrons may escape from the specimen and are collectively known as backscattered electrons. The specimen can be imaged using both backscattered and secondary electrons, thus providing a starting point from which the analyst can choose appropriate regions for analytical investigation [10].

2.3 Energy Dispersive X-ray Fluorescence (EDX)

Energy Dispersive X-Ray (EDX) analysis was used in conjunction with SEM. It is a solid-state device that measures the energy of the incident x-rays. Each element exhibits a characteristic x-ray emission spectrum. Identification is by comparison with reference library of standard spectra. A schematic diagram of the Energy Dispersive Spectrometer is illustrated in Fig. 2.3 [12, 13]. Characteristic x-ray emissions are formed upon an atom stabilising itself after ionisation by the electron beam. When the beam has dislodged an electron from an inner atomic shell, an electron from an outer shell will fill the vacancy. The difference in energies between the initial and final states of the transitional electron may be emitted as x-radiation. The various shells of an atom have discrete amounts of

energy. It follows that their energy difference, emitted as x-radiation, is also a discrete quantity and is characteristic of the atom from which it was released [3], see Fig. 2.4 [12, 13]. Differences in electron spin create slight differences in the energy between electrons in the same shell and thus in the energy of x-rays emitted by electron transitions. Because of the differing binding energy levels of the electrons around the nucleus, primary electrons of a higher potential energy (electron volts - eV) are required to displace K-shell electrons than are required to displace L-shell electrons, which is higher than that required for M-shell electrons. Most of the commonly occurring elements produce K x-rays in the 1.0 to 10.0keV region and as a result this is often a good place to begin when attempting to identify peaks. These include both K_α and K_β energies. A spectrum may also consist of L_α, L_β and L_γ peaks.

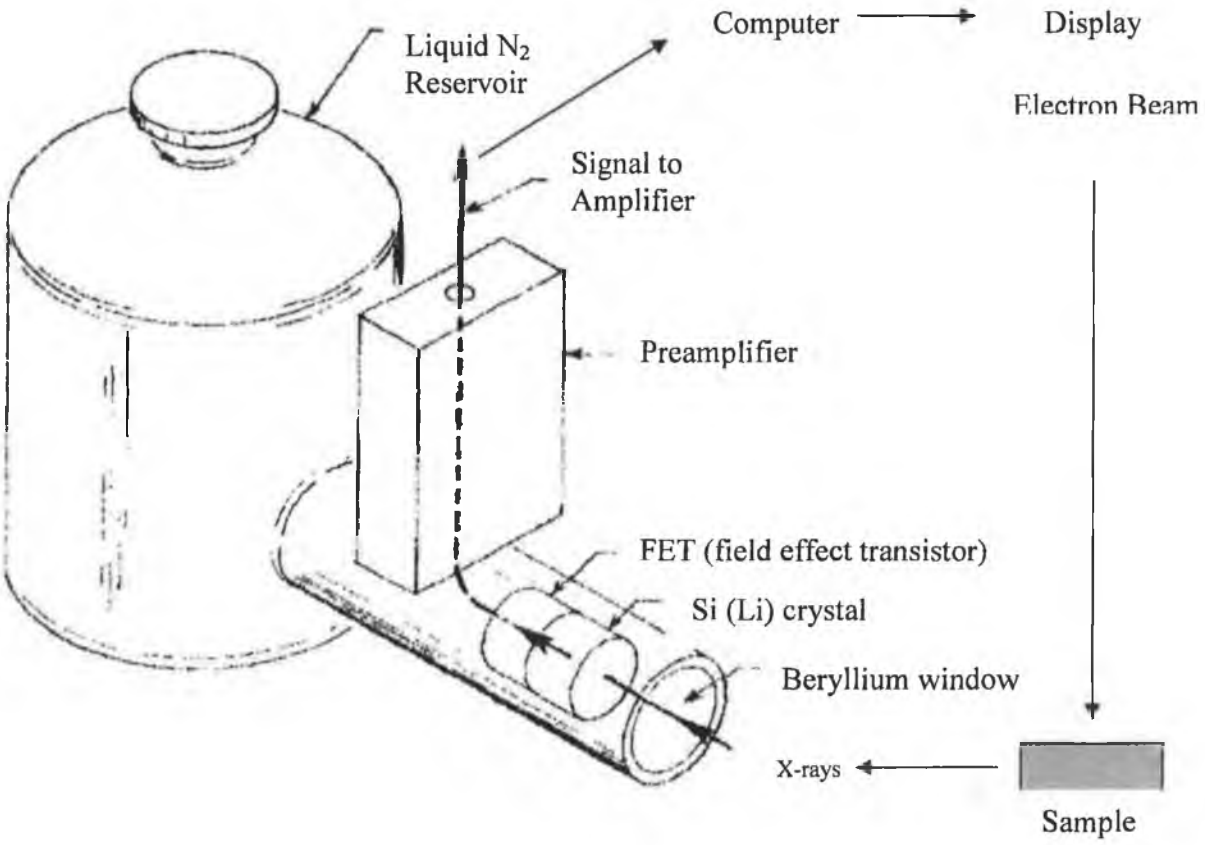

Fig. 2.3: Schematic diagram of an Energy Dispersive Spectrometer [12, 13].

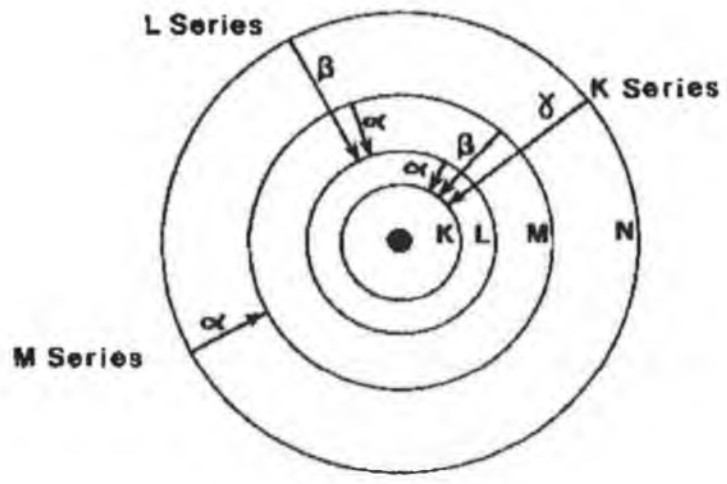

Fig. 2.4: Allowed electronic transitions to generate electronic X-rays [12, 13]

In the detector, analysis of X-rays according to their energy occurs. When an X-ray strikes the Si(Li) crystal, which is kept at liquid nitrogen temperature and under vacuum, electrons in the crystal each absorb a given amount of energy. The greater the energy of the X-rays, the greater the number of electrons excited. The energy absorbed by the electrons is then converted to an electrical signal, which is emitted and amplified. The strength of the current from the crystal is proportional to the X-ray energy. The amplified electrical pulses are then converted to digital form and fed into a multichannel analyser (MCA) which sorts these signals and in effect counts the number of X-rays at each energy level which strikes the crystal. This process occurs thousands of times to form a histogram, known as an X-ray spectrum [12], showing the elements present and their quantity. Data acquisition is extremely fast as well as accurate and therefore allows the operator to acquire high quality spectra very efficiently. Typical x-ray acquisition rates of up to 50,000 cps are possible and choice of resolution parameters enables the detection

and quantification of low concentrations of elements. Quantitative analyses to within 1% relative error or clear multi-element maps can be obtained in as little as 5 - 10seconds.

The software preloaded is Link ISIS on an S-3000N Hitachi SEM used in this study. It has an extensive complement of hardware and software options and enabled the following function to be preformed:

- Windows PC-based for speed and ease of use.
- Thin-window detector for high-resolution analysis of all elements down to and including boron.
- Fast processor electronics (up to15K counts per second) for fast acquisition of x-ray maps and spectra.
- Software for qualitative and quantitative analyses using a variety of algorithms.
- Speed Map rapidly acquires multiple-element x-ray maps in minutes.
- Auto beam provides for collection of digital images and aids in the selection of points for quantitative analysis or line profiles. It also provides for browsing around an image for survey analyses, and for collection and analysis of stereo images.
- IM-Quant, also known as Visilog (from Noesis Vision) provides a robust tool for image processing and analysis.
- PCI software provides for the passive capture, archiving, annotation, and redisplay of images.
- The system is integrated with the Hitachi for automatic control and reporting of SEM parameters.
- Storage and recall of all data for comparison.

2.4 Particle Size Distribution

There are many methods of particle size measurements in which the raw data are collected in a number distribution format [14]. These methods range from simple sieves to sedimentation techniques, electrical, light-sensing zone, electrozone sensing and microscopy methods. In this study, the particle size distribution and mean diameters of the alumina in the washcoat solution were determined using a Malvern Mastersiser S. long bed version 2.19 particle size analyser.

Malvern Instruments incorporate low angle laser light scattering (LALLS), or laser diffraction as it is more commonly known. The technology incorporated by Malvern Instruments allows rapid measurement, exceptional reproducibility and an ability to compare the results with other techniques. Particles in a wide size range, from sub-micron to a few millimeters, are measured accurately and non-destructively, allowing expensive or rare samples to be recovered. The instrument provides wide dynamic particle range size measurements from 0.05 - 3500μm. Dry powders, liquid suspensions, aerosols and emulsions can also be analysed with full quality specification, validation and documentation. The Malvern Instruments come equipped with associated software to perform the analysis and calculations.

The principle of operation involves a collimated Helium/Neon laser that passes through the sample in a cell. Some of the light is reflected, refracted and diffracted from the sample particles. The light materialising out from the sample is detected by a series of photocells. The signal is subsequently manipulated by Fourier optics and a computer displays the particle size distribution measurement tabulated and represented in graphical format.

2.5 X-Ray Diffraction (XRD)

Determination of transition phase in the starting material is an important stage in the preparation of a thermally stable surface area support material. Powder X-ray Diffraction (XRD) is one of the primary techniques used by solid state chemists to characterize such materials. Powder XRD can provide information about crystalline structure (or lack thereof) in a sample even when the crystallite size is too small for single crystal x-ray diffraction [15].

In XRD, a three-dimensional structure is defined by regular, repeating planes of atoms that form a crystal lattice. When a focused X-ray beam interacts with these planes of atoms, part of the beam is transmitted, part is absorbed by the sample, part is refracted and scattered, and part is diffracted. X-rays are diffracted differently, depending on what atoms make up the crystal lattice and how these atoms are arranged [15, 16].

In X-ray powder diffractometry, X-rays are generated within a sealed tube that is under vacuum. A current is applied that heats a filament within the tube; the higher the current the greater the number of electrons emitted from the filament. This high voltage accelerates the electrons, which then hit a target, commonly made of copper. When these electrons hit the target, X-rays are produced. The wavelength of these X-rays is characteristic of that target. These X-rays are collimated and directed onto the sample, which has been ground to a fine powder (typically to produce particle sizes of less than 10 microns). A detector detects the X-ray signal; the signal is then processed either by a microprocessor or electronically, converting the signal to a count rate. Changing the angle between the X-ray source, the sample, and the detector at a controlled rate between preset limits is an X-ray scan.

When an X-ray beam hits a sample and is diffracted, we can measure the distances between the planes of the atoms that constitute the sample by applying Bragg's Law.

$$n\lambda = 2dSin\theta$$

Where: n = the order of the diffracted beam

λ = is the wavelength of the incident X-ray beam

d = is the distance between adjacent planes of atoms (the d-spacings)

θ = is the angle of incidence of the X-ray beam.

Since λ is known and θ can be measured, the d-spacings can be calculated. The characteristic set of d-spacings generated in a typical X-ray scan provides a unique "fingerprint" of the crystalline material present in the sample. When properly interpreted, by comparison with standard reference patterns and measurements, this "fingerprint" allows for identification of the structure [15, 16].

A Philips XRD diffractometer was used to determine the alumina transition phase present in the puralox powders used in the preparation of the alumina washcoat support.

2.6 Catalysts Characterisation

2.6.1 Total Metal Content

Several analysis techniques, such as atomic absorption spectroscopy (AAS), and graphite furnace atomic absorption spectroscopy (GFAAS), for determination of total metal content have been described [17]. Atomic absorption spectroscopy technique (AAS) is the primary method used for the selective determination of metal content of a sample [17]. Flame atomic absorption spectroscopy involves the combustion of the analyte solution within an aerosol, followed by absorption of radiation by these atoms in their vapour phase freed from their chemical surrounding. The sample is introduced into the

flame by nebulisation providing a steady flow of aerosol into the flame. Atomisation of the aerosol by the flame into free analyte atoms in the ground state occurs. The temperature of the flame is controlled by the preset fuel/oxidant ratio. The free ground state atoms are excited by radiation of a suitable wavelength emitted by a hollow cathode lamp of the particular element being analysed. The spectral transitions necessary for analyte determination are thus produced. The atomic absorbance spectrum of the element consists of a series of resonance lines, all originating from the ground electronic state and terminating in various excited states, the first line (i.e. energy levels) usually displays the strongest absorptivity and gives the maximum sensitivity. Since the wavelengths of the analytical resonance lines fall in the ultraviolet–visible regions of the spectrum, the most common detectors in absorption spectroscopy are photomultiplier tubes. Unabsorbed radiation passes through a monochromator that isolates the resonance line. A photodetector measures the power of the transmitted radiation of the isolated resonance line. The resultant intensity data is then recorded and displayed as analyte absorbance. The analyte absorbance recorded and the concentration of the analyte of interest is then related to the Beer–Lambert law.

The general Beer-Lambert law is usually written as $A = \varepsilon bc$.

Where: A = measured absorbance.

ε = is a wavelength-dependent absorptive coefficient.

b = is the horizontal path length of the radiation through the flame (cm).

c = is the concentration of absorbing analyte material (grams L^{-1}).

Experimental measurements are usually made in terms of transmittance (T), which is defined as: $T = I / I_0$,

Where: I_0 = is the initial light intensity.

I = is the light intensity after it passes through the analyte solution.

Therefore, the relation between A and T becomes: $A = \log_{10} (I_0/I) = \varepsilon bc$.

2.6.2 Derivation of the Beer-Lambert Law

The Beer-Lambert law can be derived from an approximation for the absorption coefficient for a molecule. Lamberts law states that successive equal thicknesses absorb equal fractions of monochromatic incident radiation [18]. As a result, an exponential decrease in intensity of the radiation occurs as it passes through the layer. In mathematical terms,

$$I = I_0 e^{-kl}$$

Where I_0 is the incident intensity entering the sample, and I is the intensity of light leaving the sample, l is the thickness of the absorbing sample and k is a constant determined by the wavelength of radiation and nature of the sample. Converting to log to the base 10 and rearrangement of the equation,

$$\text{Log}_{10} \frac{I_0}{I} = kl$$

Beers law deals with the concentration of an absorbing sample and leads to the following equation [18],

$$\text{Log}_{10} \frac{I_0}{I} = k'C$$

By combining the two equations, Beer-Lamberts law may be expressed in the form,

$$\text{Log}_{10} \frac{I_0}{I} = A = \varepsilon Cl$$

The metal content of the prepared catalysts in this study were determined from a calibration curve of absorbance versus metal concentration [17].

2.6.3 BET Surface Area

Physical adsorption of an inert gas at low temperatures can be used to measure the total specific surface area of catalysts and/or the distribution of pore sizes [19, 20]. The total specific surface area of the catalyst is defined as the surface area per unit weight (m^2g^{-1}) [19]. The forces involved in adsorption may be strong, with activation energies and specific electronic forces as in chemical bond formation (chemisorption) or weak (physisorption) involving non-specific, long range Van der waals forces with no activation energy. Physisorption of inert gas involving multilayer adsorption describes the interaction between the solids and gases or liquids and gases with Van der Waals forces. The interacting gases molecules and surface atoms both more or less retain their identities, while chemisorption involves chemical adsorption of gas molecules on the surface, resulting in atoms, ions and radicals forming chemical bonds on the surface. In this case, the gas molecules lose their original identities.

The relationship at a given temperature between the equilibrium amount of gas adsorbed and the pressure of a gas is known as an adsorption isotherm. A Type II isotherm describing monolayer and multilayer adsorption on heterogeneous catalysts is illustrated in Fig. 2.5 [19].

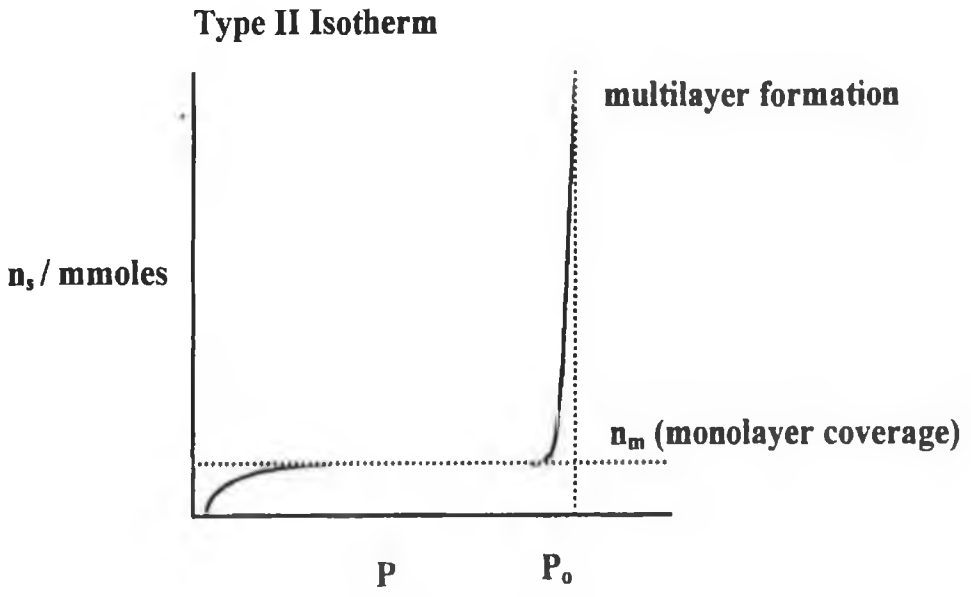

Fig. 2.5: Type II Brunauer isotherm describing a monolayer-multilayer adsorption isotherm on a heterogeneous substrate [19].

The adsorption isotherm, involving multilayer physical adsorption (i.e. physisorption) of N_2 on a surface is described by BET isotherm (i.e. Brunauer, Emmet and Teller extended Langmuir's approach of adsorption of gases to multilayer adsorption). Although adsorption of rare gases and N_2 at low temperatures may lead to multilayer or multimolecular adsorption on a solid substrate, in practise only monomolecular layer coverage of the entire solid surface maybe derived via utilisation of the BET equation [21-23].

$$\frac{P}{[n_s(P_O - P)]} = [1/(n_m C)] + [(C-1)/(n_m C)]\left(\frac{P}{P_O}\right)$$

Where: n_s = number of moles adsorbed on the surface under pressure P.

n_m = number of moles adsorbate required to achieve monolayer coverage.

P_O = saturation vapour pressure of adsorbate at 77K.

C = constant (dependent on the heat of adsorption and liquefaction).

At the saturation pressure (P_O) monolayer coverage of the surface by N_2 is achieved; above P_O (i.e. saturated vapour pressure) multilayer adsorption occurs. Langmuir equation applies to each layer in the multilayer application, however, for the first layer the heat of adsorption may have some specific value and for each subsequent layer it is equal to the heat of condensation of the liquid adsorbate. Langmuir made a further assumption in which evaporation and condensation can only take place from or on exposed surfaces [19]. The BET equation solved many of these problems in the interpretation of adsorption isotherms by plotting P/Po against P/n_s (Po-P) giving a straight-line of slope $(C-1)/(n_mC)$ and intercept of $1/(n_mC)$. Hence n_m can be calculated and knowing the cross sectional surface area (16.2×10^{-20} m^2) occupied by each N_2 molecule, the total surface area can be calculated from the following equation.

$$Total\ Area = A_N \times A(N_2) \times n_m$$

Where: Total area = effective surface area of the unknown.

$A\ (N_2)$ = cross sectional area occupied by the N_2.

A_N = Particles/mole are units for Avogadros number.

The total surface area of the support materials and catalysts in this research project were determined using Gemini III 2375 surface area analyser (i.e. Gemini– Micromeritics BET instrument) by physisorption of N_2 gas at 77K.

2.6.4 Metal surface area

The determination of metal surface area or the exposed number of surface atoms on supported metal catalysts is of major significance, as it permits reaction rates to be expressed in absolute terms [24]. Emmett and Brunauer developed specific chemisorption to measure the areas of distinctly different chemical species exposed on the solid surface [25]. This technique became very useful in characterising supported metal catalysts and metal catalysts containing various promoters.

Metal surface area, catalyst dispersion and metal particle size can be measured from selective chemisorption technique using specific adsorbate gases [21]. This is in contrast to non-selective physisorption and the BET method used to measure the total surface area of the entire solid. In selective chemisorption, only the exposed metal atoms on the surface can bond with the adsorbate gases, the metal atoms in the bulk are inaccessible to the reactant adsorbate gases. Measurements of specific surface area are made with a known stoichiometric adsorption under conditions where adsorption of the reactant gas occurs entirely or primarily on the metal surface. Therefore, it is important that the selected adsorbate gas adsorbs on the metal and not on the support. Typical gases used in selective chemisorption techniques are hydrogen (H_2), carbon monoxide (CO) and oxygen (O_2). For example, the chemisorption of hydrogen on Pt is rapid at ambient temperatures and reaches complete monolayer coverage on the exposed Pt surface atoms. The H_2 selective chemisorption technique for measuring Pt specific area requires a series of assumption to be made [21, 26].

- The H/Pt stoichiometry assumes that the average number of surface metal atoms is associated with the adsorption of each adsorbate atom or molecule (i.e. one hydrogen atom is adsorbed by each surface Pt atom).
- The number of Pt atoms per unit area of the polycrystalline surface is equal to 1.25×10^{19} Pt particles/m^2 based on the surface consisting of equal proportions of (111), (110), and (100) planes.

- Physisorption on the metal and support surface is negligible; this is a reasonable assumption for H_2, at room temperature or above.
- H_2 chemisorption should occur without diffusion or dissolution of H_2 in the metal, for example metal-support H_2 spillover, strong metal support interaction.

Therefore, the chemisorption stoichiometry must be known to allow the number of surface metal atoms to be determined and hence calculate the metal surface area. The metal surface area is denoted by:

$$S_{Pt} = n_m \times X_m \times A \times n_s^{-1}$$

Where, S_{Pt} = Pt Surface area.

X_m = chemisorption stoichiometry (i.e. the number of H_2 molecules reacting per surface Pt atom = 2.

n_m = number of moles of gas adsorbed.

A = Avogadro's constant = 6.023×10^{23} atoms/mole of Pt.

n_s = number of Pt atoms per unit area of surface ($1.25 \times 10^{19} m^2$/atom).

They are many disadvantages to using chemisorption for measurements of specific surface areas; for example, most adsorbent gases are non-specific, surface are sensitive to impurities, after reduction residual H_2 remains, dissolution of which can result in formation of hydrides.

Chemisorption measurements have also lead to kinetic measurements termed turnover number or turnover frequency (i.e. molecules converted per exposed metal atom per unit time) denoted TON and TOF. Once the number of exposed metal atoms has been determined, catalyst activity can be expressed in terms of activity per surface metal atom. These turnover numbers can be used to compare oxidation activity of different catalysts [27, 28].

The metal dispersion, expressed as the number of metal surface atoms as determined from chemisorption data over the total number of metal atoms as determined from AAS and the metal surface area, can be readily calculated by estimating the stoichiometry of the adsorption process and the average surface area occupied by the metal atom [21]. The percentage metal dispersion is often represented by the following equation:

$$\%D_m = \left[\frac{Pt_S}{Pt_T}\right] \times 100\%$$

Where, $\%D_m$ represents the percentage metal dispersion, Pt_s and Pt_t equals the number of Pt surface atoms and total number of Pt atoms present as determined from AAS. This measurement is of considerable importance in supported catalysts as it indicates the availability of the active metal sites on the surface to reactant molecules in catalytic reactions [21].

The average metal particle size can also be determined from the chemisorption measurement data by assuming a shape for the metal crystallites [24]. Therefore, the metal particle size may be estimated by the following equation [21].

$$d = \left(\frac{D}{\rho \times S_{Pt}}\right)$$

Where, D is the diameter of the metal crystallite [24], ρ is the density of Pt in g/cm^3 at room temperature and S_{Pt} is the metal surface area. Estimation of the mean particle size is quite useful in catalysis as it enables properties such as metal-support interaction, sintering and redispersion to be characterised. Other major techniques used in determination of particle size are X-ray diffraction (XRD), Transmission electron microscopy (TEM) and X-ray photoelectron microscopy (XPS) [21].

In this study, selective chemisorption using a Micrometrics Pulse flow technique with H_2 as the reactant adsorbate gas was used to measure the metal surface area, metal dispersion and mean particle size of platinum on an alumina washcoated gauze.

References

[1] P. Lagarde, T. Murata, G. Vlaic, E. Freund, H. Dexpert and J. P. Bournonville, J. Catal., **84**, 333 (1983).

[2] J. Berdala, E. Freund and J.P. Lynch, J. Phys., Colloque C8, **47**, 269 (1986).

[3] X. Huang, Y. Yang and J. Zhang, Appl. Catal., **40**, 291 (1998).

[4] A. H. J. Martens and R. Prins, Appl. Catal., **46**, 31 (1989).

[5] T. Mang, B. Brietscheidel, P. Polanek and H. Knozinger, Appl. Catal., A **106**, 239 (1993).

[6] A. V. Matyshat, I. K. Khomenko, K. N. Bonddareva, I. V. Panchishnyi and N. V. Korchat, Kinet. Catal., **39,** 93 (1998).

[7] R. J. Regalbuto, A. Navada, S. Shadid, L. M. Bricker and Q. Chen, J. Catal., **184**, 335 (1999).

[8] J. W. Geus and J. A. R. Van Veen, in Catalysis "Moulijn, J. A., Van Leeuwen, P. W. N. M. and Van Santen, R. A., eds.", Studies in Surface Science and Catalysis, **79**, 335-360, Elsevier, Amsterdam, (1993).

[9] I. M. Watt, "The Principles and Practice of Electron Microscopy", 2nd Edition, 596 (1997)

[10] S. B. Barlow, "The Principles and Practice of X-ray Microanalysis", Oxford Instruments, (1997).

[11] R. F. Egerton, "Physical Principles of Electron Microscopy", Electronics Laboratory, Plenum Press, (1996).

[12] M. T. Postek, K. S. Howard, A. H. Johnson, K. L. McMichael, "Scanning Electron Microscope", (A Students Handbook), J. Arnott, Ladd Research, Williston. (1980).

[13] D.A. Wollman, K.D. Irwin, G.C. Hilton, L.L. Dulcie, D.E. Newbury and J.M. Martinis. Journal of Microscopy, **188**, 196 (1997).

[14] T. Allen, "Particle Size Measurements", Chapman and Hall Publishing, USA, 3rd Edition (1981).

[15] V. K. Pecharsky and P. Y. Zavalij, "Fundamentals of powder diffraction and structural characterization of materials", Kluwer Academic Publishers, Boston, (2003).

[16] J. C. Speakman, Molecular Structure, "its study by Crystal Diffraction", (1977).

[17] H. H. Willard, L. L. Merritt Jr., J. A. Dean, and F. A. Settle Jr., "Instrumental Methods of Analysis", Wadsworth Press, California, (1988).

[18] F. W. Fifield and D. Kealey, Analytical Chemistry, London, International Textbook Company Limited, (1975).

[19] S. J. Gregg and K. S. W. Sing, "Adsorption, Surface Area and Porosity", Academic Press, New York, (1967).

[20] W. B. Innes, in "Experimental Method in Catalytic Research", (R. B. Anderson, ed.), Academic Press, New York, 44 (1968).

[21] J. L. Lemaitre, P. G. Menon and F. G. Delannay, "Characterisation of Heterogeneous Catalysts", (F. G. Delannay ed.), Deeker Press, New York, 299-365 (1984).

[22] P. W. Atkins, "Physical Chemistry",5th Edition, Oxford Press, University of Lincoln College, Oxford, (1994).

[23] J. D. Shaw, "Introduction to Colloid and Surface Chemistry", 4th Edition, Butterworths, London, Chapter 5, (1986).

[24] R. Oukaci, D. G. Blackmond, A. Sayari, and J. G. Goodwin Jr. "Metal-Supported Interactions in Catalysis, Sintering, and Redispersion", (S. A. Stevenson, J. A. Dumesic, R. T. K. Baker, Eli Ruckenstein., eds.), 19-34, Van Nostrand Reinhold Press, New York, (1987).

[25] P. H. Emmett and S. Brunauer, J. Am. Chem. Soc., **59**, 310, (1937).

[26] J. R. Anderson and K. C. Pratt, "Introduction to Characterisation of Heterogeneous Catalysts", Academic Press, Australia, (1985).

[27] R. F. Hicks, H, Qi, L. M. Young, and G. R. Lee, J. Catal., **122**, 280, (1990).

[28] P. Briot, A. Auroux, D. Jones, and M. Primet, Appl. Catal., **59**, 141, (1990).

Chapter 3:

Preparation and Characterisation of Pt/Al_2O_3 Gauze Catalyst

3.0 Introduction

In this chapter, the experimental preparation of a series of Pt/Al_2O_3 gauze catalysts is described and compared to commercial catalysts. The metallic substrate support onto which the alumina washcoat was impregnated is characterised and evaluated. Catalysts were characterised using AAS, BET surface area (i.e. N_2 physisorption) to determine metal loadings and surface area of the substrates and washcoat supports is also described. The metal surface area, dispersion and metal particle size of catalyst was determined by H_2 chemisorption and these results related to catalysts activity for combustion reaction will also be discussed with the aid of H_2 chemisorption and combustion activity techniques. In addition scanning electron microscopy (SEM) and energy dispersive X-ray analysis (EDX) were used to determine optimum conditions for preparation of whiskered gauze samples.

3.1 Experimental

3.1.1 Gauze Pretreatment

A gauze sample supplied by an industrial sponsor was cut up into square sections ca. 14cm×14cm in size, with a scissors wearing PVC gloves. The gauze was then washed by dipping it in acetone and left to drain, followed by rinsing in hot soapy water (ca. 40-60^{O}C). The hot soapy water residue remaining on the gauze was washed off under a flow of cold running tap water and left sitting on a clock glass to drain. A final pre-treatment to remove organic oils and remaining residue was preformed by dipping the gauze in methanol, followed by shaking to remove the excess methanol. The sample was dried at 60^{O}C overnight and further dried at 300^{O}C for 1 to 2 hours. Drying was in a muffle furnace with a static air atmosphere. After cleaning, the gauze sample was whiskered at varying temperatures over prolonged time periods in a muffle furnace. A list of gauze samples prepared is given in Tables 3.1 and 3.2. For the whiskered gauzes – the letter T in the sample code followed by a number in subscript and superscript indicates the time in hours and temperature respectively of whiskering in the muffled static air furnace, while the letter N represents whiskering in a nitrogen atmosphere within the muffle furnace.

3.1.2 Washcoat Preparation

A series of alumina washcoat substrate supports, with sample codes 250A and 140A were prepared containing SCFa-250 puralox (supplied by Condea Chemie Germany) and SCFa-140 puralox (Condea Chemie Germany). The Puralox powders employed are high purity activated aluminas, for product specification sheets see appendix. For the washcoat supports the label 250A in the sample code indicates the presences of SCFa-250, while the label 140A represents the presence of SCFa-140 puralox and superscript I denotes insufficient grinding time of the washcoat mixture. All alumina washcoat supports were

prepared by forming a slurry comprising of puralox powders, puralox suspension (25%. w/v SCFa-250:H_2O, supplied by Condea Chemie Germany), puralox disperal (highly pure, dispersible colloidal boehmite alumina supplied by Condea Chemie Germany) and conc. HNO_3 acid (BDH Laboratory Conc. 69%), the resultant slurry mix was then ground for 5 to 6 hours in a mortar and pestle. After grinding for 5-6 hrs at room temperature, the viscosity of the slurry was measured using a Viscometer ELV-S to within a 310-340cp range by diluting with milli-Q-water. The details of the alumina washcoat support materials prepared in this study are given in Table 3.3.

Table 3.1: Detailed Whiskering Conditions for Metal alloy Gauze.

Sample Code	Temperature ^0C	Atmosphere
T_0^{900}	900	Static Air
$T_{1/4}^{900}$	900	Static Air
$T_{1/2}^{900}$	900	Static Air
T_1^{900}	900	Static Air
T_2^{900}	900	Static Air
T_3^{900}	900	Static Air
T_4^{900}	900	Static Air
T_8^{900}	900	Static Air
T_{16}^{900}	900	Static Air
T_{24}^{900}	900	Static Air
T_{32}^{900}	900	Static Air
T_{64}^{900}	900	Static Air
$*T_1^{900}N$	900	Nitrogen
$*T_2^{900}N$	900	Nitrogen
$*T_4^{900}N$	900	Nitrogen
$*T_6^{900}N$	900	Nitrogen

T_x^y, where x denotes number of hours at y temperature in whiskering step.

* Samples whiskered over a specific time frame in stream of flowing N_2 at 200mls/min.

Table 3.2: Whiskering Details Employed in Accelerated Method.

Sample Code	Temperature ^{0}C	Atmosphere
T_8^*	@925 for ½ hr @960 for 7½ hrs	Static Air
T_{16}^*	@875 for ½ hr @960 for 15½ hrs	Static Air
$T_{15½}^*$	@900 for ¼ hr @940 for 15¼ hrs	Static Air
$T_{6¼}^*$	@915 for ¼hr @940 for 2 hrs @960 for 4hrs	Static Air
$T_{3¾}^*$	@925 for ¾ hrs @960 for 1 hr @990 for 2 hrs	Static Air

* In the sample code represents the varying temperature pretreatment employed through out the whiskering process.

Table 3.3: Preparation details for Washcoat Supports Used in this Study.

Sample Code	SCFa-250 Puralox (grams)	SCFa-140 Puralox (grams)	Puralox Suspension (mls)	Disperal (grams)	Conc. HNO_3 (mls)	*H_2O (mls)
250A	40	-----	80	0.125	~2	30-35
140A[1]	-----	40	80	0.125	~2	60-65
140A	-----	40	80	0.125	~2	60-65

*H_2O represents the volume of water added to obtain the required viscosity.

3.1.3 Washcoat application

After washcoat preparation, a series of the whiskered metallic substrate supports were coated with the washcoat slurry mix by washcoating on both sides in the following manner. Samples were prepared by (1) dipping one side of the whiskered gauze in the washcoat slurry mixture, followed by (2) blow-drying with N_2 gas, (3) drying at 50-60^{O}C for 20 minutes and fired at 800^{O}C for 15 minutes. Washcoating was repeated on the other side of the whiskered gauze sample by repeating steps one to three above. Table 3.4 lists the whiskered samples washcoated and the detailed quantities of both SCFa-250 and SCFa-140 puralox powder and suspension used in the alumina washcoat support.

Table 3.4: Details of Washcoat Solution used to Coat Whiskered gauze support.

Sample Code	SCFa-250 Puralox (grams)	SCFa-140 Puralox (grams)	Puralox Suspension (mls)
T_4^{900}-250A	40	------	80
T_8^{900}-250A	40	------	80
T_{16}^{900}-250A	40	------	80
T_{16}^{900}-140A	------	40	80
T_{16}^{900}-140A[I]	------	40	80
T_{24}^{900}-250A	40	------	80
T_{32}^{900}-250A	40	------	80

[I] Denotes washcoat applied was insufficiently ground (i.e. ½ hrs grinding time).

3.1.4 Catalyst Preparation

The catalyst metallic support (i.e. substrate) and support materials used in this study were expanded metal gauze (industrially supplied), puralox powders, puralox suspension, disperal (supplied by Condea Chemie) and conc. HNO_3 Acid. The Impregnating solution used in this study was a CPA based methanol solution (industrially supplied). Using the above materials a series of $Pt/\gamma-Al_2O_3$ gauze catalysts were prepared see Table 3.5:

Table 3.5: Details of Lab Prepared and Commercial Catalysts in this Study.

Sample Code	Impregnation Method	Pt wt.%	Support
T_4^{900}-250AP	W	2.9	Al_2O_3 washcoat
T_8^{900}-250AP	W	3.0	Al_2O_3 washcoat
T_{16}^{900}-250AP	W	3.2	Al_2O_3 washcoat
T_{24}^{900}-250AP	W	3.2	Al_2O_3 washcoat
T_{16}^{900}-140AP	W	3.5	Al_2O_3 washcoat
T_{16}^{900}-140AP$^{1/3}$	W	0.94	Al_2O_3 washcoat
C1	Unknown	2.2	Al_2O_3 washcoat
C2	W	2.7	Al_2O_3 washcoat

W represents incipient wet impregnation.

$P^{1/3}$ represents catalysts prepared with a 1 in 3 dilution with methanol of the original CPA solution supplied.

C1 and C2 are commercial catalysts supplied for comparison purposes with the Lab prepared catalysts.

For each catalyst prepared, the letter T in the sample code followed by a number in subscript and superscript indicates the time in hours and temperature respectively of whiskering in the muffled static air furnace. The letter P in the sample code indicates the presence of Pt, while the labels 250A and 140A are used to represent puralox powders

present in the washcoat support. Samples were prepared by contact of the whiskered gauze supports with the slurry solution of alumina washcoat. After washcoating the samples were impregnated by dipping them in a CPA based methanol solution for approximately 3 seconds, followed by drying at 45^{O}C overnight in an oven and calcining at 630^{O}C for 15 minutes in muffle static air furnace.

3.2 Catalyst Characterisation

3.2.1 Ageing Test

All catalyst samples were aged in a static air muffle furnace set to 800^{0}C for 8 hours. This was the test to determine the stability of the catalyst over time. The samples were then removed from the furnace and labelled for testing. Aged samples were investigated using BET surface area, H_2 chemisorption and combustion activity measurements. For comparison purposes measurements of fresh catalyst samples (i.e. unaged) were also examined.

3.2.2 SEM/EDX-Ray Analysis

To determine the appropriate whiskering conditions, samples whiskered at different temperatures and time were characterised by SEM. The samples of whiskered gauze were cut to approximately 1cm×1cm in size and placed on a steel sample holder with a carbon-based tape. Topographic images of different regions of the sample were obtained using a S-3000N Hitachi SEM. Determination of elemental composition of the whiskered gauze samples was carried using an Isis Oxford Energy Dispersive X-ray with preloaded Link ISIS software. The samples analysed under SEM and EDX were from gauze samples whiskered in muffle furnace for ¼-32 hrs under static air and N_2 atmospheres.

3.2.3 X-Ray Diffraction

The phase of alumina present in the washcoat solution was determined by XRD analysis. A Philips XRD diffractometer was used to record the X-ray diffraction (XRD) patterns of two different grade alumina powders (i.e. Puralox SCFa-250 and SCFa-140). Measurements were per-formed on ground samples in a rotating sample holder with a CuKα cathode radiation source (λ = 1.5418 Å) operating at 50kV and 30mA. Sample identification was achieved by comparison with a library database.

3.2.4 Particle Size Distribution

A Malvern Mastersizer S long bed V2.19 was used to determine the particle size distribution of alumina in the washcoat solution. The samples (see Table 3.6) were prepared by adding a few drops of washcoat solution to a beaker using a spatula and dispersing in water and calgon, followed by stirring in an ultrasonic water bath for 5 minutes.

Table 3.6: Details of Washcoat Preparation

Sample Code	Grinding Method	Grind Times (hours)
250A*	Ballmill	4
250A	Mortar and pestle	5-6
140A[1]	Mortar and pestle	½-¾
140A	Mortar and pestle	5-6

* One sample obtained from ball milling 250A for 4 hrs.

Using a lens with a range of 300RF mm, the sample was then flushed into the sample cell. The cell stirrer was switched on to ensure a homogeneous suspension of the mixture. The ultrasonic bath was used to ensure no particle agglomeration occurred. The particle size was measured by laser diffraction and a scattering method. The instrumental conditions used are summarised in Table 3.7.

Table 3.7: Instrumental conditions Used in Malvern Mastersizer.

Range Lens	300RF mm
Beam length	2.40 mm
Analysis model	Polydisperse
Particle R.I.	1.7600, 0.0010
Dispersant R.I.	1.3300
Obscuration	6.2%
Residual	0.825%

Measurements and calculation were obtained from software computer system attached. The results were displayed graphically on a computer.

3.2.5 Determination of Total Metal Content

A series of Pt standard solutions were prepared from a 1000ppm standard stock solution (BDH, Spectrosol) as follows. A 100ppm Pt stock solution was prepared by dilution of $10cm^3$ aliquot of the 1000ppm in a $100cm^3$ volumetric flask with milli-Q water. This solution was subsequently used to prepare the Pt standards within a linear concentration range (i.e. 10-50ppm) by dilution of a fixed aliquot of the 100ppm stock in a final volume of $50cm^3$ in a volumetric flask. $0.5cm^3$ of concentrated HCl and $1cm^3$ of 1000ppm $LaCl_3$ solution (Sigma Aldrich) were added to each of the standard solutions to counter the effects of interferences.

Sample digestion was carried out by two different methods (i.e. B and C). In method B, a known weight (typically between 0.1-0.2g) of gauze catalyst finely cut was weighted out in a Teflon beaker, followed by addition of ca. 20mls aqua regia. The solution was placed on a hot plate with a magnetic stirrer and boiled. In method C, an additional step was added, in which ca. 4mls HF (Riedel) was added prior to the addition of the aqua regia. In both methods the samples were heated to boiling and boiled to near dryness (ca. 0.5-1.0 ml solution remaining). The residues remaining were then cooled and reconstituted with 2mls of conc. HCl acid and 4mls of 1000ppm $LaCl_3$ solution and filtered into 100ml volumetric flask. After filtering, the beakers were washed out three times with milli-Q water and the washings transferred to the flask. Finally, the solutions were made up to the mark with Milli-Q water in a $100cm^3$ volumetric flask for analysis.

Each standard and sample was measured five times in the AAS, set up as summarised in Table 3.8.

Table 3.8: Instrumental condition employed in the Perkin Elmer 3100 AAS

Lamp Source	Pt - Hollow Cathode Lamp
Slit Width	0.7nm
Sensitivity	High
Lamp Current	10mA
Wavelength (λ)	265.9nm
Integration	1.0 seconds
Burner Head	Single Slot
Fuel : Oxidant ratio	Acetylene-Air 2:6 (Cu. Ft. hr^{-1})

For each catalyst sample three-repeated analyses were preformed on different parts of the same sample and the average % loading calculated.

3.2.6 Determination of Total Surface Area

Measurements of BET specific surface area of the washcoat supports and catalyst samples were determined by continuous flowing N_2 adsorption at liquid N_2 temperatures with He carrier gas using a Micromeritics Gemini III 2375 surface area analyser V4.01. The Gemini III 2375 instrument uses a series of reservoir valves, transducer and servo valves and comes pre-programmed with StarDriver software ready for analysis. A schematic of the instrument pumping diagram used is given in Figure 3.2.

To determine the specific surface area with the Gemini III 2375 an adaptive rate, static volumetric technique of operation is used. This method adapts the rate at which gas is delivered to the sample to the rate at which it is adsorbed. Each pressure point completely equilibrates before the next point is taken. The Gemini as illustrated in Figure 3.2 contains two gas reservoirs, which are filled with equal volumes of an adsorptive mixture of Nitrogen/Helium 42% V/V through a pumping system controlled by two reservoir valves. From the reservoirs, the gas is dosed into the sample and balance tubes. A transducer on the sample side monitors for the target pressure. As the sample adsorbs gas, the pressure would tend to decrease in the sample tube. The use of the transducer causes a fast response servo valve to hold the pressure constant. Transducer located between the sample and balance tubes detects any pressure difference between the two tubes and causes another servo valve to balance the pressures in both tubes. A third pressure transducer monitors the pressure between the two reservoirs to determine the amount of gas that is adsorbed on the sample. The helium passes through the balance and sample tube for free space measurement to determine any slight differences in volume. The balance tube essentially has the free space volume as the sample tube and therefore can eliminate the free-space errors. The volume of nitrogen adsorbed on the surface of the particles is then measured at the boiling point of nitrogen (-196°C) and the amount of adsorbed nitrogen is correlated to the total surface area of the particles including pores in the surface. The surface areas of the catalyst are calculated on the basis of the adsorbate gas parameters (i.e. molecular area, density conversion and nonideality factor). The Gemini III 2375 surface area analyser gives reproducible surface area result in the

minimum run time (i.e. ca. 30 minutes). Sample data are automatically calculated and displayed or printed in both tabular and graphical form for quick, easy interpretation [1].

Prior to measurements, the empty BET quartz tube was weighted out, followed by the sample (typically between 0.1-0.2grams samples were weighted out) in the BET quartz tube (supplied by Micrometrics). The sample was then degassed at $200^{O}C$ under static conditions overnight in a furnace supplied by Lenthon Thermal Design Systems Ltd. After degassing, the sample and tube were cooled and reweighed. The final sample weight was obtained by subtracting the initial weight of the empty quartz tube from the tube and sample weight after degassing. The sample was then connected to the analyser and the surface area measured. Each sample was analysed and an average reading taken for two reproducible measurements.

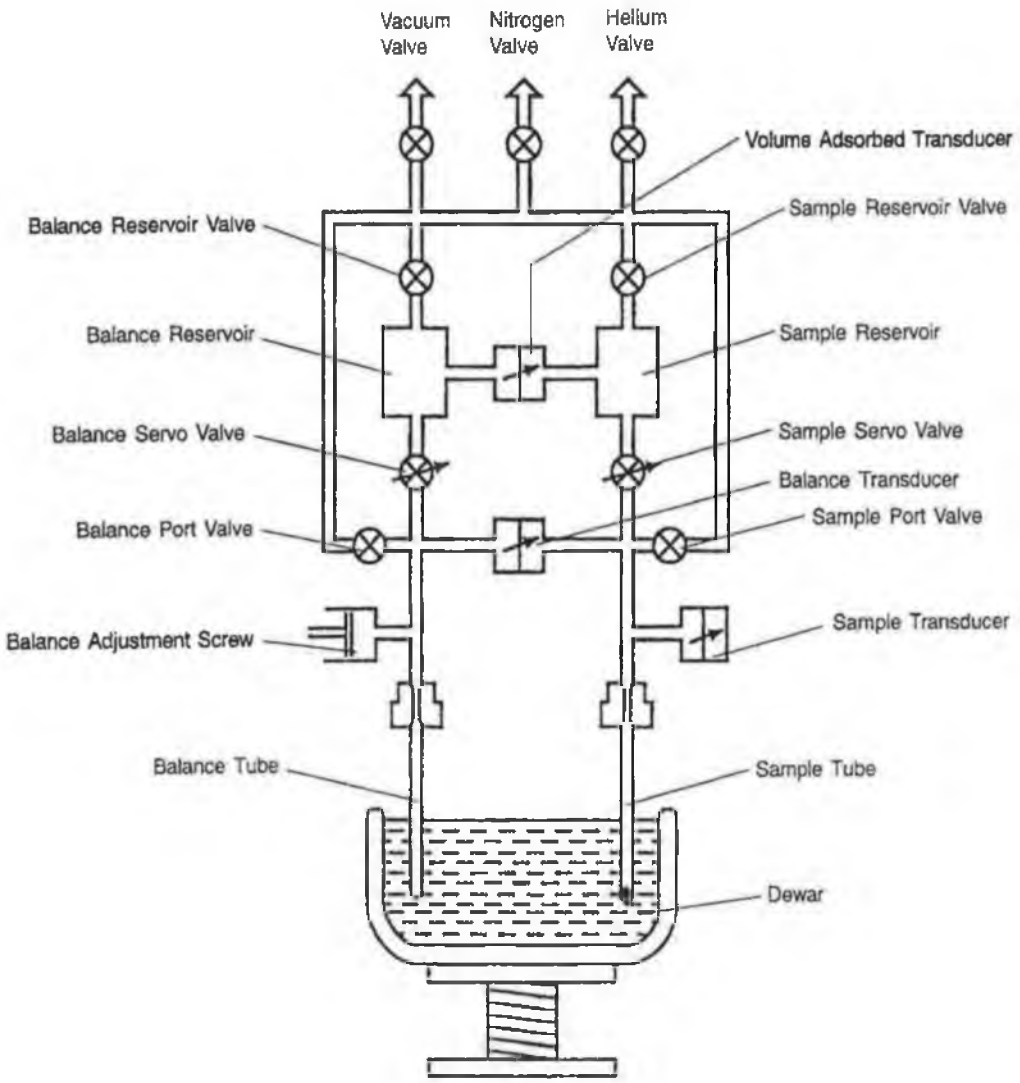

Figure 3.2: Schematic of a Plumbing diagram for a Gemini-Micrometrics BET [1].

3.2.7 Determination of Metal Surface Area

Metal surface area measurements were carried out using a pulse flow H_2 chemisorption unit. A schematic representation of the Pulse Flow unit is shown in Figure 3.3.

Prior to analysis both (Ar and H_2) gases were purified. Argon gas is firstly purified to remove all contaminants present, such as N_2, O_2, H_2, CO and CO_2. Purification was achieved using a B.O.C. rare gas purifier by passage of Ar over (1) titanium granules at 700^{O}C to remove N_2 and O_2, (2) a copper oxide furnaces at 450^{O}C for the removal of H_2 and CO and finally (3) a molecular sieve at ambient temperatures to remove moisture and CO_2. Hydrogen gas was also purified using a Johnson Matthew EP1 purifier unit by passage over a Pd-Ag membrane alloy at 250^{O}C.

After purification, argon was fed continuously over the catalyst sample and through both sides of the Thermal Conductivity Detector (TCD). A volume of 0.053ml of H_2 in a stream of Argon was passed over the sample via an injection loop. The H_2 was then passed through the catalyst and through one side of the TCD. A proportion of this H_2 was adsorbed by the sample, resulting in the reduction of H_2 detected on the other side of the TCD. A chart recording with two peaks corresponding to amount of H_2 present in the loop and amount not adsorbed was obtained (Figure 3.4).

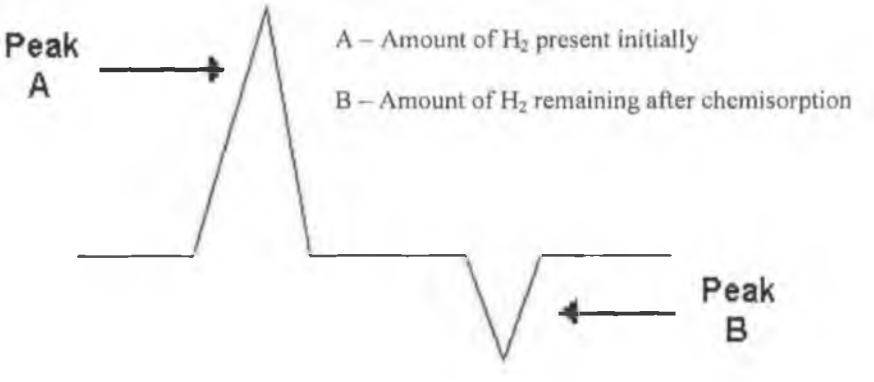

Figure 3.4: H_2 Chemisorption before and after adsorption

The difference between the areas of the two peaks indicates the quantity of H_2 adsorbed on the sample and can be used to calculate the metal surface area.

For analysis, the standard procedure used was as follows: a sample of catalyst (typically 0.1-0.2g) was weighed out in a clean dry quartz u-tube that was preweighed. The u-tube was plugged with chemically treated glass wool (soaked in 2M NHO_3 acid and washing with eight litres of milli Q water and dried at $110^{O}C$ in a furnace). The u-tube was then connected to the chemisorption unit. The catalyst pretreatment conditions prior to measurements were as follows: Argon at a flow rate of 40mls/min was passed over the sample first at room temperature and then at increased temperature (i.e. $125^{O}C$) using a furnace (supplied by Lenthon Thermal Design Systems Ltd.) mounted underneath the sample tube. A 40mls/min flow rate H_2 was then passed over the sample at 400^{0} to reduce it, followed by Argon at the same temperature to remove H_2 from the active sites. Flow rates were controlled by metering valves and measured using 250ml calibrated H_2 and Ar flow meters (supplied by Cajon Systems Ltd.) and double checked with a bubble flow meter. The sample was then cooled to room temperature under flowing Ar by immersing the u-tube in a beaker of cold water (see Table 3.9).

Table 3.9: Pretreatment conditions employed prior to analysis of catalyst samples

Gases	Temperature (^{O}C)	Time (min)
Argon (Ar)	25 (R.T.)	15
Argon (Ar)	125	60
Argon (Ar)	400	30
Hydrogen (H_2)	400	20
*Argon (Ar)	400	40
Argon (Ar)	25 (R.T.)	5

* After each Chemisorption measurement Argon was passed over the sample at $400^{O}C$ for 40 minutes to remove chemisorbed H_2.

The pre-treatment conditions employed in the chemisorption analysis were previously tested and it was found that reduction at 400^{O}C resulted in the highest H_2 uptake [2]. After each measurement Argon was passed over the sample for 40 minutes to remove chemisorbed H_2 and analysis repeated. Three-repeated chemisorption measurements were performed on every catalyst sample.

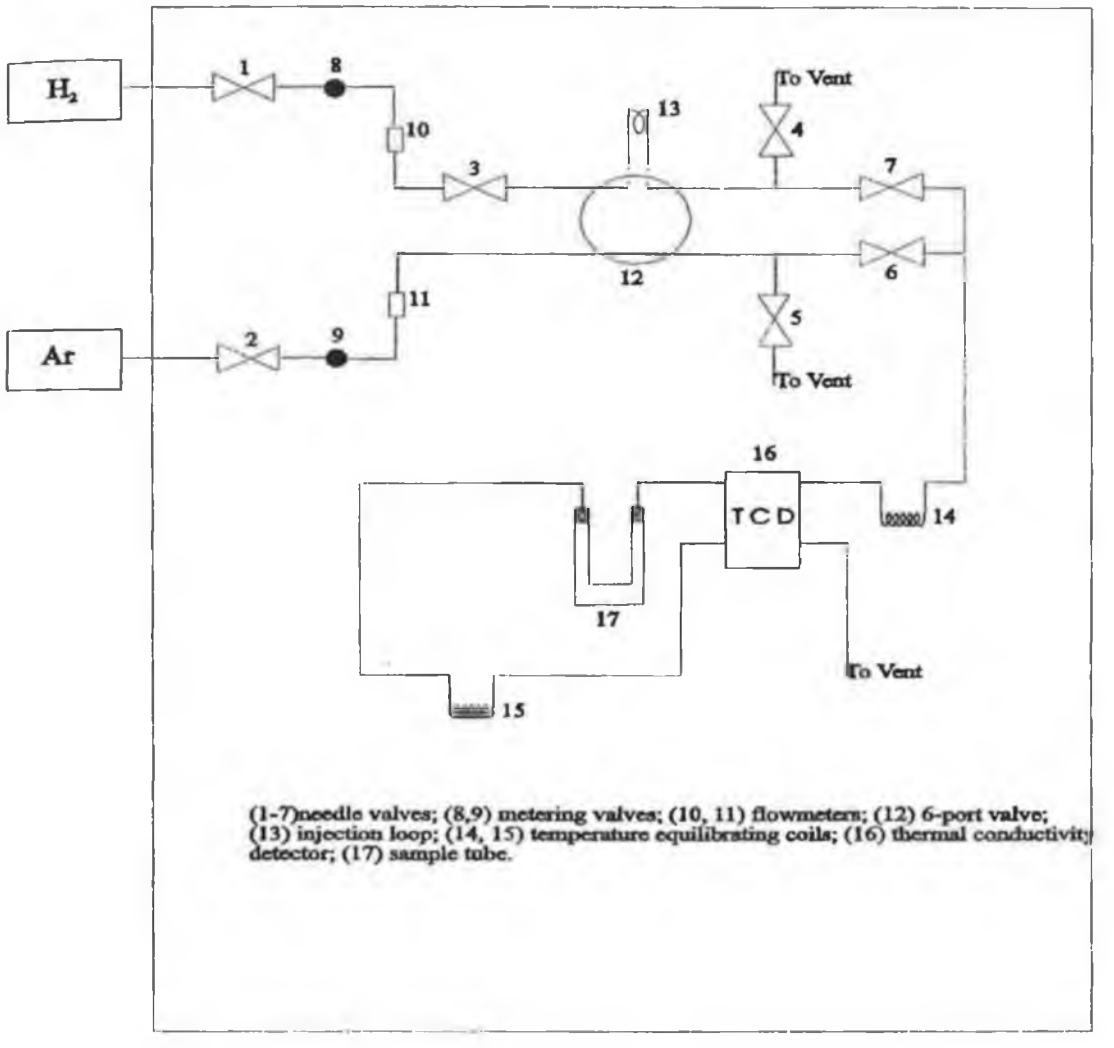

Figure 3.3: Schematic diagram of the H_2 Pulse Flow Chemisorption Unit [2].

3.2.8 Activity Measurements

The oxidation activity over different catalyst samples was determined by monitoring the combustion of hydrocarbon with oxygen as a function of temperature using a continuous flow apparatus. A schematic diagram of the activity unit is illustrated in Figure 3.5 [2]. Stoichiometric mixtures of hydrocarbon and oxygen were passed over the heated catalyst samples. Mass flow controllers with ranges of 0-5cm^3min^{-1} and 0-100cm^3min^{-1} controlled the flow rates. A 4-port switch valve allowed the reaction mixture to pass over the catalyst sample or to bypass the sample to the gas chromatograph for a blank analysis to check the 'baseline' hydrocarbon concentration prior to oxidation. The propane oxidation over the catalyst sample was measured over a Porapak Q column using a Flame Ionisation Detector. A cold trap was constructed downstream of the sample on the activity unit to trap and remove any water produced before reaching the GC. A thermal conductive detector with a chemsorb 102 packed column was used to monitor the by-products of oxidation (i.e. CO, and CO_2 peaks).

Flow rates prior to analysis were measured for both the C_3H_8 and Air with a bubble flow meter. A stoichiometric mixture of C_3H_8 in air (ratio 2:50ml/min approx) at a total flow rate of 52cm^3min^{-1} was passed over 0.3g of a heated catalyst sample on a sintered disc mounted in a quartz glass u-tube. Lenthon Thermal Furnaces were used to heat the catalyst samples. Unreacted propane at each temperature was measured by an online gas chromatograph and the percentage conversion was calculated as loss of propane. Repeated measurements were recorded until equilibrium was obtained and two analysis runs were preformed on the catalysts. Prior to the second analysis run the sample was allowed to cool down to room temperature and the analysis was repeated. The oxidation reaction was investigated in the temperature range 100-300^{O}C. The conditions employed in the GC are summarised in Table 3.10:

Table 3.10: GC Instrumental conditions employed in the analysis.

Instrument	Pye Unicam 4550
Detector	(a) Flame Ionisation detector
	(b) Thermal conductivity detector
Column	(a) Porapak Q
	(b) Chemsorb 102
Carrier Gas	Normal grade He, supplied by Air products
	Flow Rate: $60cm^3min^{-1}$
Fuel : oxidant Gases	Hydrogen/Air
	Flow Rates 0.75:0.6 Kg/cm^2
Temperatures	Column: 200^OC
	Injector: 150^OC
	Detector: 200^OC

The catalytic activity, as the percent C_3H_8 reacted, was calculated in the following manner. When the sample is bypassed, a peak corresponding to the initial amount of C_3H_8 present is obtained. As the reactant gases are passed over the catalyst at high temperatures a certain fraction (or all) of the propane reacts (i.e. oxidised), hence its peak size and area is reduced. Therefore, by determination of the area of the propane peak (after passing over the catalyst) and dividing it by the area of the peak representing the initial amount of propane present (bypass), the percentage propane present is calculated by multiplying by 100 and subtracting this value from 100 gives the % conversion. Plotting these calculated % C_3H_8 conversion versus temperature allows the light off temperature T_{50} (i.e. temperature at which 50% conversion is achieved) and T_{90} (i.e. temperature at which 90% conversion is achieved) to be determined from the graph.

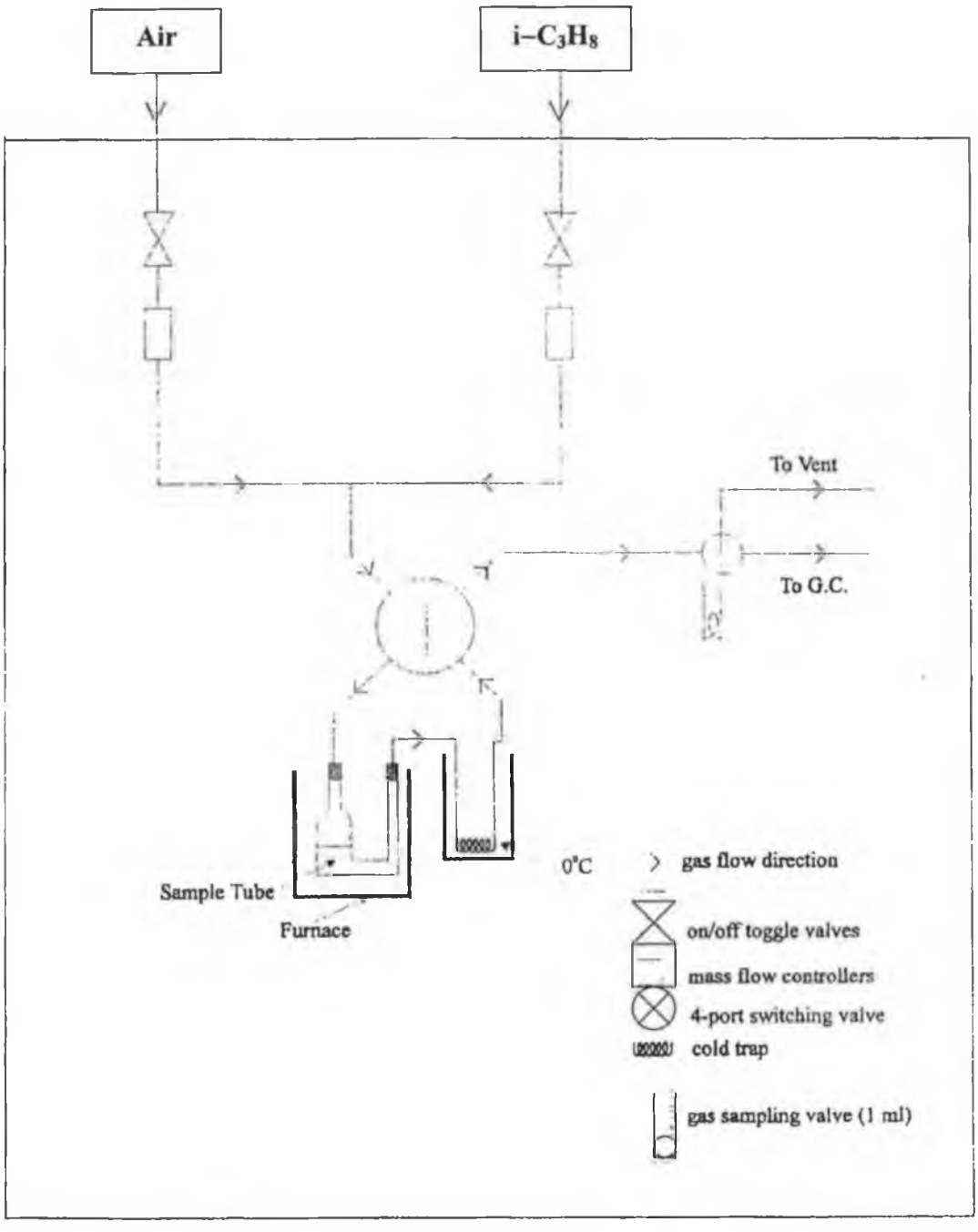

Figure 3.5: A Schematic of a Catalysts Activity Unit for C_3H_8 Combustion [2].

3.3 Results and discussion

3.3.1 Characterisation of Whiskered Surfaces

Scanning Electron microscope Images (SEM)

Figures 3.6 (a) and (b) illustrates an unoxidised cleaned gauze sample imaged for comparison work. Figures 3.7 to 3.16 show electron micrographs (i.e. SEM images) displaying oxide layers of aluminium whiskers formed on gauze surface oxidised under various conditions.

Fig 3.6(a) + (b) shows 2 high-magnification electron micrograph of a cleaned unoxidised gauze sample surface. The gauze was imaged at 2.0K and 3.5K magnification, with a working distance (WD) of 27.6mm and the scale bar was 10μm for (a) and 20μm for (b). The electron voltage acceleration employed in the scanning beam was 20.0kV. This voltage was used in preference to a higher electron voltage, since higher voltages can damage the sample. When imaging samples of a greater depth a higher electron voltage may be used. No whisker formation was observed for the cleaned gauze sample, which was expected. However, upon closer inspection, the micrograph displayed evidence of a rough layer of film grain on the alloy. The layer appears roughly coated on the metal and maybe attributed to the aluminium component of the alloy composition. Chapman et al [3] illustrated a similar electron micrograph of an unoxidised surface of a Fe-Cr-Al foil showing no whisker growth similar to Figures 3.6(a) and (b). EDX analysis of the cleaned unoxidised gauze surface revealed the presence of iron as the bulk component on the gauze surface, while chromium and aluminium are present in lower atomic percentage to iron. Trace amounts of cerium and yttrium were also detected, however, the peaks representing cerium and yttrium in the x-ray spectrum could just be due to background noise. A quantitative elemental compositional analysis method was preformed to determine the percentages of each element present. However, this was not very accurate since calibration files had not been erected for these samples being determined and thus is not included in my results.

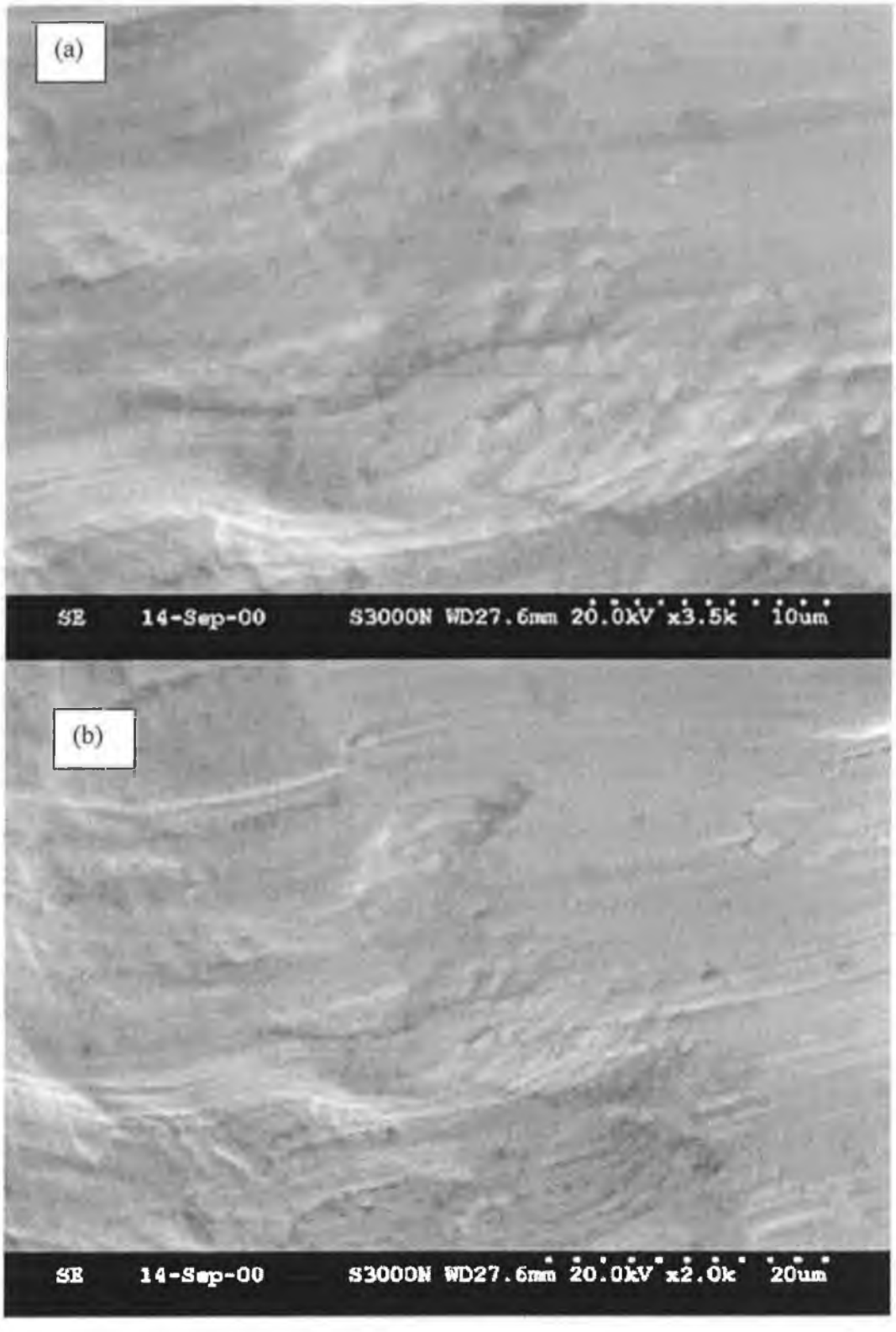

Fig 3.6(a) + (b) shows 3.5K and 2.0K magnification electron micrograph of a cleaned unwhiskered expanded Gauze Surface.

A series of pretreated gauze samples with varying whiskering times up to 1hr at 900^{0}C (Table 3.1, Figures 3.7-3.9) were also examined and were found to exhibit no whisker growth. In marked contrast, Figure 3.10 shows whisker growth in the form of nodules scattered all over the gauze surface, illustrating initial whisker formation after 2hrs heating (sample T_2^{900}). Figure 3.11-3.12 show electron micrographs, which comprised of dense immature whisker growth with occasionally scattered mature whisker formation to the edge of the gauze surface (T_3^{900}, T_4^{900}). This was in contrast to Figure 3.10, which displayed a flatter oxide whisker growth (i.e. nodules). This was attributed to insufficient whiskering time employed in the thermal pretreatment. Chapman et al [3, 4] illustrated that the time required to grow whiskers of the desired size depended upon time and temperature. They found substantially flatter oxide whiskers where produced between 1 to 4 hours whiskering time, between temperatures ranging from 870-900^{O}C. They declared that to obtain high aspect ratio whisker growth, oxidizing the FeAl alloy in temperatures between 870-930^{O}C for a time no less than 8 hours was required. Anything less was found to form immature whiskers, which were reported unsatisfactory for supporting or binding an alumina washcoat support [3, 4].

The electron micrographs of the oxides after 8hr treatment (T_8^{900}) are shown in Figure 3.13(a) and consisted of well-developed oxide whiskers randomly oriented and substantially covering the surface, agreeing with Chapman et al. findings. The whiskers were also characterized by a high aspect ratio from the EDX analysis, which displayed a much higher count for Al in marked contrast to whiskers formed in Figure 3.12 (T_4^{900}). EDX analysis also showed the presence of iron and chromium. However, reduced peak signals were obtained, which may have been due to the well-developed mature aluminium oxide whiskers masking the iron and chromium peaks.

Figures 3.13(b), 3.14(a) and (b) showed electron micrographs of gauze samples pretreated for 16 to 24 hours (Table 3.1). The resultant oxide shown comprised of densely populated mature high aspect ratio whisker growth, which substantially covered the surface. EDX analysis showed the presence of aluminium and oxygen, while iron and chromium peaks were present to a lesser extent. Chapman et al. [4] investigated whisker

growth over time frames of 8-24 hours at temperatures ranging from 870-930^{O}C. They found that whisker growth, resulting in generally large and mature high aspect ratio whiskers, was maximized between 16 to 24 hours at temperatures around 900^{O}C.

Figure 3.15(a) + (b) shows electron micrographs for a gauze whiskered for 32 hours, (a) comprised of less well developed whiskers with patches exhibiting no whisker growth and cracks forming between the whisker growth, whereas Fig. 3.15(b) consisted of some well-developed mature high aspect ratio oxide whiskers covering the surface, but also nodule whisker formation and cracks were observed. This may be due to the whiskering time being increased beyond 24 hours; another factor maybe the formation of alpha alumina, which is not suitable for whisker growth. In contrast to Figure 3.15(a) + (b), a sample treated for 64 hours in Figure 3.16(a) showed regions of very well-developed mature high aspect ratio whisker growth scattered on the surface, while Figure 3.16(b) exhibited nodules scattered throughout the bulk of the surface and less significant smaller whisker growth in comparison to the 32 hours whiskered sample. Chapman et al. [4] reported beyond 24 hours, whisker growth was less well developed and produced substantially fewer and flatter oxide whiskers.

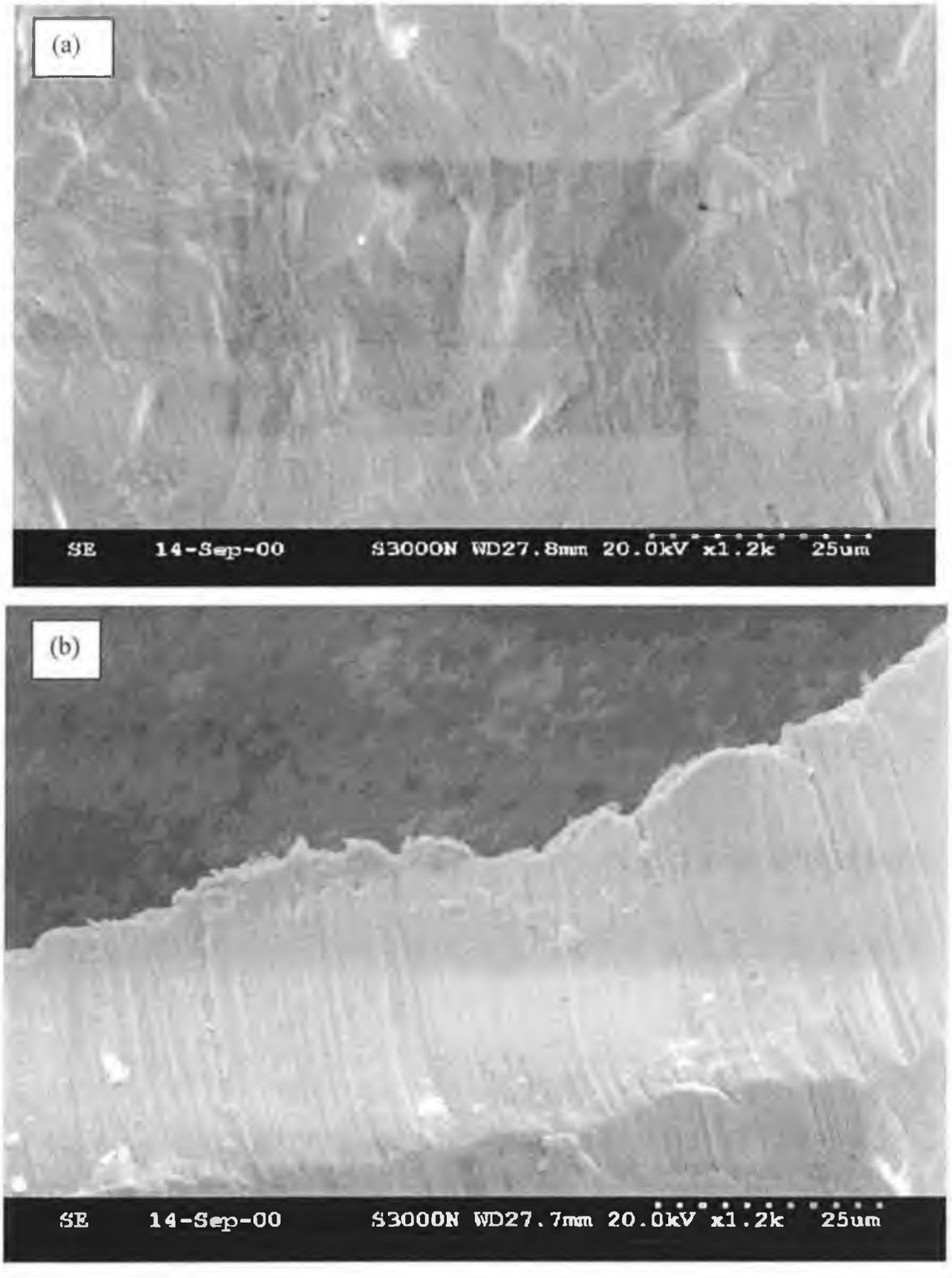

Fig. 3.7 (a) and (b) is a photomicrograph of $T_{1/4}^{900}$, taken at 1200 × magnification of a cleaned gauze oxidised for ¼ hour at 900^{O}C, showing no whisker growth.

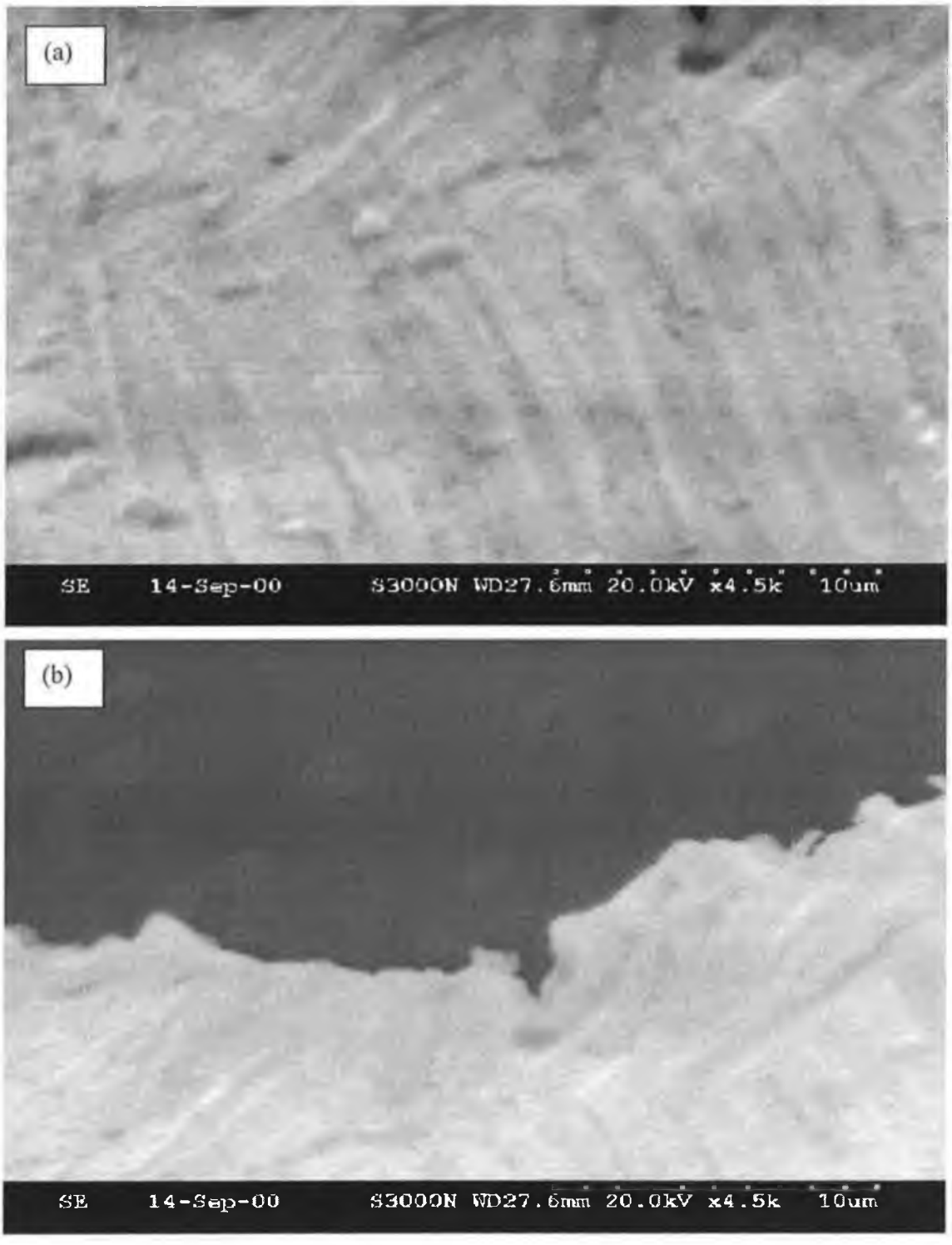

Fig. 3.8 (a) and (b) is a photomicrograph of $T_{1/2}^{900}$ taken at 4500 × magnification of a cleaned gauze oxidised for ½ hour at 900^{O}C, showing no oxide whiskers formed.

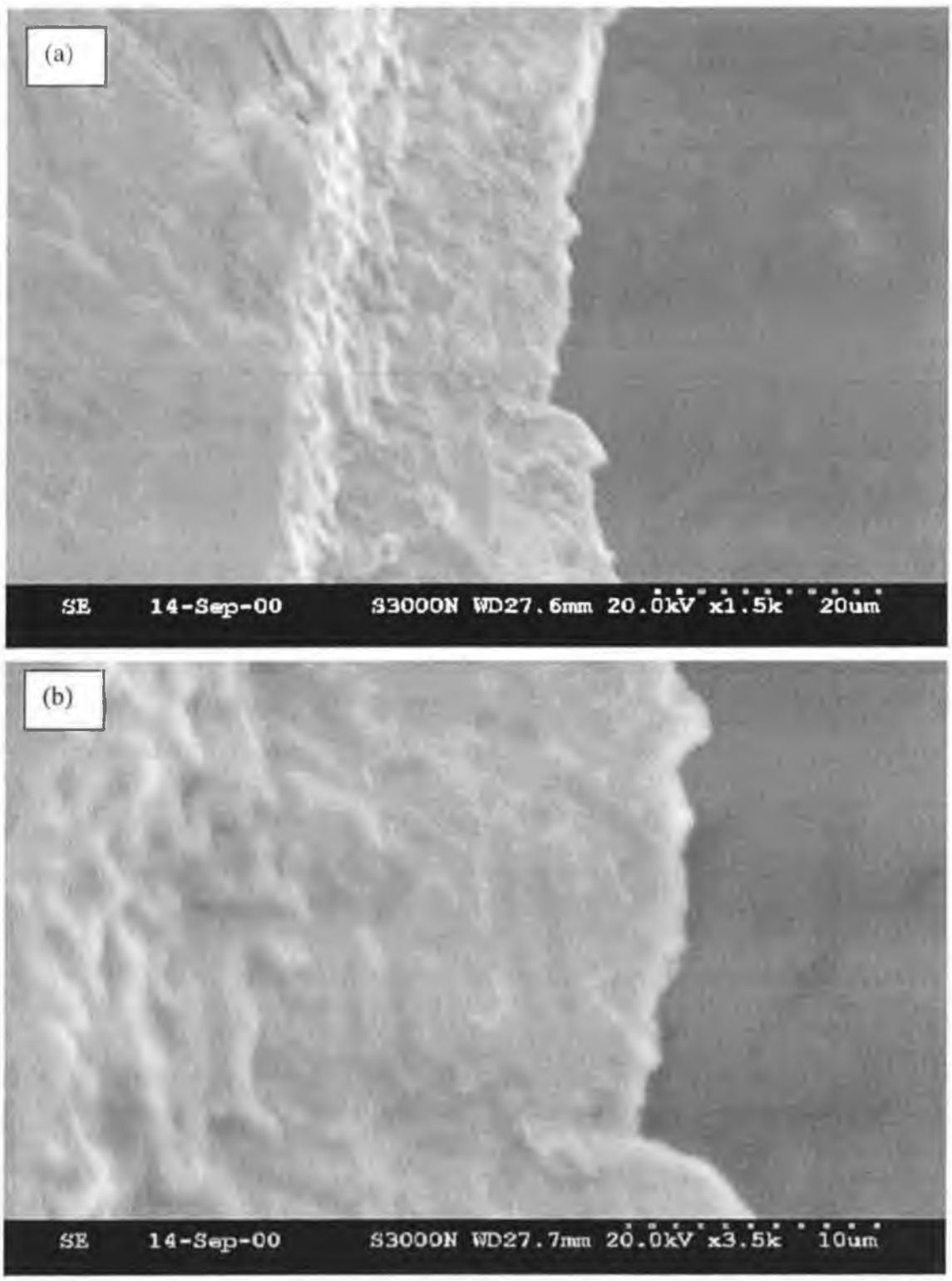

Fig. 3.9 (a) and (b) shows a photomicrograph of T_1^{900} taken at 1500 and 3500 × magnification of a cleaned gauze oxidised for 1 hour at 900^{O}C, showing no whisker growth.

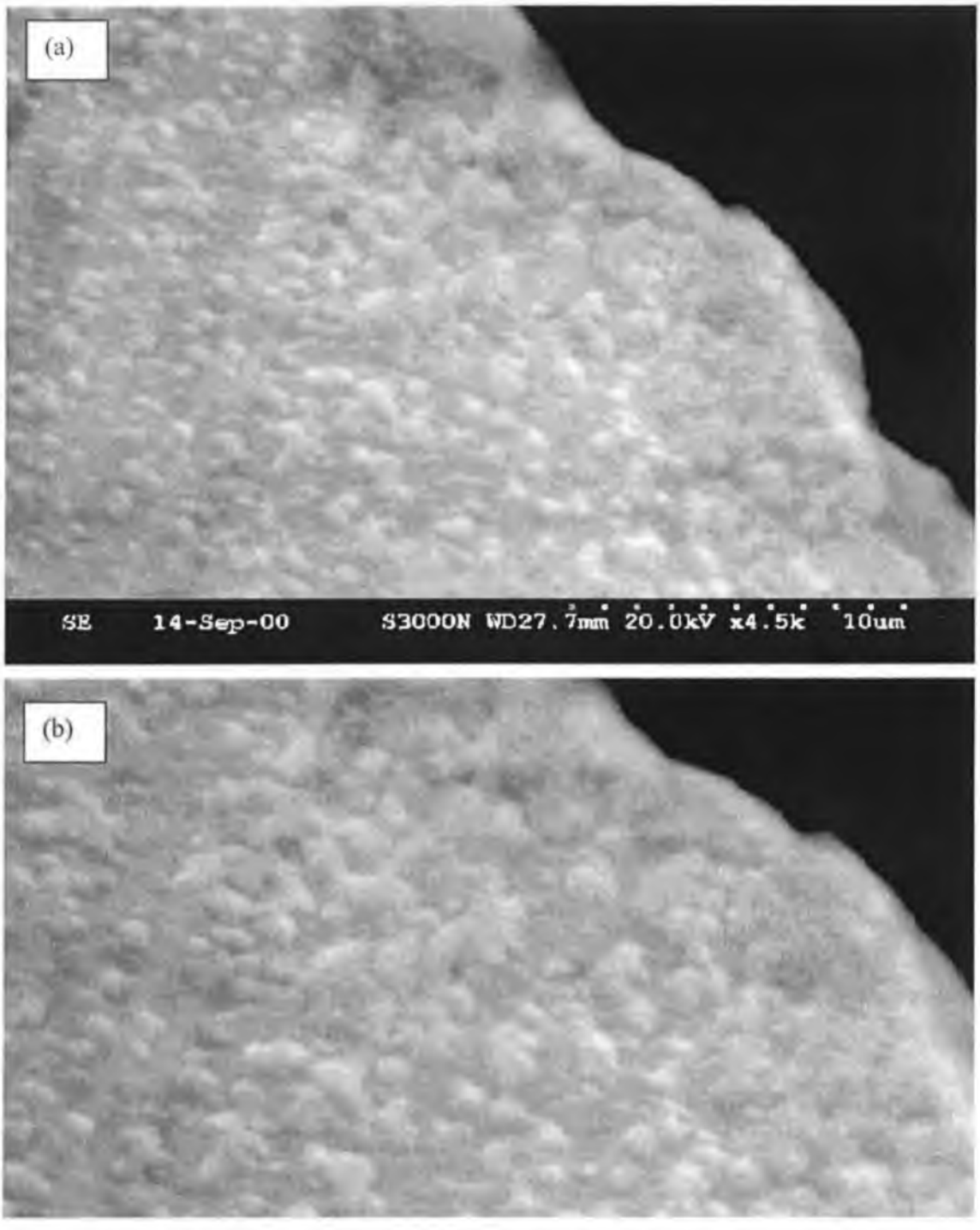

Fig. 3.10 (a) and (b) shows a photomicrograph of T_2^{900} taken at 4500 and 6000 × magnification of a cleaned gauze oxidised for 2 hour at 900^{O}C, showing nodule formation.

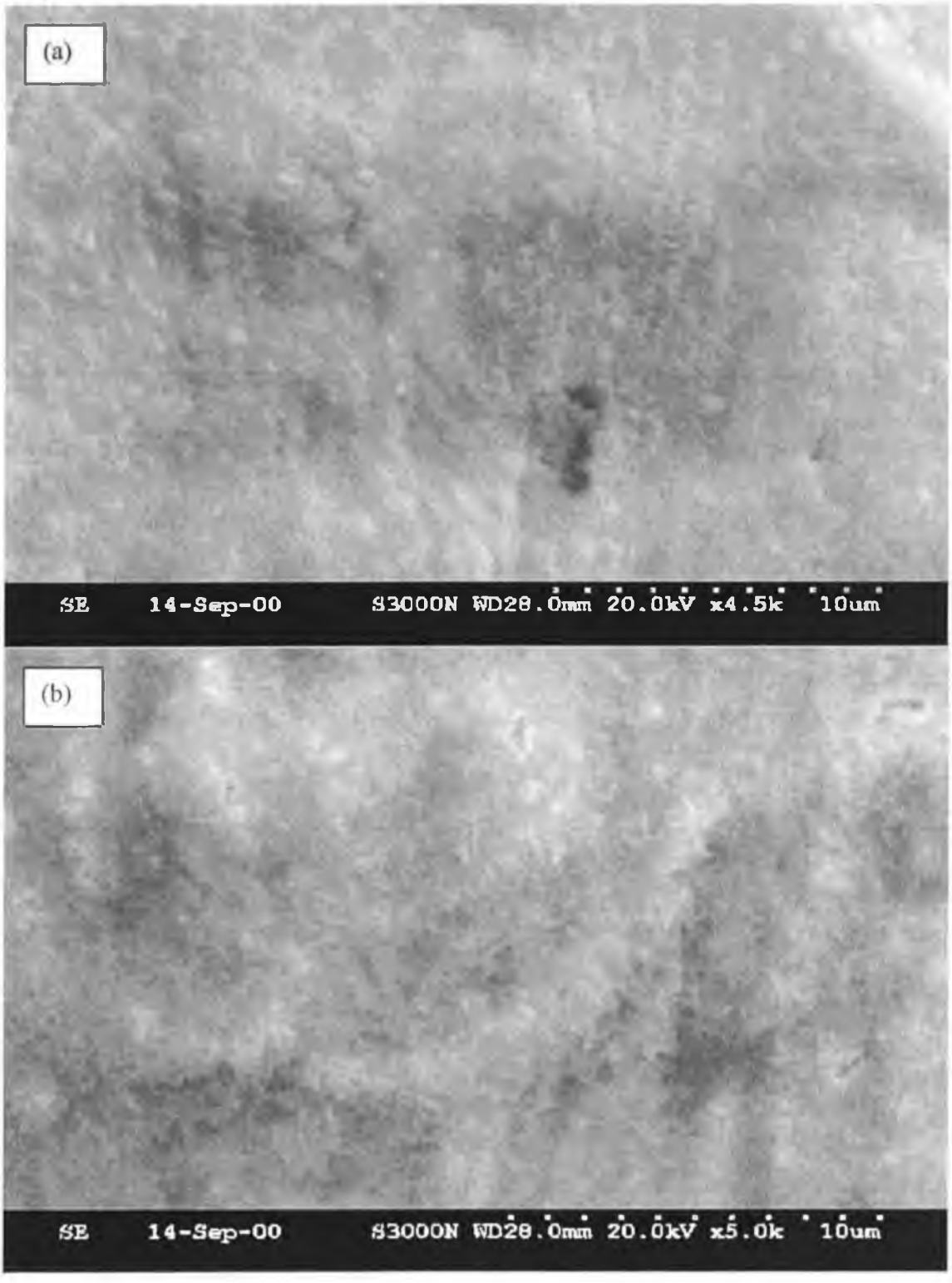

Fig. 3.11 (a) and (b) shows a photomicrograph of T_3^{900} taken at 4500 and 5000 × magnification of a cleaned gauze oxidised for 3 hour at $900^{O}C$.

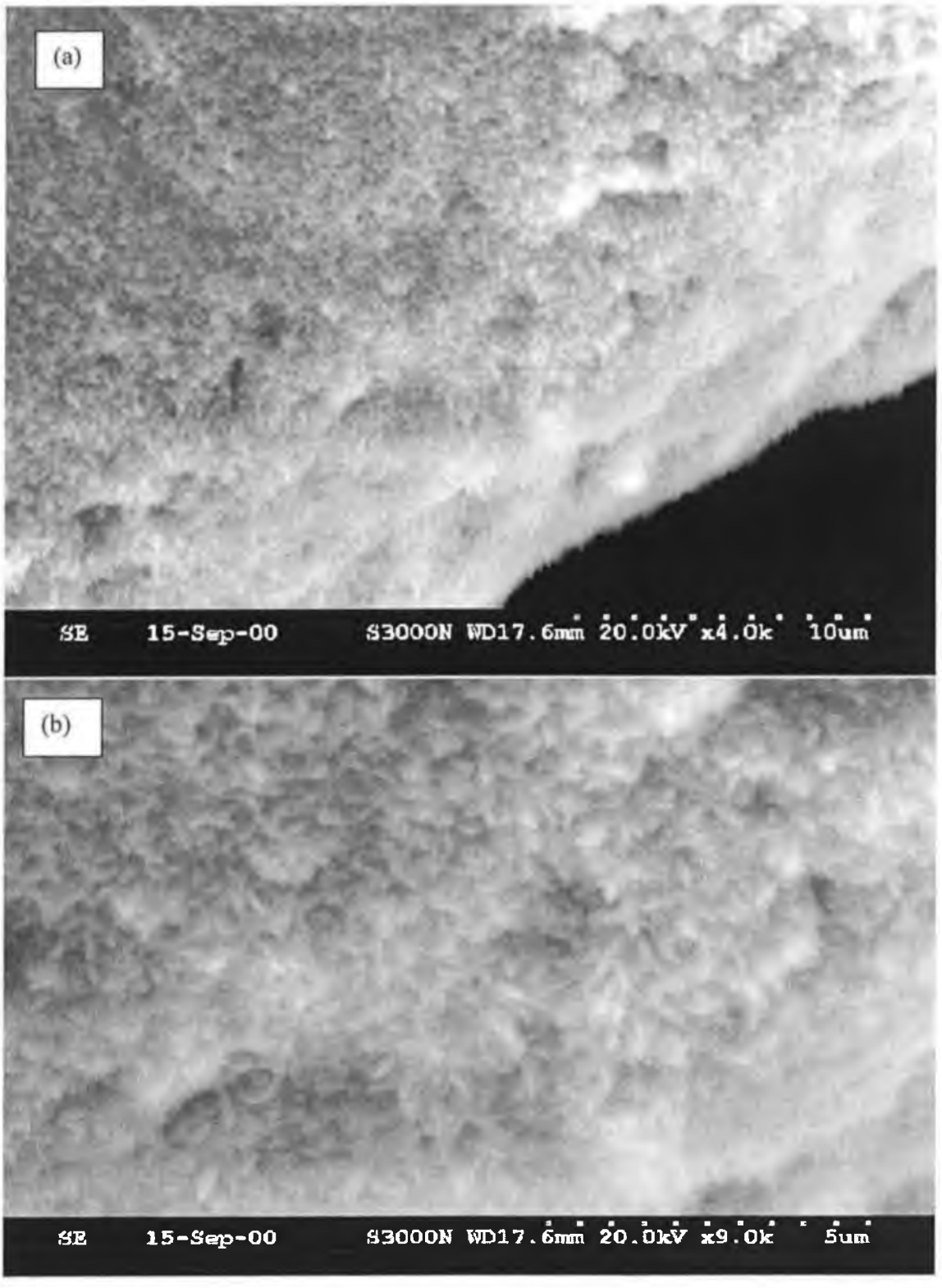

Fig. 3.12 (a) and (b) shows a photomicrograph of T_4^{900} taken at 4000 and 9000 × magnification of a cleaned gauze oxidised for 4 hour at $900^{O}C$.

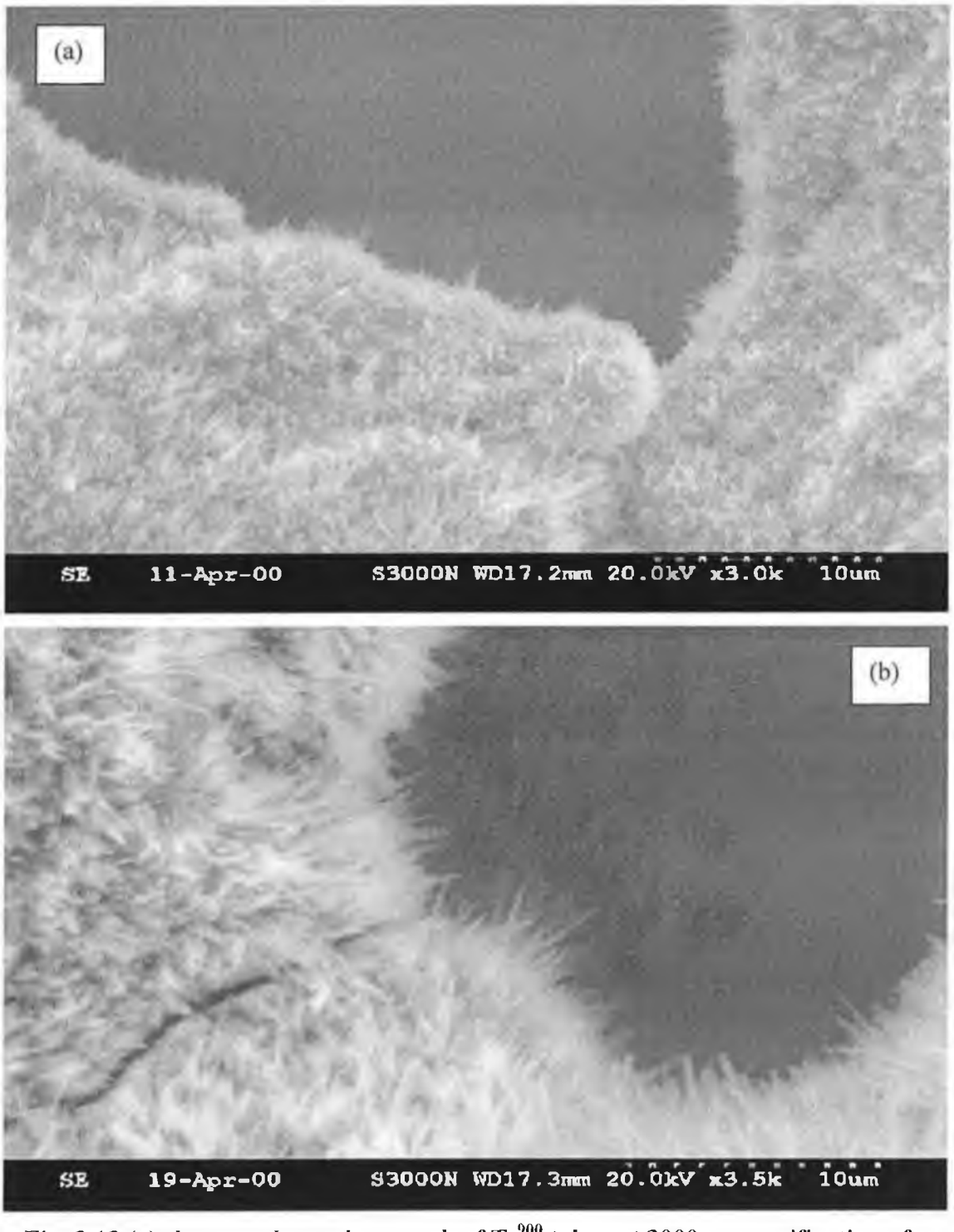

Fig. 3.13 (a) shows a photomicrograph of T_8^{900} taken at 3000 × magnification of a cleaned gauze oxidised for 8 hour at 900^{O}C, while Fig 3.13 (b) shows a photomicrograph of T_{16}^{900} taken at 3500× magnification for a gauze whiskered for 16 hours at 900^{O}C.

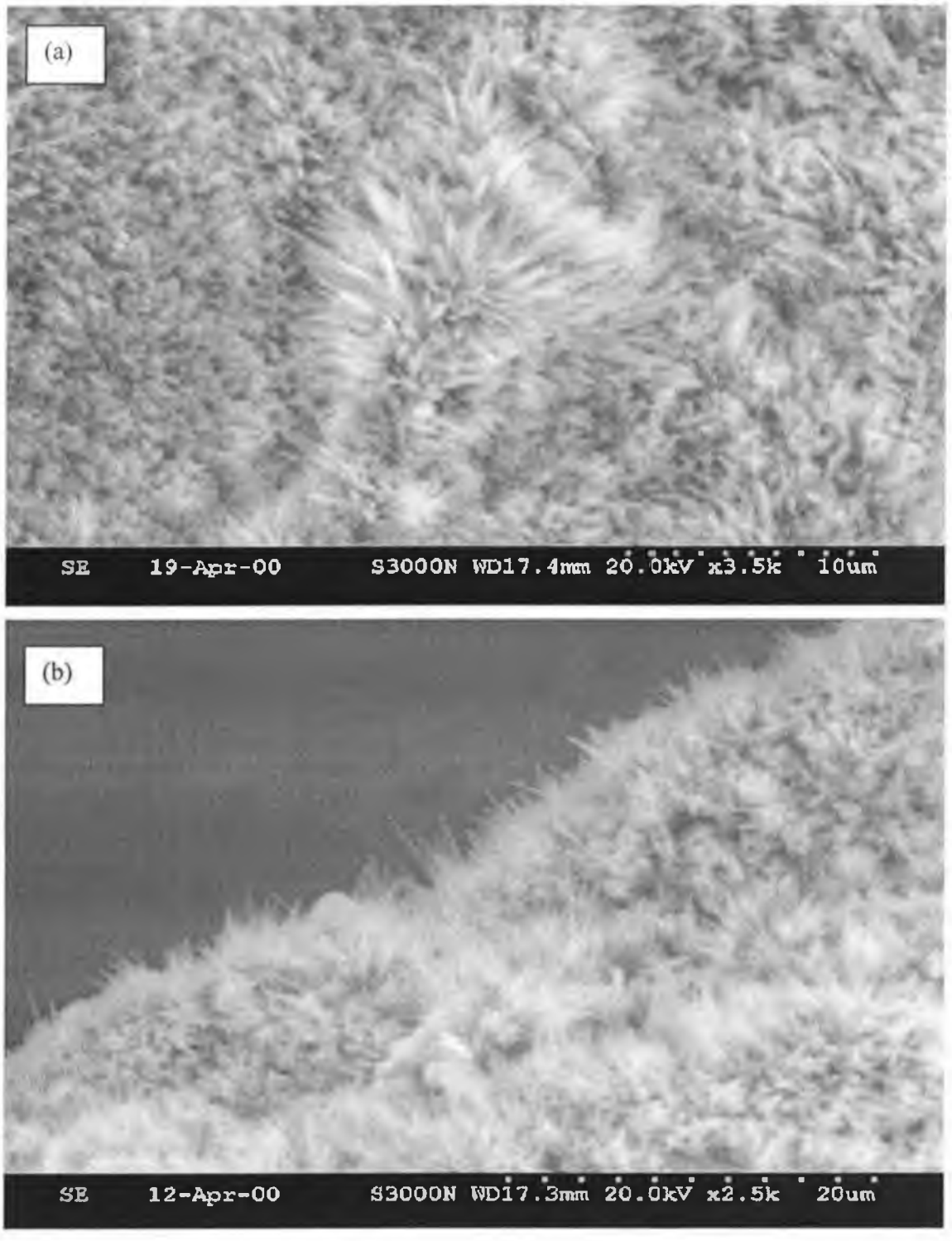

Fig. 3.14 (a) shows a photomicrograph of T_{16}^{900} taken at 3500 × magnification of a cleaned gauze oxidised for 16 hour at 900^{O}C, while Fig 3.14 (b) shows a photomicrograph of T_{24}^{900} taken at 2500 × magnifications for a gauze whiskered for 24 hours at 900^{O}C.

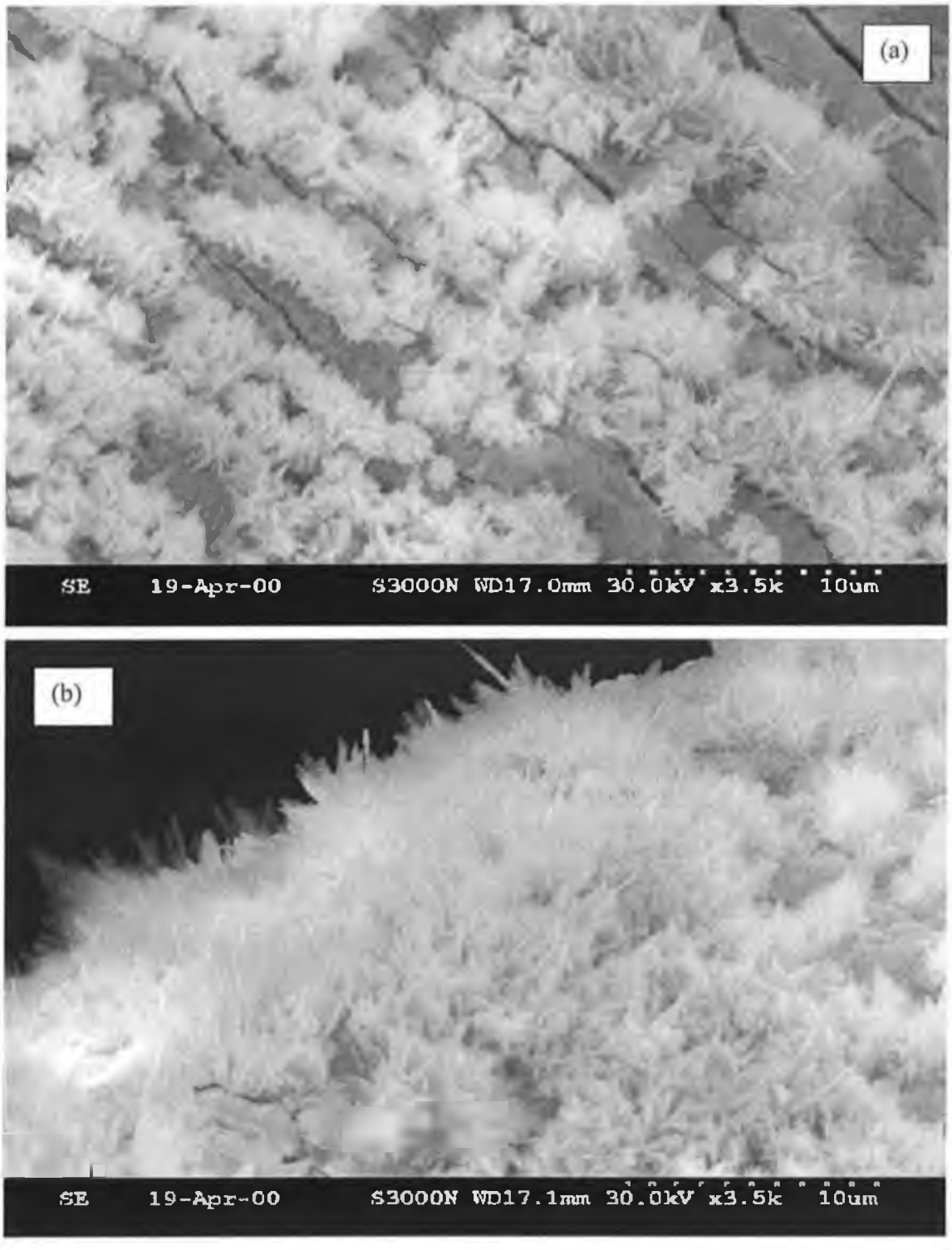

Fig. 3.15 (a) and (b) shows a photomicrograph of T_{32}^{900} for different regions of the whiskered gauze taken at 3500 × magnification of an cleaned gauze oxidised for 32 hours at $900^{O}C$.

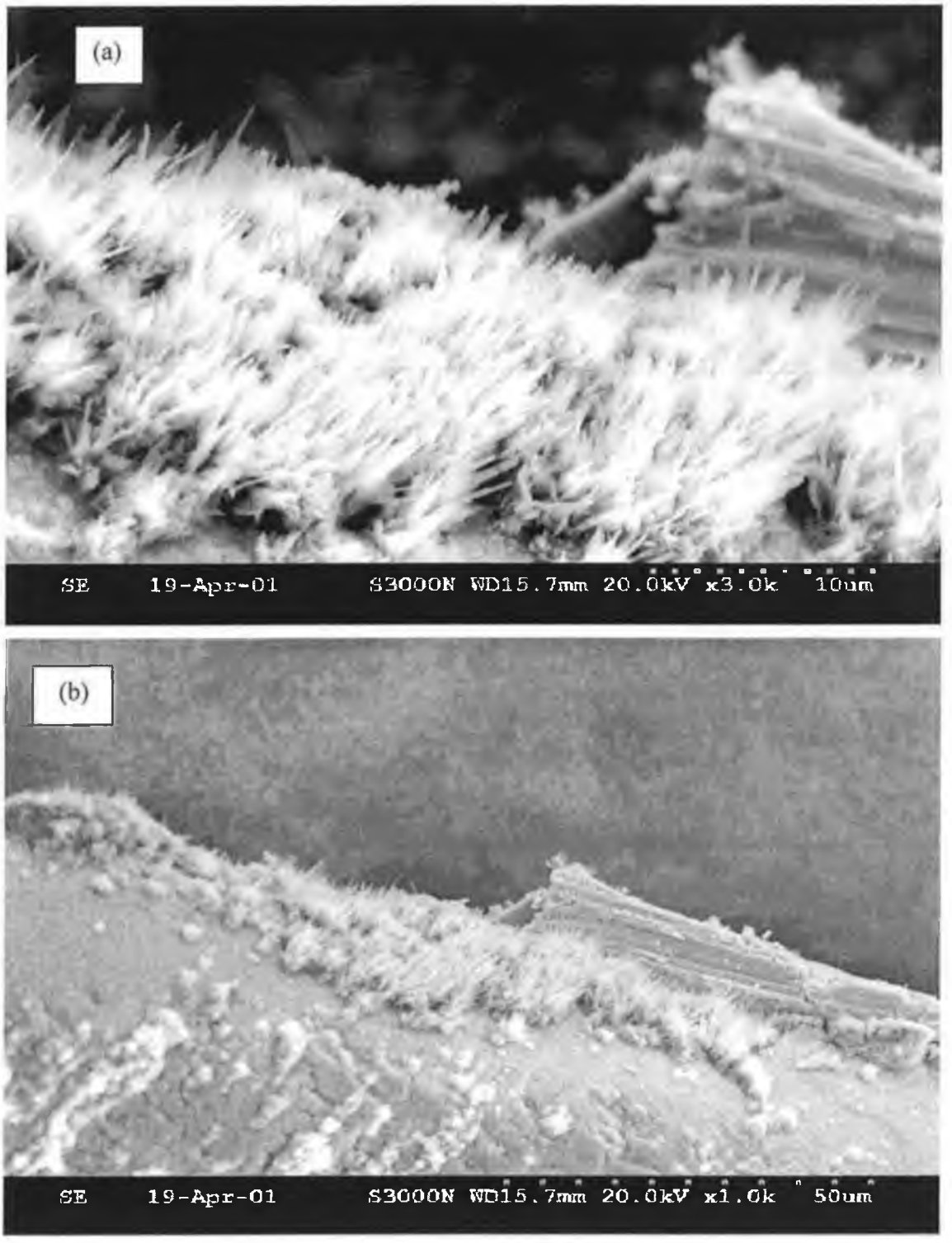

Fig. 3.16 (a) and (b) shows a photomicrograph of T_{64}^{900} for a whiskered gauze taken at 3000 and 1000 × magnification of a cleaned gauze oxidised for 64 hours at $900^{O}C$.

A series of whiskered gauze samples as described in experimental see Table 3.2 using an accelerated method are shown in electron micrographs Figures 3.17-3.21.

Figure 3.17(a) + (b) T_8^* shows electron micrographs of a gauze sample imaged at the center and edge regions, Figure 3.17(a), a low magnification micrograph, comprises of a oxide layer with well-developed mature high aspect ratio whiskers substantially covering the gauze surface. The high magnification image in Figure 3.17(b) shows predominantly mature high aspect ratio whisker growth with one or two occasional nodules of whiskers randomly oriented on the surface and directed towards the center regions of the gauze. Figures 3.18(a) show a low magnification electron micrograph of a whiskered sample treated at 875^{0}C for ½ hr, followed by 960^{0}C for 15½. The resulting oxide consists of predominantly well-developed mature high aspect ratio whiskers, which are in abundance and substantially cover the gauze surface. Figure 3.18(b) shows a higher magnification micrograph of the same region. Figure 3.19(a) and (b) illustrates an electron micrograph of a sample whiskered over 15½ hours using an accelerated method, the oxide layer displayed a surplus of high aspect ratio whiskers substantially covering the surface.

For the purpose of comparison, a single temperature oxidation treatment as in Figure 3.13(a), sample T_8^{900} and (b), sample T_{16}^{900} were compared with an accelerated method Figure 3.18(a) + (b), sample T_{16}^*. Comparable whisker growth was observed from Figure 3.18(a) + (b) for the accelerated method with that for a single temperature oxidation treatment. The micrograph of sample $T_{6¼}^{900}$ in Figure 3.20(a) whiskered under a range of temperature for 6¼hrs (i.e. 915-960^{O}C) showed strong dense whisker growth, comprising of mature high aspect ratio whiskers heavily colonizing the gauze surface. The formation of such an oxide structure may be attributed to the shorter time period used to initiate whisker growth, followed by increasing the temperature to facilitate accelerated whisker growth. Vaneman et al. [5, 6] reported that whisker growth could be initiated by heating in an air atmosphere for a shorter period insufficient to form mature whiskers, typically less than 2 hours and preferably less than 15 minutes, followed by increasing the temperature to 960-990^{O}C to continue growth at an accelerated rate. Another electron micrograph of gauze sample $T_{3¾}^{900}$ whiskered using an accelerated method is illustrated

in Figure 3.21(a) + (b), showing mature whiskers formed to the edge of the gauze surface, whereas poor whisker formation with slightly flatter whiskers growth (i.e. lumps or knots) is observed in Fig. 3.21 (b). The flatter oxide whisker formation may be due to formation of alpha alumina at the higher whiskering temperatures, which as mentioned previously is unsuitable for whisker formation and/or the alloy composition. Vaneman et al. [5, 6] found the formation of alpha alumina to be unsuitable for forming whiskers. They also found that the particular uppermost whisker growing temperature might be sensitive to alloy composition. For example, they found a typical commercial cerium-containing alloy was covered with whiskers after treatment at temperatures up to $960^{O}C$, but few scattered whisker growth occurred when heated to temperatures greater than $960^{O}C$.

Figures 3.22(a) + (b) and 3.23(a) + (b) show electron micrographs of gauze samples whiskered under flowing N_2 atmosphere. Figures 3.22(a) and (b) displayed an unoxidised surface with no whiskers formation even after whiskering for 2 hours. This is in marked contrast to the 2-hour sample whiskered in static air atmosphere, which consisted of predominantly nodules scattered throughout the surface. An electron micrograph in Figure 3.23(a) for the gauze sample whiskered after 4 hours in a N_2 atmosphere reveals a structure analogous to the 2-hour sample whiskered in static air. It was found only after 6 hours in flowing N_2 that immature whisker growth occurred. This was most likely due to the inert atmosphere, which prevents the whisker maturation process. Chapman et al [3, 4] found high aspect whiskers were grown on Fe-Cr-Al foils by initially heating in an inert atmosphere for short time periods. Thereafter, the foil was subjected to an air atmosphere to continue whisker growth. After this treatment, they found a substantially covered foil surface with mature high aspect ratio whiskers. Vaneman et al. [5] also reported heating in a low oxygen atmosphere initiated whisker formation. While in another study, Vaneman et al. [6] found that pre-treatment in a vacuum comprising of low residual oxygen or in nitrogen atmosphere containing a controlled oxygen addition, produced consistent whisker growth. Therefore, further work is required to investigate the effects of whiskering for short time periods in an inert atmosphere and continuing whiskering in an air atmosphere. The use of an accelerated method showed some good

whisker formation in a shorter time period. However, more experimental work on methods for accelerated whiskering is required. From the work to date, whiskering at 900^0C for 16 to 24 hours in a single oxidation treatment were found to produce the high aspect whiskers substantially covering the gauze surface, which were suitable for adhesion of a washcoat support.

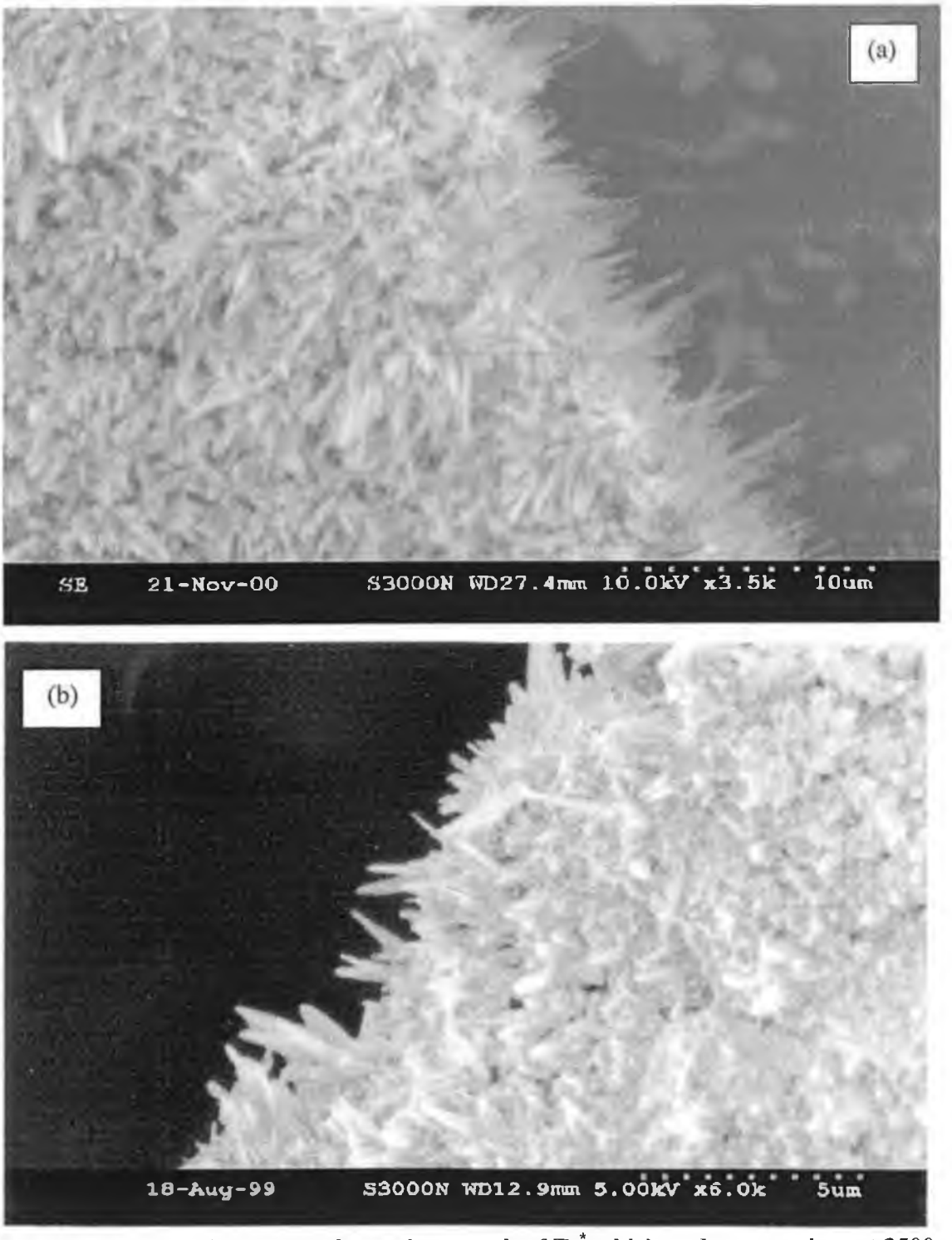

Fig. 3.17 (a) and (b) shows a photomicrograph of T_8^* whiskered gauze taken at 3500 and 6000 × magnification of a cleaned gauze, oxidised at 925^0C for ½hr followed by 960^0C for 7½hr.

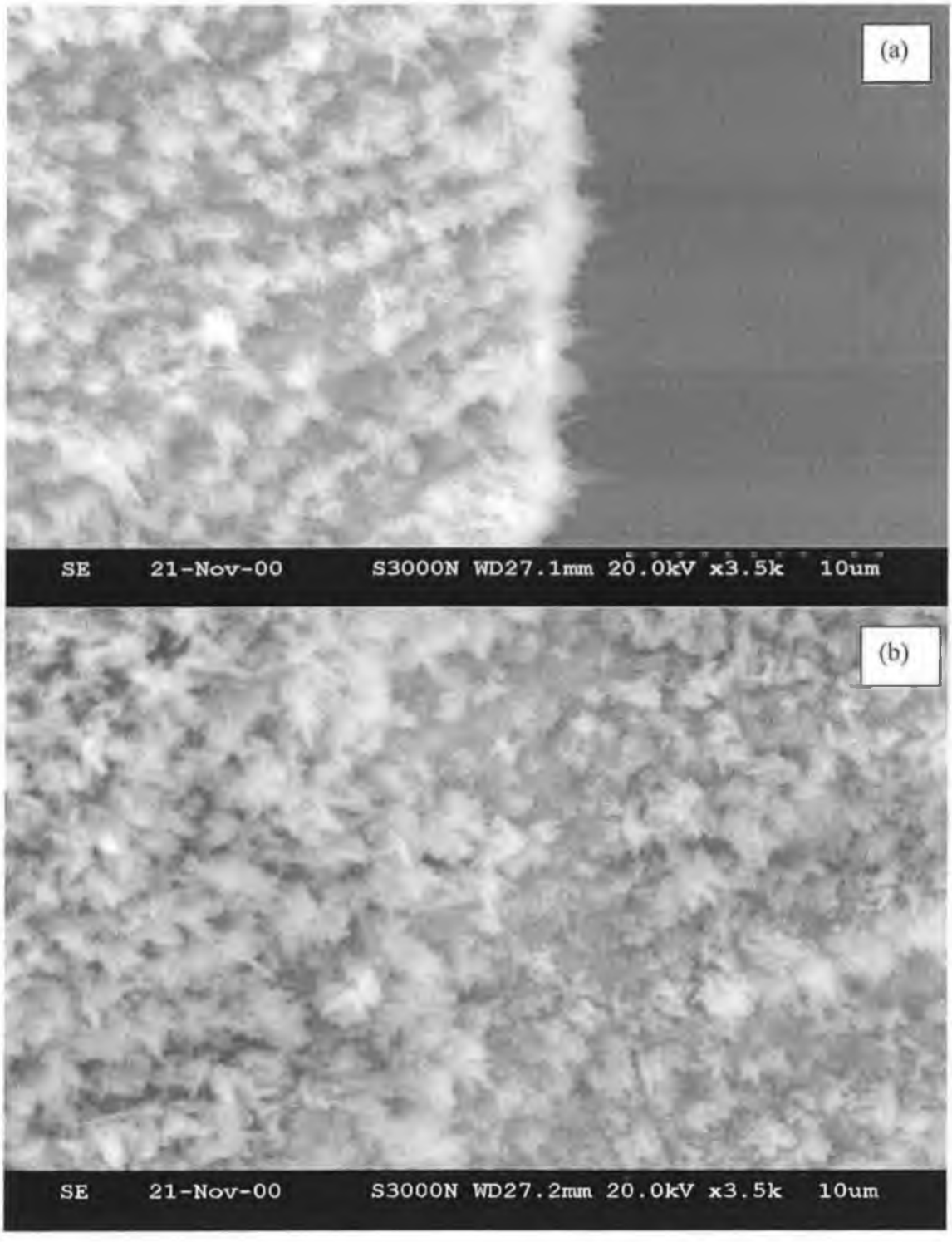

Fig. 3.18 (a) and (b) shows a photomicrograph of T_{16}^{*} whiskered gauze taken at 3500 × magnification of a cleaned gauze oxidised at 875^{O}C for ½hr followed by 960^{0}C for 15½hr.

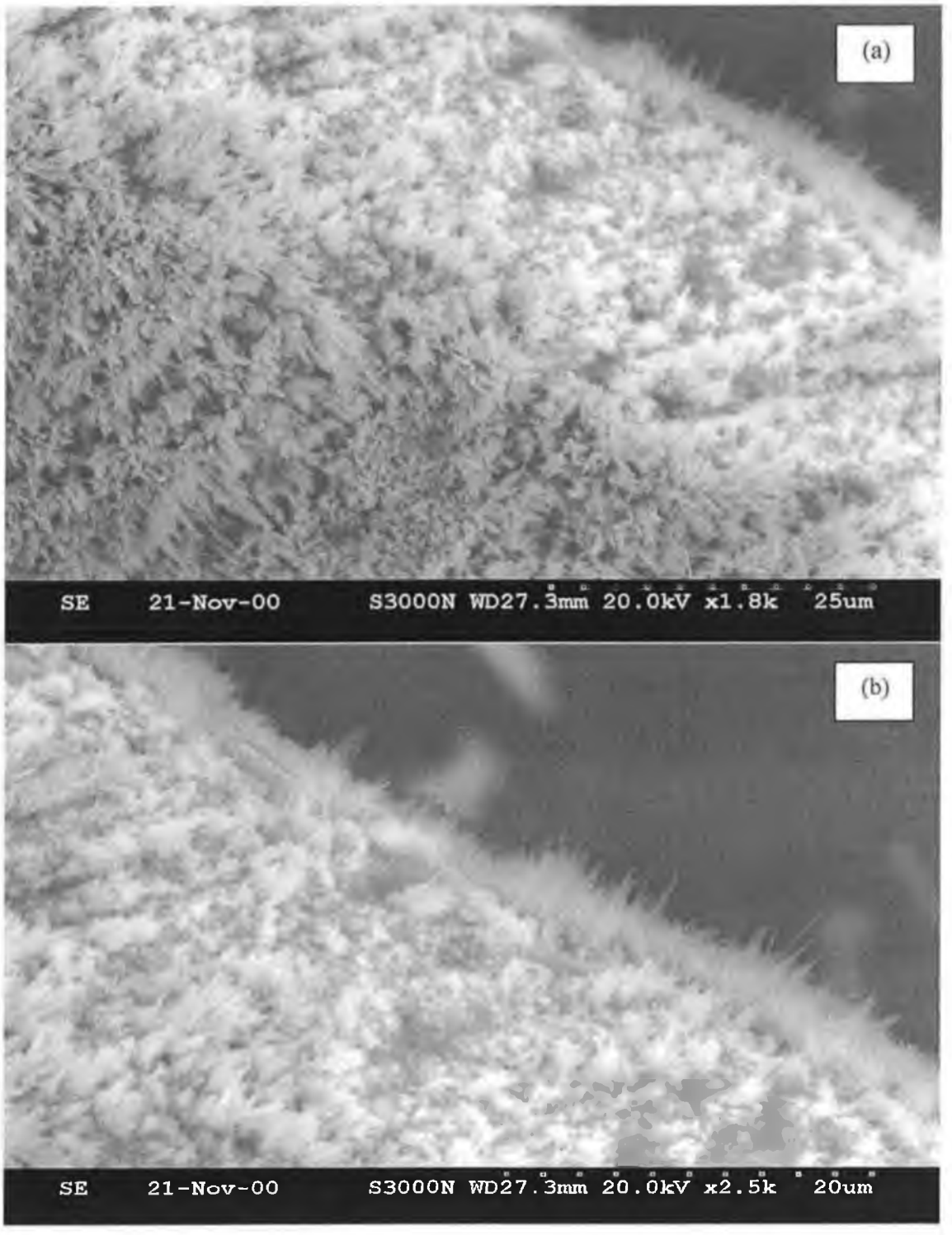

Fig. 3.19 (a) and (b) shows a photomicrograph of $T_{15\frac{1}{2}}^{*}$ whiskered gauze taken at 1800 and 2500 × magnification of a cleaned gauze oxidised at 900^{0}C for ¼ hr, followed by 940^{O}C for 15¼hr.

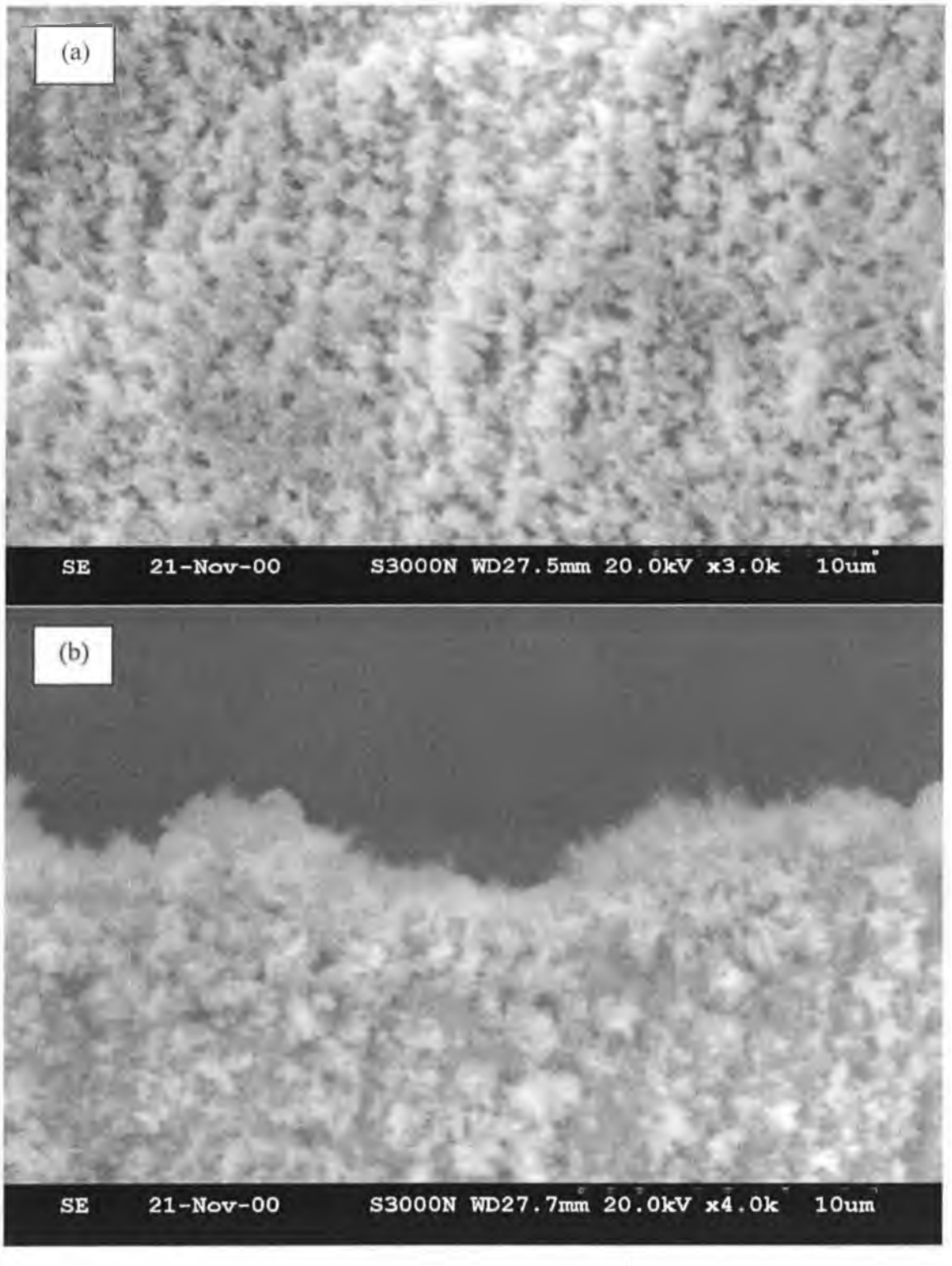

Fig. 3.20 (a) and (b) shows a photomicrograph of $T_{6¼}^{*}$ whiskered gauze taken at 3000 and 4000 × magnification of a clean gauze oxidised at 915^{0}C for ¼ hr, 940^{0}C for 2hr and 960^{O}C for 4hr.

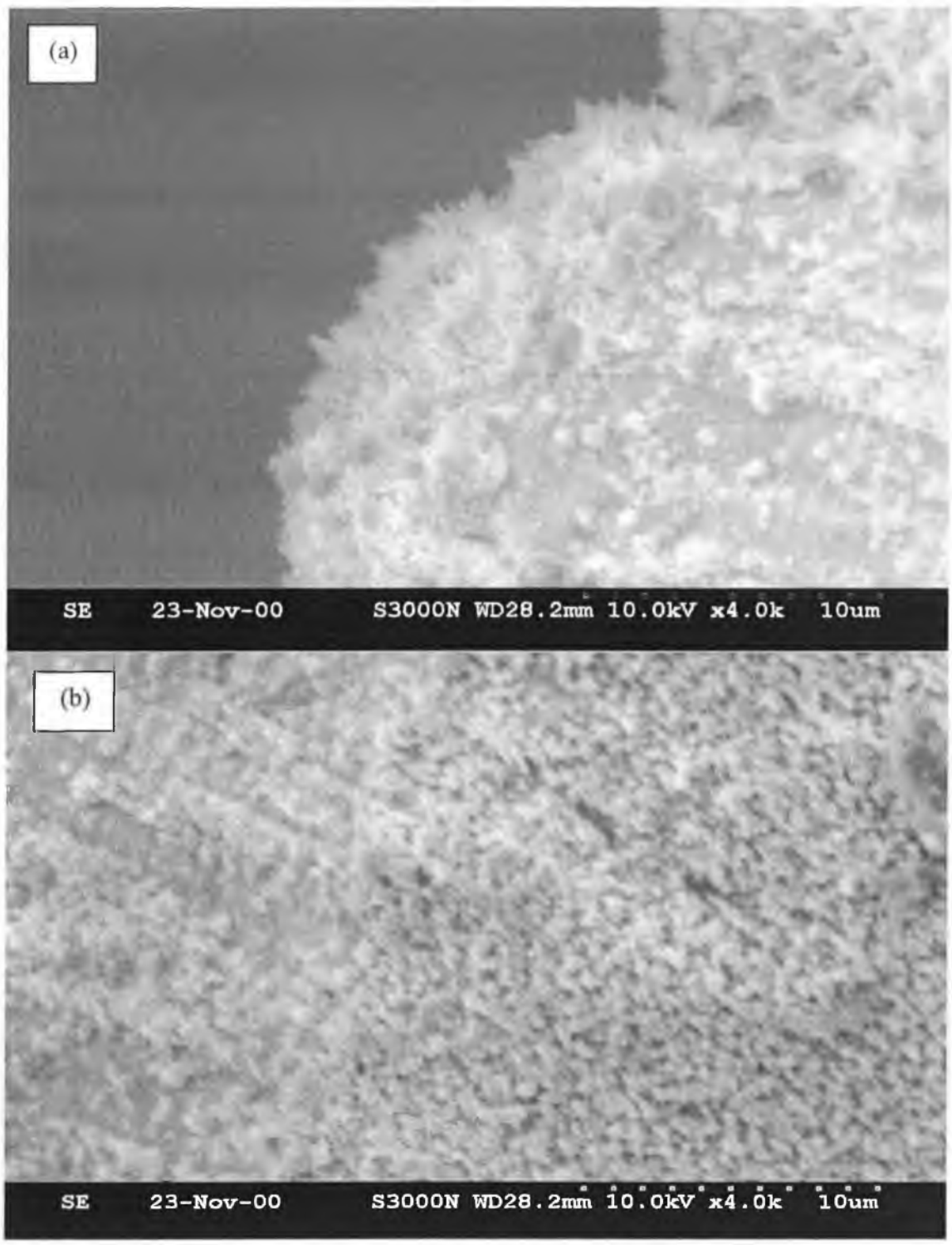

Fig. 3.21 (a) and (b) shows a photomicrograph of $T_{3¼}$ whiskered gauze taken at 4000× magnification of a cleaned gauze oxidised at 925^0C for ¾hr, 960^0C for 1hr and 990^0C for 2hr.

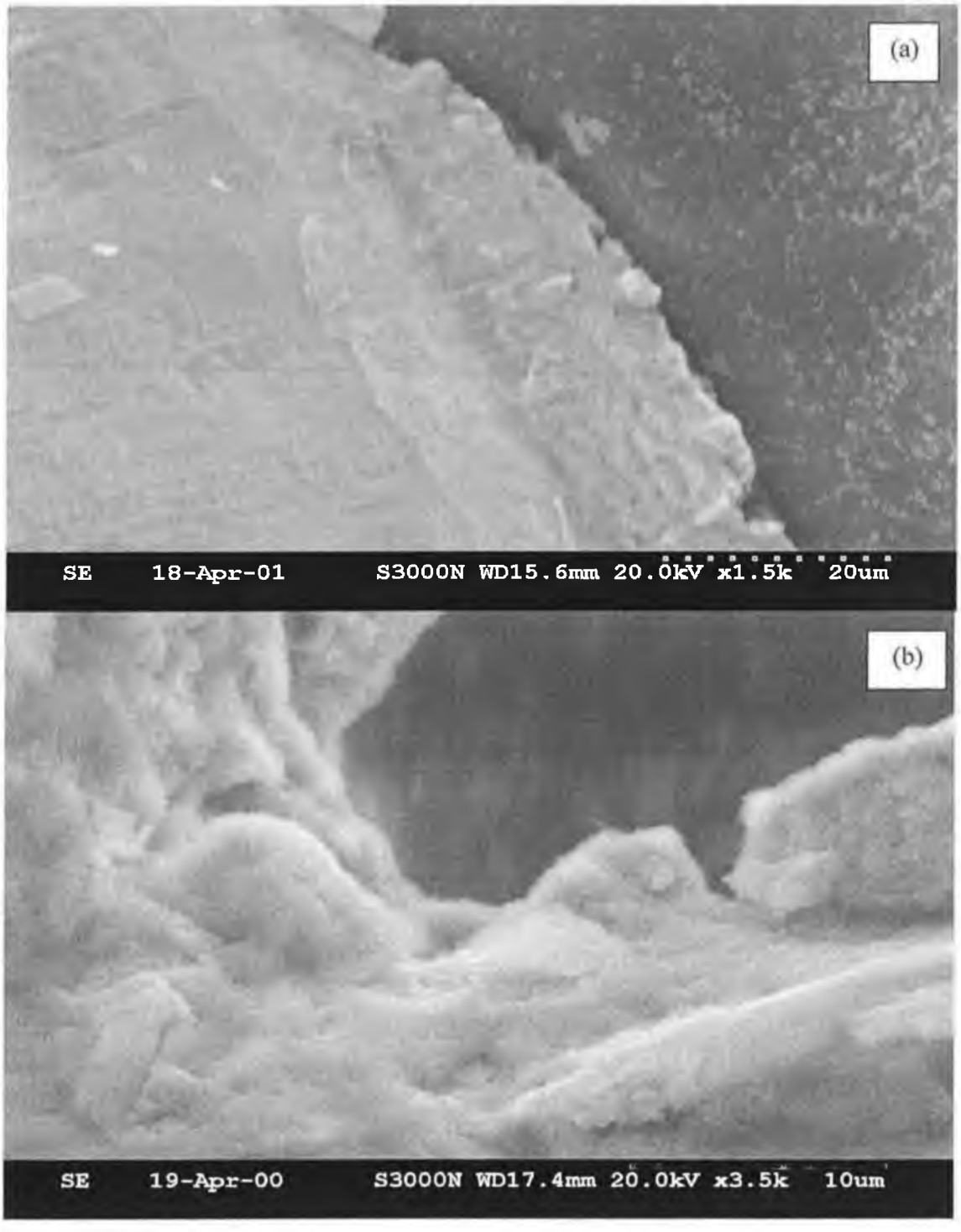

Fig. 3.22 (a) shows surface morphologies of $*T_1^{900}N$ gauze taken at 1500× magnification of a cleaned gauze heated for 1 hour,
(b) $*T_2^{900}N$ heated for 2hours at $900^{O}C$ under flowing N_2 atmosphere.

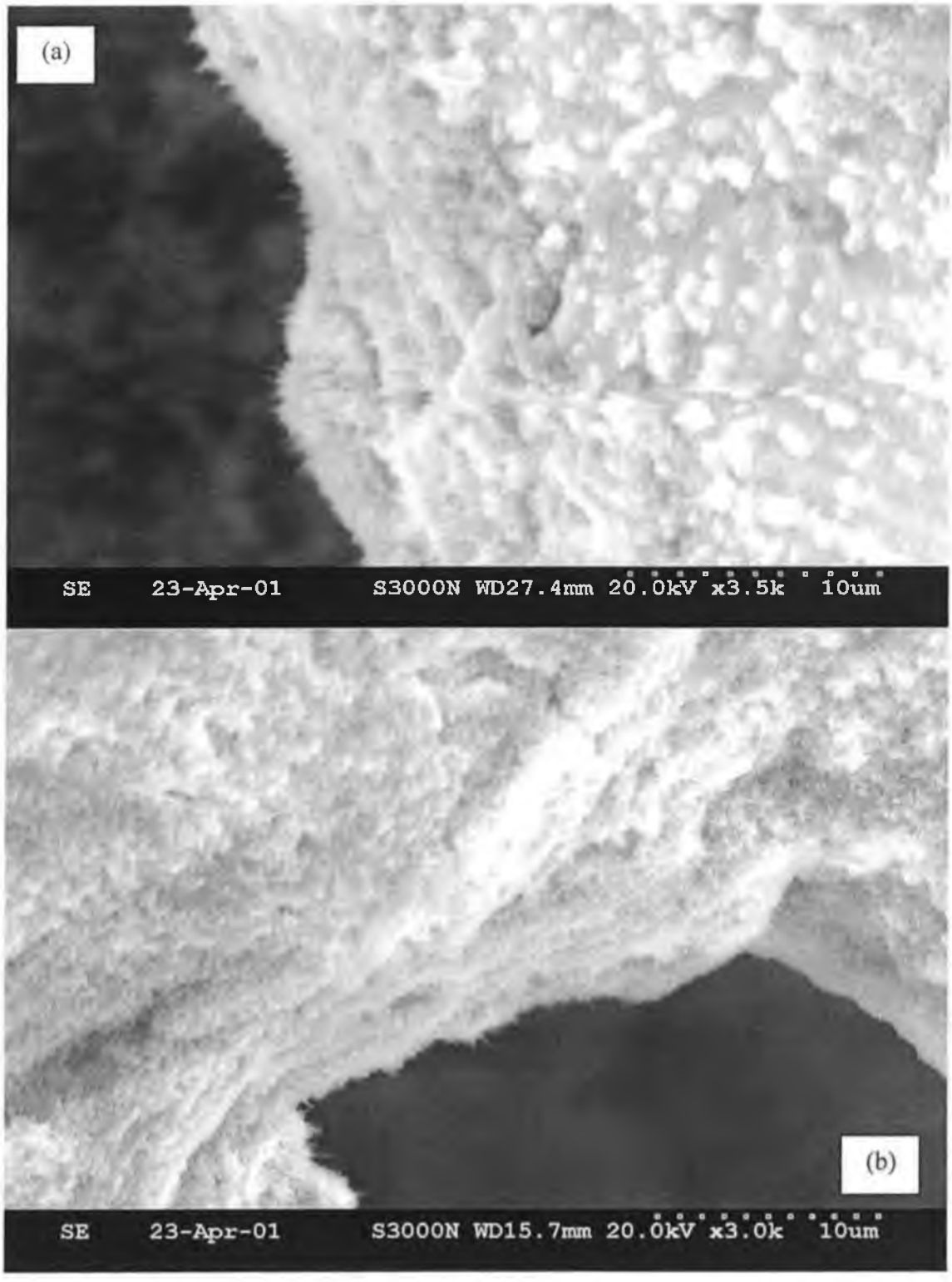

Fig. 3.23 shows surface morphologies of whiskered gauze taken at 1500× magnification of a cleaned gauze (a) $*T_4^{900}N$, (b) $*T_6^{900}N$ under flowing N_2 atmosphere.

3.3.2 Particle Size Distribution and its Effects on Surface Area

Particle size distribution measurements were preformed on 4 washcoating solutions prepared by ball milling and grinding for varying times. The variation in particle size distribution of alumina between ball milling and grinding was examined.

Figures 3.24-3.27 illustrates particle size distribution graphs for washcoat solutions with mean particle size measured in the range D (v, 0.1) to D (v, 0.9) (see Table 3.11), where D equals the characteristic diameter and v is the percentage volume of particles within a defined size range.

Table 3.11: Particle size distribution measurements of various washcoat solutions prepared.

Sample Code	Preparation	D (v, 0.1) μm	D (v, 0.5) μm	D (v, 0.9) μm
250A*	Ball-Milled 4hr	1.73	16.15	51.71
250A	Mortar&Pestle 5-6hr	2.15	26.10	74.39
140A[1]	Mortar&Pestle ½-¾hr	1.62	9.44	38.19
140A	Mortar&Pestle 5-6hr	2.09	21.36	53.05

Note v represents % volume underneath a particle size range.

Figures 3.24, 3.25 and 3.27 displayed bimodal particle size distribution after 4 hours ballmilling or mortar and pestle grinding for 5-6 hours. In contrast, Figure 3.26 illustrated a continuous particle size distribution for a washcoat solution prepared from inadequate grinding up to ¾hr. The varying shape of the particle size distribution from bimodal to continuous was thought to be attributed to the quantities of puralox powders and grinding times employed in the washcoat. It was observed that puralox SCFa-250 alone in the washcoat support with grinding times of 4-6hr, a bimodal distribution was obtained, whereas a continuous distribution was achieved with mixed proportions of SCFa-250 and SCFa-140 with grinding times of ½-¾hr. The bimodal distribution was characterised by a

high concentration of coarse particles, while a continuous distribution was characterised by higher concentration of fine particles. Ferreira et al. [7] and Taruta et al. [8] showed bimodal particle distributions for SiC and Al_2O_3 by combining both fine and coarse powders in an appropriate proportions and size ratio. Tari et al. found coarser alumina powders exhibited a bimodal distribution, while a finer powder was characterised by a continuous distribution [9]. Therefore, a bimodal distribution was found to form a closer packing arrangement in the washcoat solution, which may or may not lead to larger surface areas.

The surface areas were also found to be largely dependent on the powders used and this will be discussed later in more detail. Agrafiotis et al. [10] examined the effects ball milling on particle size distribution and reported formation of fine, uniform particle size distribution with particle sizes less than 2μm on milling $Al(OH)_3$ for 312 hours. In contrast, an γ–AlOOH sample and a sol gel sample ball milled for 24 hours produced larger agglomerates with particle sizes of 1-5μm. They examined the impact on surface area in comparison to a commercially available γ–Al_2O_3 sample after calcinations at 600^{O}C and 800^{O}C and established that the powders from the precursor materials with particle sizes in the nanometer-size showed high surface areas. They also concluded that the smaller the particle sizes the better the adhesion of the washcoat solution to the substrate support.

The average percentage volume of particle sizes measured for the 140A^{I} washcoat were lower in contrast to the ballmilled 250A washcoat and the ground washcoat solutions of 250A and 140A. This was unexpected, but was thought to be attributed to the properties of the two different grade alumina powders (i.e. Puralox) used and the grinding time employed. However, it should also be noted the 140A samples have a larger particle size than the 250A samples. This was attributed again to the different grade activated alumina employed in the washcoat mixture.

Result Statistics

Distribution Type: Volume	Concentration = 0.0034 %Vol	Density = 1.000 g / cub cm	Specific S.A. = 1.3291 sq. m / g
Mean Diameters:	D (v, 0.1) = 1.73 um	D (v, 0.5) = 16.15 um	D (v, 0.9) = 51.71 um
D [4, 3] = 21.89 um	D [3, 2] = 4.51 um	Span = 3.095E+00	Uniformity = 1.011E+00

Size (um)	Volume Under %	Size (um)	Volume Under %	Size (um)	Volume Under %	Size (um)	Volume Under %
0.227	0.06	1.17	5.42	6.01	31.97	30.92	70.73
0.258	0.12	1.33	6.68	6.82	34.06	35.07	75.77
0.292	0.21	1.50	8.16	7.74	36.11	39.78	80.75
0.332	0.34	1.71	9.80	8.77	38.16	45.12	85.45
0.376	0.51	1.93	11.57	9.95	40.26	51.18	89.68
0.427	0.72	2.19	13.60	11.29	42.48	58.05	93.25
0.484	0.99	2.49	15.81	12.80	44.88	65.85	96.04
0.549	1.32	2.82	18.11	14.52	47.53	74.69	98.02
0.623	1.72	3.20	20.48	16.47	50.49	84.71	99.23
0.706	2.19	3.63	22.86	18.68	53.79	96.09	99.87
0.801	2.78	4.12	25.25	21.19	57.47	109.0	100.00
0.909	3.50	4.67	27.56	24.04	61.53		
1.03	4.38	5.30	29.80	27.26	65.96		

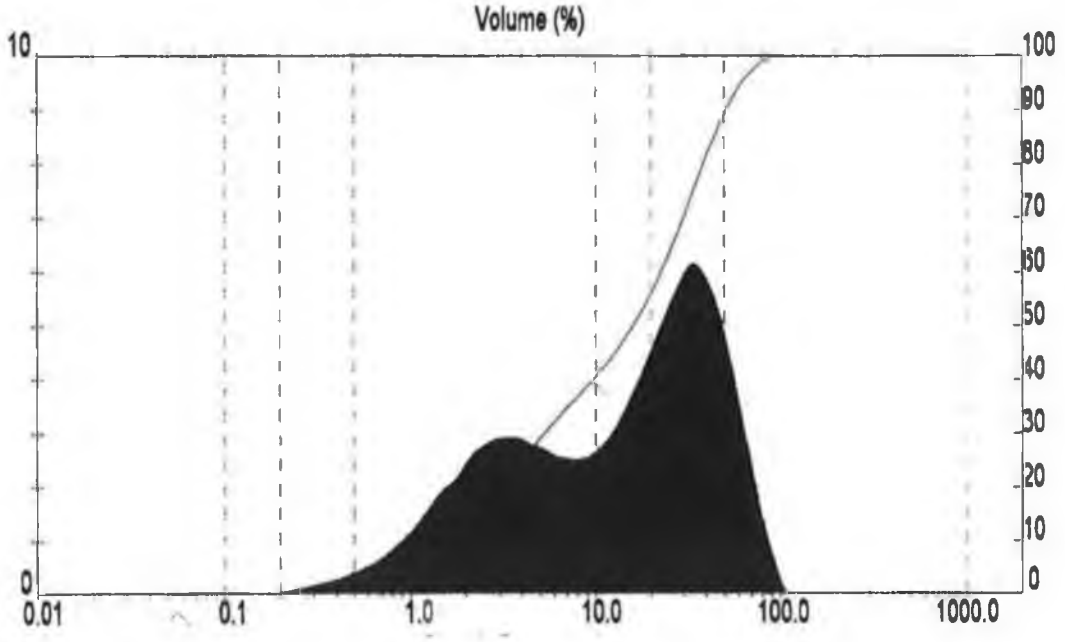

Figure 3.24: Particle size distribution measurement of a 250A* washcoat solution.

Result Statistics

Distribution Type: Volume	Concentration = 0.0036 %Vol	Density = 1.000 g / cub. cm	Specific S.A. = 1.0762 sq. m / g
Mean Diameters:	D (v, 0.1) = 2.15 um	D (v, 0.5) = 26.10 um	D (v, 0.9) = 74.39 um
D [4, 3] = 32.61 um	D [3, 2] = 5.58 um	Span = 2.768E+00	Uniformity = 8.863E-01

Size (um)	Volume Under %	Size (um)	Volume Under %	Size (um)	Volume Under %	Size (um)	Volume Under %
0.229	0.09	1.27	5.20	7.02	25.27	38.91	64.59
0.261	0.16	1.45	6.23	8.01	26.99	44.39	70.17
0.298	0.26	1.65	7.37	9.14	28.73	50.64	75.86
0.339	0.41	1.88	8.60	10.42	30.55	57.76	81.28
0.387	0.59	2.15	9.99	11.89	32.48	65.90	86.16
0.442	0.81	2.45	11.52	13.56	34.60	75.17	90.30
0.504	1.10	2.79	13.13	15.47	36.96	85.76	93.71
0.575	1.44	3.19	14.82	17.65	39.64	97.83	96.40
0.656	1.84	3.63	16.55	20.14	42.70	111.6	98.33
0.748	2.32	4.15	18.32	22.97	46.19	127.3	99.60
0.853	2.89	4.73	20.08	26.21	50.13	145.2	100.00
0.974	3.55	5.39	21.83	29.90	54.54		
1.11	4.31	6.15	23.56	34.11	59.38		

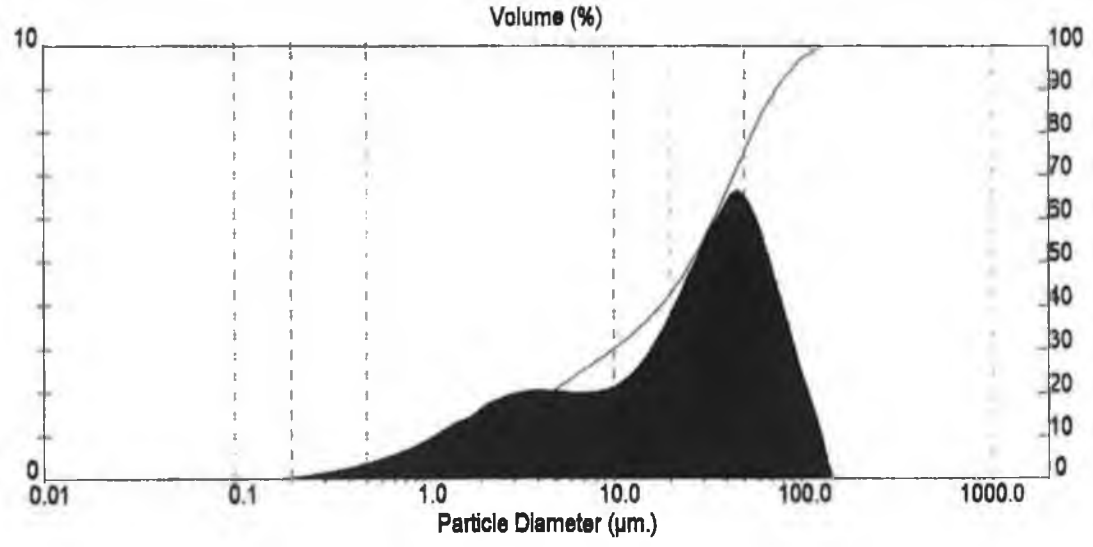

Figure 3.25: Particle size distribution measurement of a 250A washcoat solution.

Result Statistics

Distribution Type: Volume	Concentration = 0.0034 %Vol	Density = 1.000 g / cub. cm	Specific S.A. = 1.3934 sq. m / g
Mean Diameters:	D (v, 0.1) = 1.62 um	D (v, 0.5) = 9.44 um	D (v, 0.9) = 38.19 um
D [4, 3] = 15.29 um	D [3, 2] = 4.31 um	Span = 3.873E+00	Uniformity = 1.200E+00

Size (um)	Volume Under %	Size (um)	Volume Under %	Size (um)	Volume Under %	Size (um)	Volume Under %
0.510	0.13	2.00	13.37	7.84	45.22	30.75	84.11
0.567	0.37	2.22	15.43	8.71	47.92	34.16	87.08
0.630	0.71	2.47	17.61	9.68	50.65	37.94	89.84
0.700	1.17	2.74	19.88	10.75	53.43	42.15	92.34
0.777	1.77	3.05	22.22	11.94	56.27	46.82	94.53
0.863	2.51	3.38	24.61	13.27	59.17	52.00	96.37
0.959	3.39	3.76	27.07	14.74	62.12	57.77	97.82
1.07	4.40	4.18	29.60	16.37	65.15	64.17	98.88
1.18	5.57	4.64	32.14	18.18	68.23	71.28	99.65
1.31	6.90	5.15	34.71	20.20	71.39	79.18	99.94
1.46	8.39	5.72	37.31	22.43	74.60	87.95	100.00
1.62	9.97	6.36	39.92	24.92	77.82		
1.80	11.59	7.06	42.55	27.68	81.01		

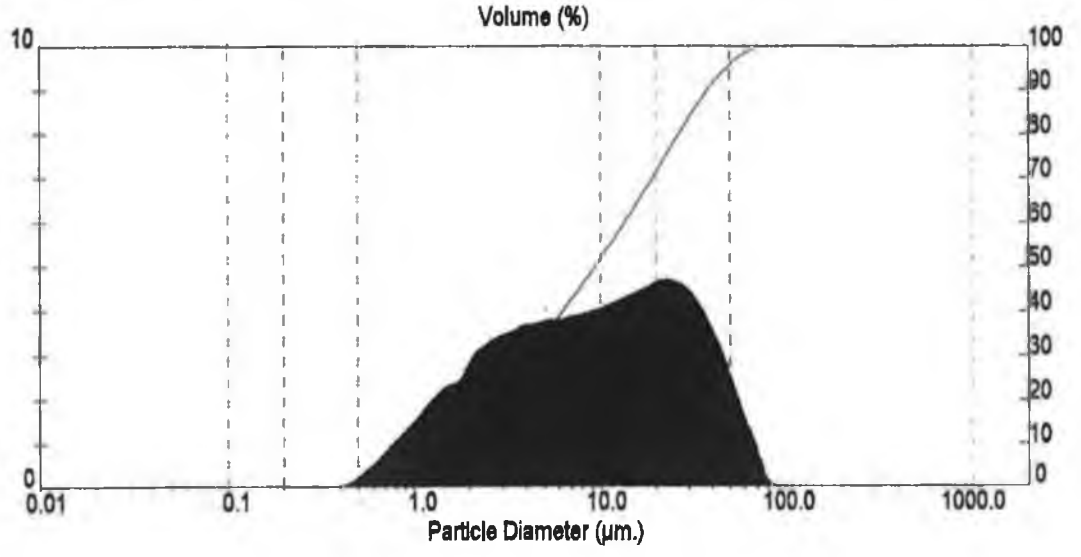

Figure 3.26: Particle size distribution measurement of a 140A[I] washcoat solution.

Result Statistics

Distribution Type: Volume	Concentration = 0.0045 %Vol	Density = 1.000 g / cub. cm	Specific S.A. = 1.0811 sq. m / g
Mean Diameters:	D (v, 0.1) = 2.09 um	D (v, 0.5) = 21.36 um	D (v, 0.9) = 53.05 um
D [4, 3] = 24.66 um	D [3, 2] = 5.55 um	Span = 2.386E+00	Uniformity = 7.547E-01

Size (um)	Volume Under %	Size (um)	Volume Under %	Size (um)	Volume Under %	Size (um)	Volume Under %
0.511	0.93	2.02	9.66	7.99	26.92	31.58	66.68
0.568	1.26	2.24	10.79	8.88	28.52	35.10	71.87
0.631	1.63	2.50	11.97	9.87	30.23	39.02	77.00
0.701	2.06	2.77	13.20	10.97	32.09	43.37	81.88
0.780	2.54	3.08	14.46	12.19	34.16	48.21	86.39
0.867	3.08	3.43	15.76	13.55	36.46	53.59	90.35
0.963	3.68	3.81	17.09	15.06	39.06	59.57	93.68
1.07	4.34	4.23	18.43	16.74	41.97	66.21	96.31
1.19	5.06	4.71	19.79	18.61	45.23	73.60	98.23
1.32	5.85	5.23	21.16	20.69	48.84	81.81	99.56
1.47	6.71	5.82	22.55	23.00	52.81	90.93	100.00
1.63	7.64	6.46	23.96	25.56	57.12		
1.82	8.62	7.19	25.41	28.41	61.74		

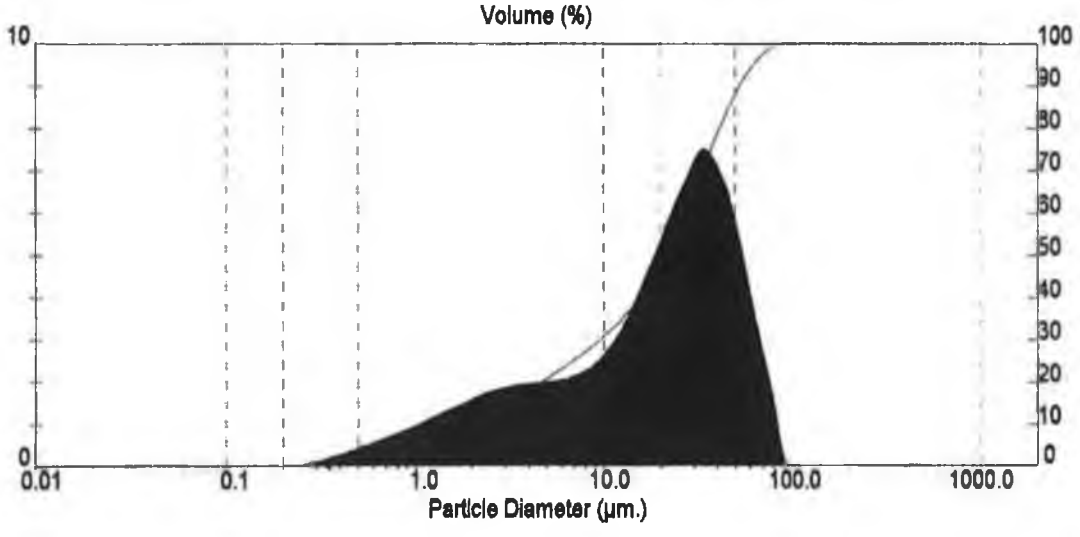

Figure 3.27: Particle size distribution measurement of a 140A washcoat solution.

3.3.3 XRD Analysis

The transition alumina phases present in the puralox powders (SCFa-250 and SCFa-140) were determined from x-ray diffraction spectra using CuKα source (λ = 1.5418 Å) and are shown in Figures 3.28 and 3.29. Fig. 3.30 illustrates the powdered XRD patterns for η-Al_2O_3, γ-Al_2O_3 and α-Al_2O_3 obtained from the powder diffraction library files [11]. From visual comparison between the powder diffraction pattern of the phase aluminas and the XRD spectra taken of the two-puralox powders, they were no visual differences in the peak position between the γ–Al_2O_3 and the XRD spectra for the puralox powders. On overlapping the two spectra the location of the peaks were also shown to be identically positioned. Therefore, the X-ray diffraction patterns in Fig. 3.28 and 3.29 revealed the presences of γ–Al_2O_3 phase in both the SCFa-250 and SCFa-140 puralox powders.

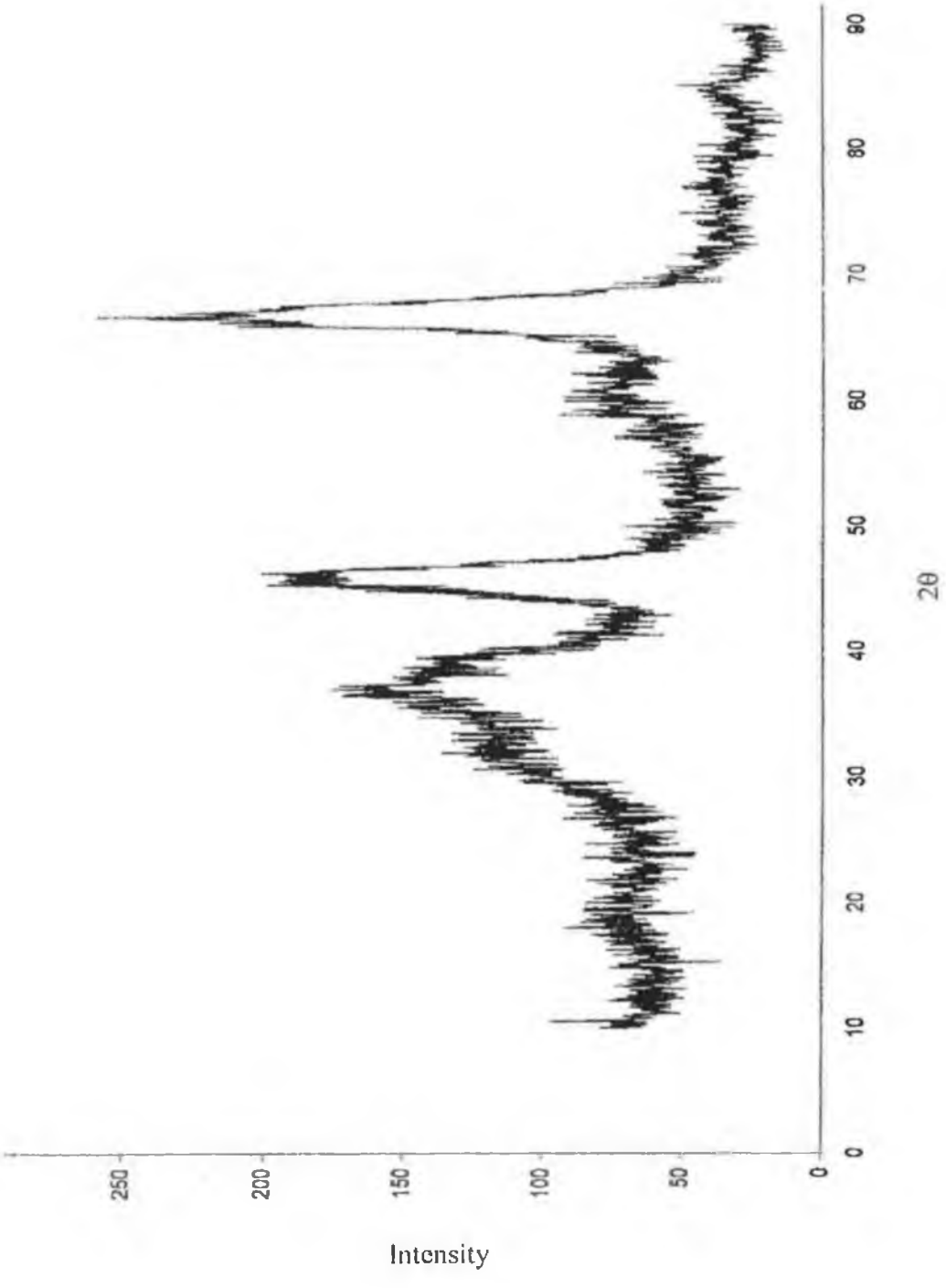

Figure 3.28: Represent the X-ray powder diffraction spectra for a fresh alumina powder (Puralox SCFa-250).

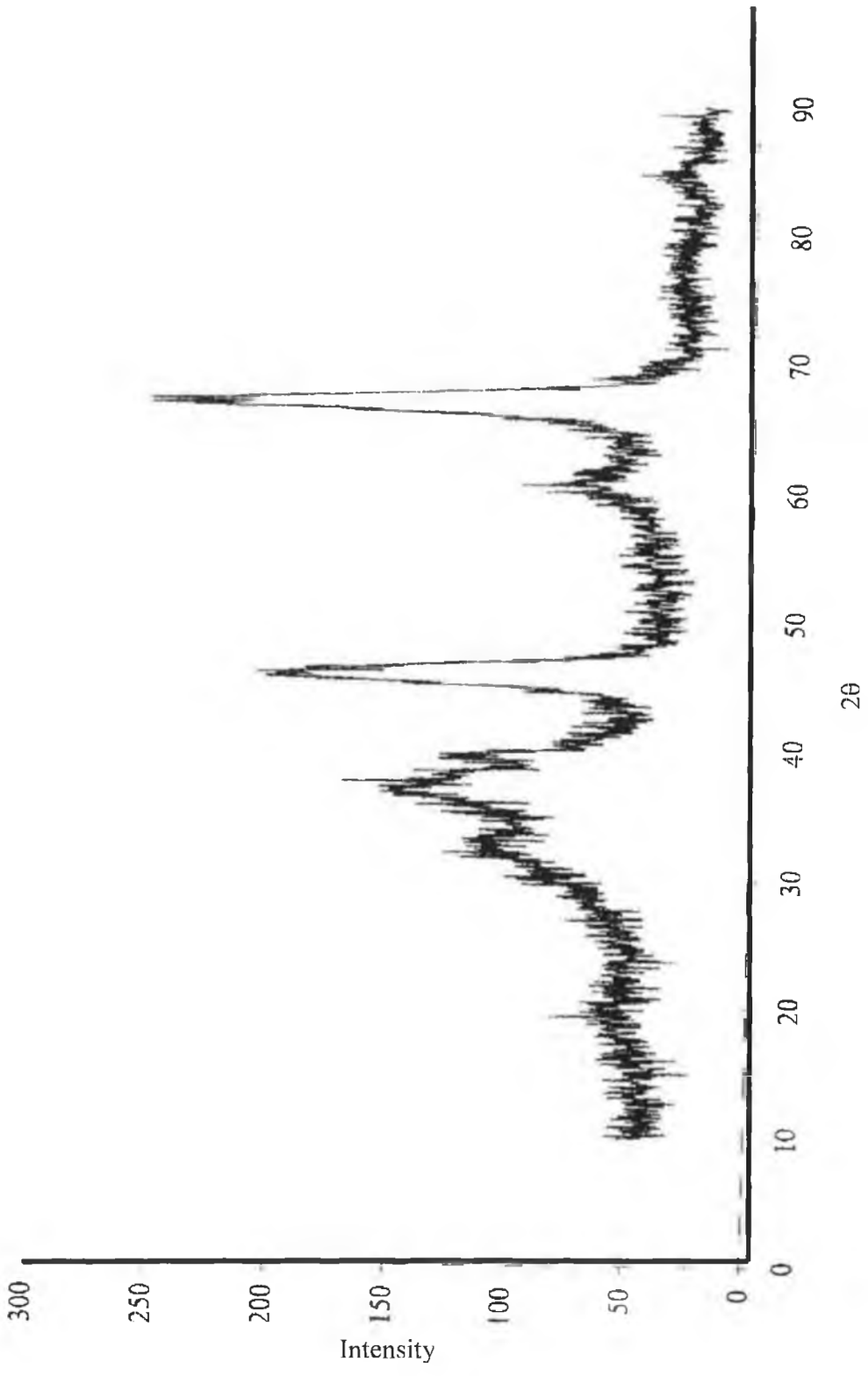

Figure 3.29: Represent the X-ray powder diffraction spectra for a fresh alumina powder (Puralox SCFa-140).

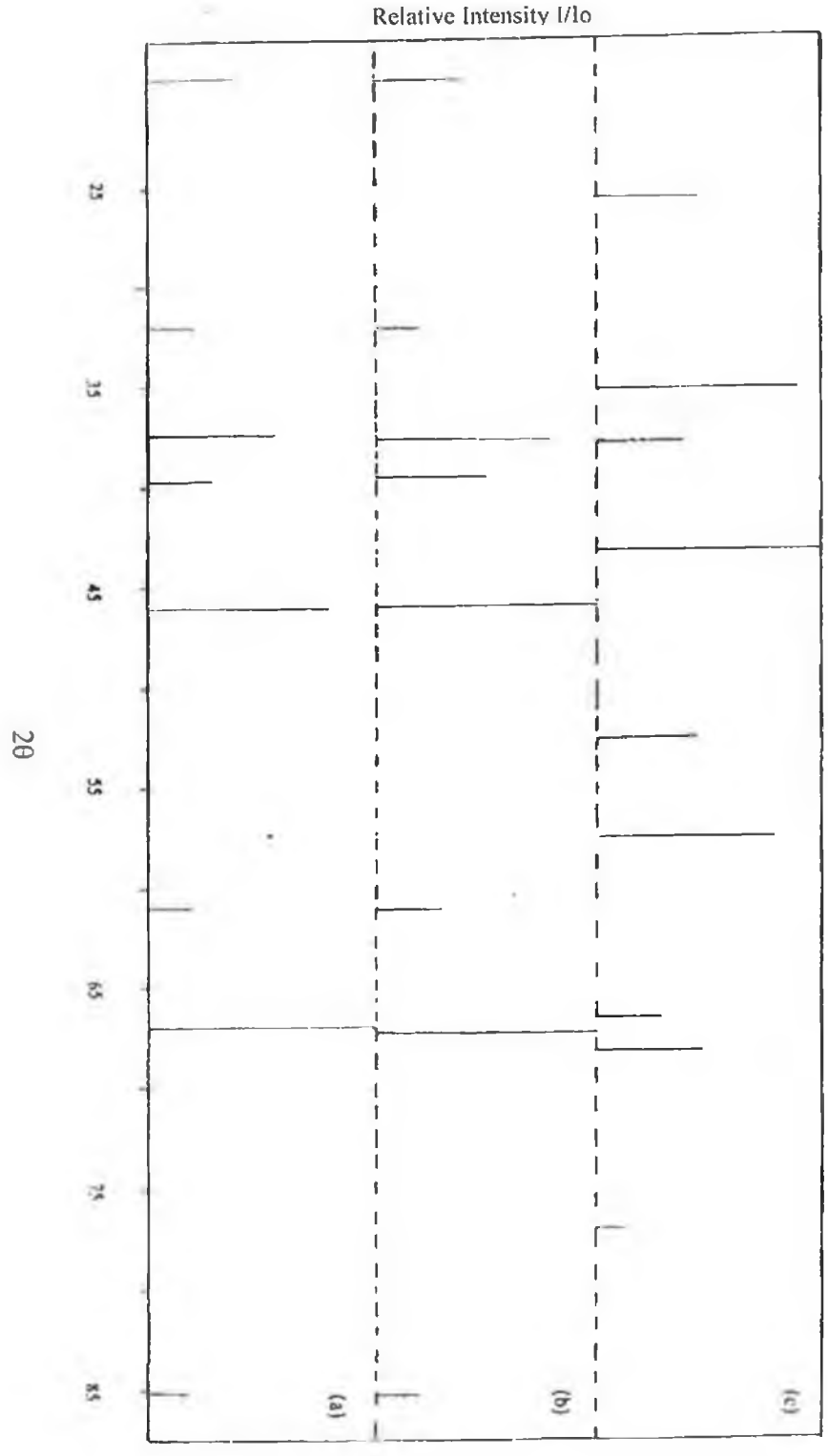

Figure 3.30: Powder X-ray Diffraction (XRD) Patterns of fresh alumina powder, where (a) η-Al_2O_3, (b) γ-Al_2O_3 and (c) and α-Al_2O_3 [11]

3.3.4 BET Surface Area

The BET surface areas of the puralox powders (shown in Table 3.12) used in preparation of the washcoat support were found to decrease in order SCFa-250 > SCFa-140. The reduction in surface area was attributed to the particle size variation between the two activated alumina powders (i.e. see appendix). The surface areas of the same samples after air-ageing were redetermined and the surface area of the SCFa-140 puralox exhibited thermal stability, whereas the SCFa-250 surface area was observed to decrease further. A reduction of 15% for the SCFa-250 compared to mean value of $220m^2/g$ for the fresh sample was recorded. This decrease may be attributed to sintering or phase transformation and encapsulation of some of the pores on the alumina surface. Chen et al. illustrated that sintering due to the collapse of micropores and the phase transformation into the more thermodynamically stable α–Al_2O_3 can account for the loss in surface area of the γ–Al_2O_3 at high temperatures (i.e. $>800^{O}C$) [12]. Horiuchi et al. also demonstrated sintering as the main cause for the decrease in surface area of alumina [13]. They found that at elevated temperatures the surface energy is minimised, resulting in surface area reduction. Atom migration on the surface from the convex to the concave surface resulting in the decrease in surface area due to the minimised energy was also calculated by Horiuchi et al [13]. However, this does not explain the thermal stability of the SCFa-140 support, since no other crystalline phase beside γ-Al_2O_3 was found in XRD spectra of the puralox support (see Fig. 3.29). Nevertheless, the thermal stability may be attributed to the particle size properties present in the SCFa-140 puralox powder.

The surface area of both fresh and air-aged washcoated whiskered substrate supports (Table 3.13) were also determined and found to increase in the order:

$$T_{16}^{900}\text{-}140A < T_4^{900}\text{-}250A < T_8^{900}\text{-}250A < T_{16}^{900}\text{-}250A < T_{32}^{900}\text{-}250A < T_{24}^{900}\text{-}250A.$$

All samples exhibited an increase in surface area with respect to whiskering with the exception of the T_{16}^{900}-140A sample. The increase in surface area was thought to be due to the increasing whisker formation on the gauze samples. Chapman and Vaneman and co

authors found that whisker growth improved adhesion of the catalyst impregnated washcoat alumina support to the Fe-Cr-Al alloy gauze [3-6]. However, this did not explain the apparently lower surface obtain for the T_{16}^{900}-140A sample. It was hypothesised the lower surface was related to the surface area properties of the starting material (i.e. puralox powder SCFa-140) used in the preparation of the washcaot mix.

The air-aged samples measured were all found to decrease in surface area, whereas the T_{16}^{900}-140A exhibited thermal stability. The reduction in surface area was most likely related to the sintering effect and phase transformation of the high surface area γ–Al_2O_3 to the more stable lower surface area α–Al_2O_3 phase [12, 13]. The thermal stability of the surface area of the air-aged T_{16}^{900}-140A samples was thought to be due to α–Al_2O_3 thermodynamically stable phase present in the puralox powders. However, from previous discussions and analyses of XRD results, the only crystalline phase present in the puralox powders was found to be γ–Al_2O_3 phase. Hence, another factor was cited to be responsible for the lower surface area and thermal stability of the sample. It was proposed the physical properties, such as particle size, surface area and attrition resistances were accountable. The present of the lanthanum oxide stabilizer in the puralox powder (see appendix) used in preparation of the washcoat support was suggested to inhibit the transformation or sintering from the high surface area to the low surface area alumina. Ferrandon et al. [14] reported that when γ–Al_2O_3 is subjected to temperatures 800^{O}C or greater phase transition occurs forming the more stable lower surface area α–Al_2O_3. They stated that addition of stabilizes inhibited this phase transformation. They examined alumina alone and doped with lanthanum and found the addition of the lanthanum oxide inhibited loss of the surface area.

The surface area of the T_{16}^{900}-140A^{I} sample prepared from insufficient grinding of the washcoat slurry solution (shown in Table 3.13) was also measured and showed a lower surface area of 17.5m^2g^{-1} compared to the 22m^2g^{-1} measured for the sample (T_{16}^{900}-140A) ground for 5-6 hours. The decrease in surface area was attributed to the fine, uniform particle size distribution of the puralox SCFa-140 in the washcoat slurry mix. The reduction was also thought to be attributed to the alumina particle size in the washcoat

suspension and its adhesion to the gauze substrate support. Grace et al. [15] stated the alumina particle size should be ground down for at least 4 hours using a ballmill, and remain in suspension for up to 4 hours with an optimum particle size of 1-10μm. Agrafiotis et al. [10] reported a correlation between adhesion ability of washcoat solution and the particle size of the alumina powders. Bowker found higher surface area support catalysts were usually prepared from small particles adhering to a refractory support material [16].

Table 3.12: Surface Area of Puralox Powders used in Washcoat Supports.

Sample Code	Surface Area (m^2/g)	*Surface Area (m^2/g)
SCFa-250	220	186
SCFa-140	146	140

* Determined after Ageing, at 800^0C for 8 hours.

Table 3.13: Surface Area of Washcoated Substrate Supports.

Sample Code	Surface Area (m^2/g)	Range (m^2/g)	*Surface Area (m^2/g)	Range (m^2/g)
T_4^{900}-250A	27	25-29	20	19-21
T_8^{900}-250A	38	36-40	33	32-34
T_{16}^{900}-250A	46	44-48	38	36-40
T_{16}^{900}-140A	22	21-23	21	20-22
T_{24}^{900}-250A	50	48-52	43	41-45
T_{32}^{900}-250A	46	44-48	37	36-38
T_{16}^{900}-140A^I	17.5	-----	17.5	-----

* Determined after Ageing.

The surface areas of both fresh and aged catalyst samples after coating with Pt, T_8^{900}-250AP, T_{16}^{900}-140AP, T_{16}^{900}-250AP and T_{24}^{900}-250AP (Table 3.14) were also determined and the same increase in order of surface areas were found. The specific

surface areas of the alumina washcoat supports were unaffected by the addition of Pt, which was thought may plug some pores on the alumina support [17].

The surface areas of the industrially supplied catalysts (C1 and C2) were measured for comparison purposes. Results showed the surface areas of the C1 sample were similar to the T_8^{900}-250AP and T_{16}^{900}-250AP samples, whereas the C2 sample exhibited lower surface areas in contrast to the C1, T_8^{900}-250AP, T_{16}^{900}-250AP and T_{24}^{900}-250AP samples.

Table 3.14: Surface Area of Lab and Industrial Catalysts.

Sample Code	Surface Area (m^2/g)	Range (m^2/g)	*Surface Area (m^2/g)	Range (m^2/g)
T_8^{900}-250AP	38	36-40	33	32-34
T_{16}^{900}-140AP	22	20-24	21	20-22
T_{16}^{900}-250AP	46	44-48	38	37-39
T_{24}^{900}-250AP	50	48-52	43	42-44
C1	41	39-43	37	36-38
C2	28	26-30	23	22-24

* Determined after Ageing.

3.3.5 Total Metal content

The total metal content was determined by AAS analysis and results averaged from 3 sample catalysts (Table 3.15). The results were within ±0.05% to 0.175% of experimental error for all samples measured. Catalysts were digested using two different procedures B and C (see 3.2.5). In general, no significant differences were observed between the two digestion procedures (i.e. B and C). They only difference observed between the digestions procedures were in the acid digestion of the gauze support. In method B,

incomplete digestion of the gauze was observed, whereas in method C, complete digestion of the gauze was observed.

Higher % Pt content was determined for samples T_{16}^{900}-250AP and T_{24}^{900}-250AP in contrast to the T_{8}^{900}-250AP sample. The degree of washcoat application and level of whiskering on the gauze of T_{16}^{900}-250AP, T_{24}^{900}-250AP samples were thought to be responsible. Chapman and Vaneman also reported well defined whisker growth allowed for a thicker washcoat application than comparably less well-developed whiskered samples [3-6]. This in turn provided more suitable catalysts sites for the active material. A variation in % Pt content determined from the result for samples T_{8}^{900}250AP, T_{16}^{900}250AP and T_{24}^{900}250AP was also observed. These results may just be due to the production procedure used in the catalyst preparation and this may account for the inconsistency. For example, in the impregnation of the Pt, prolonged exposure of the washcoated substrate (i.e. coated gauze support) could have resulted in increased quantity of adsorbed Pt onto the surface. Olsbye et al. found that the amount of Pt deposited on alumina was controlled by pH and contact time on both α- and γ-phases [18].

The fresh sample T_{16}^{900}-140AP$^{1/3}$ had much lower % Pt content determined and showed no variation in metal content. This was accounted for by the dilution of the impregnating solution used in the preparation of the samples. The total metal content for the air-aged samples did not change in comparison to the fresh samples. Any variation was considered to be within experimental error. However, the fresh samples upon visual inspection also appeared lighter in colour after ageing. Pocoroba et al. [19] proposed that following on work by Dalla Betta [20], that a change in colour of the fresh samples from black to a light grey colour was in line with ageing and they proposed that some of the Pt metal was evaporated off at the high temperatures encountered with ageing or a change in the oxidation state of the Pt metal occurred [20]. However, more conclusive evidence is required and further experimental analysis is required, for example XPS, to determine the oxidation state of Pt present.

Table 3.15: Evaluation of B and C Digestion Procedures.

C Digestion Procedure		
Sample Code	Pt Content determined Wt.%	*Pt Content determined wt.%
T_8^{900}-250AP	2.95	2.9
T_{16}^{900}-250AP	3.2	3.2
T_{16}^{900}-140AP	3.5	3.4
T_{24}^{900}-250AP	3.2	3.2
**T_{16}^{900}-140AP$^{1/3}$	0.95	0.95
C1	2.2	2.2
C2	2.8	2.8
B Digestion Procedure		
Sample Code	Pt Content determined ca. wt.%	*Pt Content determined ca. wt.%
T_8^{900}-250AP	2.9	2.9
T_{16}^{900}-250AP	3.0	3.0
T_{16}^{900}-140AP	3.2	3.2
T_{24}^{900}-250AP	3.5	3.5
**T_{16}^{900}-140AP$^{1/3}$	0.94	0.94
C1	2.2	2.2
C2	2.8	2.8

* Aged samples at 800^{0}C for 8hr, only one measurement made.

** Prepared from a 1/3 dilution of the CPA solution with methanol.

C1, C2 commercially available samples.

The difference in the value for Pt content measured between nominal Pt catalysts (i.e. 2.8-3.2 wt. %), was determined to be approximately ± 0.4 wt. %. This error was found to be less for lower Pt content samples measured and higher for samples with loadings above 3.2 wt.%.

3.3.6 Metal Surface Areas

Hydrogen adsorption was measured volumetrically on several catalysts; the results are shown in Table 3.16. For each catalyst sample, averages of 3 measurements were recorded.

Table 3.16: H_2 Chemisorption Measurements for Catalyst Samples.

Sample code	Metal Content %w/w	Mean Pt Surface Area (m^2g^{-1})	Dispersion %	*Mean Pt Surface Area (m^2g^{-1})	*Dispersion %
T_8^{900}-250AP	2.9	0.67	9	0.58	7
T_{16}^{900}-140AP	3.0	0.74	11	0.42	7
T_{16}^{900}-250AP	3.2	0.89	13	0.62-0.72	10
T_{24}^{900}-250AP	3.5	0.89	14	0.63-0.75	11
T_{16}^{900}-140AP$^{1/3}$	0.94	0.46	22	N/A	N/A
C1	2.2	0.82	16	0.76-0.79	13-14
C2	2.8	0.56	9	0.52-0.53	8

* Air-aged samples.

Pt Surface Areas and Dispersion values averaged from 3 measurements.

C1, C2 commercially available samples.

N/A not determined.

For samples T_8^{900}-250AP, T_{16}^{900}140AP, T_{16}^{900}-250AP and T_{24}^{900}-250AP an increase in metal surface area of 0.67m^2g^{-1} to 0.89 m^2g^{-1} with increasing total surface area and metal loading was observed. Sample T_{16}^{900}-140AP was found to exhibit a slightly higher metal surface area value to T_8^{900}-250AP. This maybe attributed to the higher % Pt content in the T_{16}^{900}-140AP sample.

The % Pt dispersion was found to increase with increasing metal surface area for samples T_8^{900}250AP, T_{16}^{900}140AP, T_{16}^{900}250AP and T_{24}^{900}250AP. Sample T_{16}^{900}140AP$^{1/3}$ showed

an increase in dispersion with decreasing metal surface area. The impact on Pt dispersion was found to vary with % Pt loading and total surface area for different catalyst samples. For example, samples T_{16}^{900}-250AP and T_{24}^{900}-250AP exhibited higher % dispersion in contrast to T_{16}^{900}-140AP. It was proposed the Pt distribution and dispersion were dependent on the larger total specific surface area of the washcoats and lower total metal content of T_{16}^{900}-250AP and T_{24}^{900}-250AP samples.

Summers and Otterstedt [21, 22] stated that high surface area washcoat supports with dispersal alumina achieve high Pt dispersion no matter what the Pt concentration. Edmond et al. [23] also showed among the group of supports, that Pt dispersion increased in the order:

$$ZrO_2 < SiO_2 \leq \text{Zeolite Y} < Y_2O_3 < Nb_2O_5 < SiO_2/Al_2O_3 < Al_2O_3 < TiO_2.$$

They also observed that the ability of the support to disperse Pt on its surface does not correspond with the surface area of the carrier. However, the Pt dispersion was observed to be effectively dispersed on alumina support material [23]. Another factor suggested the reduction in Pt dispersion was attributed to Pt loading. Otto et al. showed from CO chemisorption measurements, Pt dispersion decreased as the % Pt loading was increased above 0.40% wt [24]. They also found formation of larger particles with a larger portion of subsurface atoms and attributed the reduction in Pt dispersion to the formation of large Pt particles [24]. Further evidence to support this theory was found with sample T_{16}^{900}-140AP$^{1/3}$, which had smaller metal surface areas in contrast to T_8^{900}-250AP, T_{16}^{900}-140AP, T_{16}^{900}-250AP and T_{24}^{900}-250AP. This was attributed again to lower Pt loading on the catalyst. An increase in dispersion was also observed as expected, resulting in an increase in availability of active surface Pt. The commercial catalyst, C1 was comparable to that of the T_{16}^{900}-250AP and T_{24}^{900}-250AP samples. However, a lower metal surface area and a higher Pt dispersion were obtained for the C1 catalyst sample in contrast to T_{16}^{900}-250AP and T_{24}^{900}-250AP catalysts. This was attributed to the lower metal loading on the C1 sample. The C2 sample exhibited lower metal surface area value and % dispersion in contrast to the T_{16}^{900}-250AP, T_{24}^{900}-250AP and C1 catalysts. It was

proposed a combination of the total surface area of the washcoat and % Pt loading of the C2 catalyst might have contributed to the decrease in Pt surface area and dispersion.

All catalyst samples air-aged showed a decrease in metal surface area with the exception of the C1 aged sample, which appeared less effected indicating a more stable surface. The effects on air-aged samples were attributed to sintering of the dispersed Pt at $800^{O}C$ forming larger Pt particles. The decrease in metal area may also be attributed to the fact that only external Pt atoms (i.e. surface/exposed Pt atoms) are capable of H_2 adsorption. Stewart and Bowlden [25] found that with freshly impregnated catalysts, the ratio of H_2 atoms adsorbed to the total Pt present was greater than one. They therefore concluded that dispersed Pt adsorbs much more efficiently than large Pt crystallites or bulk platinum. Several authors have reported sintering of alumina supported Pt (i.e. coalescence of smaller Pt particles into larger particles) in an oxygen containing atmosphere above $500^{O}C$ [24, 26-29]. As can be observed from the chemisorption results, a larger deviation between measured values for both metal surface areas and dispersion occurs. A number of factors may have contributed to this; one probable explanation may be experimental error, either in the chemisorption measurements or in the determination of total metal content. However, the former is unlikely since reproducibility was obtained for chemisorption measurements of a Euro-Pt standard [35].

The average particle sizes of platinum were also measured from the chemisorption data (see Table 3.17).

Table 3.17: Average Pt Particle Size for Prepared and Industrial Catalyst Samples.

Sample Code	Pt Particle Size (Å)	*Pt Particle Size (Å)
T_8^{900}-250AP	113	133
T_{16}^{900}-140AP	98	221
T_{16}^{900}-250AP	88	126
T_{24}^{900}-250AP	86	121
T_{16}^{900}-140AP[173]	59	N/A
C1	72	77
C2	138	164

* Air-aged samples.

Pt Particle Diameter values averaged from 3 calculated measurements.

C1, C2 commercially available samples.

N/A not determined.

The average Pt particle sizes of the fresh catalyst samples were found to increase with decreasing Pt metal surface area and decreasing dispersion for T_8^{900}–T_{24}^{900}250AP samples. A marked increase in Pt particle size from the fresh to air-aged catalyst samples was also observed. This was attributed to sintering of the smaller Pt particles into larger particles. As already discussed, a severe loss of Pt surface area resulted when samples were aged, which was expected to occur due to agglomeration of the smaller Pt particles at the high temperatures in the air atmosphere of the muffle furnaces. Several authors have contributed this to sintering of the Pt particles, which possess thermal energy at these temperatures which enables them to move across the surface of the catalyst resulting in agglomeration into large Pt particles [24, 26-27]. Labalme et al. stated small

Pt particles are not stable on alumina at elevated temperatures and tend to sinter leading to particle size increases [30].

Sample T_{16}^{900}-140AP showed the biggest increase in particle size, which indicated severe sintering of the Pt atoms. This resulted from the low surface area washcoat used in the catalyst preparation. The C1 catalyst samples illustrates the greatest resistances to sintering, which may be attributed to its low Pt loading and high uniformed surface area in contrast to all other catalyst samples.

3.3.7 Activity Measurements

Figures 3.31-3.37 illustrate the activity graphs for propane combustion as a function of temperature for the various catalysts examined. From the activity plots, the light-off temperatures T_{50} and T_{90} were measured (i.e. temperature at which 50% and 90% conversion of a 4% V/V C_3H_8/Air mixture was achieved); the results are shown in Table 3.18

Table 3.18: Temperatures (^{O}C) of 50% and 90% Propane Conversion over Catalyst Samples

Sample Code	Fresh		Air-aged		Fresh	Aged
	T_{50} (^{O}C)	T_{90} (^{O}C)	T_{50} (^{O}C)	T_{90} (^{O}C)	Figures	Figures
T_8^{900}-250AP	180	215	166	200	3.31	3.31
T_{16}^{900}-140AP	206	221	186	198	3.32	3.32
T_{16}^{900}-250AP	147	212	133	189	3.33	3.33
T_{24}^{900}-250AP	177	223	160	220	3.34	3.34
T_{16}^{900}-140AP[173]	233	251	----	----	3.35	
C1	220	275	152	198	3.36	3.36
C2	265	308	170	193	3.37	3.37

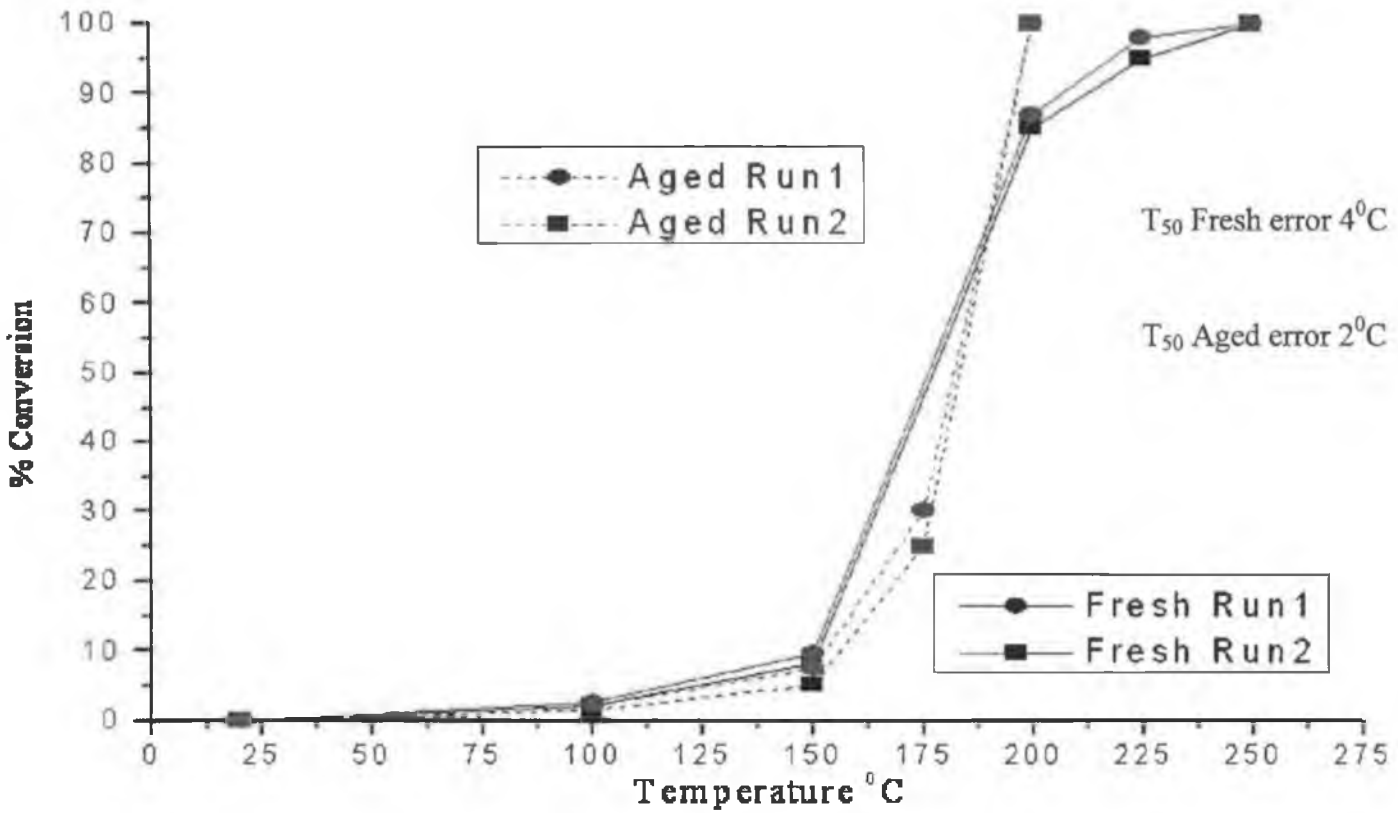

Fig. 3.31: A plot of C_3H_8 oxidation rate versus temperature for T_8^{900}-250AP sample

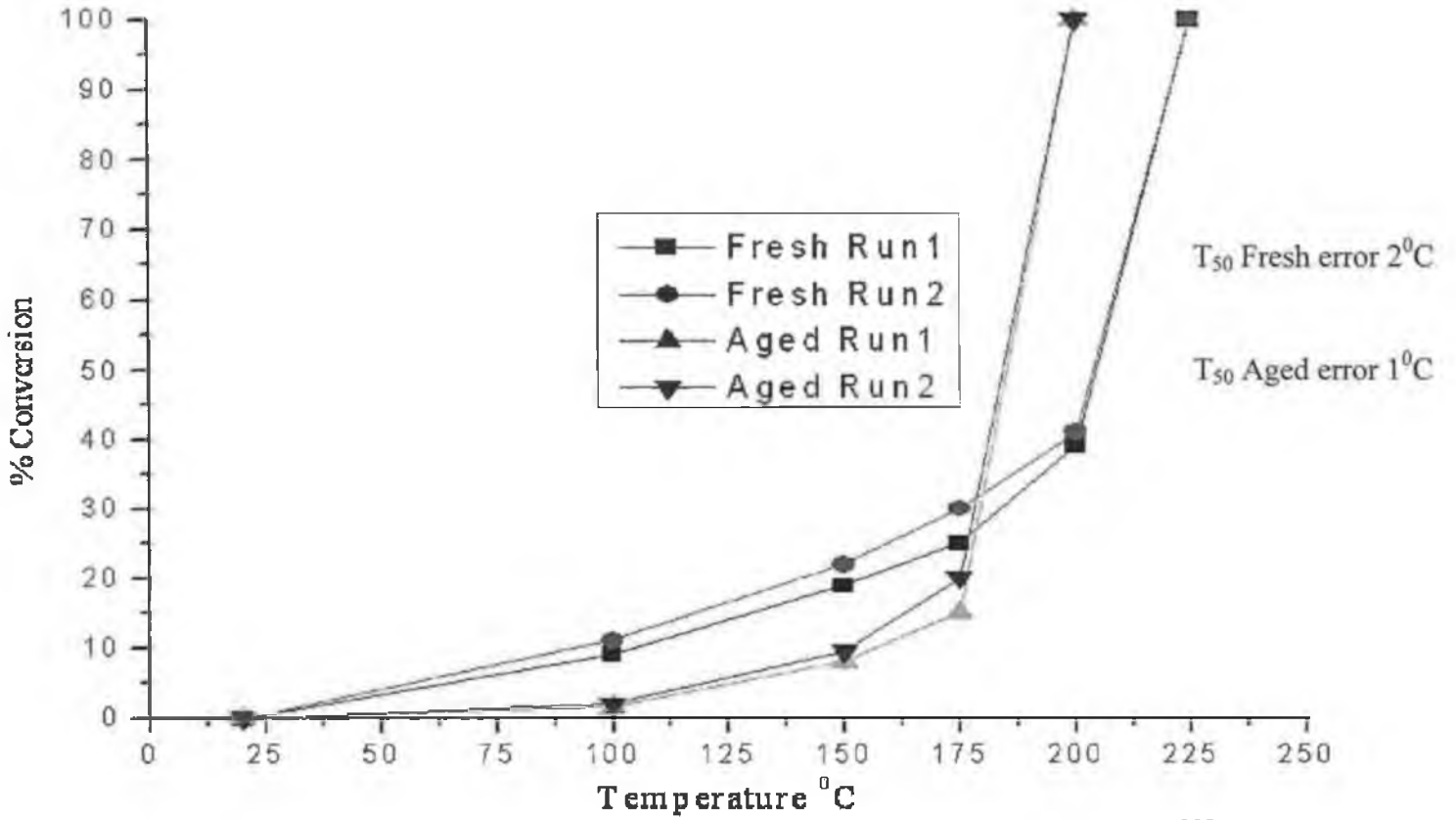

Fig. 3.32: A Plot of C_3H_8 oxidation rate versus temperature for T_{16}^{900}-140AP sample

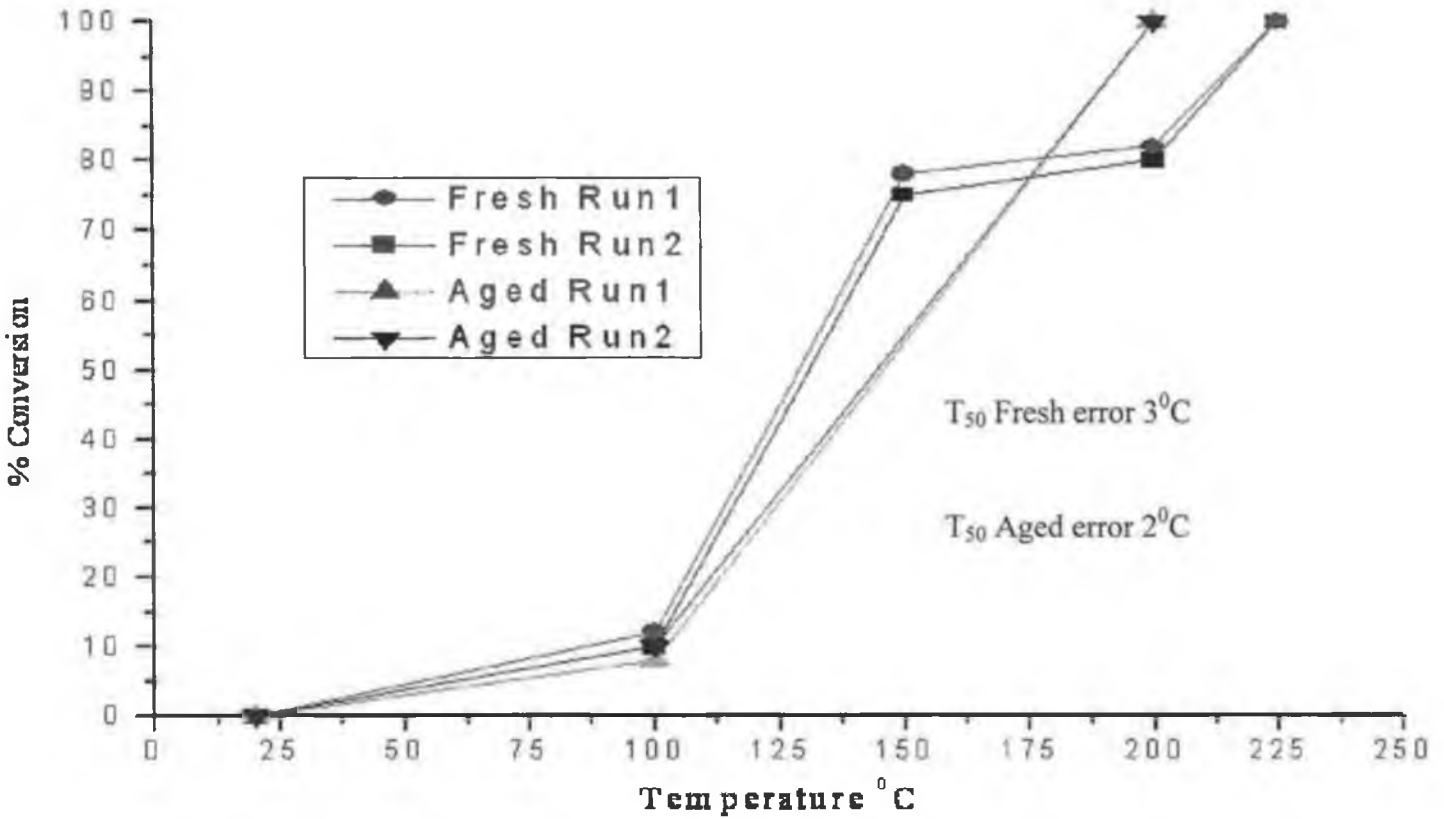

Fig.3.33:A plot of C_3H_8 oxidation rate versus temperature for T_{16}^{900}-250AP sample

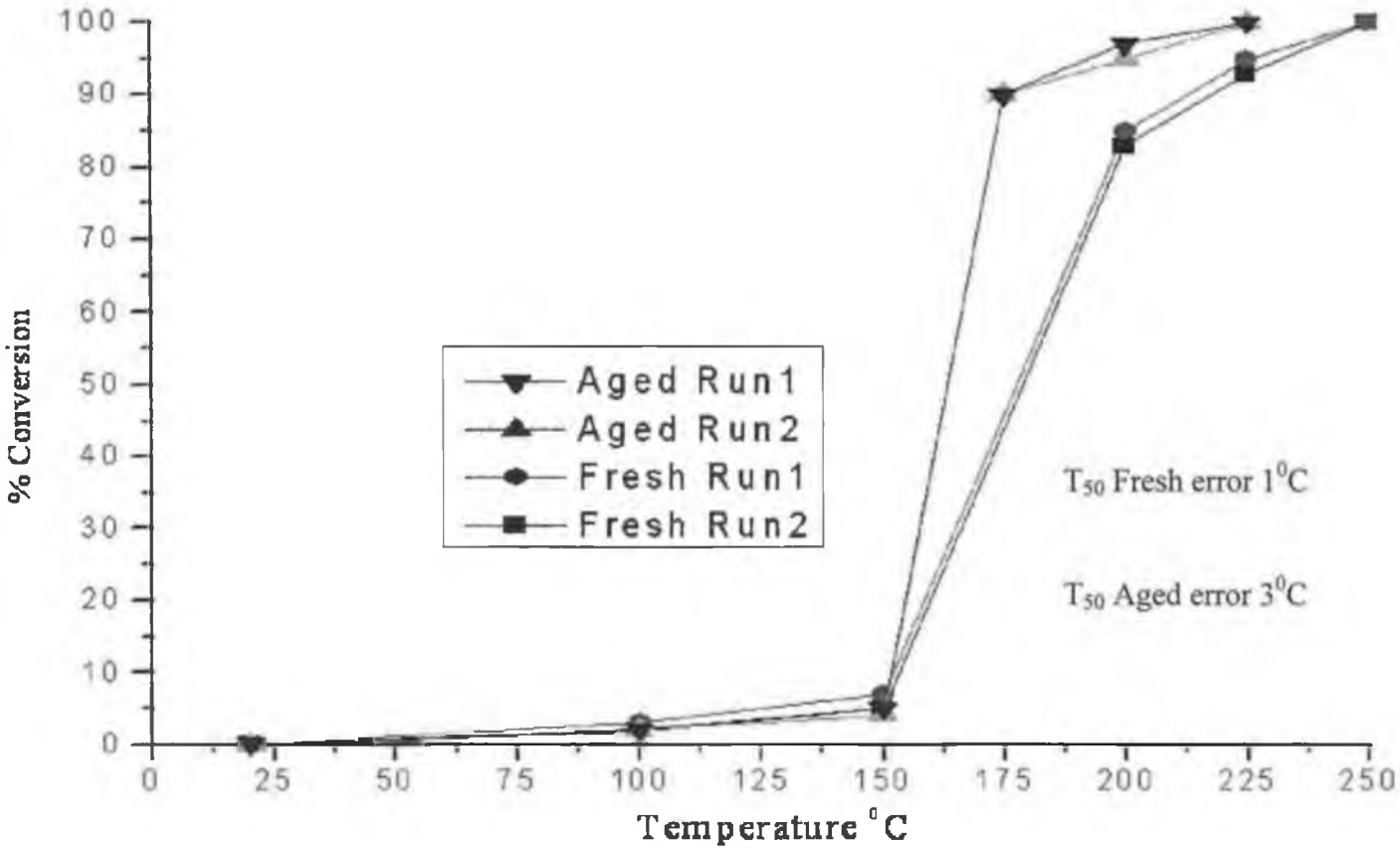

Fig. 3.34: A plot of C_3H_8 oxidation rate versus temperature for T_{24}^{900}-250AP sample

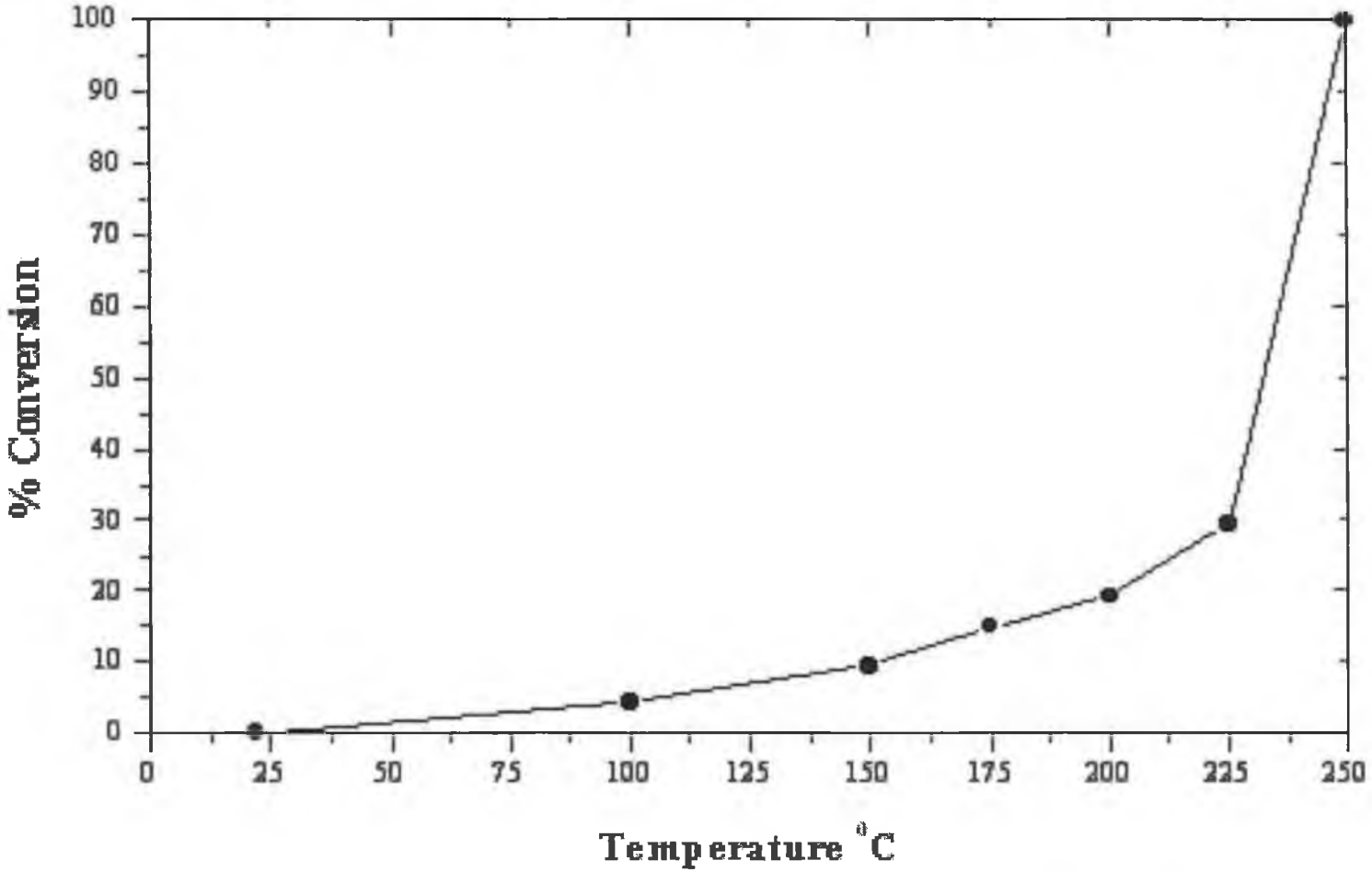

Fig. 3.35: A plot of C_3H_8 oxidation rate versus temperature for fresh T_{16}^{900}-140AP$^{1/3}$ samples

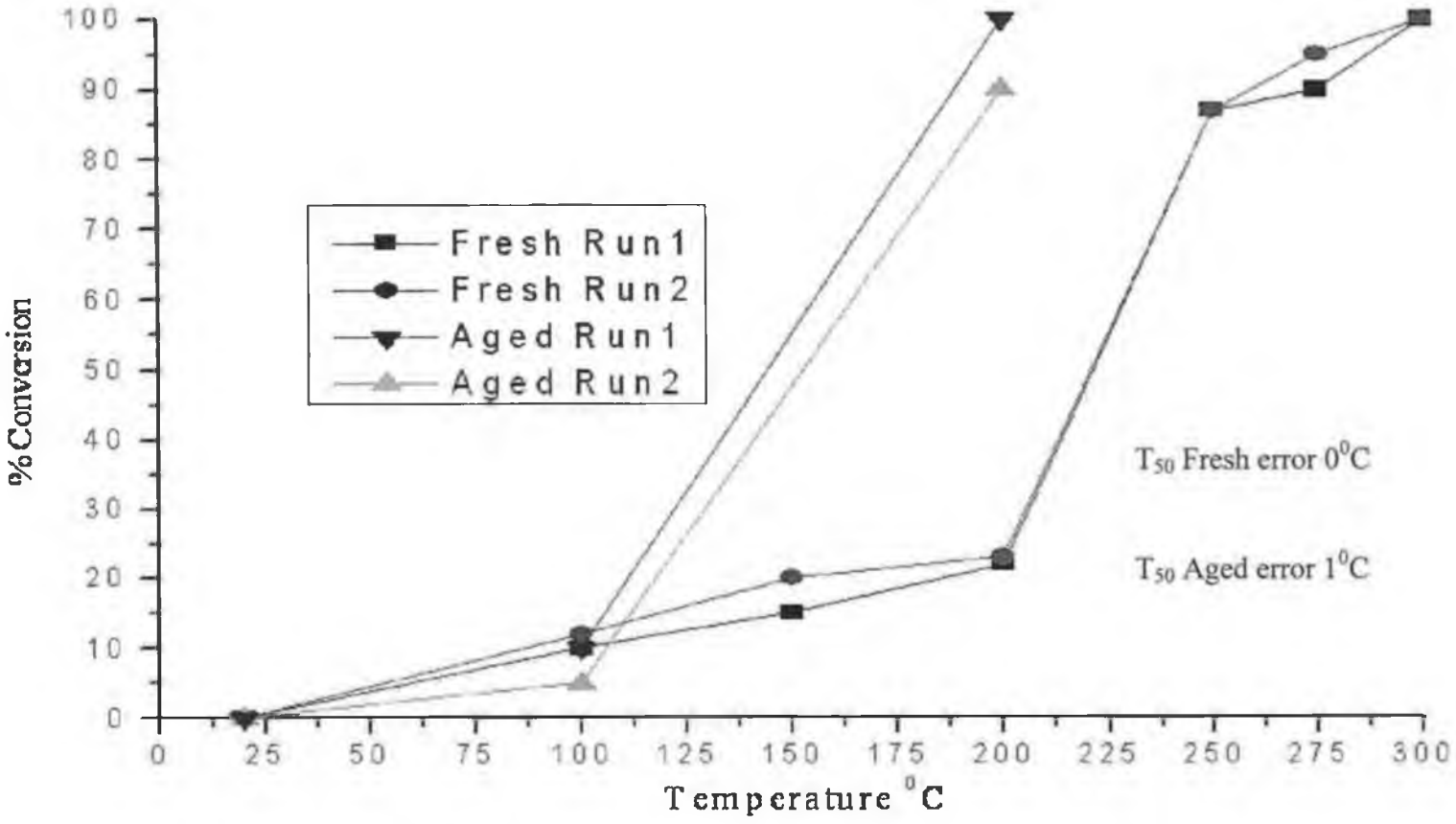

Fig. 3.36: A plot of C_3H_8 oxidation rate versus temperature for C1 sample

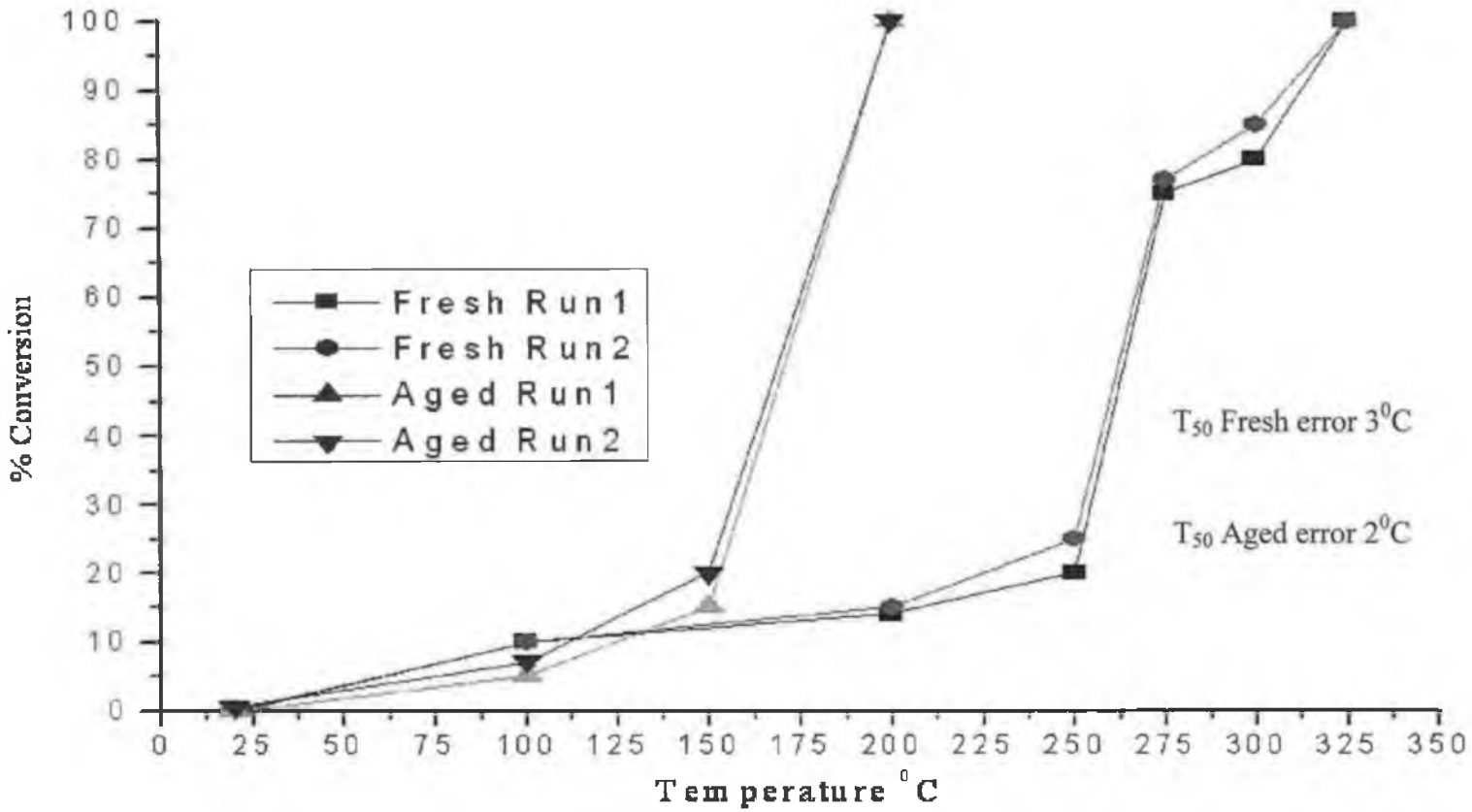

Fig. 3.37: A plot of C_3H_8 oxidation rate versus temperature for C2 sample

The shape of the activity curves for the fresh catalysts displayed a two step activity curve (i.e. sigma shape) with a slow initial activity step analogous for all catalysts measured, followed by a brisk rise in activity evident from the T_{50} value. Complete conversion was achieved with a second step process from the light-off temperature within a narrow temperature range (see Fig 3.31-3.37). The curves obtained for the air-aged samples showed a similar one step activity trend prior to T_{10}, followed by light-off and complete conversion within a small narrow temperature range. Sample T_{16}^{900}-140AP$^{1/3}$ fresh along with T_{16}^{900}-140AP sample (both fresh and aged) exhibited different activity shape curves. In contrast, they were found to resemble the activity curve trends as displayed by the air-aged catalysts. The support materials used and effects of ageing were thought responsible for the shape variations in the activity curves.

Comparison of the light-off temperatures (T_{50}) for the various fresh catalysts investigated showed the following trend in activity.

$$T_{16}^{900}250AP > T_{24}^{900}250AP \geq T_{8}^{900}250AP > T_{16}^{900}140AP > C1 > T_{16}^{900}140AP^{1/3} > C2$$

The light off temperatures (T_{50}) were in the range 180-265^{O}C. A similar activity trend was observed for T_{90} with the exception of T_{16}^{900}-140AP$^{1/3}$ catalyst the order was as follows.

$$T_{16}^{900}250AP \approx T_{8}^{900}250AP > T_{16}^{900}140AP \approx T_{24}^{900}250AP > T_{16}^{900}140AP^{1/3} > C1 > C2$$

The values were within a slightly greater temperature range of 212-308^{O}C.

From the activity data presented in Table 3.18 and the activity curves, the fresh catalyst samples showed a rapid increase between 100-150^{O}C for samples T_{16}^{900}-250AP, T_{24}^{900}-250AP, T_{8}^{900}-250AP, while C1, C2, T_{16}^{900}-140AP, T_{16}^{900}-140AP$^{1/3}$ displayed activity at 200-250^{O}C, but all samples were subsequently slow to reach 100% conversion. The presences of two or more types of Pt surface atoms (i.e. species) were thought to be responsible or may be attributed to some form of interaction between the Pt crystallites

and the support, which alters the strength of the metal-carbon bond. The higher Pt concentration of the catalyst as determined by AAS was also thought to contribute to the higher catalytic activity of T_8^{900}-250AP, T_{16}^{900}-140AP, T_{16}^{900}-250AP and T_{24}^{900}-250AP in comparison to the C1, C2 and T_{16}^{900}-140AP$^{1/3}$ samples. Hubbard et al. [31] showed that the specific rate of propane oxidation over Pt/γ–Al_2O_3 increased with increasing Pt concentration. They also stated that small highly dispersed Pt crystallites supported on alumina undergo a metal-support interaction resulting in deactivation of the small Pt particles. Otto et al. [24] also noted an increase in propane oxidation with increasing Pt concentration. They attributed these larger Pt particles formed with a substantial amount of subsurface Pt atoms on increasing Pt concentration.

After air-ageing, all the catalyst samples were found to exhibit increased catalytic activity in contrast to the fresh samples. The conversion goes rapidly to 100% as illustrated from the activity curves (Figures 3.31-3.37). For example, the T_{50} values for C1 and C2 catalysts were lower by 70^{O}C and 95^{O}C respectively relative to the freshly calcined samples. Larger Pt particles (as calculated from chemisorption data) in the aged samples indicated catalytic activity was enhanced on large Pt particles in contrast to smaller more dispersed Pt particles. Hence, it was proposed the oxidation of propane was a structure sensitive reaction. Labalme et al. reported small Pt particles were not stable on alumina at elevated temperatures and tend to sinter leading to particle size increases [30]. Several authors also reported similar results suggesting the oxidation of propane was more active on larger Pt crystallites than highly dispersed Pt [24, 26, 32-34].

Complete combustion of propane was reached at a temperature of 220^{O}C for all catalysts. The catalytic activity of the T_{16}^{900}-140AP sample was observed not to increase substantially on ageing. From chemisorption data, the Pt particle size measured for T_{16}^{900}140AP was substantially larger than for any other catalysts measured. Therefore, it was suggested a loss in activity for T_{16}^{900}140AP occurred due to excessive sintering of the Pt. Otto et al. [24] reported sintering of Pt supported on alumina caused an increase in activity for C_3H_8 oxidation, but found that extreme sintering resulted in considerable loss of surface metal and subjugated the advantage of increase in site activity. In

agreement with this observation, other authors found propane oxidation over Pt/γ–Al_2O_3 to be a structure sensitive reaction [24, 32], since a change in the turnover frequency with the Pt particle size was observed. The propane oxidation rate was observed to increase substantially with particle size. Nevertheless, it was found that excessive sintering was detrimental to the activity, as the surface fraction becomes too small [33]. Therefore, the sintering of Pt particles on the T_{16}^{900}-140AP catalyst suggests that other species other than surface metal atoms must be considered as active, such as:

- Species containing Pt in oxidised state,
- Participation of oxygen species from the support.

Activity may be attributed to the presence of dispersed platinum oxides (PtO, PtO_2), which can be formed during ageing in air [24, 32, 33]. Edmond et al. [23] observed from oxidation of CO over Pt that very small Pt crystallites exhibited lower activity; in contrast they found the specific rate to increase sharply with increasing particle size but then decrease and level off at a certain crystallite size. They attributed this to the fact that smaller particles chemisorb reactant molecules more powerfully than larger particles. Thus, the strong adsorption of CO on small Pt crystallites may render it difficult for oxygen to adsorb or displace the CO adsorbed molecule. Although several literature reviews have found hydrocarbon oxidation to increase with larger Pt particle size, the catalytic activity of the air-aged C2 sample with larger Pt crystallites was less active in contrast to C1 aged, with half the particle size. Therefore, it may indicate other types of Pt surface atoms are involved. In agreement with this observation, several authors [24, 30, 32] stated the oxidation of propane might involve other active species, such as Pt in an oxidised state and/or participation of an oxygen species from the support other than the large Pt particles.

3.4 Conclusion

A series of Al_2O_3 washcoat supported Pt gauze catalysts were prepared in an attempt to obtain characteristics and performances similar to the C1 catalyst and C2 catalyst. Each individual step during the preparation was evaluated and characterised. The following conclusions were reached.

Oxidising alloy gauze at 900 to 990^{O}C results in growth of a mature oxide surface layer chiefly composed of γ–Al_2O_3 with EDX analysis showing a small percentage of chromium and iron detected. The use of higher temperatures (i.e. >900 ^{O}C) caused accelerated whisker growth. It was also observed that temperatures greater than 960^{O}C for prolonged periods resulted in the formation of alpha alumina whiskers.

From analysis of the micrographs of the whiskered gauzes under the whiskering conditions of ¼-4hrs, 8, 16, 24, 32 and 64hrs, it was observed that at the 16 - 24hrs stage, the whisker growth was optimised. The ¼-2hr samples gave little or no whisker formation with an image similar to that of precleaned gauze. However, it can be concluded that initially the whisker growth occurs in the form of immature low aspect ratio whiskers (i.e. nodules) and from this point on, growth into mature whiskers occurs.

The effect of whiskering under a nitrogen flow in contrast to a static air atmosphere was also studied to determine the impact of atmosphere on whisker growth. The results under a nitrogen atmosphere showed no detectable improvement in whisker growth on the gauze. Comparison of micrographs for whiskered samples within 1-4 hour range under static air produced whiskers of higher aspect to those whiskered under a nitrogen atmosphere.

In addition, the effects of whisker growth on catalyst preparation were investigated. Whisker growth was found to protect the metal substrate from further oxidation at the elevated temperatures. The whiskers were also found to improve adhesion of the

washcoat alumina support to the alloy gauze. The mature whiskers of high aspect ratio formed after 16-24 hours were found to retain a thicker washcoat application than comparably less well developed whiskered samples. The measured surface areas of these washcoated samples revealed larger surface area values. These larger surface area catalysts in turn provided more suitable catalyst sites for the Pt metal and produced higher metal surface, better dispersion, smaller Pt particle size, and lower temperatures for T_{50} conversion rates.

The use of different grade alumina powders in the washcoat preparation was studied to determine the impact on surface area properties of the gauze catalysts using particle size distribution measurements, XRD and BET surface area analysis. The lower surface area puralox powder used in the preparation produced lower surface area catalysts, but was found to be thermally stable at elevated temperature. The higher surface area puralox material produced high surface area catalysts but didn't exhibit thermal stability in contrast to the lower surface area puralox. XRD analysis on both the puralox powders revealed the presence of only one phase γ–Al_2O_3. Particle size measurements revealed the presence of a bimodal distribution for both the low and high surface area puralox with ballmilling and grinding between 4-6 hours, whereas a continuous distribution was observed for the low surface area puralox with insufficient grinding. From this continuous distribution a more uniform packing of the particles was observed. However, the effects of grinding and altering the composition of the low and high surface area powders were found to impact on surface area properties and its thermal stability.

In summing up, the following conclusions may be made. For the purposes of washcoating, mature whiskers of high aspect ratio are most appropriate for bonding a washcoat support for the type employed in combustion catalysis. In accord with this statement, Pt supported on 16 or 24-hour whiskered alumina washcoated gauze were shown to be highly active catalysts for the combustion of propane and similar in characteristics and performance to the commercial catalyst.

References

[1] Micromeritics Gemini 2375 V-Series Surface Analyser, 'Particle & Surface Sciences 1993-2004.

[2] M. J. Tiernan, 'An Investigation of Supported Platinum and Bimetallic Oxidation Catalysts', PhD, Thesis, DCU, (1996).

[3] General Motors Corporation, Detroit, Michigan, Chapman, US Patent, 4,331,631 May 25, 1982.

[4] General Motors Corporation, Detroit, Michigan, Chapman, US Patent, 4,318,828 March 9, (1982).

[5] General Motors Corporation, Detroit, Michigan, G. L. Vaneman, European Patent, 0,358,309 A1, June 29 (1989).

[6] General Motors Corporation, Detroit, Michigan, G. L. Vaneman, US Patent, 4,915,751 April 10 (1990).

[7] J. M. F. Ferreira and H. M. M. Diz, J. Hard Materials, **3**, 17-27 (1992).

[8] S. Taruta, N. Takusagawa, K. Okada and N. Otsuka, J. Ceram. Soc. Japan, **104**, 47-50 (1996).

[9] G. Tarì, J. M. F. Ferreira, A. T. Fonseca and O. Lyckfeldt, J. Euro. Ceram. Soc. **18**, 249-253 (1998).

[10] C. Agrafiotis and A. Tsetsekou, J. Euro. Ceram. Soc. **20**, 815-824 (2000).

[11] J. W. Curley, 'Oxidation Studies on Supported Metal Catalysts', PhD, Thesis, DCU, (1995).

[12] X. Chen, Y. Liu, G. Niu, Z. Yang, M. Bian and A. He, Appl. Catal. A: General, **205**, 159-172 (2001).

[13] T. Horiuchi, T. Osaki, T. Sugiyama, K. Suzuki and T. Mori, J. Non-Crystalline Solids, **291**, 187-198 (2001).

[14] M. Ferrandon, and E. Björnbom, J. Catal. **200**, 148-159 (2001).

[15] General Motors, Detroit, Michigan, Grace U.S. Patent 4,762,567, August 9, (1988).

[16] M. Bowker, 'The Basis and Application of Heterogeneous Catalysis", Oxford University Press Inc., New York, 1998

[17] A. Hinz, P. Larsson, B. Skårman, and A. Anderson, Appl. Catal. B: Environmental, **34**, 161-178 (2001).

[18] U. Olsbye, R. Wendelbo and D. Akporiaye, Appl. Catal. A: **152**, 127-141 (1997).

[19] E. Pocoroba, E. M. Johansson and S. G. Jaras, Catal. Today **59**, 179-189 (2000).

[20] R. A. Dalla Betta, Catal. Today, **35**, 129 (1997).

[21] J. C. Summers and S. A. Auser, J. Catal., **52**, 445-452, (1987).

[22] J. E. Otterstedt, L. O. Lowendahl and L. B. Lansson, 'Catalysis and Automobile Pollution Control', in A Crucq and A. Frennet, (Eds.) Studies in Surface Science and Catalysis, Elsevier Amsterdam **30**, 333 (1987).

[23] C. Edmond, X. Akubuiro and E. Verykios, Appl. Catal., **14**, 215-227 (1985).

[24] K. Otto, J. M. Andino and C. L. Parks, J. Catal., **131**, 243-251 (1991).

[25] C. A. Stewart and J. H. Bowlden, Parma Research Laboratory, Cleveland, Ohio, **61**, 210 (1959).

[26] P. Briot, A. Auroux, D. Jones and M. Primet, Appl. Catal., **59,** 141 (1990).

[27] J. Völter, G. Lietz, H. Spindler and H. Lieske, J. Catal., **104**, 375 (1987).

[28] A. F. Diwell, R. R. Rajaram, H. A. Shaw and T. J. Truex, in "Catalysis and Automotive Pollution Control II" (Crucq, Eds.,), "Studies in Surface Science and Catalysis", Elsevier Amsterdam, **71**, 193-202 (1995).

[29] F. M. Dautzenburg and H. B. M. Wolters, J. Catal., **51,** 26 (1978).

[30] V. Labalme, E. Garbowski, N. Guilhaume and M. Primet, Appl. Catal., A: General, **138**, 93-108 (1996).

[31] P. C. Hubbard, K. Otto, S. H. Gandhi and S. Y. K. Ng, Chemical Eng. Dept., Wayne State University, Detroit, Michigan, 268-275 (1992).

[32] H. Lieske, G. Lietz, G. Spindler and J. Volter, J. Catal., **81,** 8 (1983).

[33] K. Otto, Langmuir, **5**, 1364 (1989).

[34] R. F. Hicks, H. Qi, M. L. Young and R. G. Lee, J. Catal., **122**, 280 (1990).

[35] A. Frennet and P. B. Wells, Appl. Catal., **18**, 243 (1985).

Chapter 4:

Preparation and Characterisation of Co/Al_2O_3, Co/ZrO_2 and Co/CeO_2 Catalysts.

4.0 Introduction

Catalytic combustion of methane and other lighter hydrocarbons is receiving considerable attention in the chemical industry with the aim of producing new solutions for reducing emissions of air pollutants. In particular, the interest in new materials for high temperature applications [1], such as gas turbines, domestic heaters, and for exhaust gas treatments, especially VOC [2] for removal of unburned hydrocarbons, has boasted research in this area. Compared to thermal combustion processes, the presence of a catalyst gives better control of oxidation over wider fuel/air ratios, it lowers the operating temperatures, which results in reduced emissions of nitrous oxides and also provides improved energy recovery giving a more efficient use of fuel [3]. The most widely used catalysts are noble metals of Pt and Pd, transition metal oxides (e.g. Co_3O_4) and mixed oxide systems (e.g. perovskite oxides, $CoAl_2O_4$, $CuAl_2O4$ and $NiAl_2O_4$) [4]. The intrinsic activity of noble metals is known to be higher than that of simple metal oxides for hydrocarbon oxidation so their use as combustion catalysts is normally favoured [5]. For example, in automobile catalytic convertors a mixture of noble metals (Pt, Pd and Rh) stabilised on an Al_2O_3 support is used to clean up exhaust emissions with Pt and Pd being the most active ingredients for the combustion of the hydrocarbons to CO_2 and H_2O. However, the depletion of Pt and Pd reserves and the associated rise in cost of the precious metals means the discovery of cheaper, more abundant alternatives for catalytic combustion applications is of prime importance in the chemical industries.
The current investigation reports on the potential use of supported and unsupported cobalt oxides for the combustion of methane. Particular emphasis is placed on the role played by various thermal analysis techniques in the elucidation of factors which affect catalyst performance.

Since the concentration of methane in the atmosphere is rising, its elimination via catalytic conversion to carbon dioxide, which has a lesser greenhouse effect, is becoming increasingly important [6]. Methane is the most inert and difficult hydrocarbon to oxidise by combustion at low temperatures. World-wide efforts to find less expensive alternatives to the expensive noble metal catalyst for this process are

being made [6-8]. Early studies on the use of simple metal oxides tested for the oxidation of paraffins including methane [5, 9, 10]. More recently, the potential of cobalt as a viable alternative to, or additive in, noble metal combustion catalysts has been highlighted [11-14]. Deactivation problems exist due to sintering of the active Co_3O_4 phase and reaction with the alumina support forming inactive mixed oxides (i.e. $CoAl_2O_4$ spinel). However, despite such problems with the existing formulation, research into the use of Co_3O_4 may provide a greater understanding of the origins to low-temperature combustion activity. This is particularly important in terms of automotive exhaust applications in the drive to develop new catalytic technologies to reduce 'cold-start' emission problems [12]. Such difficulties relate to the fact that a large proportion of the uncontrolled emissions from cars fitted with catalytic convertors stem from the first few minutes of driving when the catalyst has not yet reached a temperature at which it can operate effectively. Hence, there is a need for the development of catalytic materials that start to convert pollutants at lower temperatures thereby reducing the emissions of toxic nitrous oxides.

It is known that the support material employed for the dispersion of the noble metal or metal oxide active species can have a significant effect on the methane combustion activity of the dispersed species [9, 15]. On evaluation of a wide variety of supported and unsupported oxides, Anderson et al. [9] reported that the Co_3O_4 was the most active catalyst for the combustion of methane. However, when impregnated on an alumina support, performance was found to be lower than a range of other supported oxides. This deactivation was explained in terms of a possible formation of $CoAl_2O_4$ spinel structure. Strong interactions of dispersed Co species with the alumina support materials have been widely reported to cause a decrease in the catalytic activity of supported Co_3O_4 combustion catalyst [12, 16]. In the present study, a variety of different materials (e.g. alumina, ceria and zirconia) have been employed as supports for cobalt oxide catalysts, in an attempt to determine the importance of the support material on catalytic activity for methane combustion.

Solid-insertion probe-mass spectrometry (SIP-MS) was used to study the decomposition of the catalyst precursor species on the various support materials. The advantages of using this technique for the study of thermally induced decompositions have been previously described [17]. In brief, a combination of small sample mass,

which reduces temperature gradients and high vacuum (10^{-5}Pa), which minimises diffusion problems and the possibility of back reaction between the solid product and evolved gases. This makes the technique (i.e. SIP-MS) highly suitable for the study of calcination or decomposition processes. This is the first example of an application of the technique in the study of catalyst preparation.

A temperature programmed reduction (TPR) - mass spectrometer (TPR-MS) technique was employed for the characterisation of the oxide catalysts formed following calcinations of the precursor in air with the aim of defining a correlation between redox properties and catalytic activity. The use of a mass spectrometer as the detector for TPR studies allows for direct simultaneous monitoring of H_2 uptake and H_2O evolution, providing a greater insight into the reduction process relative to the more commonly used thermal conductivity detectors which monitor only H_2 uptake as a function of temperature [18] or the use of a hygrometer to monitor H_2O evolution but which provides no information on H_2 uptake [19].

A major advantage of using a mass spectrometer is, therefore, the ability to reveal the evolution or adsorption of H_2, (i.e. where no H_2O is evolved) and the drying of the samples (i.e. where no H_2 is consumed) and to clearly distinguish these processes from reduction where there is a simultaneous decrease in hydrogen and increase in water vapour.

In addition to the use of conventional linear heating rate TPR, the reduction of supported cobalt oxide was also studied under constant rate thermal analysis (CRTA) conditions. In constant rate- temperature programmed reduction (CR-TPR), the rate of reduction is regulated to maintain a constant rate of reactant consumption or product formation by controlling the sample temperature appropriately. This approach is capable of producing higher resolution of overlapping events, allowing easier quantification of reduction events while the shape of the temperature profile obtained provides an insight into the reduction mechanism [19].

4.1 Experimental

4.1.1 Catalyst Preparation

Unsupported cobalt oxide samples (CoO and Co_3O_4) were supplied by Aldrich. Supported cobalt oxide samples were prepared by a wet impregnation technique using aqueous solutions of $Co(NO_3)_2.6H_2O$ (BDH, laboratory reagent, >97% purity). The powdered support materials used were γ- Al_2O_3 (supplied by Condea), ZrO_2 (Aldrich, 99%), CeO_2 (Sigma, 99.9%) and CeO_2 (prepared by Co-precipitation method). The CeO_2 Co-precipitated support was prepared by dissolving10 grams of cerium nitrate tetra-hydrate in 25 ml of water. Then 10 mls of ammonia solution (35% V/V) was added and the precipitate formed was left overnight. The precipitate was then filtered with distilled water until the filtrate was clear of chloride ions (silver nitrate test). The filter cake was then dried overnight at 45°C and 110°C. The support was calcined in a static air furnace at 600°C for 6 hours to produce the oxide.

Impregnation was achieved by dissolving an appropriate amount of the nitrate salt in 9 cm^3 of H_2O followed by addition of 3g of the support material. After mixing for 90 minutes, excess water was removed using a cold trap (liquid N_2- toluene) rotary evaporator. Samples were then dried at 45 ^{0}C overnight and at 110 ^{0}C for 8 hours. An alternative method of preparation was using ethanol as our solvent and removing the excess using a normal rotary evaporator set-up. Calcination of supported nitrate samples to produce cobalt oxide(s) was achieved in a static air muffle furnace at either 400 ^{0}C or 600 ^{0}C for 1 hour. The level of cobalt in the supported samples prepared was nominally 5 wt. % or 15 wt. % based on the amount of the nitrate employed in the impregnation step. γ - Al_2O_3 supported Pt and Pd samples, containing a nominal noble metal loading of 0.5 wt. %, were prepared by impregnation of the support with solution of $H_2PtCl_6H_2O$ and $PdCl_2$ respectively. After drying, calcination was performed by heating at 630 ^{0}C in static air for 15 minutes.

4.1.2 Catalyst Characterisation Techniques

The specific surface areas of catalysts were determined by N_2 adsorption at –196 degrees Celsius according to the BET method using a micromeritics Gemini instrument. X-ray diffraction (XRD) spectra were obtained using CuKα (λ = 1.5418 Å) radiation in order to allow identification of the crystalline phases present.

TPR-MS experiments were performed on supported and unsupported cobalt oxide samples using a reduction atmosphere of 5 % hydrogen in helium at a flow rate of 50-cm3 min^{-1}. Supported samples were analysed after calcinations at 400 ^{0}C. After passage through the sample bed (30-50 mg) the effluent gas stream passed into the source chamber of the VG Micromass 7070HS mass spectrometer via a jet separator. The MID unit was used to directly monitor the following ions; m/z = 18(H_2O), m/z = 17 (H_2O) and m/z = 2(H_2) and m/z = 1 (H_2) as the sample was heated up to 850 ^{0}C. Conventional TPR experiments were performed using a linear heating rate of 10 ^{0}C min1. CR-TPR was performed using maximum heating and cooling rates of + 10 ^{0}C min^{-1} and – 10 ^{0}C min^{-1}, respectively, with the heating rate varied between these limits in order to maintain a constant pre-selected water evolution rate (i.e. reduction rate) of ca. 7 x 10^{-3} mg H_2Omin^{-1}. The software and instrumentation used for data acquisition and control in CRTA-MS experiments have been described in detail previously [17].

4.1.3 Combustion Activity

Catalytic activity for the combustion of methane was monitored as a function of temperature using a continuous flow apparatus. A stoichiometric mixture of methane in air (ratio: 1:10) at a total flow rate of 33cm^3 min^{-1} was passed through 0.3 g of the catalyst sample held on a sintered disc in a quartz u-tube. As the sample was heated, unreacted methane was monitored at specific temperatures, within the range 20-600 ^{0}C, by in-situ gas chromatography (Schimadzu GC-14A) using a packed Poropak Q column and a flame ionisation detector. At each furnace temperature, the effluent stream leaving the sample was monitored for at least 15 minutes until equilibrium was

attained. After a first cycle of tests (Run 1) all catalysts were cooled to room temperature and re-tested (Run2).

4.1.4 Decomposition Analysis

The decomposition process of unsupported cobalt nitrate hexahydrate was studied by simultaneous TG-DSC (STA) using a Stanton Redcroft STA 625 instrument. The sample (10mg) was placed in an aluminium crucible and heated at 10 ^{0}C min^{-1} from room temperature to 600 ^{0}C in an air atmosphere.

The decomposition of supported and unsupported cobalt nitrate samples was also studied using the SIP-MS system, which has been described in detail previously [17]. The SIP consists of a cylindrical microfurnace (12mm x by 5 mm) positioned at the end of a water-cooled stainless steel rod which can be located, via airlock valves, directly into the source chamber of a VG Micromass 7070HS mass spectrometer. Important instrumental features include sample temperature measurement via a thermocouple (type k, chrome-alumel) located at the base of the sample holder to place it in virtually direct contact with the sample itself. The SIP can be heated to 1000 ^{0}C and sample masses are typically less than 10 mg. Linear heating rate experiments were performed using 10 ± 0.3 mg of sample at various heating rates of between 1 and 10 ^{0}C min^{-1}. The mass spectrometer is a sensitive and stable double-focusing magnetic sector instrument which was operated in "peak selected" mode with a MID (multiple ion detector) unit operated in field switching mode to allow direct monitoring of five ions; m/z = 18 (H_2O), m/z = 30 (NO), m/z = 32 (O_2) and m/z = 44 (N_2O or CO_2) and m/z = 46 (NO_2). Ions were monitored consecutively for a period of 500 ms each as the SIP temperature was increased from room temperature to 600 ^{0}C.

4.2 Results and Discussion

4.2.1 Decomposition Analysis

Figure 4.1 illustrates thermo-analytical curves obtained for the unsupported nitrate using simultaneous TG and DSC.

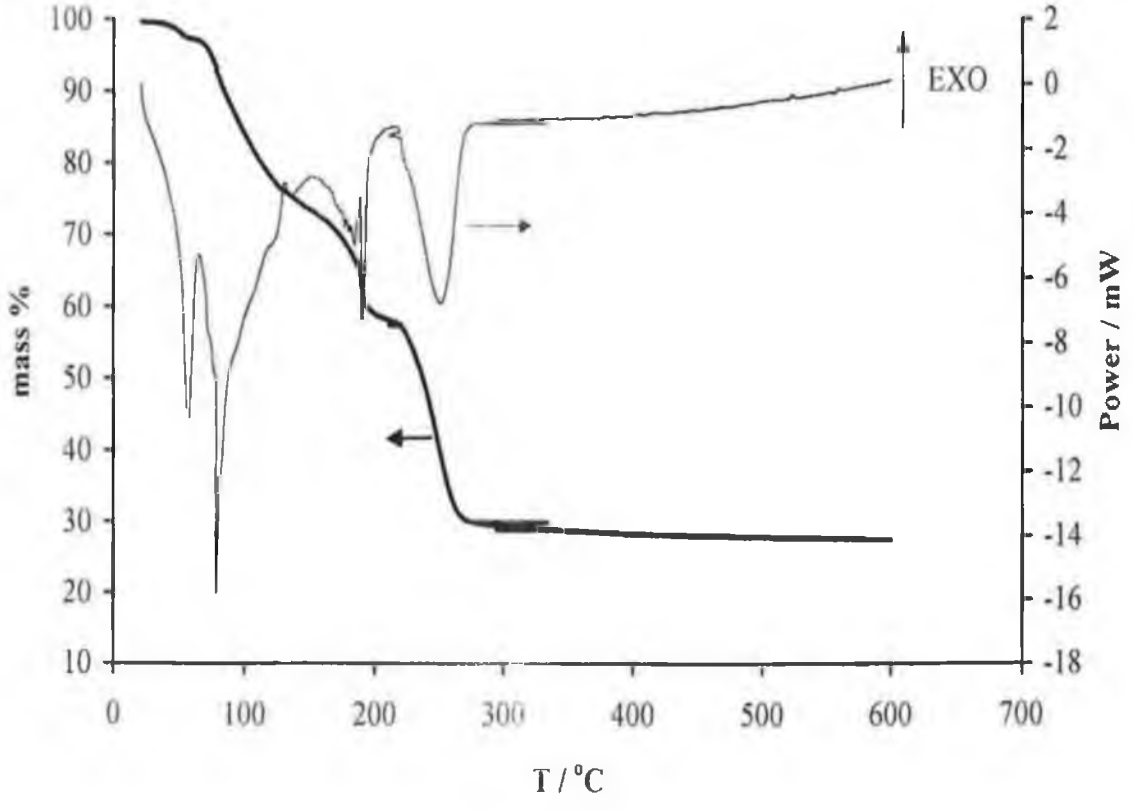

Fig. 4.1: Simultaneous TG-DSC curves of the decomposition of $Co(NO3)_2.6H_2O$

The overall weight loss observed corresponds to conversion to Co_3O_4 as the product of decomposition. The weigh loss below 200 ^{0}C can be accounted for by loss of water of crystallisation, along with a small amount of adsorbed water. Subsequent decomposition evolving NO_x species and yielding the oxide product occurred in a single endothermic step between ca. 210- 280 ^{0}C. In agreement with previous studies [20, 21], SIP-MS data showed that water evolution was almost complete prior to the onset of the nitrate decomposition see Figure 4.2 below.

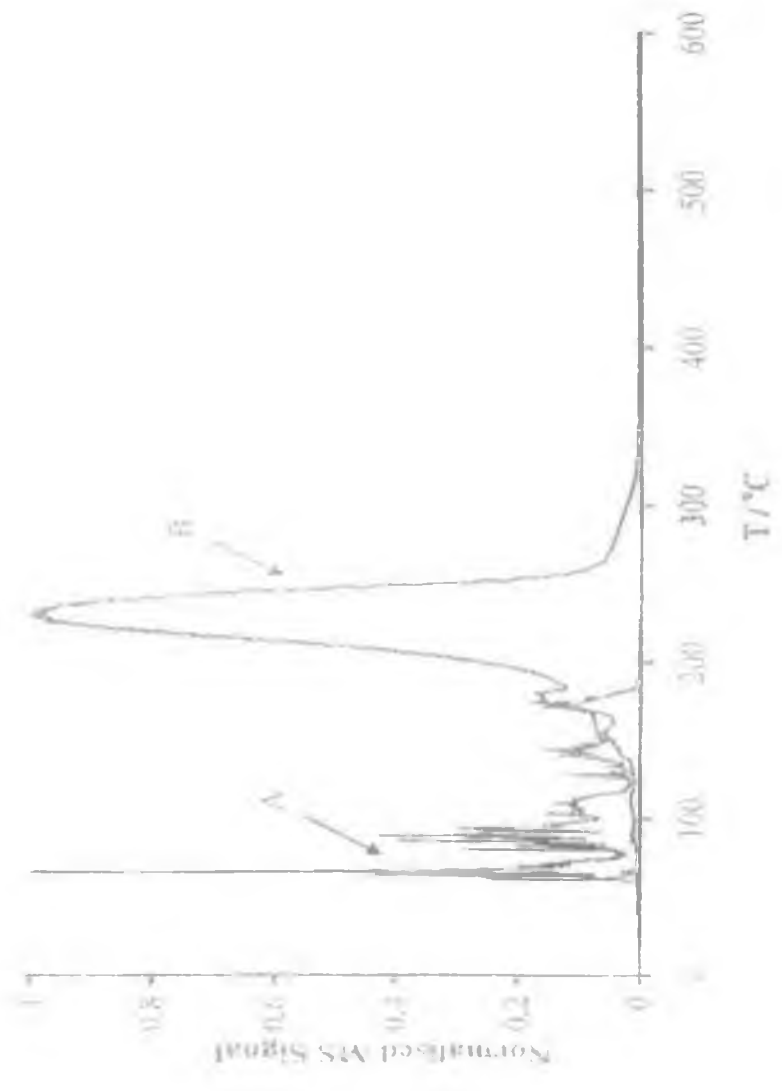

Fig. 4.2: SIP-MS profile of the decomposition of $Co(NO_3)_26H_2O$ at a linear heating rate of 6 ^{0}C min^{-1}, showing the evolution of H_2O (A) and NO_x (B) species as a function of temperature.

The decomposition of bulk metal nitrate can occur with or without concomitant dehydration [20]. In the case of cobalt nitrate, Cseri et al. [20] reported that loss of water occurred in a preliminary step separate to the main decomposition to the oxide. However, as found in the current study, this H_2O release was not completed prior to the onset of NO_x evolution as shown by TG-DTG-DTA-MS experiments performed using a heating rate of 6 ^0C min^{-1} in flowing N_2 atmosphere [20]. Similarly, Mansour [21] reported that the decomposition proceeded to Co_3O_4 as the final product in flowing air with decomposition completed at 280 ^0C. The nitrate hexahydrate was found to undergo melting at 75 ^0C followed immediately by dehydration to produce cobalt nitrate monohydrate and again nitrate decomposition began prior to completion of the dehydration process [21].

The effect of the support on the nitrate decomposition process was investigated in the current work using SIP-MS to follow the evolution of NO_x species as a function of temperature. Results obtained for the unsupported and supported (5 wt. % Co) samples using a linear heating of 6 ^0C min^{-1} are compared in Figures 4.3-4.6. A marked effect of the support on the decomposition profile was observed. For the unsupported sample (Fig 4.3), most of the decomposition occurred in a single peak within a temperature range of 150-300 ^0C with a maximum rate of evolution of NO_x species at 230 ^0C. In the case of the zirconia (Fig. 4.4) and ceria (Fig. 4.5) supported materials, decomposition occurred over much broader temperature ranges of ca. 150-400 ^0C. The most marked difference between supported and unsupported samples was observed for the alumina-based system with decomposition being split into two separate processes with peak temperatures of 355 ^0C and 465 ^0C, based on the NO evolution profile, and completion of decomposition was delayed until 600 ^0C (Fig. 4.6).

For all samples investigated, peaks corresponding to the evolution of NO, NO_2 and N_2O species were observed in the decomposition profiles. Whiles the mass spectrometer response for m/z = 44 could be associated with residual CO_2 in the source chamber, where peaks in the response were observed simultaneously with the evolution of other nitrogen oxides it is considered that the response is associated with N_2O. See figures 4.3-4.6 below.

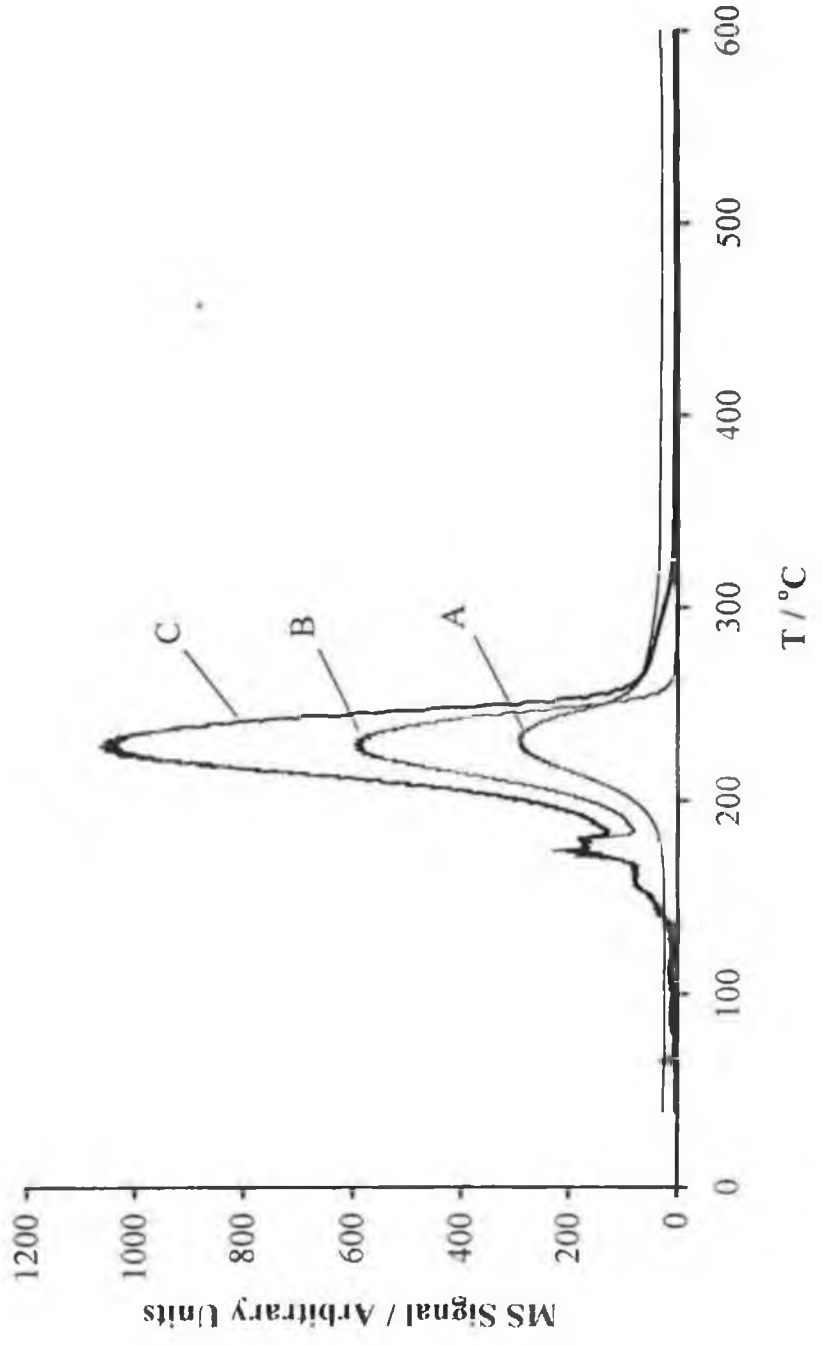

Fig. 4.3: SIP-MS profile of the decomposition of $Co(NO_3)_2.6H_2O$ at a linear heating rate of 6 ^0C min^{-1}, showing the evolution of O_2 and NO_x species as a function of temperature. (A)- O_2; (B) - NO_2; (C) - NO.

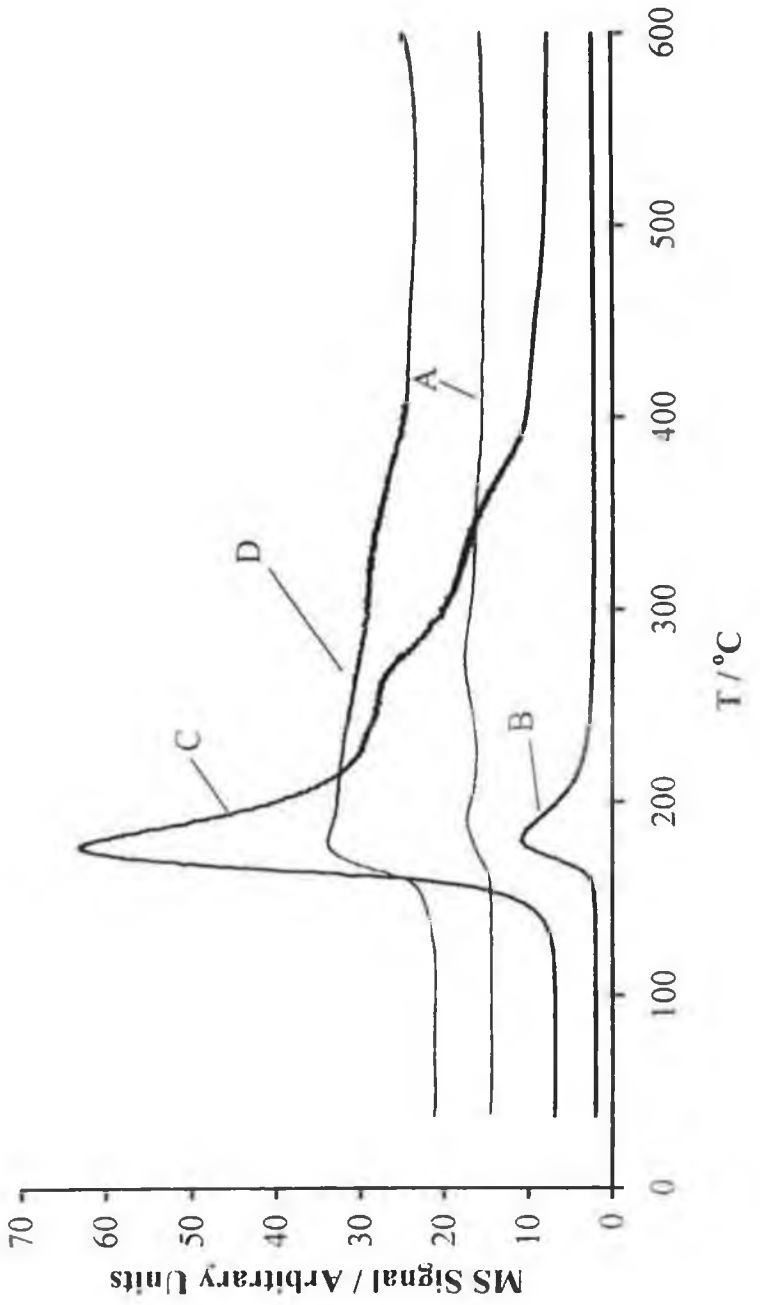

Fig. 4.4: SIP-MS profile of the decomposition of Zro2-supported $Co(NO_3)_2.6H_2O$ at a linear heating rate of 6 $^0Cmin^{-1}$, showing the evolution of O_2 and NO species as a function of temperature. (A) - O_2; (B) - NO_2; (C) - NO; (D) - N_2O.

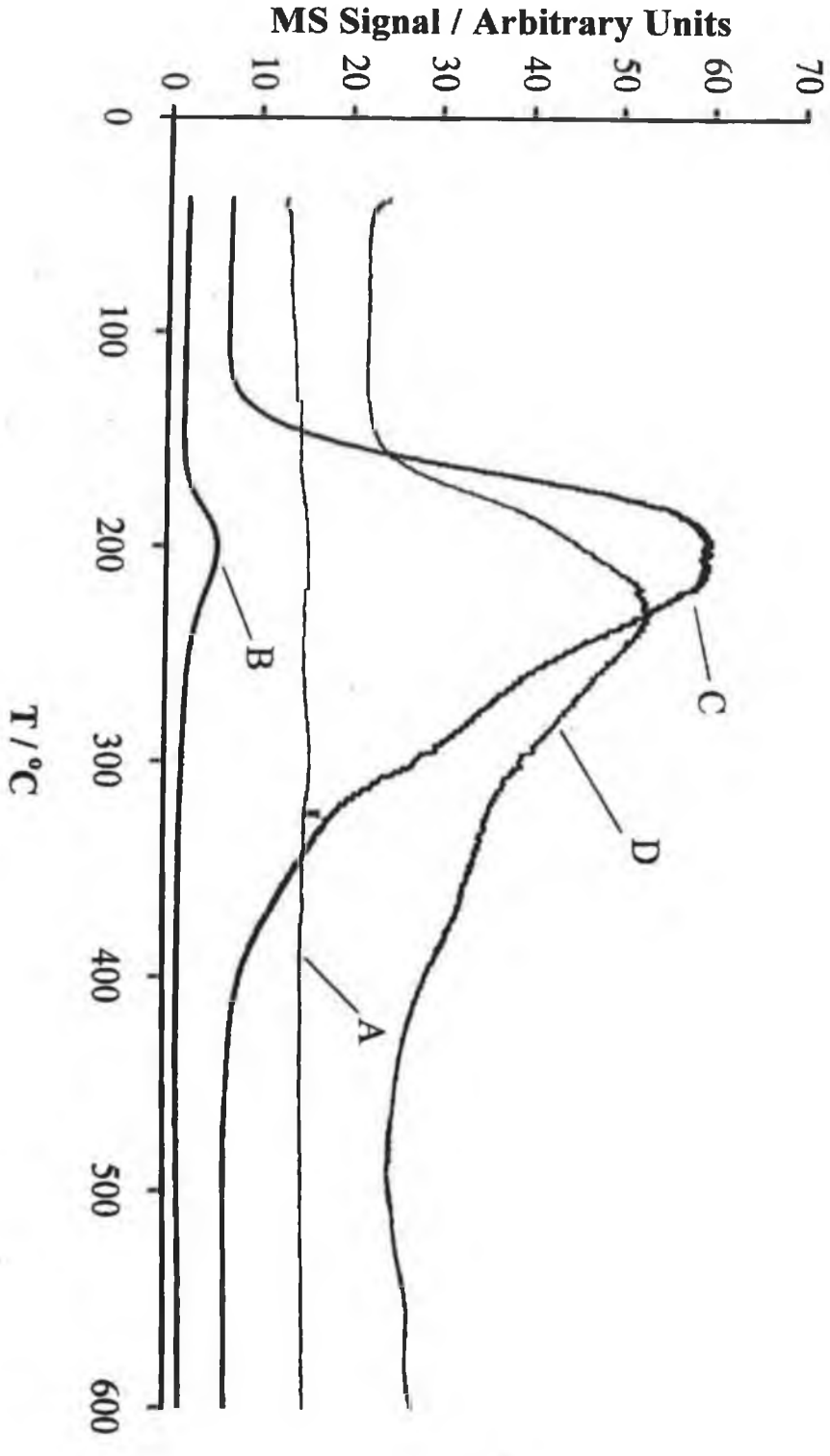

Fig. 4.5: SIP-MS profile of the decomposition of CeO_2-supported $Co(NO_3)_2.6H_2O$ at a linear heating rate of 6 ^0C min^{-1}, showing the evolution of O_2 and NO_x species as a function of temperature. (A) - O_2; (B) - NO_2; (C) - NO; (D) - N_2O.

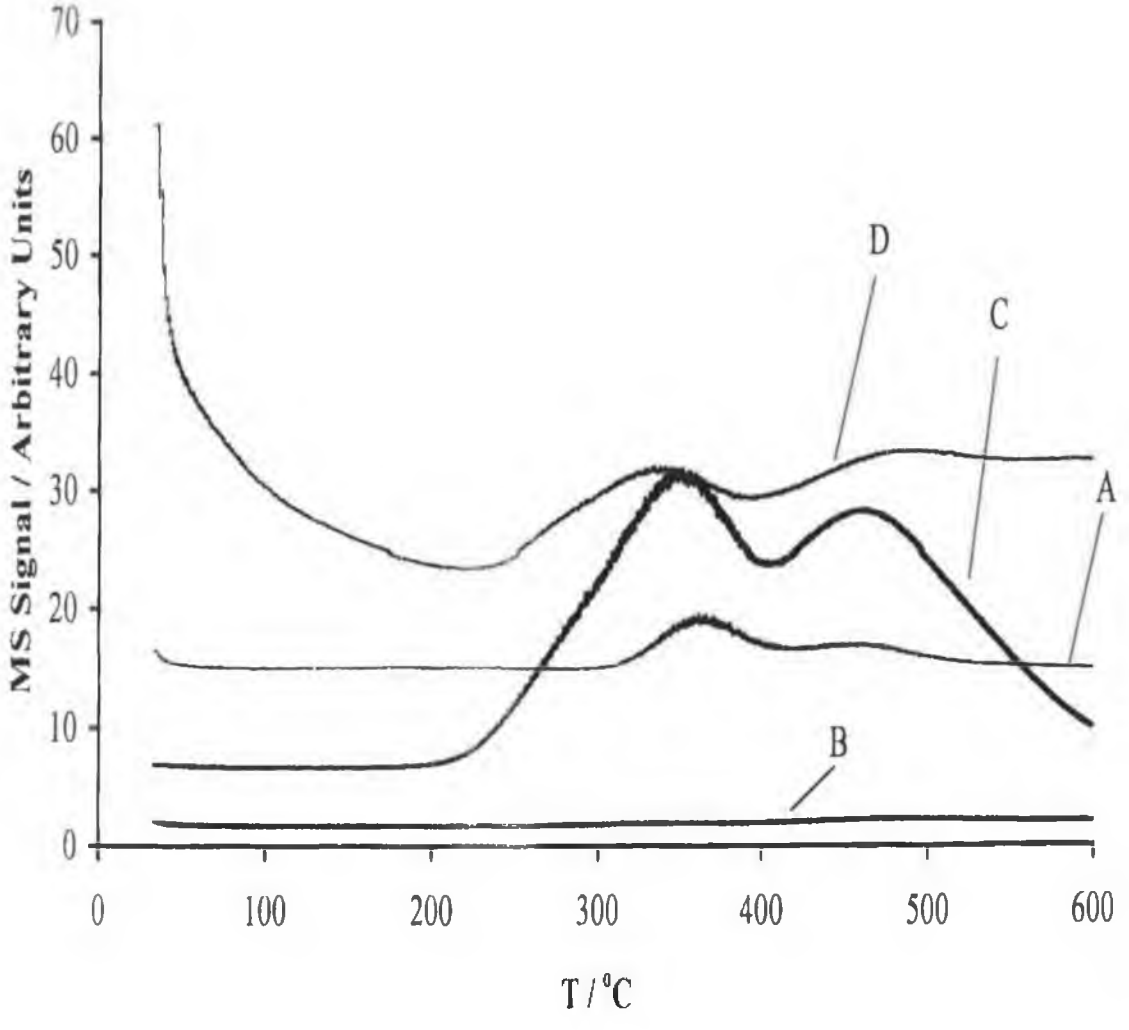

Fig. 4.6: SIP-MS profile of the decomposition of Al_2O_3-supported $Co(NO_3)_2.6H_2O$ at a linear rating of 6 ^0C min^{-1}, showing the evolution of O_2 and NO_x species as a function of temperature. (A) - O_2; (B) - NO_2; (C) - NO; (D) – N_2O.

4.2.2 Catalysts Characterisation

Table 4.1 summarises the BET surface areas measured for supported and unsupported cobalt oxide samples and for the support materials themselves.

Table 4.1: BET Surface Area of supported and unsupported catalysts.

Sample	Co content (mass %)	Surface Area ($m^2 g^{-1}$)
CoO	-	8
Co_3O_4	-	23
ZrO_2	-	5
Co/ZrO_2	5	4
CeO_2	-	33
Co/CeO_2	5	22
Al_2O_3	-	215
Co/Al_2O_3	5	191

Due to the high surface area of the γ-Al_2O_3 support, a higher dispersion of supported Co species will be expected relative to the CeO_2 and ZrO_2-based systems. XRD patterns obtained for samples with 15 wt. % Co showed the presence of Co_3O_4 crystallites on all support materials after calcinations at 400 ^{0}C.

TPR profiles of supported samples are shown in Figure 4.7-4.9 on pages 16 and 17 illustrating H_2 uptake (m/z = 2) and H_20 evolution (m/z = 18) as a function of sample temperature. The relative areas of the H_2 uptake and H_2O evolution peaks could not be compared quantitatively due to the use of a jet separator inlet which, due to mass discrimination effects, resulted in a much smaller proportion of the H_2 (compared to H_2O) content of the product gas entering the source chamber. However, it is apparent from Figures 4.7-4.9 that H_2 uptake and H_2O evolution occurred simultaneously in the reduction peaks observed.

For the 15-wt% Co/ZrO_2 sample (Fig. 4.7), two overlapping peaks are apparent with maxima at 312 ^{0}C and 357 ^{0}C. Both peaks can be associated with the reduction of

cobalt oxide species as the support showed no reduction peaks within this temperature range. Arnone et al. [13] reported a similar TPR profile for unsupported Co_3O_4 containing two overlapping peaks (maxima 382 ^{0}C and 470 ^{0}C) which was explained in terms initial reduction from the average oxidation state of 2.7+ (Co_3O_4) to 2+(CoO) followed by subsequent reduction from the 2+ to metallic oxidation state to metallic product. Complete reduction to Co^0 was confirmed by XRD carried out after TPR up to 600 ^{0}C at 10min^{-1} [13]. Meaningful comparison of peak temperatures with those found in the current study is difficult due to variations in experimental conditions [19] and known differences in the reducibility of supported and unsupported metal oxides [22]. The TPR profile for 15 wt. % Co/CeO_2 in the current study (Fig 4.8) also shows two overlapping peaks at temperatures of 305 ^{0}C and 352 ^{0}C, which again may be attributed to a two-stage reduction of Co_3O_4 to metallic cobalt via CoO. A higher temperature reduction peak observed at above 700 ^{0}C can be attributed to some support reduction, as was confirmed by TPR experiments on the pure support material.

For the 15-wt. % Co/Al_2O_3 sample, a more complicated TPR profile was produced (Fig 4.9). The initial H_2O evolution peak below 100 ^{0}C maybe associated with adsorbed water on the high surface area support material as it decreased considerably in size when the sample was dried overnight at 110 ^{0}C in flowing Helium. It is known from numerous previous investigations [23-25] that γ-Al_2O_3 supported cobalt oxide catalysts comprise mainly of two types of cobalt-containing phases namely (i) surface phases of Co bonded to the support which are relatively difficult to reduce and which prevail at lower Co concentrations and on higher surface area supports, and (ii) a more easily reducible Co_3O_4 phase which appears above a Co concentration of ca. 2 wt. %. The former phases include cobalt aluminates such as $CoAl_2O_4$ formed when Co ions occupy tetrahedral positions in the Al_2O_3 lattice during preparation, and overlayer Co^{3+} and Co^{2+} species [23-25]. On this basis, the peak at 350 ^{0}C in Fig 4.9 maybe attribute to the reduction of Co_3O_4 phase while the higher temperature reduction feature (up to > 800 ^{0}C) is most probably associated with the reduction of one or more phases involving strong interaction of dispersed Co species with the support material formed during catalyst preparation. Formation of such phases, which might also explain the retarded thermal decomposition of γ-Al_2O_3-supported cobalt nitrate (see Fig 4.6), was difficult to ascertain from the XRD patterns obtained

because of the broad nature of support peaks observed and the highly dispersed (and/or X-ray amorphous [24, 25]) nature of the species involved.

In linear heating rate TPR profiles, difficulties can exist with the resolution and hence quantification of overlapping reduction events [19, 24] with supplementary techniques such as XRD often required to elucidate on the steps observed [26]. For example, Arnoldy and Mouligan [24] reported that only one reduction peak was observed for bulk Co_3O_4 in a linear heating rate TPR profile with evidence for two stage reduction coming solely from the fact that the peak was broader than that obtained in the profile for CoO under the same experimental conditions. A less pronounced lack of resolution of overlapping peaks in the current study means that exact quantification of the two events involved in the reduction of Co_3O_4 crystallites supported on ZrO_2 and CeO_2 is difficult to achieve from the linear heating rate profile obtained (see Figures 4.7 and 4.8).

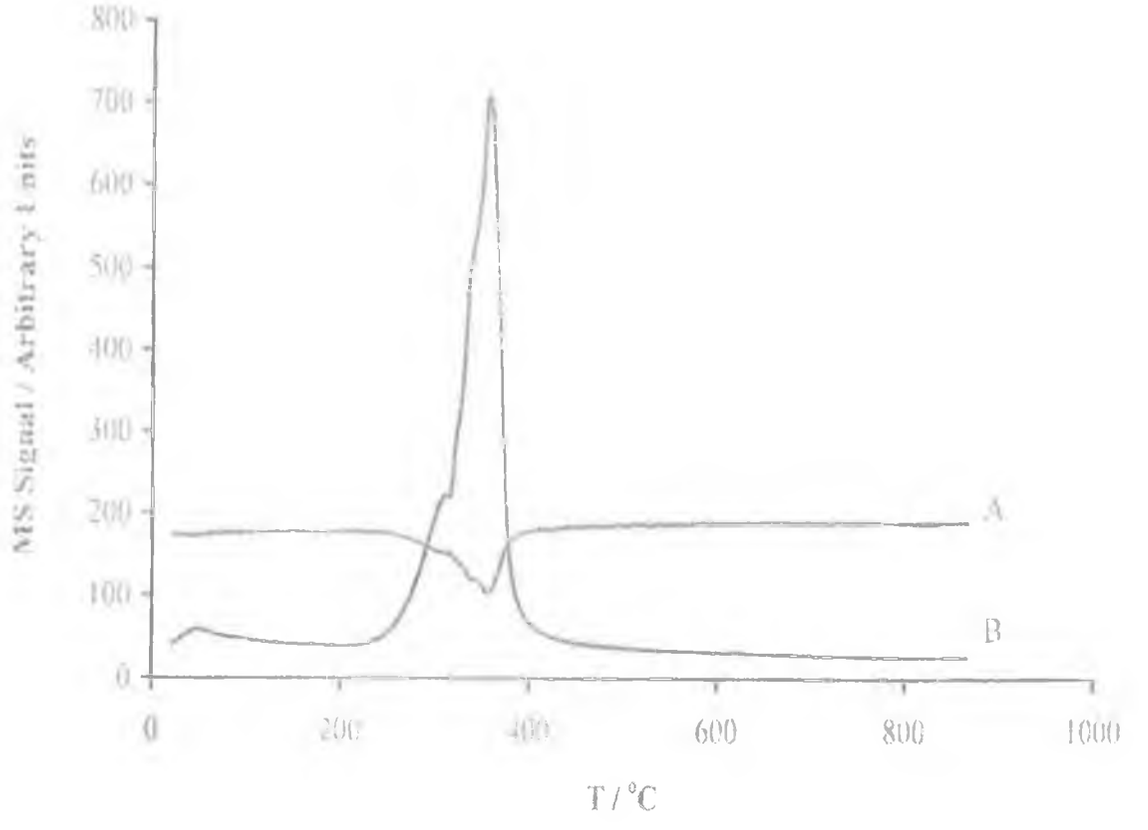

Fig. 4.7: TPR profile of 15 wt. %Co/ZrO2 at a linear heating rate of 10 ^{0}C min^{-1}. Sample size = 42mg. (A) – H_2; (B)-H_2O.

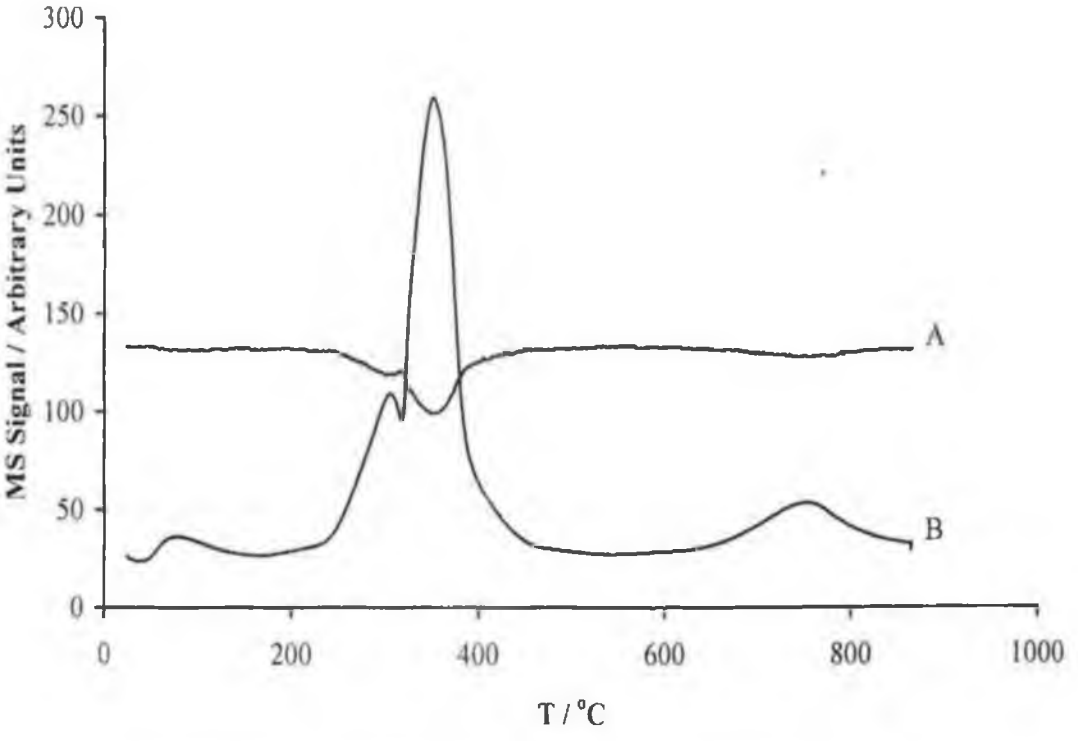

Fig. 4.8: TPR-profile of 15wt%Co/CeO_2 at a linear heating rate of 10 ^{0}C min^{-1}. Sample size = 34 mg. (A) - H_2; (B) - H_2O.

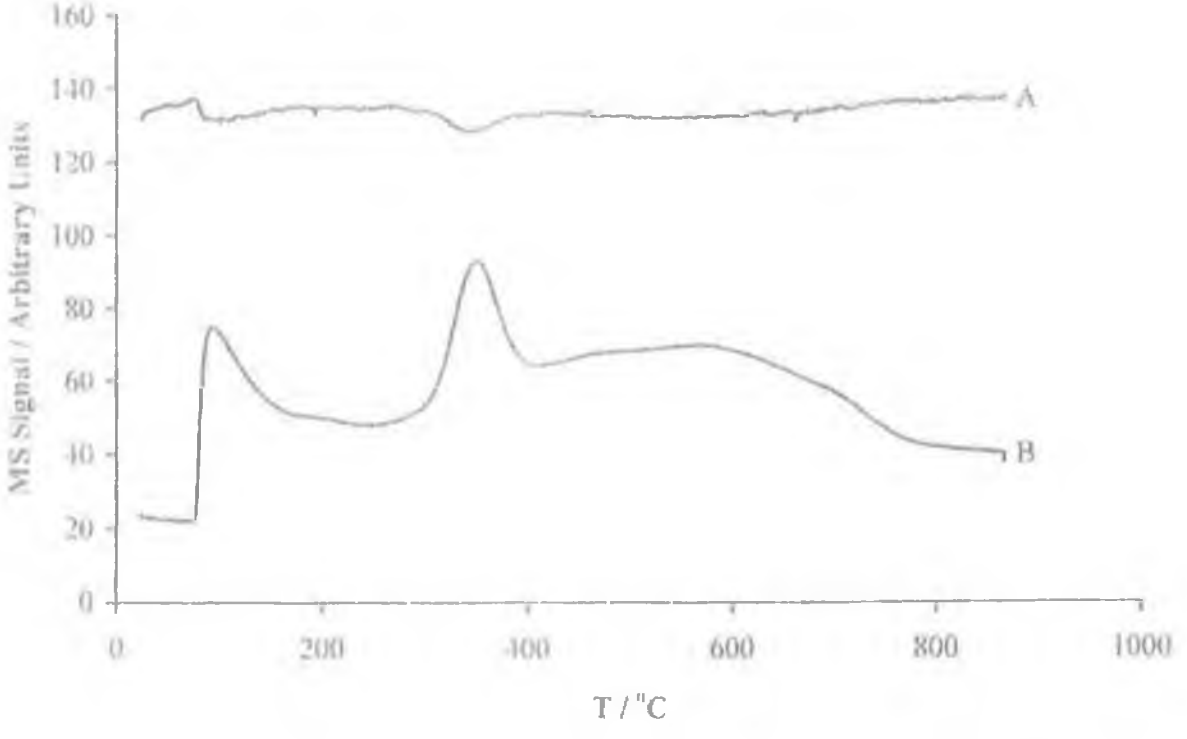

Fig. 4.9:TPR- profile of 15 Wt.% Co/Al_2O_3 at a linear heating rate of 10 ^{0}C min^{-1}. Sample size = 40mg. (A) - H_2; (B) - H_2O.

In order to provide greater resolution and an improved quantitative insight in to the reduction process, the reduction of the CeO_2-supported sample was studied under CRTA conditions. Fig 4.10 shows a CR-TPR profile obtained for 15-wt. % Co/CeO_2.

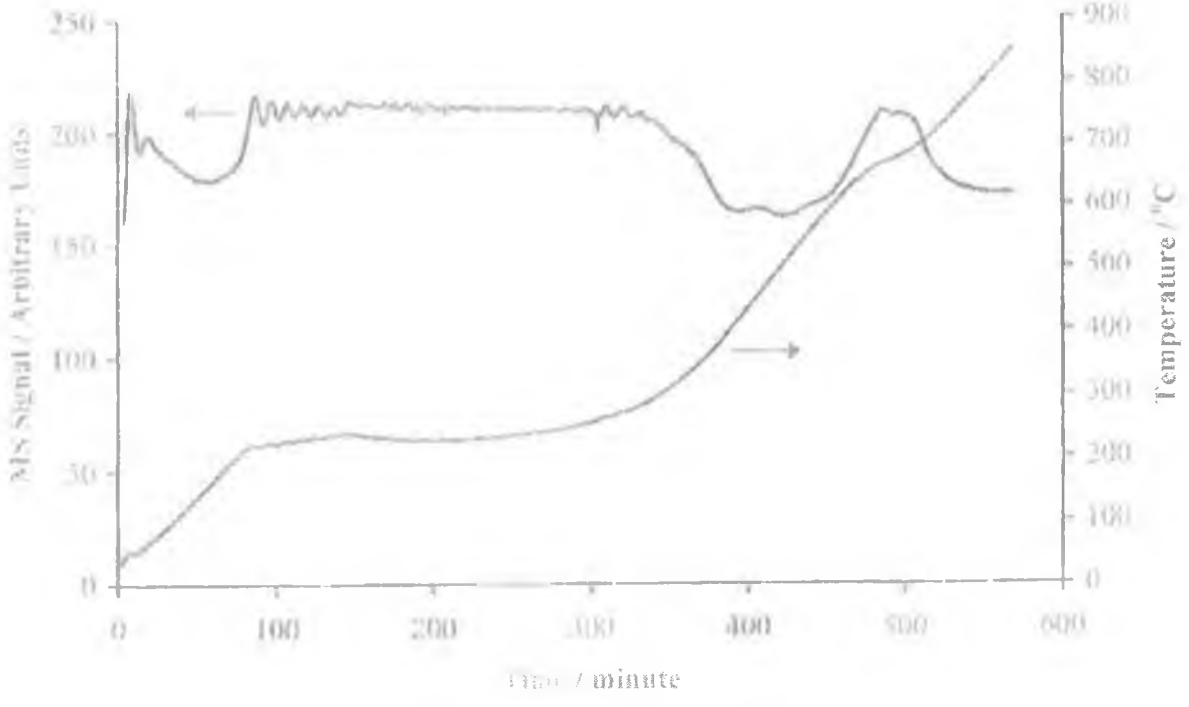

Fig. 4.10: Illustrates CR-TPR profile for the reduction of 15-wt. %Co/CeO_2. Sample size = 33mg.

The temperature trace shows how the sample temperature was continuously altered to maintain, as far as possible, the constant pre-selected rate of reduction. It can be seen that the rate of H_2O production was maintained at an approximately constant level throughout the reduction of cobalt oxide occurring in temperature rate of 220 ^{0}C – 400 ^{0}C. As for the linear heating rate profile (Fig. 4.8), the reduction feature at higher temperatures in Fig 4.10 is again attributable to support reduction.

Figure 4.11 compares the approximate $\propto$ (extent of reaction) versus temperature (T) profiles for the reduction of cobalt oxides in a 15 wt. % Co/CeO_2 catalyst under linear heating (Fig 4.11(A)) and CR-TPR (fig 4.11(B)) conditions. In both cases, the reduction feature associated with the support material in not shown (i.e. $\propto = 1$ refers to completion of cobalt oxide reduction only). The profiles obtained under CR-TPR conditions were found to be somewhat dependent on sample preparation and

experimental parameters. Under the conditions employed to obtain the profile in Fig 4.11(B), it is apparent that reduction proceeds at a lower temperature in the CR-TPR experiment. This is due to the fact that the target reduction rate was considerably lower than the maximum rate of reduction achieved in the linear heating experiment. No distinct resolution of the two reduction events is apparent in the ($\propto$) versus (T) curve obtained in the linear heating experiment (Fig 4.11(A)). However, under the CR-TPR conditions employed a change in the nature of the heating regime required to maintain a constant of reduction is apparent after $\propto \cong 0.25$. This indicates that the reduction of Co_3O_4 proceeds in a step-wise manner possibly involving complete conversion to CoO prior to subsequent reduction to metallic Co as follows:

$$Co_3O_4 + H_2 \longrightarrow 3\ CoO + H_2O \qquad \text{Step 1}$$

$$3CoO + 3H_2 \longrightarrow 3\ Co + 3\ H_2O \qquad \text{Step 2}$$

With step 1 accounting for 25% of the total H_2O production. The unfamiliar shape of the $\propto$ versus T profile in Fig 4.11 (B) can be explained in terms of the kinetic mechanism of each reduction step and the effect which the mechanism has on the heating regime required as follows:

The change in shape of $\propto$ versus T profile in Figure 4.11 (B) after the reduction is ca. 25% complete suggests that the mechanism of reduction in Steps 1 and 2 are different. The kinetics of solid-state reactions such as gas-solid reactions are generally interpreted in terms of kinetic models categorised as involving either diffusion-controlled, boundary-controlled or nucleation-controlled processes and each of these three classes of mechanism produces a characteristic $\propto$ versus T curve shape in CRTA experiments [17, 27]. In Figure 4.11 (B), it is seen that below $\propto = 0.25$ the temperature has to increase continuously to maintain the pre-selected constant rate of H_2O evolution indicating that step 1 (i.e. reduction of Co_3O_4 to CoO) followed a phase boundary controlled mechanism ('n-order' expression) where nucleation or diffusion are not the rate-controlling factors [17, 27]. In contrast, the 'u-shaped $\propto$ versus T curve seen at $\propto > 0.25$, corresponding to subsequent reduction of CoO to Co, is characteristic of a nucleation and/or autocatalytic reduction mechanism [19, 22, 27].

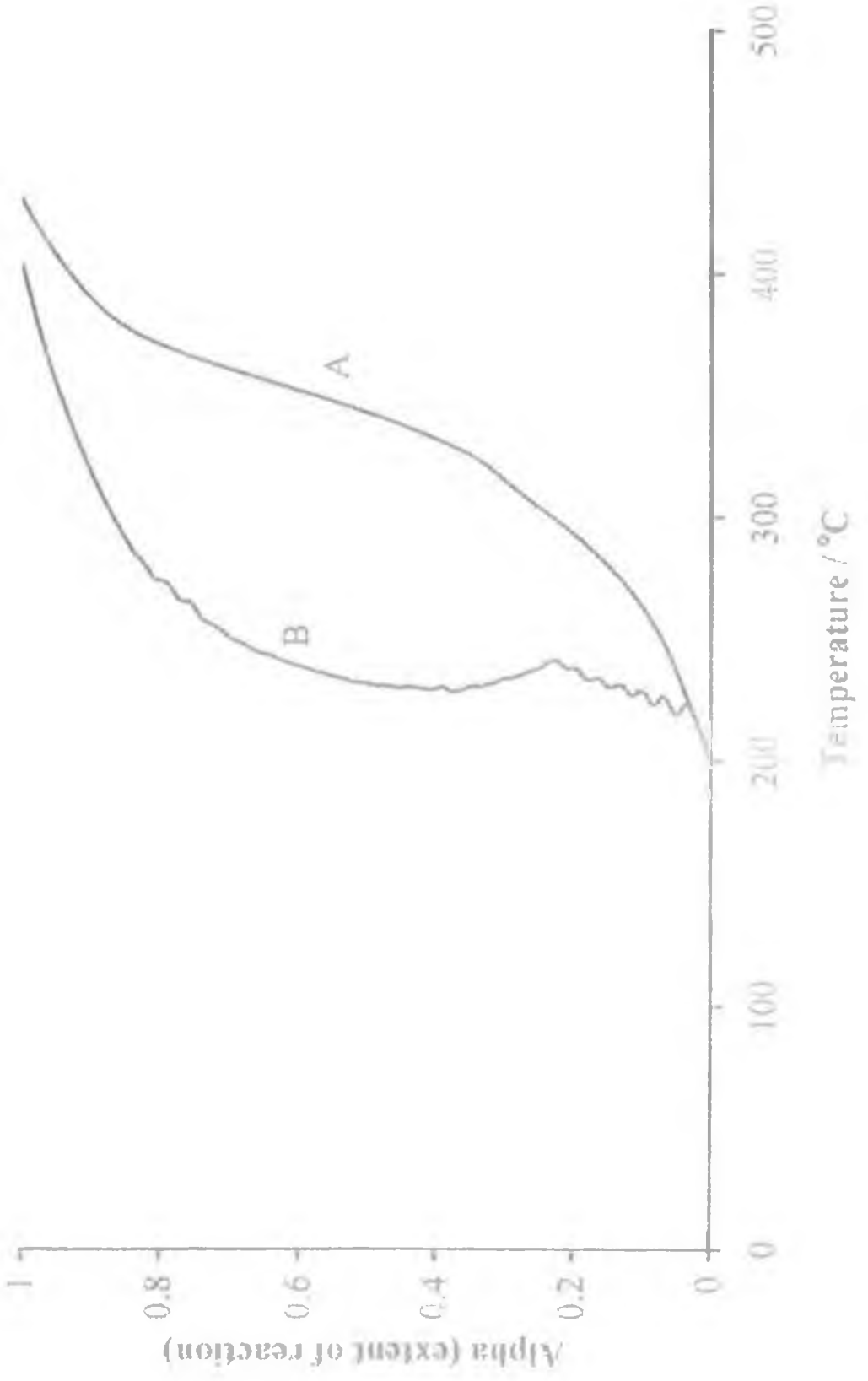

Fig.4.11: Represents a ∝ vs. temperature profile for the reduction of 15-wt. % Co/CeO2 under (A) linear heating and (B) CR-TPR conditions.

4.2.3 Activity Measurements

Preliminary tests, performed under the same conditions as the catalytic tests, but without any catalyst, showed that homogenous reactions are negligible under the experimental conditions investigated.

The results of catalytic activity for unsupported Co_3O_4 and CoO are shown in Figures 4.12(A) and 4.12(B). Both catalyst gave almost complete conversion of methane (>99%) within 600 ^{0}C. Co_3O_4 (Fig 4.12 (A)) was found to be more active than CoO (Fig. 4.12(B)) with equivalent levels of conversion achieved at lower temperatures on the former phase. In a review of the principles of oxidative catalysis, Sokolovskii [28] noted that the most active metal oxide combustion catalysts, including cobalt oxide, bind oxygen at a fast rate to produce a high concentration of reactive negatively charged species on the catalyst surface. Finocchio et al. [29] also predicted that the mechanism of hydrocarbon combustion over metal oxides, including Co_3O_4, involved surface nucleophilic lattice oxygen species. Arnone et al. [13] reported a relationship between the catalytic activity of metal oxides in methane combustion and catalytic reducibility with availability of surface lattice oxygen believed to significantly affect catalytic properties. Therefore, increased activity for Co_3O_4 relative to CoO is not unexpected in the light of its increased reductibility at lower temperatures and the higher surface area of the Co_3O_4 sample. On re-testing the unsupported oxides in Run 2, both showed a loss of activity (see Fig 4.12(A) and Fig 4.12(B)) suggesting that both undergo deactivation under the reaction conditions. This may be attributable to sintering of the active phase (which has been previously reported to occur on heating of Co_3O_4 to 600 ^{0}C [21]) resulting in a lower surface area available for adsorption or reaction of gaseous components [12]. The BET surface area of the CoO and Co_3O_4 samples decreased by 63% to 3 m^2 g^{-1} and by 43% to 13 m^2 g^{-1}, respectively, upon testing in the reaction mixture for Runs 1 and 2. In the case of Co_3O_4, deactivation may also have been related to conversion to less active CoO phase at temperatures above 450 ^{0}C [13]. A plot [Fig 4.13(A) and 4.13(B)] of methane conversion versus time for both bulk Co_3O_4 and CoO shows this trend in deactivation. However, the deactivation for the unsupported CoO is less pronounced than the Co_3O_4 phase. This maybe attributed to the bulk properties of Co_3O_4 and CoO, which show reduction of

the Co_3O_4 to CoO at temperature of <500 Kelvin whereas the second reduction step which produces metallic cobalt occurs in a much wider temperature range (623-873 K). The presence of CoO, as well as Co_3O_4, was indicated in the XRD pattern of the Co_3O_4 sample obtained after testing in Runs 1 and 2.

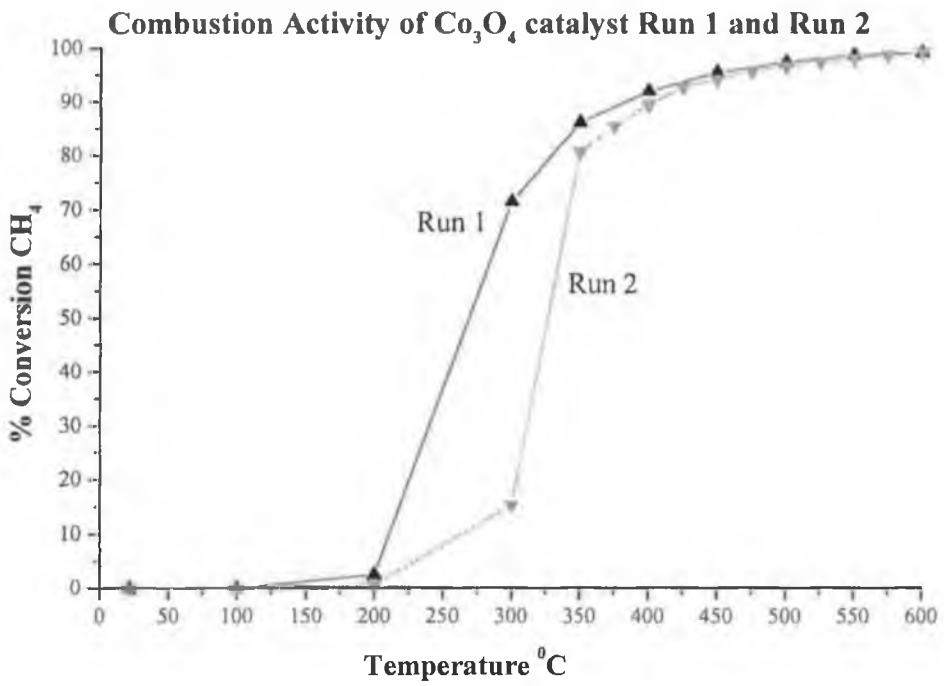

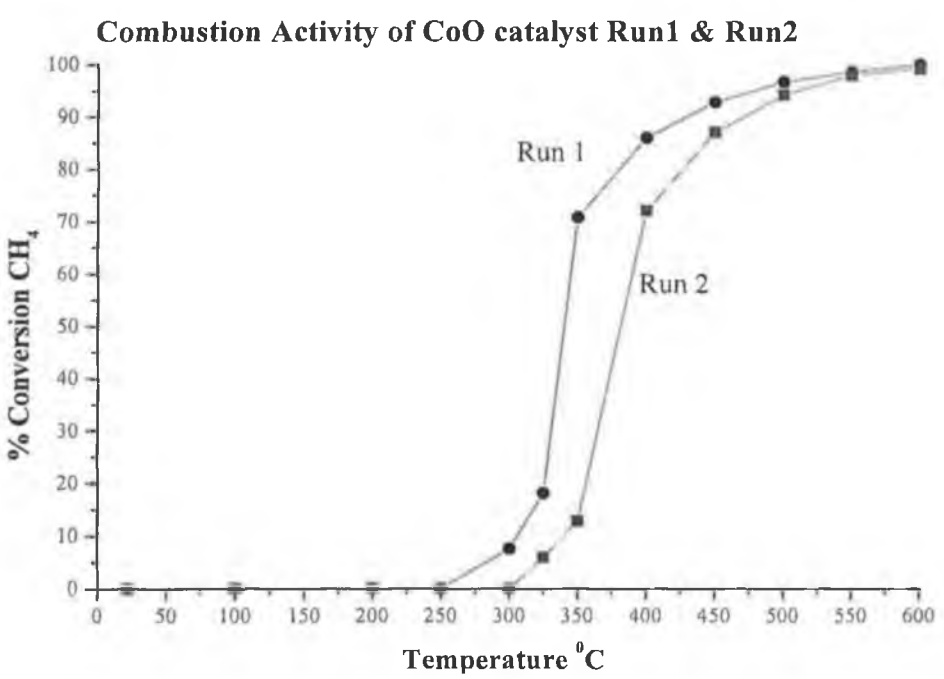

Fig 4.12(A) and 4.12(B): Above represents a graph of the CH_4 conversion as a function of temperature for both bulk Co_3O_4 and CoO.

Fig 4.13(A) and 4.13(B) shows plots of CH_4 conversion as a function of time for both bulk Co_3O_4 and CoO.

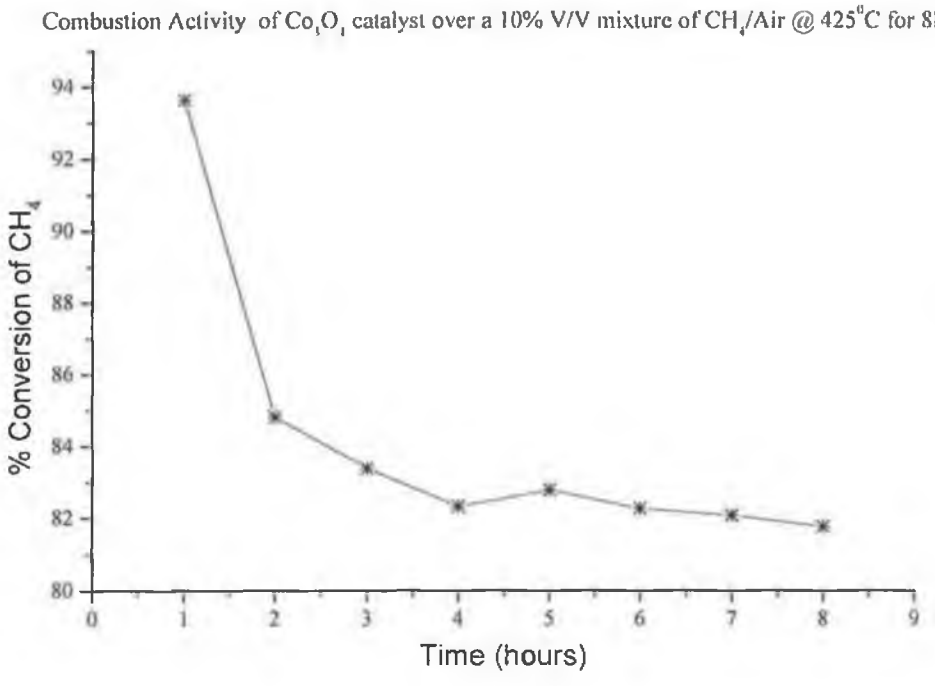

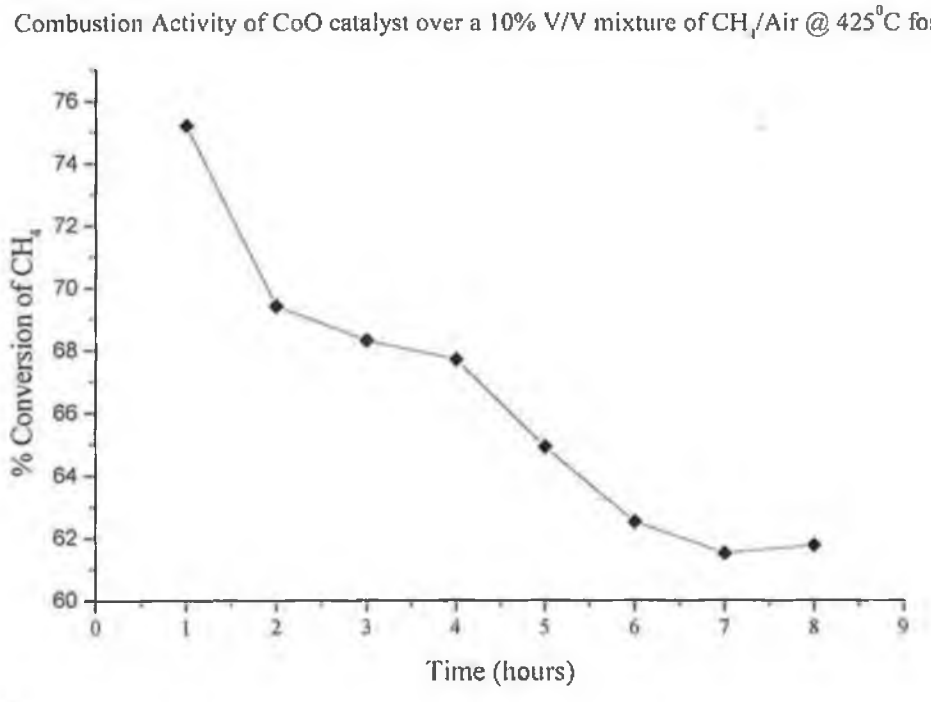

Table 4.2 reports the temperatures (T_{50} values) at which methane conversion exceeded 50% over the various supported and unsupported samples tested. T_{50} values for Al_2O_3-supported Pt and Pd catalysts are also sown for comparison purposes. This temperature is usually denoted the 'light-off' temperature and is of particular importance in relation to the 'cold-start' emissions problem in automotive exhausts discussed above [12].

Table 4.2: Temperature of 50% CH_4 conversion for cobalt catalysts

Sample	Metal content (mass %)	Calcination Temperature (°C)	T_{50} (°C)	
			Run 1	Run2
Pt/Al_2O_3	0.5	630	470	475
Pd/Al_2O_3	0.5	630	330	340
Co/Al_2O_3	5	400	>500	>500
Co/ZrO_2	5	400	390	425
Co/Al_2O_3	5	600	>500	>500
Co/ZrO_2	5	600	490	500
Co/CeO_2	5	600	410	495
Co/Al_2O_3	15	400	>500	>500
Co/ZrO_2	15	400	395	420
Co/CeO_2	15	400	[illegible]	[illegible]
Co_3O_4	-	-	370	380
CoO	-	-	540	580
CeO_2	-	400	540	535

The most active supported catalyst tested was 0.5 wt. % Pd/Al_2O_3 which achieved 50% conversion at a temperature of 330 ^{0}C (see table 4.2). Higher activity for Pd relative to Pt for the combustion of methane has been related to the different abilities of the two metals to adsorb oxygen [30-32]. In the current study, both Co/ZrO_2 and

Co/CeO_2 samples, which were calcined at 400 ^0C prior to testing, showed higher activity than Pt/Al_2O_3 although it should be noted that the concentration of metal (wt.%) was 10 to 20 times higher in the case of the cobalt samples tested. Considering the support materials in the absence of cobalt, CeO_2 support [Fig 4.14(A) and 4.14(B)] below showed some combustion activity at higher temperatures within the range investigated in line with previous observations that it is an active methane combustion catalyst at elevated temperatures [33]. However, T_{50} was considerably lower in the presence of Co, particularly for Run 1 (see Table 4.2) during which CeO_2 did not contribute to the light-off activity (i.e. conversion at T_{50}) of the supported Co catalysts tested since on its own it shared no combustion activity at or below 400 ^0C. During Run 2, a methane conversion of 5% was achieved over CeO_2 at the light-off temperature of the 15 wt. $\%Co/CeO_2$ sample indicating that the majority of light-off performances for this sample is related to the presence of cobalt. In the case of both ZrO_2 and Al_2O_3 supports, no appreciable activity existed below 500 ^0C.

It is known that the use of Al_2O_3 as the support medium can significantly decrease the activity of cobalt-based combustion catalyst [9, 23]. From Table 4.2 it can be seen that ZrO_2 and CeO_2 supported samples were considerably more active than the corresponding Al_2O_3 supported catalyst. This is further illustrated in Figure 4.15 below which compares results for the conversion of methane as a function of temperature up to 500 ^0C over supported cobalt catalysts containing 15 wt.% Co

The lower activity for the high surface area Al_2O_3-supported sample is most probably attributable to the formation of a spinel $CoAl_2O_4$ phase or other inactive surface species involving intimate contact between highly dispersed Co and surface Al_2O_3 sites [23, 26] as indicated in the TPR profile.

Previously a correlation between the ease of catalyst reducibility and methane combustion activity has been proposed with oxides reduced at a lower temperature giving rise to a mechanism with a lower activation energy [13]. A similar correlation exists in the current study for supported oxides with alumina-supported samples which required particularly high temperatures of reduction in TPR experiments (see Figure 4.9) showing poorest performance in catalytic tests (see Table 4.2).

From table 4.2, it can be seen that for supported cobalt oxide catalysts, exposure to the stoichiometry air-methane reaction mixture during Run 1 generally resulted in decreased light-off activity during subsequent testing in Run 2. As discussed above, this also was the case for the unsupported cobalt oxides with possible explanations for

the deactivation including sintering of the active phase during testing or conversion of an active Co_3O_4 phase to less active CoO when exposed to temperatures above 450 ^{0}C [13]. A 5 Wt. % Co/ZrO_2 catalyst calcined at the higher temperatures of 600 ^{0}C was considerably less active than a corresponding sample calcined at 400 ^{0}C which again is probably associated with such sintering or phase conversion phenomena causing decreased activity after exposure to the higher temperatures. This shows that, even in the absence of alumina, the possibility of catalyst deactivation during operation must be considered if cobalt oxide is to become a viable commercial alternative to, or addictive in, noble metal combustion catalysts. The potential of employing higher surface area CeO_2 and ZrO_2 materials will be investigated in a further study.

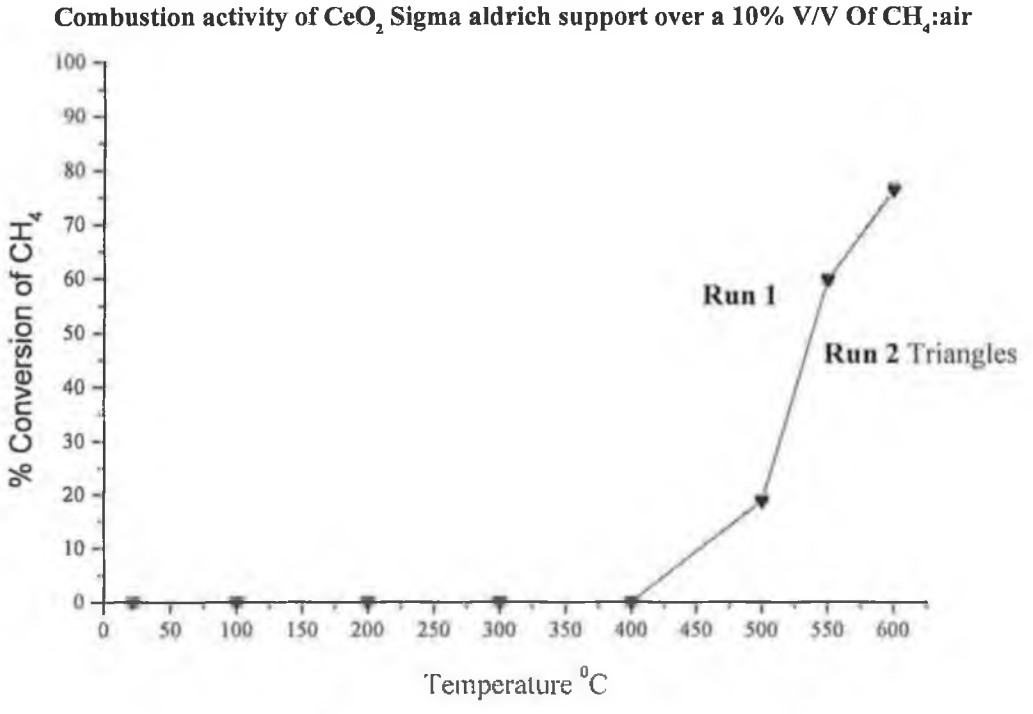

Fig. 4.14(A): Represent a plot of methane conversion as a function of temperature for a CeO_2 support (sigma Aldrich, 99.9%)

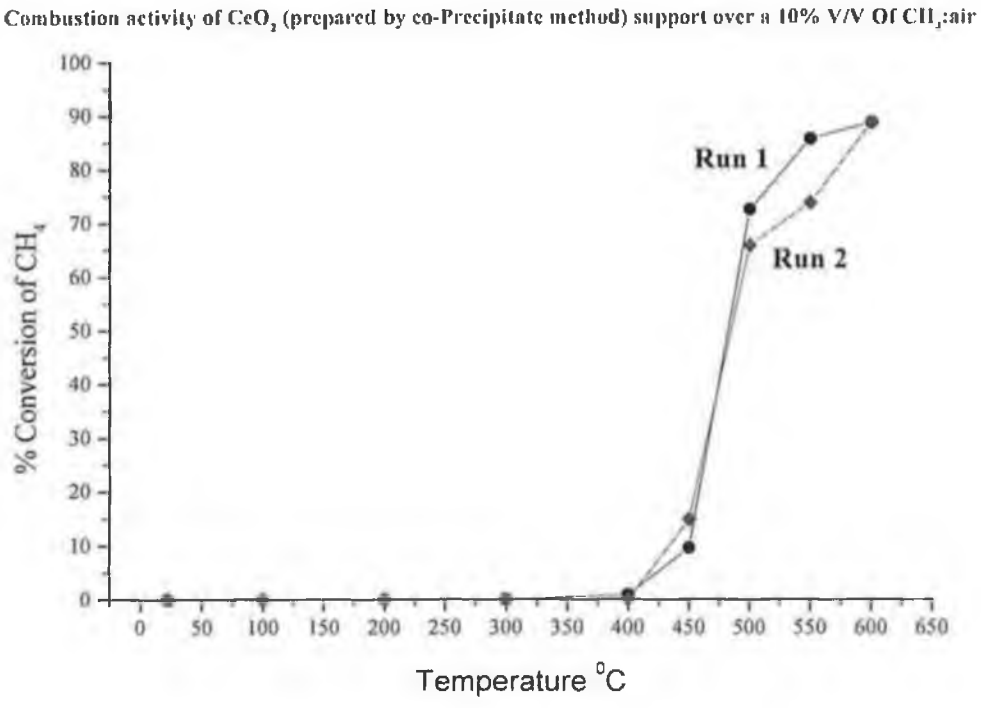

Fig. 4.14(B): Represent a plot of methane conversion as a function of temperature for a CeO_2 support (prepared via co-precipitate method).

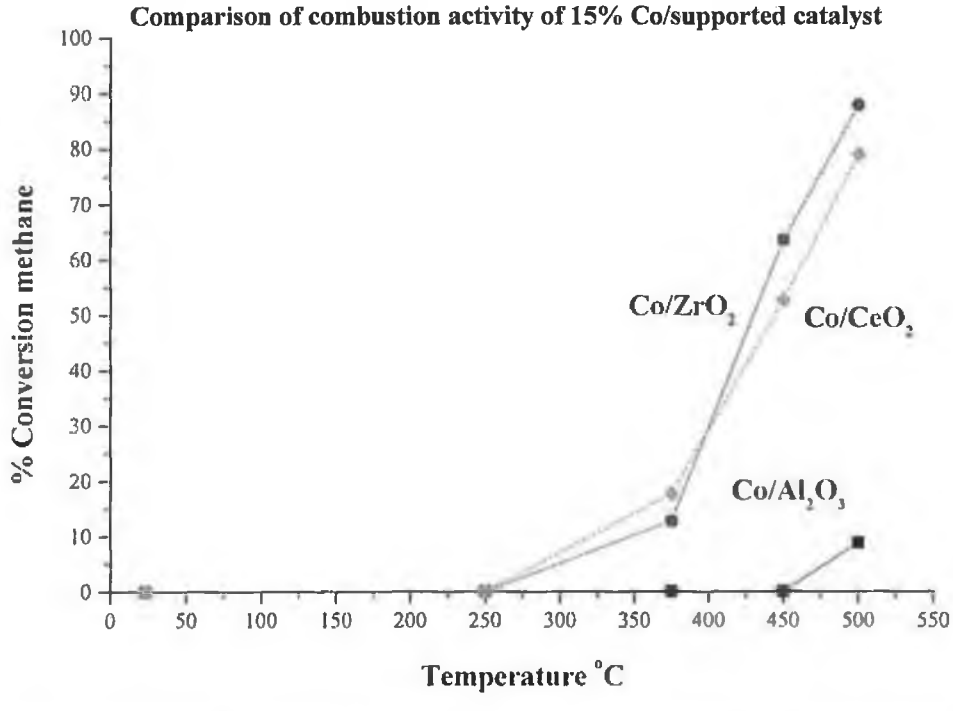

Fig. 4.15: Represents a plot of CH_4 conversion as a function of temperature for supported Co (15 Wt.%) catalysts, (A) Co/ZrO_2 (B) Co/CeO_2 and (C) Co/Al_2O_3

4.3 Conclusions

SIP-MS was used to determine the effects of different support materials on the thermal decomposition of cobalt nitrate hexahydrate under linear heating rate conditions. Compared to the unsupported nitrate completion of the decomposition process was delayed until higher temperatures for all the supported samples analysed. In particular, dispersion of $Co(NO_3)_2.6H_2O$ on Al_2O_3 had a pronounced effect on the decomposition profile observed while ZrO_2 and CeO_2 supports resulted in more subtle changes to the decomposition profile. This was attributed to strong interactions between cobalt ions and the high surface area Al_2O_3- support material during preparation. TPR-MS profiles also indicated the presence of an intimate metal-support interaction upon calcinations of Al_2O_3-supported cobalt nitrate in air, which had a strong detrimental effect on the activity for methane combustion. For CeO_2 and ZrO_2 supported samples, TPR profiles were consistent with a two-step reduction of Co_3O_4 via CoO to metal. CR-TPR indicated that the first step of the reduction followed a phase-boundary controlled mechanism while the second step proceeded via nucleation or autocatalytic mechanism. Cobalt oxide supported on ceria or zirconia as well as cerium support were shown to be a highly active catalyst for the combustion of CH_4 although in both cases deactivation was observed upon exposure to the reaction mixture which maybe associated with sintering or the conversion of Co_3O_4 to a less active CoO phase. Experiments to determine the extent of deactivation of these catalysts over long periods of exposure in the reaction mixture were analysed using a pulse microcatalytic technique to measure the % methane conversion Vs time. Deactivation of the active phase was observed during their exposure time to the reaction mixture.

This work has been published, the application of CRTA and linear heating thermoanalytical techniques to the study of supported cobalt oxide methane combustion catalyst, Thermochimica Acta 379 (2001) 163-175.
M. J. Tiernan, E. A. Fesenko, P. A. Barnes, G. M. B. Parkes and M. Ronane

References

[1] E. E. Wolf, 'Methane Conversion by Oxidative Processes', Van Norstrand Reinhold, New York (1992).

[2] T. H. Etsell and S. N. Flengas, J. Electroch. Soc., **118**, 1890 (1971).

[3] D.L. Trimn, Appl. Catal., **7**, 249 (1983).

[4] M. F. M. Zwinkels, S.G. Jaras and P.G. Menon, Catal. Rev. Sci. Eng., **35**, 319 (1993).

[5] J. T. Kummer, Prog. Energy Combust Sci., **6**, 177 (1980).

[6] V. R Choudary, B. S. Uphade, S. G. Pataskar and A Keshavaraja, Agnew. Chem. Int. Ed. Eng., **35**, 2393 (1996).

[7] L. A. Isupova, G. M. Alikina, O. I. Snegurenko, V. A. Sadykov and S. V. Tsbulya, Appl. Catal. B, **21**, 171 (1999).

[8] R. J. H. Grisel, P. J. Kooyman and B. E. Nieuwenhuys, J. Catal., **191**, 430 (2000).

[9] R. B. Anderson, K. C. Stein, J. J. Feenan and L. J. E. Hofer, Ind. Eng. Chem., **53**, 809 (1961).

[10] W. P. Yant and C. O. Hawk, J. Am. Chem. Soc., **49**, 1454 (1927).

[11] P. Y. Lin, M. Skoglundh, L. Lowendahl, J. E. O Tterstedt, L. Dahl, K. Jansson and M. Nygren, Appl. Catal. B, **6**, 237 (1995).

[12] A. Torncrona, M. Skoglundh, P. Thormahlen, E. Fridell and E. Jobson, Appl. Catal. B, **14,** 131 (1997).

[13] S. Arnone, G. Bagnasco, G. Busca, L. Lisi, G. Russo and M. Turco, in A. Parmaliana, D. Sanfilippo, F Frusteri, A. Vaccari and F. Arena (Eds.), Natural Gas Convertion V, Studies in Surface Science and Catalysis, Vol. **116**, Elsevier, Amsterdam, p. 113 (1998).

[14] M. Skoglundh, A. Torncrona, P. Tormählen , E. Fridell, A. Drewsen and E. Jobson, N. Kruse, A. Frennet, J.M. Bastin (Eds.), in Catalysis and Automotive Pollution Control IV, Studies in Surface science and Catalysis, Vol. **116**, Elsevier, Amsterdam, pg. 113 (1998).

[15] M. Niwa K. Awano and Y. Murakami, Appl. Catal., **7**, 317 (1983).

[16] Y.M. Yang and B.Z. Wan, Appl. Catal. A, **114**, 35 (1994).

[17] M.J. Tiernan, P.A. Barnes and G. M. B. Parkes, J Phys. Chem. B, **103**, 6944 (1999).

[18] N. W. Hurst, S. J. Gentry, A. Jones and B. D. Mc. Nicol, Catal. Rev. Sci. Eng., **24**, 233 (1982).

[19] M. J. Tiernan, P. A. Barnes and G. M. B. Parkes, J. Phys Chem. B, **103**, 338 (1999).

[20] T. Cseri, S. Bekassy, G. Kenessy, g. Liptay and F. Figureas, Thermochim. Acta, **288**, 137 (1996).

[21] S. A. A. Mansour, Materials Chemistry and Physics, **36**, 317 (1994).

[22] P. A. Barnes, M. J. Tiernan, G. M. B. Parkes, J. Therm. Anal and Calorim., **56**, 733 (1999).

[23] P. G. Dimitroa and D. R. Mehandjiev, J. Catal., **145**, 356 (1994).

[24] P. Arnoldy and J. A. Mouljin, J. Catal., **93**, 38 (1985).

[25] H-C. Tung and C-H. Yeh, J. Catal., **122**, 211 (1990).

[26] R. Bechera, D.Balloy, J. Y. Dauphin and J. Grimblot, Chemistry of Materials, **11**, 1703 (1999).

[27] J. M. Criado, A. Ortega and F. Gotor, Thermochim. Acta, **157**, 171 (1990).

[28] V. D. Sokolovkkii, Catal. Rev. Sci. Eng., **32**, 1 (1990).

[29] E. Finocchio, G. Busca, V. Lerenzelli and V. S. Escribano, J. Chem. Soc. - Farad. Trans., **92**, 1587 (1996).

[30] C. F. Cullis and B. M. Willatt, J. Catal., **83**, 267 (1983).

[31] S. H. Oh, P. J. Mitchell and R.M. Siewert, J. Catal., **132**, 287 (1991).

[32] R. F. Hicks, H. Qi, M. L. Young and R. G. Lee, J. Catal., **122**, 280 (1990).

[33] F. Zamar, A Trovarelli, C. de Leitenberg and G. Dolcetti, J. Chem. Soc., Chem. Commun., **9**, 965 (1995).

Appendix

High purity activated aluminas

Puralox Powders - aluminium oxides (gamma-delta-theta phase).

Chemical / Physical Properties	Puralox SCFa-250	Puralox SCFa-140 L3
Al_2O_3 %	98	95
Na_2O %	0.002	0.002
La_2O_3 %	---	3
L.O.I. %	2	2
Loose bulk density [g/l]	500-800	500-700
Packed bulk density [g/l]	800-1000	700-1000
Particle size (d_{50}) [µm]	20	30
Surface area (BET)** [m^2g^{-1}]	210	140
Pore volume [ml/g]		
Pore size radius [nm]	0.35-0.50	0.50
	4-10.0	8
Thermal stability:		
Surface area: Aged 24h/1100°C [m^2g^{-1}]	15	80
Surface area: Aged 24h/1100°C [m^2g^{-1}]	5	40

** Figures show the range of surface areas (± 10m^2g^{-1})

Appendix A:

Calculation of Total Surface area by Physisorption of N_2 was determined from the BET equation as follows,

$$\frac{P}{[n_s(P_O - P)]} = [1/(n_m C)] + [(C-1)/(n_m C)]\left(\frac{P}{P_O}\right) \quad (1)$$

Using a Gemini III 2375 surface area analyser (i.e. Gemini– Micromeritics BET instrument) with in built software programme containing all the necessary data as read below.

Set-up Conditions

System options

Language – English
Instrument ID. – Blank
Date/Time – Set
Sample ID. - Set
Sample Weight – Set
Saturation pressure (P_O) – 760mmHg
Correction Volume - +0.000 @ STP

Analysis Conditions

Evaluation Time – 3.0 minutes
Free Space – Previous
Sample Density – Blank
Pressure table – Replace

First Relative Pressure – 0.0500 P/P_O

Last Relative Pressure – 0.3000 P/P_O

Number of Data Points measured – 5

Analysis Mode – Scan

Equilibration Time – Blank

Scan Rate - 10

Report Options

Transmission Format – Single Column

Area Points measured from - 0.400 P/P_O

Area Points measured to – 0.3100 P/P_O

BET Multipoint Measured - Yes

Reported Langmuir – No

Total Pore Volume – None

N_2 Molecular area – 0.162 $(Nm)^2$ (i.e. 16.2×10^{-20})

Density Conversion – 0.0015468

Non-Ideality Factor – 5.0% / atm

From this data programmed into the Gemini III 2375 surface area analyser, a linear plot of P/Po against $P/n_s(Po-P)$ giving a of slope $(C-1)/(n_mC)$ and intercept of $1/(n_mC)$. Hence, the surface area of the catalyst can then be obtained by multiplying the number of N_2 molecules (required for monolayer coverage) by the exact surface area of one N_2 molecule ($0.162nm^2$). So the overall formula for calculating the surface area becomes:

$$\text{Surface area} = n_m . (6.023\times10^{23}) . (1.62\times10^{-19}\ m^2) \qquad (2)$$

The value obtained from this equation is related to the weight of sample used, to get the specific surface area, this value is represented per unit weight as m^2g^{-1}. This equation has become the standard one for determining surface areas, usually with N_2 at 77K as the adsorbate. However, the region of fit is not very great, the linear region of a plot lies

between a partial pressures of 0.05 and 0.3. This deviation is such that the best-fitted BET equation predicts too little adsorption at low pressures and too much at high pressures.

Appendix B:

Calculations of Pt Surface Area, % Dispersion and Particle Size from H_2 Chemisorption Data:

Pt Surface Area

$$S_{pt} = n_m \times X_m \times A \times n_s^{-1} \quad (1)$$

Where, S_{Pt} = Pt Surface area.

X_m = chemisorption stoichiometry (i.e. the number of H_2 molecules reacting per surface Pt atom = 2.

n_m = number of moles of adsorbed gas by the catalysts.

A = Avogadro's constant = 6.023×10^{23} atoms/mole of Pt.

n_s = number of Pt atoms per unit area of surface ($1.25 \times 10^{19} m^2$/atom).

$$\text{Vads (ml)} = \left(\frac{PeakArea1 - PeakArea2}{PeakArea1} \right) \text{x } 0.053 \quad (2)$$

Where, Peak area 1 is prior to chemisorption, Peak area 2 is after chemisorption and 0.053mls is the loop volume (cm^3).

$$\text{Vad ml/g @ STP } (cm^3 g^{-1}) = \frac{Vads(ml)}{W} x \frac{273K}{R.T.} x \frac{R.P}{760} \quad (3)$$

$V_{ads}g^{-1}$S.T.P = volume of H_2 adsorbed per gram of catalysts sample at standard temperature and pressure

w = final catalysts sample weight

R.T. = room temperature (kelvins)

R.P. = atmosphere pressure (mmHg)

$$N_m\,(\text{molesg}^{-1}) = V_{ads}\,g^{-1}S.T.P./22414 \qquad (4)$$

Where 22414 = volume occupied by one mole of gas at standard temperature and pressure S.T.P (cm^3mole^{-1}).

Substituting equation n_m into equation 1 gives us S_{Pt},

$$S_{Pt}\,(m^2Pt/g\ \text{Catalyst}) = \frac{(n_m)(2\times 6.023\times 10^{23}/1.25\times 10^{19})}{STP} \qquad (5)$$

This equation (5) was used to calculate the Pt surface area in the catalysts.

% Metal Dispersion

Dispersion is the ration of the total number of surface atoms to the total number of metal atoms present. Therefore the % metallic dispersion, $\%D_m$ maybe calculated by the equation:

$$\%D_m = Pt_s/Pt_t \times 100 \qquad (6)$$

Where, Pt_s is the number of Pt surface atoms and Pt_t is the total number of Pt atoms present.

Using the previous equation derived above, an equation for Pt_s can be derived and Pt_s can be calculated as follows,

$$Pt_s = (V_{ads}\,g^{-1}S.T.P/22414)(X_m \times A) \qquad (7)$$

Pt_t is calculated from the total metal content determined by AAS. The number of grams Pt per gram catalysts is given by,

(1g/100) %w/w × %Pt (8)

Then convert one gram of Pt into the number of Pt atoms by,

$A/m = 6.023 \times 10^{23}/m$ (9)

Where, m = 195.1 g/mole (i.e. molecular weight of Pt metal). Hence, combining equation 8 and 9 gives us Pt_t.

Pt_t (atoms/g catalyst) = (0.01 × % Pt) (6.023×10^{23}/195.1) (10)

Now combining the equation of Pt_s and Pt_t gives us %Dm,

$$\% \text{ (Dm)} = \frac{(V_{ads}\, g^{-1} S.T.P \times 2 \times 6.023 \times 10^{23} / 22414)}{\frac{(0.01 \times \%Pt \times 6.023 \times 10^{23})}{195.1} \times 100} \text{ or } D = \frac{AU}{vW} \times 100\% \quad (11)$$

Average Mean Pt Particle Diameter

The mean particle size of Pt can be calculated by making an assumption that the Pt particles are spherical in shape.

D= 6 × (volume)/ (surface area) (12)

Where, D = the diameter equation of a sphere,

Now after calculation the diameter of a sphere, the average diameter of the Pt particle can be calculated using the equation,

$$D\,(\text{Å}) = 6 \times 10^4 / 21.5 \times S_{Pt}) \text{ or } d\,(\text{Å}) = (D/\rho \times S_M) \quad (13)$$

Where, 21.5 is the density of Pt in gcm^{-3} at R.T., and S_{Pt} is the Pt surface area in m^2g^{-1} of Pt.